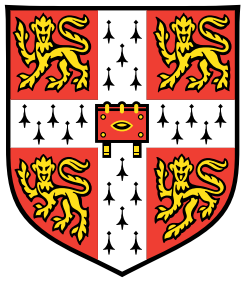

University of Cambridge
Institute of Astronomy

A dissertation submitted to the
University of Cambridge for the degree
of Doctor of Philosophy

Protoplanetary discs across the stellar mass range

Dominika Maria Rita Boneberg
Murray Edwards College

Submitted to the Board of Graduate Studies
March 2018

Under the Supervision of
Prof. Cathie J. Clarke
Dr John D. Ilee

ABSTRACT

In this thesis, I discuss two studies concerned with modelling protoplanetary discs around stars from different ends of the stellar mass range. In Chapters 1 and 2, I give an introduction to the field of protoplanetary discs, both from an observational and a modelling point of view, and describe the radiative transfer methods I have employed.

In Chapter 3, I present my work regarding the disc around the Herbig Ae star HD 163296. I show the results of applying a new modelling technique to this disc: I combine SED modelling with fits to the CO snowline location and $C^{18}O$ $J = 2 - 1$ line profile from ALMA. I find that all of the modelling steps are crucial to break degeneracies in the disc parameter space. The use of all of these constraints favours a solution with a notably low gas-to-dust ratio ($g/d < 20$). The only models with a more interstellar medium (ISM)-like g/d require $C^{18}O$ to be underabundant with respect to the ISM abundances and a significant depletion of sub-micron grains, which is not supported by scattered light observations. I propose that the technique can be applied to a range of discs and opens up the prospect of being able to measure disc dust and gas budgets without making assumptions about the g/d ratio.

In Chapter 4, I present my work on characterising the disc around the very low mass star V410 X-ray 1. Protoplanetary discs around such low mass stars offer some of the best prospects for forming Earth-sized planets in their habitable zones. The SED of V410 X-ray 1 is indicative of an optically thick and very truncated dust disc, with my modelling suggesting an outer radius of only 0.6 au. I investigate two scenarios that could lead to such a truncation, and find that the observed SED is compatible with both. The first scenario involves the truncation of both the dust and gas in the disc, perhaps due to a previous dynamical interaction or the presence of an undetected companion. The second scenario involves the fact that a radial location of 0.6 au is close to the expected location of the H_2O snowline in the disc. As such, a combination of efficient dust growth, radial migration, and subsequent fragmentation within the snowline leads to an optically thick inner dust disc and larger, optically thin outer dust disc. I find that a firm measurement of the CO $J = 2-1$ line flux would distinguish between these two scenarios by enabling a measurement of the radial extent of gas in the disc. Many models I consider contain at least several Earth-masses of dust interior to 0.6 au, suggesting that V410 X-Ray 1 could be a precursor to a system of tightly-packed inner planets, such as TRAPPIST-1.

In Chapter 5, I summarise the work presented in this thesis, give an overview of future applications of the methods outlined in this dissertation, and an outlook on potential future projects.

DECLARATION OF ORIGINALITY

I, Dominika Maria Rita Boneberg, declare that this dissertation entitled *'Protoplanetary discs across the stellar mass range',* and the work presented in it, is the result of my own work and includes nothing which is the outcome of work done in collaboration except as declared in the Preface and specified in the text. Those parts of this thesis which have been published or accepted for publication are as follows:

- **Chapter 3** is based on work completed in collaboration with O. Panić, T.J. Haworth, C.J. Clarke and M. Min and is published as Boneberg et al. (2016):

  Boneberg, D.M.; Panić, O.; Haworth, T.J.; Clarke, C.J., Min, M. (2016) *'Determining the mid-plane conditions of circumstellar discs using gas and dust modelling: a study of HD 163296'*, MNRAS, 461, 385-401

  The code MCMax used in this chapter was kindly provided by M. Min, the code TORUS by T. Haworth. I was responsible for the complete modelling with both codes, the joint development of their interfacing, the analysis of the models obtained and the comparison to observations. I wrote the initial draft of the publication and then incorporated comments from all co-authors for the final draft.

- **Chapter 4** has been completed in collaboration with S. Facchini, C.J. Clarke, J.D. Ilee, R.A. Booth and S. Bruderer and has been accepted for publication in MNRAS as Boneberg et al. (2018):

  Boneberg, D.M.; Facchini, S.; Clarke, C.J.; Ilee, J.D.; Booth, R.A.; Bruderer, S. (2018) *'The extremely truncated circumstellar disc of V410 X-ray 1: a precursor to TRAPPIST-1?'*, MNRAS, 477, 325-334

  The code DALI was kindly provided by S. Facchini and S. Bruderer, I significantly adapted it in order to obtain models in vertical hydrostatic equilibrium. I was responsible for the modelling, the analysis of its outputs, and the comparison to observations. I wrote the initial draft of the publication and then incorporated comments from all co-authors for the final draft.

I confirm that this thesis is not substantially the same as any that I have submitted, or, is being concurrently submitted for a degree or diploma or other qualification at the University of Cambridge or any other University or similar institution except as declared in the Preface and specified in the text. I further state that no substantial part of my dissertation has already been submitted, or, is being concurrently submitted for any such degree, diploma or other qualification at the University of Cambridge or any other University or similar institution. The length of this thesis does not exceed the stated limit of the Degree Committee of Physics and Chemistry of 60,000 words.

Dominika Maria Rita Boneberg *Cambridge, May 10, 2018*

ACKNOWLEDGEMENTS

There are many people to whom I am immensely grateful for supporting me during these past 3.5 years. I would like to especially thank Cathie Clarke and John Ilee for their supervision and brilliant support, help and guidance. Cathie, I have learned so much from you and your enthusiasm and fascination for astronomy and physics in general is truly contagious. John, thanks so much for answering all my questions, your patience and invaluable encouragement.

A special thanks goes to all the members of the DISCSIM group: Olja, thanks a lot for being my secondary supervisor during the first half of the PhD. Giovanni, Attila, Richard, Marco, Farzana, Andrew and Mihkel, your encouragement and help have been great and I'm so sorry for popping up at your doors and asking so many questions. Discussing and working with you has been a pleasure. Attila, many thanks for your help with the observational data and CASA. I must also say a huge thank you to Tom Haworth and Stefano Facchini for the amazing collaboration. I have learned so much from you and the projects wouldn't have been the same without your constant support. A big 'thank you' also to Luca, for all his help with ALMA and NOEMA proposals. Thanks must also go to Michiel Min and Simon Bruderer for providing the codes I have used, joining the projects and your valuable input.

Many thanks also to my examiners Paul Hewett and Jane Greaves. Thanks for your positive feedback, the interesting questions and discussion during the viva, and for making me feel so comfortable.

I would like to especially thank the PhD students in my year group: Björn, Matt, Clare, Matthew, Lindsay, Nimisha, Sarah, Anna and Deyan. We had so much fun (just thinking about the Friday pub evenings including the mighty jar), and our joint moaning about thesis writing has made it so much easier. The same holds true for all the office mates I had during the past years: Sophie, Simon, Matt, Lindsay, Clare, Matthew, Chris, Daniel and Haonan. It's been great fun working in the same offices (Obs 14 with the Christmas tree and Halloween/Easter decoration, H26 with all the squirrels) and the cakes have been a blast. A big 'thank you' must also go to my housemates (past and present): Matt, Björn, Christina and Clare. We had a lot of fun and I will miss our British BBQs and the whiteboard with the special German-English dictionary.

I must also say a huge 'thank you' to everybody at the IoA, especially Debbie Peterson and Margaret Harding for making me feel so welcome in the department, their open door, advice and support in all administrative matters. Thanks a lot also to Mandy Cockrill for always being so cheerful and all the kind words. I would also like to thank the IoA helpdesk team for so quickly solving all my computer related issues. Carolin Crawford and Sonali Shukla, thanks so much for the opportunity to share my passion and enthusiasm for sci-

ence and astronomy with the general public. I very much enjoyed writing the handouts for the Open evenings, giving a talk there and participating in the Science Festivals. All of this has given me the chance to improve my writing and presenting skills and has been decisive for my future career.

A huge thank you also goes to Harald Lesch and Cecilia Scorza for all their advice and guidance and encouragement to pursue a career in outreach and science communication/journalism. It is amazing to have you as mentors.

Thanks a lot also to Ann and Nessa, who have supported me so wonderfully when the PhD was difficult. I have learned a lot from you and am immensely grateful for your encouragement.

A special thanks goes to my good friends Philippa and Marie and all the people at the CBC. You have made my time here in Cambridge such an amazing experience, I will miss your encouragement, Saturday brunch at Murray Edwards and all our interesting and fun conversations. I am also very grateful to Maddie, David and the other members of the King's gardening crew. We had so much fun and being outside with you working on the allotments has been a wonderful balance to my daily computer work.

I would like to especially thank my family. Mum, Dad, Raphi and Aline, this PhD would not have been possible without you. Your positivity and constant belief in me have made such a difference and have kept me afloat when the PhD was tough. Thanks so much for your honest advice and constant interest in my work. A big thank you must also go to Björn's family, your encouragement has been so valuable.

And last but not least, Björn. I cannot put into words how grateful I am for your love and constant support throughout these past 9 years. You cheer me up when all else fails and I am so happy that we went through all this together.

Contents

List of Figures xiii

List of Tables xv

1 Introduction 1
- 1.1 The formation of protoplanetary discs . . . 1
- 1.2 Disc structure and evolution . . . 5
  - 1.2.1 Density and temperature structure . . . 6
  - 1.2.2 Disc evolution . . . 8
  - 1.2.3 Viscosity . . . 9
  - 1.2.4 Grain growth and dust opacities . . . 12
- 1.3 Observations of dust in protoplanetary discs . . . 15
  - 1.3.1 The spectral energy distribution (SED) . . . 15
  - 1.3.2 Degeneracies in SED modelling . . . 19
  - 1.3.3 Physical properties from dust emission . . . 21
- 1.4 Observations of gas in protoplanetary discs . . . 24
  - 1.4.1 Molecular line observations . . . 25
  - 1.4.2 Examples of depletion mechanisms . . . 29

2 Methods: Radiative transfer 33
- 2.1 The formal radiative transfer equation . . . 33
- 2.2 The source function . . . 36
- 2.3 The 'Monte Carlo' method . . . 36
- 2.4 Ray tracing . . . 38
- 2.5 Dust continuum radiative transfer . . . 38
- 2.6 Molecular line radiative transfer . . . 41
- 2.7 Computational codes used in this thesis . . . 50
  - 2.7.1 MCMax . . . 50
  - 2.7.2 TORUS . . . 52
  - 2.7.3 DALI . . . 53
- 2.8 Thesis work in context . . . 55

3 The midplane conditions of protoplanetary discs: a case study of HD 163296 57
3.1 Introduction . . . 57
3.2 Observations . . . 62
3.3 Methods . . . 65
3.3.1 Modelling the 2D disc structure and the SED with MCMax . . . 65
3.3.2 Molecular line modelling with TORUS . . . 67
3.4 Results and discussion . . . 70
3.4.1 Initial mass estimate from the SED modelling . . . 70
3.4.2 Description of models obtained with MCMax . . . 73
3.4.3 Disc regions contributing to the SED . . . 76
3.4.4 Models matching the CO snowline location . . . 77
3.4.5 Modelling the $C^{18}O$ $J = 2 - 1$ emission with TORUS . . . 79
3.4.6 Physical properties of the models . . . 87
3.5 Conclusions . . . 95

4 The extremely truncated circumstellar disc of V410 X-ray 1: a precursor to TRAPPIST-1? 97
4.1 Introduction . . . 97
4.2 Observations . . . 99
4.3 Methods . . . 102
4.4 Results and discussion . . . 108
4.4.1 Constraining the radial extent of the dust via SED fitting . . . 108
4.4.2 The origin of the truncated disc: truncation or dust migration? . . . 110
4.4.3 Gas radius as discriminant between scenarios . . . 116
4.5 Conclusions . . . 125

5 Conclusions and outlook 127
5.1 The midplane conditions of protoplanetary discs . . . 127
5.1.1 The disc of HD 163296 . . . 127
5.1.2 Future studies . . . 128
5.2 Truncated discs around low mass stars . . . 129
5.2.1 The disc of V410 X-ray 1 . . . 129
5.2.2 Future studies . . . 130
5.3 Final remarks . . . 133

Bibliography 137

List of Figures

1.1 Schematic depiction of star formation process. 2
1.2 Schematic representation of the SED of a star with disc. 3
1.3 Diagram of a protoplanetary disc. 6
1.4 Schematic depiction of a thin protoplanetary disc. 7
1.5 Self-similar solution for the time evolution of the surface density. 9
1.6 Frequency of Sun-like stars with a NIR excess as a function of age. 11
1.7 Dust opacity as a function of wavelength. 15
1.8 Schematic depiction of an SED and the disc regions contributing at various wavelengths. 17
1.9 Disc regions dominating the wavelengths regime within the SED of a disc. 18
1.10 Impact of varying disc parameters on the SED. 20
1.11 Dust continuum emission of TW Hya at $870\,\mu$m. 24
1.12 CO $J = 3 - 2$ emission from HD 100546. 25
1.13 Iso-velocity contours of a disc and their corresponding line profile. 27
1.14 Channel maps of the CO emission of a protoplanetary disc. 28
1.15 Schematic picture of the temperature structure of a protoplanetary disc. . 28
1.16 Schematic picture of the water and CO snowline in a protoplanetary disc. 30

2.1 Schematic depiction of a ray between points s_0 and s_1. 34
2.2 Schematic picture of the random walk of a photon packet. 37
2.3 First four energy levels of the CO molecule. 47
2.4 Schematic picture of line broadening. 47
2.5 Schematic depiction of the iterative process used in MCMax. 51

3.1 Integrated line emission and intensity-weighted velocity maps. 63
3.2 Schematic description of the modelling process 65
3.3 SEDs of the best-fitting models. 74
3.4 SED of the whole disc, from within $R = 240$ au and from within $R = 90$ au. 76
3.5 Radial midplane temperature profile of the models. 78
3.6 $C^{18}O$ $J = 2 - 1$ line profile (ALMA observations). 80
3.7 $C^{18}O$ flux density for one model (from within $R = 90$ au) employing different column density thresholds for photodissociation. 82

3.8 $C^{18}O$ $J = 2 - 1$ line profiles of the five models. 83
3.9 $C^{18}O$ $J = 2 - 1$ line profile of the five fiducial models and the observations. 86
3.10 Column number density of $C^{18}O$ and of H_2 for some of the models. 88
3.11 Diagram of carbon sequestration. 90
3.12 Gas-to-dust mass ratio in the disc midplane. 92
3.13 Range of Toomre Q parameter for the models. 94

4.1 SED of V410 X-ray 1. 100
4.2 Gas density and temperature structure of the model after step 1. 103
4.3 Gas density and temperature structure of the model after step 2. 104
4.4 Gas density and temperature structure of the model after step 3. 104
4.5 Comparison of $\rho_3(z)$ and $\rho_4(z)$. 105
4.6 Schematic depiction of the steps to obtain vertical hydrostatic equilibrium. 106
4.7 SEDs of models with a range of inclinations. 107
4.8 SEDs of models with various $R_{\mathrm{dust,1}}$. 109
4.9 Schematic illustration of the two scenarios. 111
4.10 Top: Schematic depiction of the behaviour of dust at the water snowline. Left: Surface density of solids as a function of radius. Right: Maximum grain size as a function of radius. 113
4.11 SED of the truncated model and the one with dust outside of 0.6 au. . . . 115
4.12 Dust density structure of the truncation and migration models. 117
4.13 Dust temperature structure of the truncation and migration models. . . . 118
4.14 Gas density structure of the truncation and migration models. 119
4.15 Gas temperature structure of the truncation and migration models. 120
4.16 Fractional abundance of CO and CH_4 throughout a disc model in the 'migration' scenario with time-dependent chemistry. 122
4.17 Fractional abundance of CO and CH_4 throughout a disc model in the 'migration' scenario with time-independent chemistry. 123
4.18 ^{12}CO $J = 2 - 1$ fluxes of model grid for varying gas radius and gas mass. . 125

5.1 Water abundance in V410 X-ray 1. 131
5.2 Frequency coverage and collecting area of ngVLA and ALMA. 132
5.3 SEDs of 8 candidate truncated discs. 133

List of Tables

3.1 Observational stellar and disc properties of HD 163296. 61
3.2 Summary of the available ALMA observations. 62
3.3 PAs and inclinations of the molecular species and continuum emission. . 64
3.4 CASA routines and a selection of the parameters used. 71
3.5 Parameters of the 15 models that fit the observed SED. 72
3.6 Freeze-out temperatures and fractions of the CO mass removed in the models due to freeze-out. 81
3.7 Properties of the five best-fitting (fiducial) models. 84
3.8 "Extreme" cases of model series A-E. 85

4.1 Wavelengths and associated flux densities used for the SED of V410 X-ray 1. 101
4.2 Stellar and disc parameters of V410 X-ray 1. 106

1

Introduction

The question whether we are alone in the Universe has been of great interest to people for centuries. Therefore one of the goals of modern astronomy is to understand how planetary systems such as our own solar system formed, what their progenitors are and what we can learn about them from observations. Protoplanetary discs - discs of gas and dust that surround young pre-main sequence stars - are the birthplaces of planets and are therefore of great interest in order to understand planet formation. State-of-the-art modelling tools offer the opportunity to self-consistently model the physical and chemical processes taking place in protoplanetary discs. Together with new observational facilities like the *Atacama Large Millimeter/submillimeter Array* (ALMA) providing data of unprecedented resolution and sensitivity, we have the unique chance to study the disc structure and through it the processes that lead to planet formation.

1.1 The formation of protoplanetary discs

In order to understand the formation of protoplanetary discs we must take a step back and take a brief look at the formation of stars around which these discs can be found. Star formation can take place when parts of Giant Molecular Clouds (GMCs) undergo gravitational collapse, overcoming stabilising effects such as thermal pressure and magnetic fields. In the simplest case, when the only competing forces are between gravity and thermal pressure, the free fall time of the cloud $\tau_{\rm ff}$ (Shu et al., 1987) must be significantly smaller than the sound crossing time $\tau_{\rm sc}$,

$$\frac{\tau_{\rm ff}}{\tau_{\rm sc}} \propto \frac{\rho^{-1/2}}{R/c_{\rm s}} \propto \rho^{-1/6} T^{1/2} \ll 1\,, \tag{1.1}$$

where ρ is the density of the cloud, R its radius, T the temperature and $c_{\rm s}$ the sound speed. Therefore cold regions of high density are most prone to undergo gravitational collapse. The molecular cloud cores have scales of the order of 10^4 au and are the immediate precursors of star formation. During the early stages of the gravitational collapse, rotation

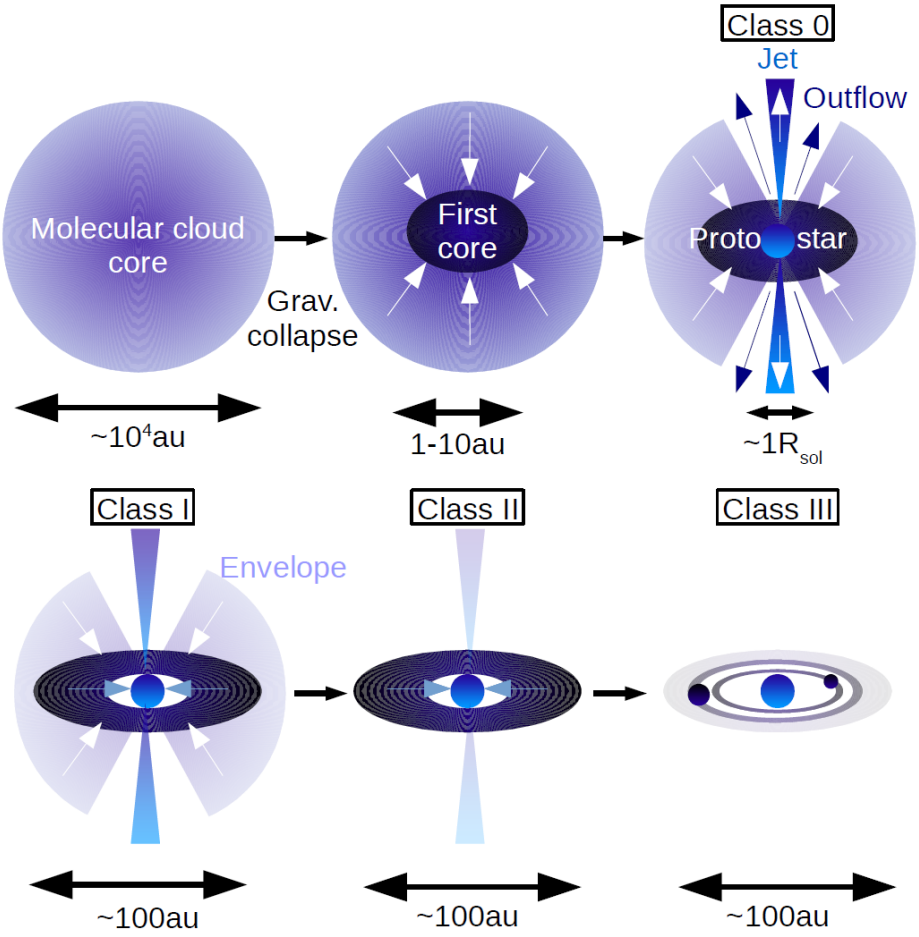

Figure 1.1 Schematic depiction of the star formation process from the collapse of a molecular cloud core, subsequent formation of a protoplanetary disc and finally of a planetary system (from top left to bottom right). Approximate scales are indicated in each panel, but individual components are not to scale. Based on a figure in Tsukamoto (2018).

is unimportant from a dynamical point of view. By contrast, the angular momentum of the gas in such a system is large ($J \sim 10^{54}\,\mathrm{g\,cm^2\,s^{-1}} \gg J_{\mathrm{solar\,system}}$, Armitage 2007). During the collapse, cloud cores will shrink in size by orders of magnitude from $\sim 10^4$ au to ~ 100 au. Due to the conservation of angular momentum the angular velocity of the gas will increase during the collapse, flattening the rotating cloud. This can be seen schematically in Figure 1.1. Over time, a dense central region will form that attracts material from its surroundings, eventually leading to the formation of a protostar, surrounded by an initially massive protoplanetary disc. The protostar continues to accrete material from its surroundings, collapses further and therefore heats up until eventually temperatures high enough for nuclear fusion to take place are attained and the star reaches the main-sequence. During this evolution, the star also clears away the envelope that surrounds it, leaving a star-disc system. This is the general picture of the formation of rather low mass stars. The distinction between low and high mass stars can be made from the following

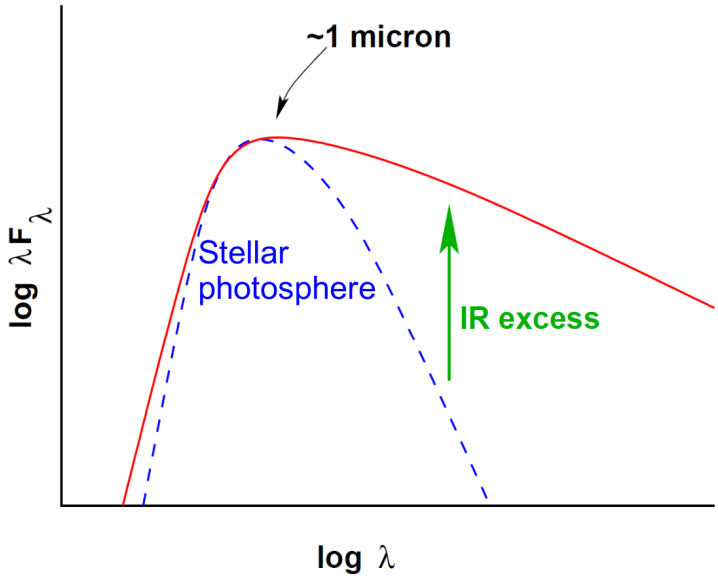

Figure 1.2 Schematic representation of the SED of a star (stellar photospheric emission: blackbody, plotted in blue) with protoplanetary disc. Figure adapted from Armitage (2007).

considerations: material that is collapsing undergoes the conversion of gravitational potential energy into heat. This can be quantified by the *Kelvin-Helmholtz timescale*

$$\tau_{\rm KH} \approx \frac{GM_*^2}{R_* L_*}, \tag{1.2}$$

where M_*, R_* and L_* are the mass, radius and luminosity of the protostar. With this timescale one can estimate the time it takes a protostellar object to reach a point where it is just about to start nuclear fusion in its core. For a star of solar mass, $\tau_{\rm KH} \sim 10^7$ yr and therefore relatively long, whereas for a star of high mass and luminosity this timescale is much shorter. For stars with $M_* \gtrsim 8\,{\rm M}_\odot$, one obtains $\tau_{\rm KH} \lesssim \tau_{\rm ff}$ and therefore fusion in the star begins before the core has actually collapsed to stellar densities, which will have an effect on the surroundings and star formation itself.

Let us first consider the case of a **low mass star** (i.e. $M_* < 8\,{\rm M}_\odot$). The presence of a dusty disc around a Young Stellar Object (YSO) can be inferred from its spectral energy distribution (SED). This is depicted schematically in Figure 1.2: There is excess emission on top of the stellar photosphere (essentially a blackbody) in the infra-red and longer wavelengths due to the emission of dust in the disc.

YSOs can then be classified according to the (logarithmic) slope of their IR emission in an SED (classification dating back to Lada and Wilking, 1984) as given by

$$\alpha_{\rm IR} = \frac{{\rm d}\log(\lambda F_\lambda)}{{\rm d}\log(\lambda)}. \tag{1.3}$$

Typically the wavelengths for which this is measured are approximately $\lambda = 2\,\mu$m and $\lambda = 25\,\mu$m (Armitage, 2015), sometimes also between 10-100 μm, yielding the following classification (see also review by Williams and Cieza, 2011):

- **Class 0:** No flux detectable in the wavelengths regime between $\sim 1 - 5\,\mu$m; the SED peaks at longer wavelengths ($\sim 100\,\mu$m) as the protostar is still surrounded by a dusty envelope that absorbs and re-emits the energy from the protostar. The SED is of blackbody shape. Class 0 objects have strong bipolar outflows and have $\alpha_{\rm IR} > 3$.
- **Class I:** Rather flat or slightly rising SED with $0 < \alpha_{\rm IR} < 3$ out to wavelengths of a few 10s of μm. The infalling material accumulates in an accretion disc, which shows up in the SED as additional flux at wavelengths of a few μm.
- **Class II:** SED falls for wavelengths of a few 10s of μm with $-1.5 < \alpha_{\rm IR} < 0$; this indicates that the envelope that had originally obscured the star is now dispersed due to winds and outflows from the star. There might also be a component of the SED in the UV, which is indicative of accretion onto the star that is magnetically funnelled. This stage is also known as a *T Tauri* star.
- **Class III:** little or no IR-excess; SEDs resemble those of isolated pre-main sequence stars with $\alpha_{\rm IR} < -1.6$. This stage is characterised by a stellar blackbody with a faint tail in the IR.

This has often been interpreted in terms of an evolution (Adams et al., 1987), where an object ends up in the Class I phase after $10^4 - 10^5$ yr, and then in Class II after $10^5 - 10^6$ yr. After $10^6 - 10^7$ yr, the star eventually disperses or accretes its disc and ends up as a Class III object.[1] This is also schematically depicted in Figure 1.1. However, this is a simplifying picture and in order to study discs in detail, detailed modelling of the gas and dust in protoplanetary discs is needed.

Intermediate mass stars (bridging the threshold of $8\,M_\odot$ i.e. between $\sim 2 - 10\,M_\odot$) are believed to form from Herbig Ae and Be stars, which are pre-main sequence stars (ages $\lesssim 10$ Myr). They were first described in Herbig (1960) and have spectral type A or B and are situated in an obscured environment. The *e* denotes that they have been observed to have Balmer emission lines. These are very useful in order to understand the difference in the accretion mechanism between low and high mass stars. I will present the example of a disc around a Herbig Ae star in Chapter 3.

The formation of **high mass stars** is more uncertain and poorly understood than that of low mass stars (see e.g. Zinnecker and Yorke, 2007) as they influence their surroundings

[1] Note however that the viewing angle might also influence the classification of a disc into Class I or II (Armitage, 2007).

due to their radiation and injection of kinetic energy. As mentioned above, their Kelvin-Helmholtz timescales are very short ($\tau_{\rm KH} \sim 10^4 - 10^5$ yr), so they form very quickly in contrast to their lower mass counterparts. That means that they reach the main-sequence while still surrounded by an envelope. The strong ionising radiation from the protostar and its radiation pressure can hinder the accretion onto it, so the question arises how these stars can actually become so massive in such a short time (see e.g. Larson and Starrfield, 1971). Another complicating factor is that they are very rare and located far away. Because of these complications it remains uncertain whether these high mass stars can actually be formed by a scaled-up version of the formation of lower mass stars as described above (Shu et al., 1987).

Let us now consider objects that are of **even lower mass** than the low mass stars described above. A number of theories have been proposed for the formation channel of brown dwarfs (BDs) and very low mass (VLM) stars (see e.g. Whitworth et al., 2007). These objects are distinguished according to their mass, where a BD falls below the hydrogen-burning mass limit of $\sim 0.08\,{\rm M}_\odot$ (Oppenheimer et al., 2000) and a VLM object would lie above this mass boundary. The formation scenarios of these objects can be broadly divided into two categories. Firstly, BD formation may be a scaled-down version of ordinary (solar mass range) star formation, involving the collapse of an essentially isolated low mass gas core. Secondly, a range of other scenarios exist in which the BD properties are impacted by their formation environment. The latter includes dynamical influences, such as the ejection of stellar embryos from systems with a small number of stars (Reipurth and Clarke, 2001) and the possibility of BD formation and subsequent ejection from the outer regions of massive circumstellar discs (Stamatellos and Whitworth, 2009).

In this thesis, I will focus on systems of protoplanetary discs around young stars from different ends of the stellar mass range: one example of a Herbig Ae star (see Chapter 3) and one disc around a VLM star or BD (see Chapter 4).

1.2 Disc structure and evolution

Protoplanetary discs consist of gas and dust. In the *Interstellar Medium* (ISM), their mass ratio has been measured to be $g/d = 100$ (see e.g. Bohlin et al., 1978; Frerking et al., 1982; Lacy et al., 1994). As discs form from the ISM, this value is usually also adopted for discs. Therefore this ratio seems plausible for young discs, but as they evolve, dust grains can grow (see e.g. Dullemond and Dominik, 2005) and radially migrate and therefore change the local g/d ratio. Nevertheless, a canonical value of $g/d = 100$ is often used in discs, also due to the lack of observational constraints of this ratio. The gas governs the disc

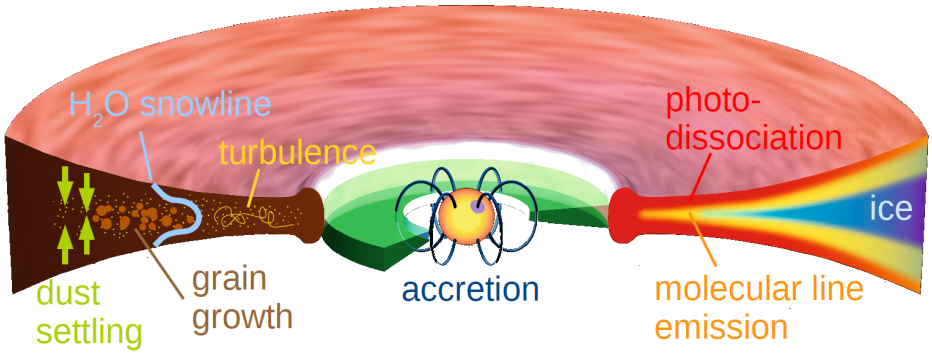

Figure 1.3 Schematic depiction of a protoplanetary disc and its physical and chemical structure around a Sun-like star. Figure adapted from Henning and Semenov 2013.

dynamics and motion of the dust, whereas dust is important as it provides the opacity to capture the stellar flux, re-radiate it and heat the disc. During the lifetime of the disc, most mass is accreted onto the star, while gas is also photoevaporated (Hollenbach et al., 1994; Font et al., 2004; Alexander et al., 2006) and dust is in addition agglomerated to build planetesimals and planets (see e.g. reviews by Natta et al., 2007; Testi et al., 2016).

1.2.1 Density and temperature structure

I will only give a short introduction to disc structure and evolution here, a detailed derivation of the equations can for example be found in Pringle (1981); Armitage (2007); Williams and Cieza (2011); Armitage (2015). A complex interplay of processes takes place in circumstellar discs: dust evolution and dynamics, influenced by the presence of gas and its degree of turbulence, chemical processes influencing the abundances of molecules and the direct impact of the stellar X-ray or UV radiation, to name just a few. This is depicted schematically in Figure 1.3.

These will mostly be taken into account in the modelling tools described later in this thesis. However in contrast to this complicated picture, in the following I will describe a simple model of a protoplanetary disc, following the derivation in the review papers by Armitage (2007); Dominik (2015).

To study the vertical structure of a disc, we assume vertical hydrostatic equilibrium:

$$\frac{dP}{dz} = -\rho(r,z)\, g_z \approx -\rho(r,z)\, \frac{GM_*}{r^2+z^2} \sin(\Theta)\,, \tag{1.4}$$

where P is the pressure, ρ the gas density and g_z the z-component of gravity. This structure is schematically depicted in Figure 1.4. For a thin disc (with $z \ll r$) in Keplerian rotation,

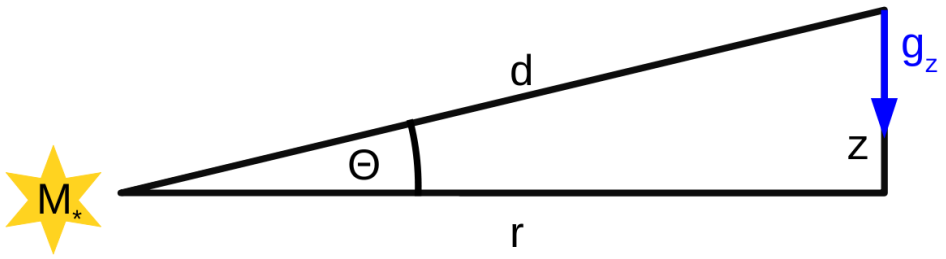

Figure 1.4 Schematic depiction of a thin protoplanetary disc as used in the calculation of vertical hydrostatic equilibrium.

$$g_{\rm z} = \frac{GM_*}{(r^2+z^2)^{3/2}}\, z \approx \Omega_{\rm k}^2 z\,, \tag{1.5}$$

with the Keplerian orbital frequency $\Omega_{\rm k} = \sqrt{GM_*/r^3}$. For a disc that is vertically isothermal and assuming an ideal gas $P = \rho c_s^2$ (where $c_s^2 = k_{\rm B}T/(\mu m_{\rm H})$ is the sound speed, k_B the Boltzmann constant, μ the mean molecular weight and $m_{\rm H}$ the mass of a hydrogen atom), Equation 1.4 can be rewritten as

$$c_{\rm s}^2 \frac{d\rho}{dz} = -\Omega_{\rm k}^2 \rho z \tag{1.6}$$

and can be integrated to obtain the vertical density profile

$$\rho(r,z) = \rho_{\rm mid}(r)\exp\left(\frac{-z^2}{2H^2(r)}\right)\,, \tag{1.7}$$

where $H = c_s/\Omega$ is the vertical scale height and $\rho_{\rm mid}$ the density in the disc midplane. Thus the surface density is given by

$$\Sigma(r) = \int_{-\infty}^{\infty} \rho(r,z)dz = \sqrt{2\pi}\rho_{\rm mid}(r)H(r)\,. \tag{1.8}$$

The flaring of the gas is determined by the radial dependence of the pressure scale height and is often parametrized as $H \propto r^{\beta}$, where observationally β is between 1.13 and 1.25 (Kenyon and Hartmann, 1987). If the feedback of the H-profile on the temperature structure of the disc is taken into account, $\beta = 9/7$ can be derived (Chiang and Goldreich, 1997). Note that in reality, the vertical density structure will deviate from a Gaussian shape as discs are not vertically isothermal. This is explored in more detail in Chapter 4.

One can derive an approximation of the radial temperature structure of a disc from basic considerations (see e.g. Armitage, 2015). For a dust grain of radius a at a distance r from the star that is exposed to stellar irradiation, the radiative equilibrium can be calculated.

One can equate the radiation absorbed by the grain with surface πa^2 (l.h.s.) with the radiation subsequently emitted by the dust grain with surface $4\pi a^2$ basically as a blackbody with emissivity j (r.h.s.):

$$\frac{L_*}{4\pi r^2}\pi a^2 = \sigma_{\rm SB}\, T_{\rm eqm}^4\, j(T_{\rm eqm}) 4\pi a^2\,, \tag{1.9}$$

where $T_{\rm eqm}$ is the equilibrium temperature and $\sigma_{\rm SB}$ the Stefan-Boltzmann constant. The emissivity of small dust grains is $j = 1$ for wavelengths $\lambda \leq 2\pi a$. For longer wavelengths, $j \propto \lambda^{-1}$. I will come back to this in Section 2.1. One can then calculate the equilibrium temperature from Equation 1.9:

$$T_{\rm eqm}(r) \propto \left(\frac{R_*}{r}\right)^{1/2} T_* \propto r^{-1/2}\,. \tag{1.10}$$

Note that this is only an estimate of the radial temperature profile, but more sophisticated disc models often end up with temperature profiles that are not too different from this simple expression (see e.g. Chapters 3 and 4).

1.2.2 Disc evolution

For the case of an active (i.e. accreting) disc, we can study the conditions for the gas to be accreted. The specific angular momentum of the gas in Keplerian rotation is

$$l(r) \approx r^2\Omega = \sqrt{GM_* r}\,, \tag{1.11}$$

which for a typical disc configuration is much higher than that of a star rotating at break-up velocity. Therefore a process needs to be at play that transports angular momentum outwards so it does not accumulate on the star during the accretion of material onto it. Possible solutions are magnetic fields, disc winds or viscosity of the disc, which will be discussed in more detail later in this section (see e.g. Armitage, 2015).

Combining the continuity equation for an axisymmetric flow and angular momentum conservation, one can show that the time evolution of the surface density of an accreting disc (with $z \ll R$) is given by (Pringle, 1981):

$$\frac{\partial \Sigma}{\partial t} = \frac{3}{r}\frac{\partial}{\partial r}\left[\sqrt{r}\frac{\partial}{\partial r}\left(\Sigma\nu\sqrt{r}\right)\right]\,, \tag{1.12}$$

where ν is the shear viscosity.[2] For large radii, discs can obtain a steady state where $\nu\Sigma$

[2] Note that the letter ν will later be used to denote the frequency. However, from the context it should always be clear which one of the two is considered.

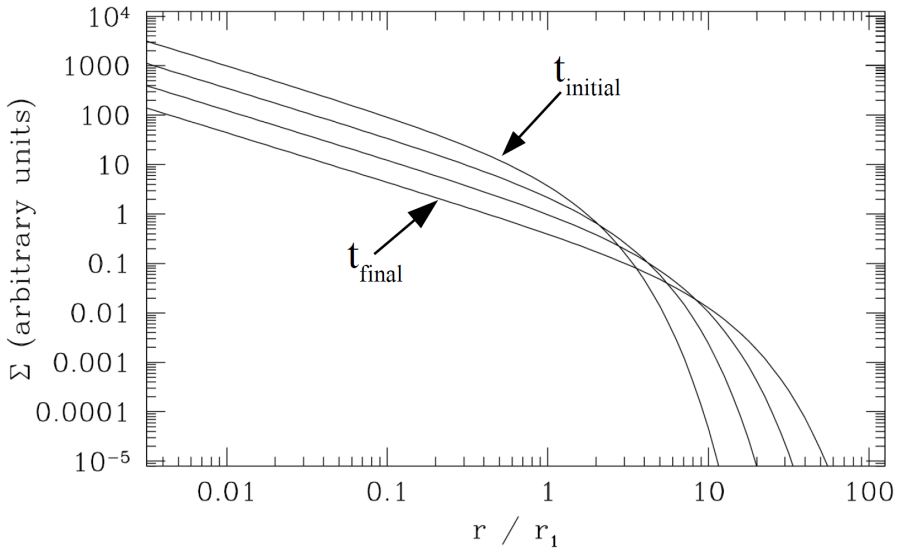

Figure 1.5 Self-similar solution for the time evolution of the surface density: gas is accreted onto the star and the disc spreads to conserve angular momentum (evolution from time $t_{\rm initial}$ with initial exponential cut-off radius r_1 to $t_{\rm final}$). Plot adapted from Armitage (2007).

is constant (Pringle, 1981). Equation 1.12 can be solved analytically if $\nu \propto r^{\gamma}$ (Lynden-Bell and Pringle, 1974) and we obtain a self-similar solution for the surface density (see Figure 1.5). It can be shown that the overall disc mass decreases as material is accreted onto the star and the disc spreads in order to conserve angular momentum.

1.2.3 Viscosity

The question remains what is the source of viscosity in discs. One possible candidate is *molecular viscosity*, arising from the random motions of gas particles caused by the diffusion of molecules. It can be estimated as

$$\nu_{\rm mol} \approx \lambda c_{\rm s}\,, \tag{1.13}$$

where $\lambda = (n\sigma_{\rm m})^{-1}$ is the mean free path of the molecules with gas particle number density n and collisional cross section between the particles $\sigma_{\rm m}$. We can estimate the molecular viscosity for typical values in a disc, using $\sigma_{\rm m} \sim \pi r_{\rm mol}^2 \sim 10^{-15}\,{\rm cm}^2$ for a molecule of radius $r_{\rm mol} \sim 3\times10^{-8}\,{\rm cm}$, assuming $T(r = 10\,{\rm au}) \approx 70\,{\rm K}$ and a density of $n \sim 10^{12}\,{\rm cm}^{-3}$:

$$\nu_{\rm mol} \approx 10^{7}\,{\rm cm}^2\,{\rm s}^{-1}\,. \tag{1.14}$$

The corresponding viscous timescale τ_ν for a radial location of 10 au can be estimated as

$$\tau_\nu = \frac{r^2}{\nu_{\rm mol}} \sim 10^{13}\,{\rm yr} \tag{1.15}$$

and molecular viscosity therefore cannot be the main source of viscosity in a disc, as these evolve on timescales of 10^6 yr (as we will see in a moment).

Therefore another mechanism causing turbulent motion in a disc needs to be invoked. Possible candidates for this include turbulence or the magneto-rotational instability (MRI), which however requires a substantial fraction of the disc to be ionised, which is usually not the case for cold protoplanetary discs. Shakura and Sunyaev (1973) parametrised the viscosity using the α-parameter without going into detail about the source of viscosity in order to describe the efficient transport of angular momentum in discs. The largest scale for turbulence in a disc is given by the scale height of the gas in the disc $H_{\rm gas}$ and a typical turbulent velocity by the sound speed $c_{\rm s}$. Therefore the viscosity can be written as

$$\nu = \alpha c_{\rm s} H_{\rm gas}\,. \tag{1.16}$$

The corresponding viscous timescale is given by (Dominik, 2015)

$$\tau_{\rm visc} = \frac{r^2}{\nu} = \left(\frac{r}{H_{\rm gas}}\right)^2 \frac{1}{\alpha_{\rm visc}\Omega}\,. \tag{1.17}$$

In order to estimate the order of magnitude of the $\alpha_{\rm visc}$-parameter, we can use typical values. For $\tau \sim 10^6$ yr at $r = 50$ au and for a thin disc with $H_{\rm gas}/r \sim 0.05$, one obtains $\alpha_{\rm visc} \sim 0.01$.

The mass accretion rate onto the central star can be written as

$$\dot{M}(R) = -2\pi r v_r \Sigma \tag{1.18}$$

and is constant at all radii for the case of steady-state accretion. Therefore the flow timescale related to this process at a given radius can be described by

$$\tau_{\rm flow}(R) = \frac{M(r<R)}{\dot{M}}\,. \tag{1.19}$$

Typical mass accretion rates for protoplanetary discs are around $\dot{M} \sim (10^{-9} - 10^{-7})\,{\rm M_\odot yr^{-1}}$ (e.g. Gullbring et al., 1998; Muzerolle et al., 2000). For brown dwarfs in young star forming regions, they can even be as low as $\dot{M} \lesssim 10^{-9.5}{\rm M_\odot yr^{-1}}$ (Manara et al., 2015).

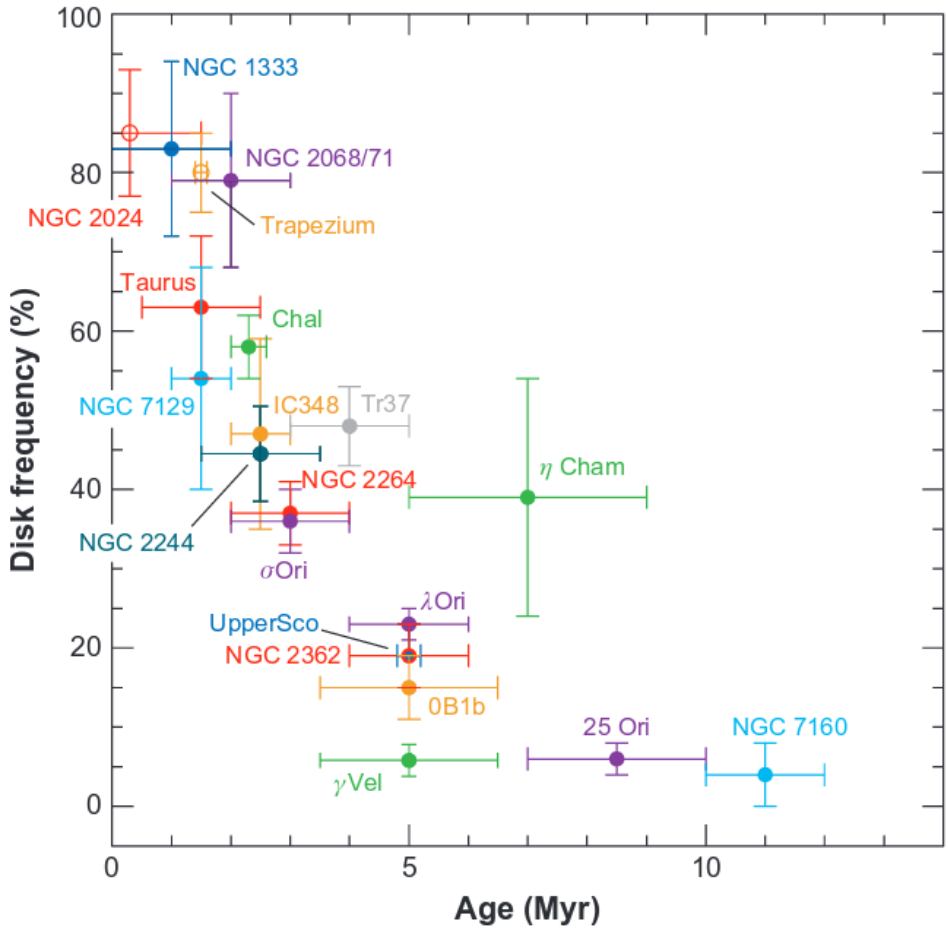

Figure 1.6 Frequency of Sun-like stars with a NIR excess as a function of age (Figure from Wyatt (2008), based on Hernández et al. 2007).

Various types of discs are observed: discs that are massive and rich in gas and small dust, and debris discs which have lost most of their gas and in which the dust grains have grown, partially fragmented again and settled to the disc midplane. This allows to study the evolution of discs. As disc evolution takes too long to be monitored in individual objects, disc lifetimes can be estimated by observing populations of stars and measuring their IR-excess. One therefore studies the evolution of incidence of dusty discs in the respective regions. This is plotted in Figure 1.6, where the disc frequency as inferred from IR fluxes is given as a function of age. After a few Myr, a high fraction of the discs has dispersed, indicating that typical disc lifetimes are of the order of a few million years (see e.g. Fedele et al., 2010). The parameters of analytical calculations by Hartmann et al. (1998) are for example tuned to the observational data in order to study the evolution and accretion of T Tauri discs. On the one hand, gas is accreted onto the star, on the other hand the star photoevaporates the upper layers of the disc (Scally and Clarke, 2001; Adams et al., 2004; Clarke, 2007).

Gas dispersal is difficult to measure as the total gas mass is hard to constrain observationally. The mass accretion rate influences not only the disc structure locally, but also disc evolution in general by determining the spreading of the disc due to angular momentum conservation (Hartmann et al., 1998). Which process dominates the dispersal depends on the disc structure (T and ρ), but one can conclude that the speed of dispersal sets the timescale available for the formation of gas giants. Overall, it is thus important to understand the interplay of gas and dust, whose evolution is tightly coupled, and also to determine the density and temperature structure of discs. It is essential to study and model both components simultaneously.

1.2.4 Grain growth and dust opacities

There are many studies of dust in discs as the mm continuum emission is relatively bright and thus easier to observe (Andrews and Williams, 2007; Andrews et al., 2009, 2010; Qi et al., 2011). Inferring the disc mass from dust observations is however difficult due to the uncertain g/d-mass ratio and dust grain properties. So far, we have considered discs whose gas structure is set by vertical hydrostatic equilibrium. However, the distribution of dust grains does not necessarily have to follow the gas due to dust settling and grain growth. Under the right conditions, grains can coagulate upon collision (Weidenschilling, 1980) and form larger grains. These can then decouple from the gas motion (which is sub-Keplerian). As grains grow, their collision velocities get bigger up to a point where they reach the fragmentation velocity and the stock of small grains is replenished (Dullemond and Dominik, 2005).

As grains decouple from the gas, their vertical structure will also change as they settle towards the disc midplane. How strongly the dust is coupled to the gas can be expressed by the Stokes number:

$$\mathrm{St} = \frac{t_{\mathrm{stop}}}{t_{\mathrm{dyn}}} = \Omega_{\mathrm{k}} t_{\mathrm{stop}} = \Omega_{\mathrm{k}} \frac{a \rho_{\mathrm{grain}}}{\rho_{\mathrm{gas}} v_{\mathrm{t}}} = \Omega_{\mathrm{k}} \frac{a \rho_{\mathrm{grain}}}{\rho_{\mathrm{gas}} \sqrt{8/\pi} c_{\mathrm{s}}} , \tag{1.20}$$

where t_{stop} is the stopping time, t_{dyn} is the dynamical timescale, v_{t} the mean thermal velocity of the gas, a is the grain size (assuming a spherical grain) and ρ_{grain} the density of the dust grain (see e.g. Booth and Clarke, 2016). This means that for $\mathrm{St} < 1$, dust grains are coupled to the gas motion, whereas they decouple for $\mathrm{St} > 1$. Upon decoupling from the gas, grains can settle towards the midplane, where the local gas density ρ_{gas} is higher. Thus their St gets smaller again and the grains will recouple with the gas motion. Therefore for each grain size one obtains a typical height above the midplane above which dust of this size is much less prevalent (Dullemond and Dominik, 2004).

Turbulent motions of the gas can loft small dust grains up to greater heights above the midplane, constituting a diffusion process. The theory behind this is for example explained in detail in Voelk et al. (1980); Cuzzi et al. (1993); Weidenschilling (1997), I will only give an overview here. The particle stopping time $t_{\rm stop}$ is the timescale for the acceleration or deceleration of dust grains due to the gas motion (and increases with particle size, see e.g. Youdin and Lithwick 2007). The eddy turnover time $t_{\rm eddy}$ can be defined as the correlation time of turbulent fluctuations or as the turnover time of eddies on the largest scales (usually taken to be H in a disc). One can then write the Stokes number as

$$\mathrm{St} = \frac{t_{\rm stop}}{t_{\rm eddy}} \,. \tag{1.21}$$

We can also define dimensionless timescales $\tau_{\rm s} = \Omega_{\rm k} t_{\rm stop}$ and $\tau_{\rm e} = \Omega_{\rm k} t_{\rm eddy}$. For a scenario where $\tau_{\rm s} < \tau_{\rm e} < 1$ (i.e. particles are influenced by the turbulent motions) the scale height of the dust particles $H_{\rm p}$ in comparison to the scale height of the gas $H_{\rm gas}$ scales as (Dubrulle et al., 1995; Youdin and Lithwick, 2007)

$$\frac{H_{\rm p}}{H_{\rm gas}} = \sqrt{\frac{\alpha_{\rm turb}}{\tau_{\rm s}}} \,. \tag{1.22}$$

The derivation of this equation is based on considerations about the terminal velocity of a dust grain and the turbulent velocity. The ratio of $H_{\rm p}$ to $H_{\rm gas}$ is also explored in more detail in Section 2.7.1 for the case of the dust settling in the Monte Carlo radiative transfer code MCMax. This process therefore leads to a vertical dust profile, where it is easier for small grains to be situated at large heights above the disc midplane. Small grains are also needed in order to explain observations of silicate emission features in discs, which are due to grains of sizes smaller than a few μm (Cohen and Witteborn, 1985; van Boekel et al., 2003). Large dust grains on the other hand provide most of the dust emission at (sub-)millimetre wavelengths (Weintraub et al., 1989). Note that once dust grains have grown and decoupled from the sub-Keplerian gas motion, they will travel at Keplerian velocity and experience a headwind due to the gas. This causes them to drift radially inwards towards the star. Thus the gas and dust components can extend to different outer radii, which is also observed (see e.g. Panić et al. 2009; Rosenfeld et al. 2012).

Dust grains consist mostly of silicates and graphite. Commonly, a power law grain size distribution of

$$n(a)\, da \propto a^{-q}\, da \tag{1.23}$$

is assumed, where a is the grain size. The value for ISM grains that is often also adopted for discs is $q = 3.5$ (see e.g. Mathis et al. 1977; Clayton et al. 2003), thus most of the dust mass is in the largest grains. Note however that in Chapter 4, I will use a value of $q = 3$,

which is suitable for an evolved grain population (see e.g. Birnstiel et al., 2012). Models often contain two populations of grains, small (with sizes between $a_{\text{min, small}}$ and $a_{\text{max, small}}$) and large ones (with sizes between $a_{\text{min, large}}$ and $a_{\text{max, large}}$). This is for example used in Chapter 4. One can then calculate the fraction of large grains

$$f = \frac{\left(\frac{a_{\text{max, large}}}{a_{\text{max, small}}}\right)^{4-q}}{\left(\frac{a_{\text{max, large}}}{a_{\text{max, small}}}\right)^{4-q} + 1}, \tag{1.24}$$

using the fact that the mass in large grains is given by

$$M_{\text{large}} \propto \int_{a_{\text{min, large}}}^{a_{\text{max, large}}} a^3 a^{-q} da \tag{1.25}$$

and equivalently for the small grains.

The dust emission of a protoplanetary disc depends on the opacities of the dust grains. These are influenced by the chemical composition, size, porosity and shape of the grains. One property that is especially important is the dust particle size. It is possible to calculate the opacity of a grain for a given grain size and given refractive index (which can be obtained from lab experiments). In order to do so, one approach that is frequently used is *Mie theory*, where analytical solutions to the Maxwell equations are computed for the interaction of photons with the electric field of a compact and spherical grain (Mie, 1908). One can also take into account more complex particle shapes, which changes the opacities and provides better fits to emission features that are observed. The dust opacities of grains with maximum grain sizes of $a_{\text{max}} = \{1\,\mu\text{m},\ 1\,\text{mm},\ 10\,\text{cm}\}$ are plotted in Figure 1.7. The left panel shows the case where the grain size distribution is characterised by a power law index of $q = 3.5$, and in the right one $q = 2.5$ is used.

The *resonance regime* for a given grain size is the wavelength range where $\lambda \sim 2\pi a_{\text{max}}$. As shown in Figure 1.7, the opacity in the short-wavelength regimes is dominated by the micron-sized grains, whereas large grains only contribute substantially to the flux in their resonance regime. Thus, relatively large (mm-sized) grains dominate the opacity in the (sub-)mm wavelength regime (Draine, 2006). This can be understood as follows: for $q < 4$ the mass in grains is dominated by the larger grains (see e.g. Miyake and Nakagawa, 1993). Therefore increasing a_{max} implies less mass in small grains (which are the most efficient absorbers in the NIR wavelength regime) and therefore decreasing opacities at short wavelengths. At the same time, for bigger a_{max} the resonance regime occurs at longer wavelengths, so the opacity at $\lambda \sim a_{\text{max}}$ increases. Changing the power law index q of the size distribution from 3.5 to 2.5 implies that comparatively more larger grains are

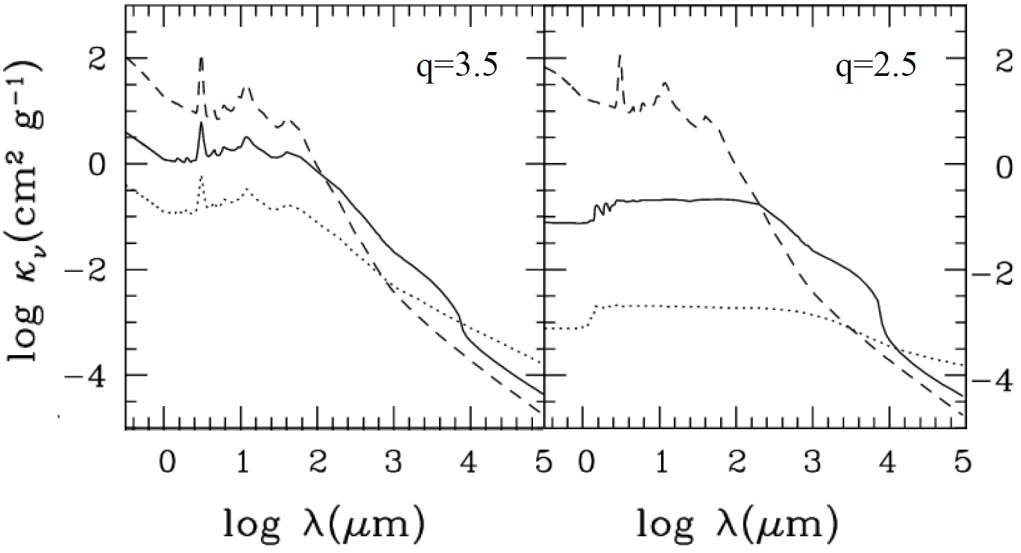

Figure 1.7 Dust opacity of grains with different maximum sizes and power law index q of the grain size distribution as a function of wavelength. The left panel shows the case $q = 3.5$, whereas the right one shows $q = 2.5$. The dashed line is for grains of maximum size $a_{\rm max} = 1\,\mu$m, the solid line for $a_{\rm max} = 1$ mm and the dotted line for $a_{\rm max} = 10$ cm. Figure adapted from D'Alessio et al. (2001).

present. This decreases the opacity in the short wavelength regime, but increases it for the larger grains at longer wavelengths.

1.3 Observations of dust in protoplanetary discs

As mentioned previously, discs consist of gas and dust and the g/d-mass ration is usually assumed to be 100. In order to understand the structure of discs, it is crucial to study the spatial distribution of gas and dust as this determines the temperature structure. We will come back to this in Chapters 3 and 4, where I present the detailed modelling of the gas and dust components of two discs. As shown previously the interplay of gas and dust depending on T and ρ is of enormous importance for both planet formation and disc evolution.

1.3.1 The spectral energy distribution (SED)

The presence of a disc around a star can be inferred from excess emission in the IR wavelength regime on top of the stellar photospheric emission, as mentioned earlier in this chapter. Therefore one important tool for studying discs is using their SEDs.

One can understand the overall shape of the SED from some basic considerations (see e.g. Woitke, 2015), which I will present in the following. Let us consider an annulus of

width dr at a radius r in a razor-thin disc with inclination i (where $i = 0°$ is face-on). The solid angle of the disc as seen from distance D is then

$$d\Omega = \frac{2\pi r dr}{D^2} \cos(i)\,. \tag{1.26}$$

The intensity I_ν of a vertically isothermal disc with temperature $T(r)$ that is optically thick is given by the frequency-dependent Planck function

$$B_\nu = \frac{2h\nu^3}{c^2} \left[\exp\left(\frac{h\nu}{k_\mathrm{B}T}\right) - 1 \right]^{-1}\,, \tag{1.27}$$

where h is the Planck constant. The flux from the annulus can be calculated as $dF_\nu = I_\nu d\Omega$ such that the total flux of the disc (integrated over all annuli) is then

$$F_\nu = \int B_\nu\left[T(r)\right] d\Omega = \frac{2\pi\cos(i)}{D^2} \int_{R_\mathrm{in}}^{R_\mathrm{out}} B_\nu\left[T(r)\right] r dr\,. \tag{1.28}$$

For a disc where the radial temperature dependence is given by a power law $T(r) \propto r^{-q}$, one can estimate the index q from observations of the disc temperature at two radial locations[3]. A typical temperature at the inner radius $R_\mathrm{in} \approx 0.1$ au is $T \sim 1500$ K (which is approximately the dust sublimation temperature) and $T(R_\mathrm{out} \approx 200\,\mathrm{au}) \sim 10$ K. One thus obtains a value of $q \approx 0.7$ as an estimate. This is broadly in line with the value of 0.5 obtained from considerations of the absorbed and emitted energy by a dust grain (see Equation 1.10). In the FIR wavelength regime this can be interpreted as follows: at a given wavelength λ the flux is dominated by the emission from a certain disc location r. There the temperature is such that the "peak" of its local $B_\nu(T)$ coincides with this λ. This is presented schematically in Figure 1.8. Disc regions that are further out have a $T(r)$ that is too low to emit at this wavelength and are therefore negligible. Locations of the disc inside of this radial location can be neglected as their $d\Omega \propto r dr \propto r^2$ are comparatively small (see Figure 1.8).

One can now derive the slope of the SED in this wavelength regime (see also Beckwith et al., 1990; Woitke, 2015). Substituting $x = h\nu/(k_\mathrm{B}T)$ and approximating $R_\mathrm{in} \to 0$ and $R_\mathrm{out} \to \infty$, one obtains

$$\nu F_\nu \propto \nu^{4-\frac{2}{q}} \propto \lambda^{\frac{2}{q}-4}\,. \tag{1.29}$$

Alternatively, we can also consider the following: according to *Wien's displacement law*, the maximum of $B_\nu(T)$ is located at a frequency of $\nu \propto T$. Considering that the maximum

[3] Note that the index q here is not the same as the one in Equation 1.23, but it should always be clear from the context which one is considered.

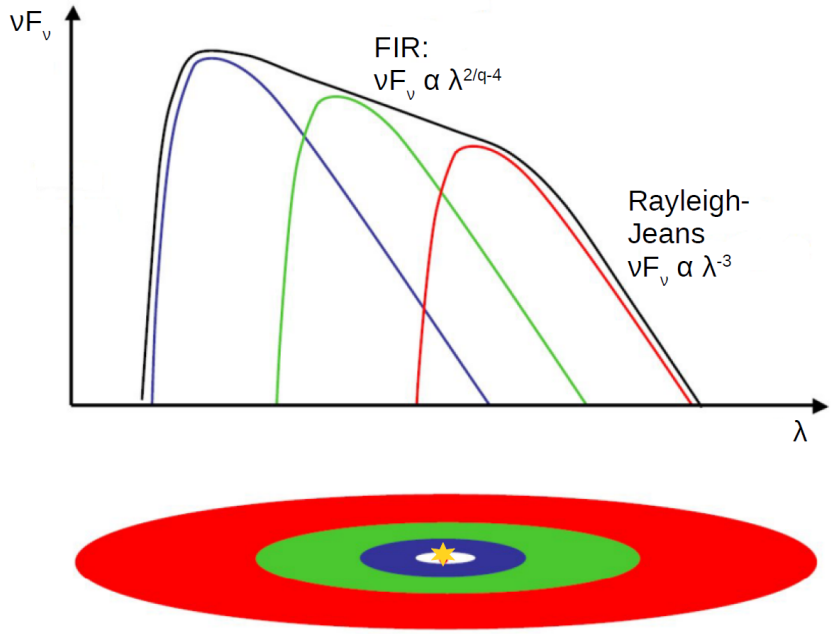

Figure 1.8 Schematic depiction of an SED and the disc regions contributing at various wavelengths. The SED can thus be represented as a superposition of Planck functions at various wavelengths. Figure adapted from Woitke (2015).

of $\nu B_\nu(T)$ is proportional to T^4 one can derive :

$$\nu F_\nu \propto [\nu B_\nu(T)]_{\max} d\Omega \propto [\nu B_\nu(T)]_{\max} r^2 \propto T^4 T^{-\frac{2}{q}} \propto \nu^{4-\frac{2}{q}} \propto \lambda^{\frac{2}{q}-4}. \tag{1.30}$$

One can now again use Wien's displacement law to calculate where the turnover from this regime is, i.e. at which wavelength λ_{turn} the disc has its lowest temperature $T_{\min}$. This means we can calculate at which λ the maximum of $B_\nu(T_{\min})$ is reached (see red curve in Figure 1.8):

$$\lambda_{\text{turn}} = \frac{2900\,\mu\text{m}}{T_{\min}[\text{K}]}. \tag{1.31}$$

For $T_{\min} \approx 10\,\text{K}$ this thus yields $\lambda_{\text{turn}} = 290\,\mu\text{m}$. We will use this relation in Chapter 4 to estimate the temperature at the outer edge of the optically thick dust disc.

We can now consider the wavelength regime where $\lambda > \lambda_{\text{turn}}$. There, all disc regions contribute to the SED, however with decreasing impact as their B_ν tails off. For even longer wavelengths, one approaches the Rayleigh-Jeans limit where $B_\nu \approx 2\nu^2 k_{\text{B}} T c^{-2}$ and therefore

$$\nu F_\nu \propto \nu^3 \propto \lambda^{-3}. \tag{1.32}$$

This is also marked in the schematic picture in Figure 1.8. The fact that $\nu F_\nu \propto \lambda^{-3}$ will play an important role for the truncated, optically thick dust disc in Chapter 4.

Note however that this is only a rough estimate for the optically thick parts of a disc.

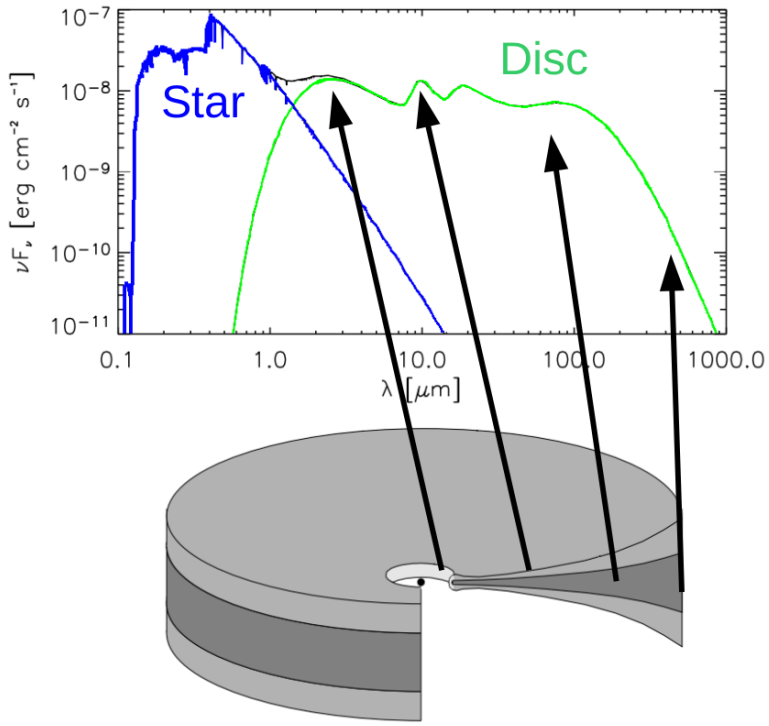

Figure 1.9 Disc regions dominating the various wavelength regimes within the SED of a protoplanetary disc. Figure adapted from Dullemond et al. (2007).

For a more realistic picture, we need to include the opacity of the disc. I will come back to this later in this section when we estimate the disc mass from optically thin continuum emission in the mm wavelength regime (see Equation 1.36).

Let us now consider a more realistic disc with some vertical extent, flaring and inner rim. A schematic representation of the SED of a star with a disc as well as the main disc regions contributing to the fluxes at different wavelengths can be seen in Figure 1.9. Depending on the wavelength in which one is observing, different physical parts (i.e. radii or heights) of the disc will be observed as the emission becomes optically thick at different heights (see e.g. Meijer 2007). The wavelength regime of the SED can be divided into four parts, near-infrared (NIR), mid-infrared (MIR), far-infrared (FIR) and millimetre (mm).

- **NIR** [$\sim 1\,\mu$m - $5\,\mu$m]: the emission in the NIR traces the hottest, innermost regions of the inner gas disc and the puffed up inner dust rim. The emission that dominates this wavelength regime is reflected or scattered starlight, thus tracing the refractory dust, and it is therefore dependent on the properties of the star. Dust grains dominating the emission in this range are micron-sized and positioned mainly in the inner disc ($r \approx 1$ au). The scattered light traces a very narrow layer on the disc surface which is directly illuminated.

- **MIR** [$5\,\mu$m - $\sim 40\,\mu$m]: The emission in the MIR is a tracer of the optically thin surface layer of the disc that is heated to a few 100 K. The size of dust grains affecting the emission in the MIR is between a few and up to $10\,\mu$m. The MIR emission arises from the inner regions of the disc ($\lesssim 20$ au) and from layers deeper than the region emitting in the NIR. Discs often display a bump in the SED at $\sim 10\,\mu$m, which is a feature due to silicate dust grains.

- **FIR** [$\sim 40\,\mu$m - $\sim 300\,\mu$m]: The emission in the FIR traces the outer disc, in regions deeper down than the MIR. Also, the emitting area extends further out than the one in the MIR. The mechanism of emission is thermal. Dust grains that dominate the emission in the FIR have sizes between a few and a few hundred μm and are situated preferentially in the outer disc, out to radii of about 100 au for a classic T Tauri disc.

- **mm** [<few cm]: The emission in the mm is optically thin throughout the whole disc, in contrast to all the shorter wavelengths. The mechanism that dominates this wavelength regime is thermal emission from the dust grains. It is most efficient for the larger dust grains ($\geq$ 1mm up to a few cm) in the disc midplane.

1.3.2 Degeneracies in SED modelling

The SED is not inferred from a single observational constraint, but an assembly of values from separate observations that probe various dust grain sizes and different physical regions of the disc. It is thus important to fit the *whole* SED in the modelling process, although we will see in Chapter 3 that due to the degeneracies of the disc parameters this is only a necessary, but not sufficient criterion for our model of the disc of HD 163296.

In order to examine the effects and degeneracies of disc parameters on the SED, I will present the results of varying the following four quantities: the mass of dust $M_{\rm dust}$, the minimum dust grain size $a_{\rm min}$, the maximum grain size $a_{\rm max}$ and the gas-to-dust mass ratio g/d. This is using the Monte Carlo radiative transfer code MCMax, which will be introduced in Section 2.7.1 below. It is however important to note that in this tool the gas mass is not set explicitly, but is given by multiplying $M_{\rm dust}$ with g/d. Also note that I present the case of a disc with optically thin dust emission in the (sub-)mm wavelength regime here. This variation of parameters mimics disc evolution because as they evolve during their lifetime, discs lose both gas (accretion and photoevaporation) and dust (mostly accretion). Also dust grain properties (such as their sizes and overall mass) will change as the disc evolves and dust grains grow and settle to the midplane.

Understanding the influence of the respective parameters on the SED is a crucial precondition for our aim to find disc models that match the observed SEDs. The fiducial

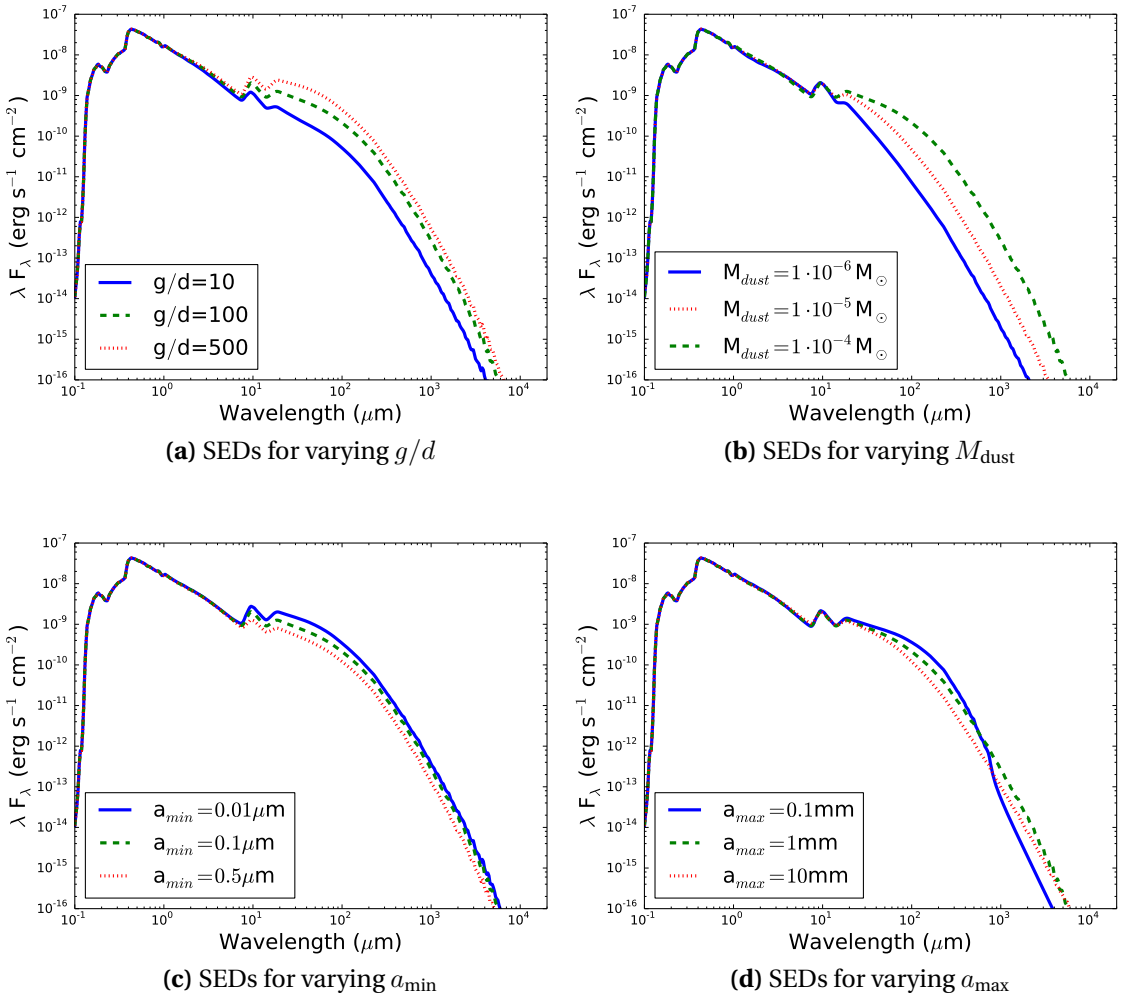

(a) SEDs for varying g/d

(b) SEDs for varying $M_{\rm dust}$

(c) SEDs for varying $a_{\rm min}$

(d) SEDs for varying $a_{\rm max}$

Figure 1.10 SEDs for varying parameters (see individual labels). The fiducial model is plotted in green (dashed lines) and is the same in all panels.

model underlying all the models presented here has the following parameters: $M_{\rm dust} = 10^{-4}\,{\rm M}_\odot$, $g/d = 100$, $a_{\rm min} = 0.4\,\mu$m and $a_{\rm max} = 1\,$mm, corresponding to the dashed green line in all the plots of Figure 1.10. I vary one parameter in every plot and leave the others unchanged[4]. This is similar to parameter studies done by Meijer (2007); Panić and Min (2017). For a study that includes the variation of even more parameters such as the grain composition, see e.g. Woitke (2015).

[4]The only exception is Figure 1.10b: Here we vary g/d as well in order to keep $M_{\rm gas}$ constant and see the effect of $M_{\rm dust}$ alone.

Gas loss

As $M_{\rm dust}$ is kept constant in Figure 1.10a, an increase of g/d directly corresponds to an increase in $M_{\rm gas}$. Increasing this parameter has similar effects as enhancing $M_{\rm dust}$ at constant g/d, which also increases $M_{\rm gas} = M_{\rm dust} \times g/d$. The SED is primarily a tracer of the dust in the system, but by making $M_{\rm gas}$ larger, gas and small dust can be present higher above the midplane. Thus the disc can intercept more stellar light and re-emit it. This effect is strongest in the MIR and FIR fluxes.

Dust evolution

As can be seen in Figure 1.10b, increasing $M_{\rm dust}$ boosts the flux in the SED, especially in the FIR. Making $M_{\rm dust}$ bigger introduces more smaller grains into the disc (see the grain size distribution described earlier in Equation 1.23), this increases the opacity and the disc heats up. More small dust particles can follow the gas to greater heights, thus the disc flares more, can intercept more stellar light and re-radiate it in the FIR.

In Figure 1.10c one can see that bigger minimum grain sizes lead to a decrease in the flux of the SED. Making $a_{\rm min}$ larger means that there is relatively more mass in larger grains, reducing the opacity. These bigger grains are not as efficient at emitting in the MIR and FIR, where the emission is dominated by the smaller grains (see e.g. Figure 1.7). Also, by making $a_{\rm min}$ bigger, less grains will be able to follow the gas up to great heights, so the disc is more optically thin in the upper layers and thus the emission is reduced in the FIR. The mm-part of the SED is dominated by the largest grains and does not change significantly for the three cases presented here.

In Figure 1.10d, $a_{\rm max}$ is varied, here the effect is a bit more complicated: Increasing $a_{\rm max}$ leads to a lower SED in the MIR and FIR, but to more emission in the mm. By boosting $a_{\rm max}$, mass is shifted from the small grains population to the larger ones, which have lower opacities. Thus the opacity in the upper regions decreases, which leads to less flaring of the disc and thus lower emission in the FIR. The emission in the mm is higher for larger grains as this part of the SED is dominated by the large dust in the disc midplane.

1.3.3 Physical properties from dust emission

For typical disc temperatures (below the dust sublimation temperature $T_{\rm subl} \sim 1500\,{\rm K}$), the disc opacity is dominated by the dust. From observations of the dust continuum emission, disc properties such as the temperature distribution, mass of dust and sizes of the dust grains can be inferred. I will present a toy model here, following the description in

Armitage (2015). Let us consider a disc that is thin and vertically isothermal with dust emitting thermal radiation, such that the temperature is a function of the radial location, but has a single value at each radial location. Assuming again that the dust temperature as well as the dust surface density are of power law shape then yields

$$T_{\rm d}(r) \propto r^{-q} \text{ and } \Sigma_{\rm d}(r) \propto r^{-p} \,. \tag{1.33}$$

One can employ a frequency dependent opacity (per unit dust mass)

$$\kappa_\nu \propto \nu^\beta \,, \tag{1.34}$$

then the vertical optical depth in the disc is then given by

$$\tau_\nu(r) = \Sigma_{\rm d}(r)\kappa_\nu(r) \,. \tag{1.35}$$

Solving the radiative transfer equation for a face-on disc[5] (see e.g. Rybicki and Lightman, 1979, and also described in Equations 1.28 and Chapter 2) gives a frequency dependent flux density of

$$F_\nu = D^{-2} \int_{R_{\rm in}}^{R_{\rm out}} 2\pi r B_\nu \left[T_{\rm d}(r)\right] \left[1 - e^{-\tau_\nu(r)}\right] dr \,, \tag{1.36}$$

where D is again the distance of the source, $R_{\rm in}$ and $R_{\rm out}$ are the inner and outer disc radii and B_ν is the Planck function as defined in Equation 1.27. In the optically thick limit $\tau_\nu \gg 1$ and therefore $e^{-\tau_\nu} \to 0$, so one recovers Equation 1.28. The entire disc will however generally only be optically thick at IR wavelengths, therefore the slope of the IR part of the SED will provide a constraint on $T(r)$.

At (sub-)mm wavelengths, most of the emission will be optically thin ($\tau_\nu < 1$), therefore $(1-e^{-\tau_\nu}) \to \tau_\nu = \Sigma_{\rm d}\kappa_\nu$ and thus Equation 1.36 yields (assuming that the dust opacity is independent of radius)

$$F_\nu = B_\nu(\hat{T}_{\rm d})\kappa_\nu D^{-2} \int_{R_{\rm in}}^{R_{\rm out}} 2\pi r \Sigma_{\rm d}(r) dr = B_\nu(\hat{T}_{\rm d})\kappa_\nu D^{-2} M_{\rm d} \,, \tag{1.37}$$

where

$$\hat{T}_{\rm d} = \frac{\int T_{\rm d}(r)\Sigma(r) r dr}{\int \Sigma(r) r dr} \tag{1.38}$$

is the average temperature of the emitting dust (see also Woitke, 2015). Thus for a known distance of the disc, opacity, a measure of its temperature and a measurement of its flux density at an optically thin wavelength, one can estimate the dust mass of the disc. Note

[5] Note that for a disc with inclination $i \neq 0$ Equation 1.36 will have an overall factor of $\cos(i)$ as well as a factor of $1/\cos(i)$ in the exponential term.

that this is however only the *minimum* of the dust mass present, as optically thick dust will be hidden, particularly in more massive discs (see e.g. Evans et al., 2017) and not contribute to the measured flux. The same holds true for dust grains that have grown to much bigger sizes than the wavelengths at which the observations take place. This means that especially large dust grains in the cold outer disc midplane regions might not be taken into account in this estimate. Also, this requires detailed knowledge of the dust opacity, which introduces additional uncertainty. I will nevertheless use Equation 1.37 to obtain an initial estimate of the dust mass in Chapter 3 for the example of the disc of HD 163296.

Note that for very long wavelengths (small frequencies), $B_\nu \propto \nu^2$ (Rayleigh-Jeans tail) and thus

$$\nu F_\nu \propto \nu^{\beta+3} \propto \lambda^{-(3+\beta)} \,, \tag{1.39}$$

which is a modification to the optically thick disc presented in Equation 1.32. Therefore in this optically thin limit at (sub-)mm wavelengths, the slope of the SED determines κ_ν. As mentioned in Section 1.2.4, the opacity is influenced by the grain properties such as their size distribution, chemical composition, porosity, geometry and the grain size distribution (Testi et al., 2016). Observationally many discs show $\beta \approx 1 \pm 0.5 \ll \beta_{\rm ISM} \approx 2$ (Beckwith and Sargent, 1991). Calculations of the opacities for grains with different properties however show that for grains with sizes $a \gtrsim 1$ mm, the dust opacity spectral index $\beta < 1$ (Natta and Testi, 2004). Therefore $\beta < 1$ is indicative of grains of up to mm or cm size being present in discs around stars from T Tauris down to BDs (see e.g. Rodmann et al., 2006; Ricci et al., 2010a,b; Pinilla et al., 2017).

In recent times, spatially resolved continuum observations have revealed the presence of rings and gaps in the radial dust distribution of discs around many young stars (see e.g. ALMA Partnership et al., 2015; Benisty et al., 2015; Andrews et al., 2016; Isella et al., 2016; Pérez et al., 2016; Fedele et al., 2018). This has particularly been possible due to the power of ALMA. Images of the dust in discs with ALMA are showing an unprecedented amount of detail, revealing a wealth of disc structure. One famous example is the disc of TW Hya whose dust emission is shown in Figure 1.11.

Spatially resolved dust emission at different wavelengths offers the possibility of determining the disc regions where the respective emission is coming from, therefore tracing different populations of dust. Observations of smaller dust grains seem to show a bigger radius for these small grains, whereas emission from larger dust grains is predominantly coming from disc regions further in (see e.g. Rosenfeld et al., 2013; Tazzari et al., 2016). This is consistent with the picture that dust grains can grow to bigger sizes and will then drift towards the central star. As we will see later in Chapter 3, there is a growing number of discs now where gas radii are observed to be bigger than the dust radii. It is also possible

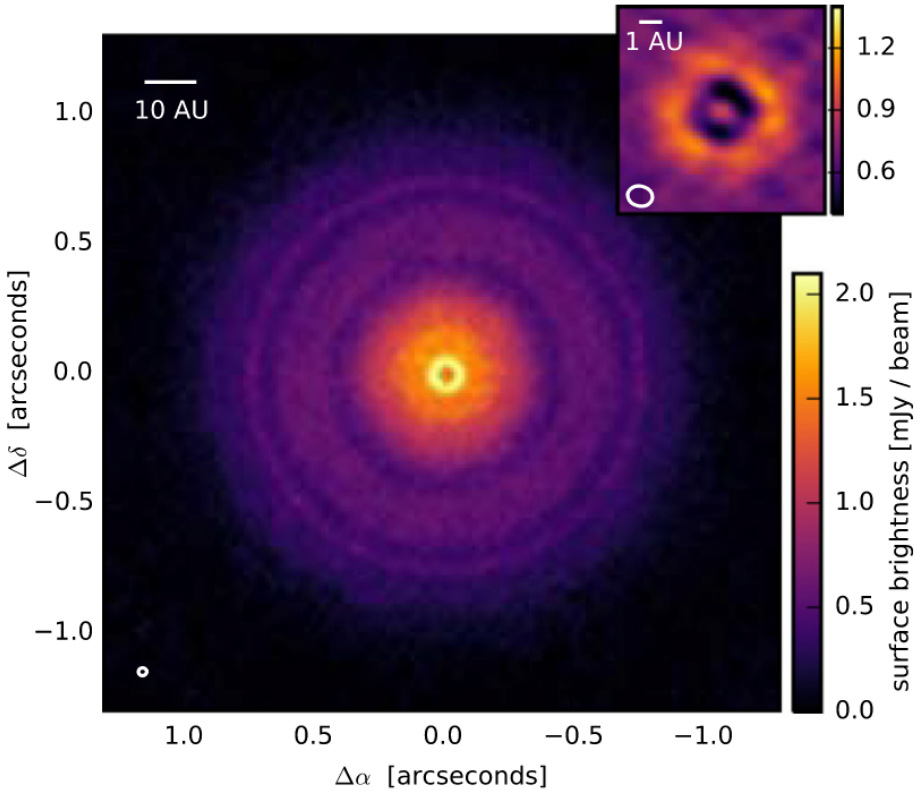

Figure 1.11 Dust continuum emission of TW Hya at a wavelength of $870\,\mu$m. The beam size is $0.03\,$arcsec and is shown in white in the bottom left corner. The small panel shows a zoom-in of the central region. Image from Andrews et al. (2016).

to make maps of the spectral index measured in discs from dust continuum observations at different wavelengths, therefore providing even more information about the properties of dust and its spatial distribution in discs (see e.g. ALMA Partnership et al., 2015, where this is presented for the HL Tau disc).

1.4 Observations of gas in protoplanetary discs

An additional method is to observe emission lines of molecules and to infer the spatial and temperature structure from these gas observations. The most abundant molecule in discs is cold H_2 gas, which is however difficult to observe due to the lack of a dipole moment (see e.g. Rybicki and Lightman, 1979). Thus rotational transitions of molecules such as ^{12}CO (which I will call CO from now on) and its isotopologues ^{13}CO and C^{18}O are employed instead (Thi et al., 2004; Dent et al., 2005). These are accessible with the ALMA telescope and provide information, especially in the IR and (sub-)mm wavelengths regime. Other species that are abundant enough to be observed are for example N_2H^+, DCO^+, DCN, CN, CS, CO_2, H_2O, OH, HCN and CH_4 (see e.g. review by van Dishoeck, 2017). It has for example

been possible to observe N_2H^+ (Qi et al., 2015), DCO+ (Mathews et al., 2013; Huang et al., 2017), HCN (Huang et al., 2017) and H_2CO (Öberg et al., 2017) with ALMA, to name just a few molecules.

1.4.1 Molecular line observations

The molecular tracers are observed as emission lines at certain frequencies, depending on the transition we are interested in. One example of the spatially resolved CO $J = 3-2$ emission of a disc is presented in Figure 1.12. The colours there are representative of the velocity of the respective disc regions, I will explain this in more detail later in this section.

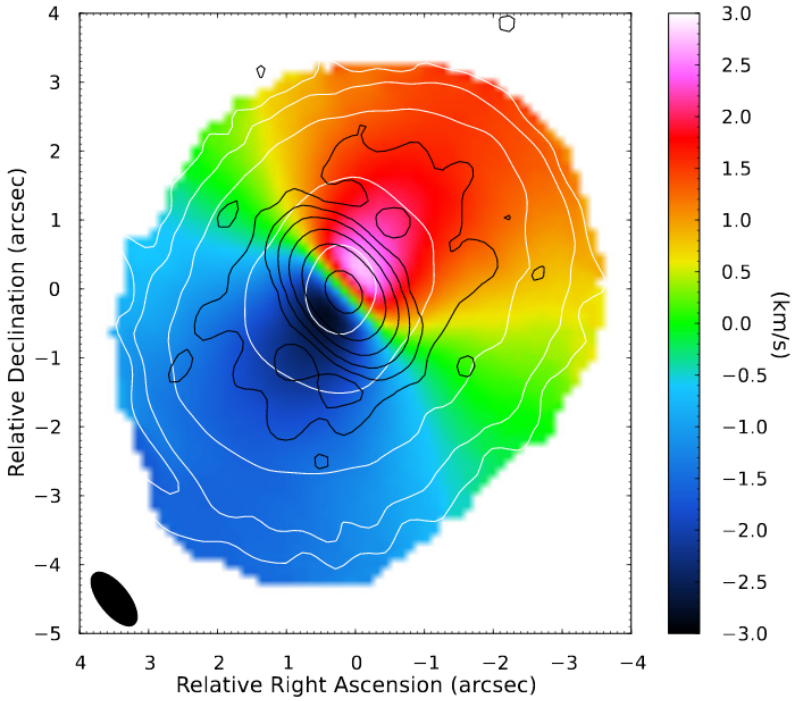

Figure 1.12 CO $J = 3-2$ emission from the disc around the Herbig Be star HD 100546. The colours give the moment 1 map (velocity map) of the CO emission, which is overlaid with integrated intensity contours (white) and the 870 μm continuum emission contours (black). The beam size is $0.95\,\mathrm{arcsec} \times 0.42\,\mathrm{arcsec}$ (see bottom left corner). Image from Walsh et al. (2014).

The line profile of a face-on disc (i.e. with no contribution to the line-of-sight velocity because of the disc rotation) will in general just be a sharp peak, broadened by thermal and turbulent motions in the gas (for an overview see e.g. Kamp, 2015). I come back to this in more detail in Chapter 2. As the disc as a whole is moving at a certain velocity, this frequency will be shifted slightly and centred on the systemic velocity. However, for protoplanetary discs, the main effect broadening the line profile is caused by the Keplerian

rotation of the gas, creating a characteristic double-peaked profile centred around the rest frequency (see also Equation 2.28). This profile is determined by the mass of the central star, the inclination of the disc and the radial brightness profile of the tracer. In a disc that is in Keplerian rotation, iso-velocity curves can be parametrized as follows (Dionatos, 2015):

$$R_{\rm iso} = R_{\rm out} \left(\frac{v_{\rm out}}{v} \right)^2 \cos^2(i) \,, \tag{1.40}$$

where $R_{\rm out}$ is the outer disc radius, $v_{\rm out}$ the Keplerian velocity at that location, v the line-of-sight velocity and i the disc inclination ($i = 0°$ is face-on). This is presented schematically in Figure 1.13 for a disc with $i = 60°$. In order to interpret this, let us assume for simplicity that the disc is face-on (with $i = 0°$) although this would not lead to a double-peaked profile. Nevertheless, the $\cos^2(i)$ term only introduces a constant factor of order unity for a fixed i and does not change the considerations presented here. We can thus interpret Equation 1.40 as follows:

- For $v \to 0$, $R \to \infty$ and therefore the iso-velocity contours approach the contour given by the line-of-sight velocity (between the yellow and green region in the figure), which gives the minimum of the double-peaked line profile.
- For $v < v_{\rm out}$, $R > R_{\rm out}$, so the iso-velocity contours are open (orange and light blue areas) and truncated at the outer disc radius.
- For $v = v_{\rm out}$, $R = R_{\rm out}$ and so the first closed contour appears (red, blue), which is not truncated. It is indicative of the line peaks.
- For $v > v_{\rm out}$, $R < R_{\rm out}$, so the contours stay closed but become smaller (dark red and blue). These disc regions contribute to the line wings and are indicative of the inner disc regions where the material rotates fastest.

For cases where the disc inclination and outer radius are known, the limiting $v_{\rm out}$ can be calculated using the peak separation of the line. Therefore, line profiles of high spectral and spatial resolution can be used to probe the stellar mass if disc inclination and radius are known[6] (see e.g. Greaves, 2004). However, it is important to keep in mind that optical depth effects will influence the line profiles and might bias results derived from them. This was for example found by Elitzur et al. (2012) who in their studies obtain double-peaked line profiles that are not due to rotation but due to modelling effects. It is also important to keep in mind that for a disc that is completely face-on (inclination $i = 0$) the double-peaked feature vanishes as there are no line-of-sight contributions to the velocity. This

[6]To be more precise, for a given inclination and disc radius $R_{\rm out}$, the mass *enclosed* in this radius can be calculated assuming Keplerian rotation ($v = \sqrt{GM_{\rm tot}/R_{\rm out}}$). So strictly speaking this is the stellar mass + the mass of the disc, however in general the enclosed mass will be dominated by the star.

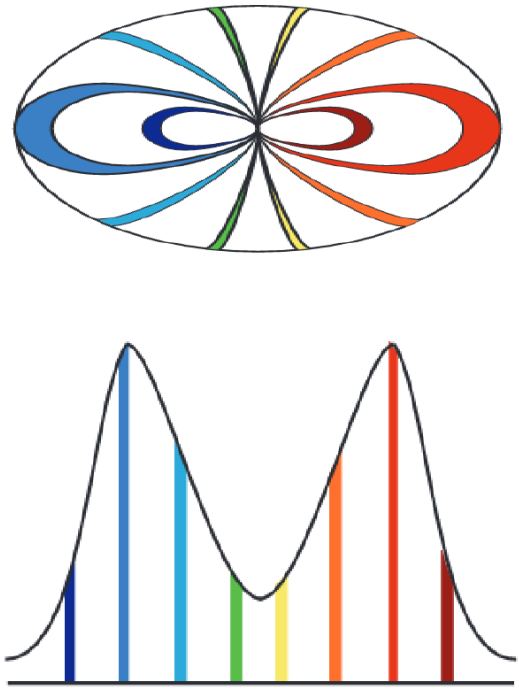

Figure 1.13 Iso-velocity contours (colour) of a disc and their corresponding contribution to the typical double-peaked line profile due to the Keplerian rotation of the disc. The regions of the disc with the largest surface area correspond to the largest peaks of the flux in the line profile. Figure adapted from Dionatos (2015).

has for example been found in the case of TW Hya (see dust emission in Figure 1.11), that has a very small inclination $i \sim 5°$ and therefore its line profiles are basically given by single peaks (Favre et al., 2013). In general, the overall shape of the line profile of a disc is determined by macroscopic effects (such as the disc rotation), whereas the width of the line is influenced by microscopic processes (such as microturbulence and thermal motion of the molecules). The latter will be discussed in more detail in Section 2.6.

In cases where the gas line cannot be spectrally resolved, an upper limit on the integrated flux (integrated along the velocity axis) might still be derived. This is a procedure that I have applied in Chapter 4, where observations of the CO $J = 2 - 1$ line emission of V410 X-ray 1 yielded a non-detection. Note that uncertainties on the knowledge of the stellar mass as well as the disc inclination do not bias results on the integrated line flux, as both these parameters will shift the line width, but do not alter the area under the line profile (and thus the integrated flux density).

In gas observations, these signatures of the Keplerian rotation can be seen when observing over a range of wavelengths. Figure 1.14 shows the emission of a protoplanetary disc in various velocity channels (i.e. at slightly different frequencies): different parts of the discs contribute to the emission at different wavelengths as the disc material is mov-

ing at different velocities. Adding the emission from all the channels gives the contours

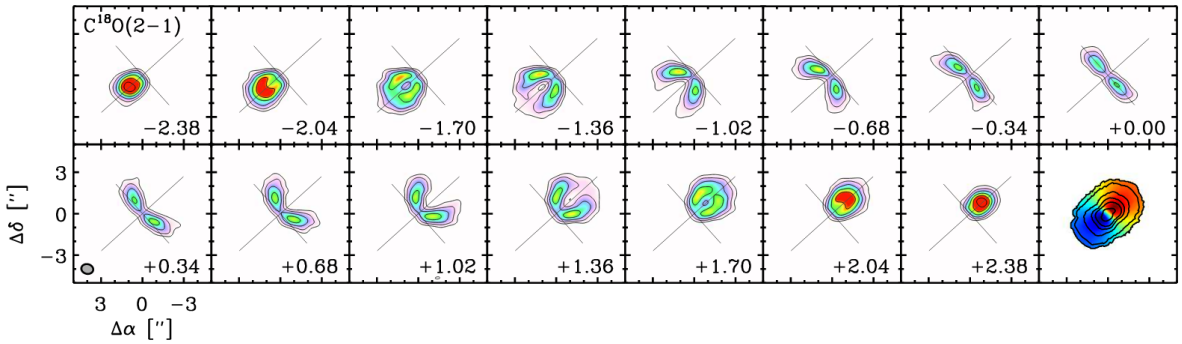

Figure 1.14 Channel maps of the $C^{18}O$ $J = 2 - 1$ emission of the disc of HD 163296 as observed with ALMA. Figure from Rosenfeld et al. (2013).

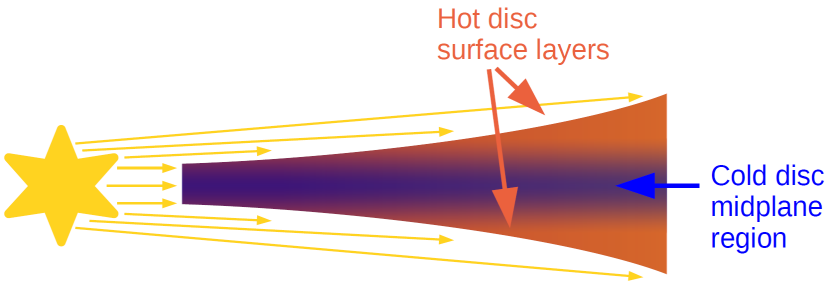

Figure 1.15 Schematic picture of the temperature structure of a protoplanetary disc.

shown in the bottom right panel (moment 0 map of frequency-integrated intensity), the colours represent the velocity information (moment 1 map of intensity-weighted velocity). The inclination i of a disc can be obtained from the ratio of its semi-minor axis b to its semi-major axis a using

$$\frac{b}{a} = \cos(i)\,. \tag{1.41}$$

A schematic depiction of the vertical and radial temperature structure of a disc is given in Figure 1.15. In order to probe this structure observationally, various transitions of the CO molecule can be employed as different transitions are excited at different temperatures. Therefore the comparison of the emission of e.g. the CO $J = 3{-}2$ and $J = 2{-}1$ transitions provides information about the temperature structure of a disc. The rest frequencies of the transitions are 345.796 GHz and 230.538 GHz respectively, where the $J = 3 - 2$ emission comes from hotter disc regions higher up in the atmosphere. The theory behind the CO line emission is explained in more detail in Section 2.6.

1.4.2 Examples of depletion mechanisms

When using gas observations to infer the disc mass, CO alone can be misleading as its emission is usually optically thick and therefore not a good tracer of the mass. However, the less abundant $C^{18}O$ can be employed instead due to its optically thin nature which makes it a good tracer of the disc midplane (see Chapter 3 where I use the $C^{18}O$ emission of HD 163296 to get a handle on the disc mass). However, there are additional complications to be taken into account: The emission lines of the CO isotopologues are influenced by the conditions in the disc. Depending on temperature and density, CO can be frozen out onto dust grains in the disc (below a temperature of $T \approx 19 - 25$ K, Qi et al. 2011) or photodissociated in the disc atmosphere.

The *CO snowline radius* is the location in the disc midplane at which CO condenses from the gas phase and freezes out onto dust grains. This radius can be observed as a steep decline in the $C^{18}O$ density or by the presence of other molecular tracers such as N_2H^+ and DCO^+ (Qi et al., 2011; Mathews et al., 2013; Qi et al., 2013a, 2015). However, the formation path of DCO^+ is not fully understood and this molecule does not probe the disc midplane but the entire surface of the $19 - 21$ K isotherms. Hence Qi et al. (2015) find that DCO^+ is not a reliable tracer of the CO snowline location. They employ ALMA N_2H^+ $J = 3-2$ observations instead that originate predominantly from the midplane and are therefore more reliable. The presence of gas-phase CO slows down the formation of N_2H^+ (as most H_3^+ will preferentially react with CO rather than with N_2) and accelerates its destruction. In terms of formation routes, the reaction of $H_3^+ + CO \longrightarrow HCO^+ + H_2$ is preferred over the reaction of $H_3^+ + N_2 \longrightarrow N_2H^+ + H_2$. In terms of destruction routes, the reaction $N_2H^+ + CO \longrightarrow N_2 + HCO^+$ acts to remove N_2H^+ from the gas phase. Thus, gas-phase N_2H^+ exists in regions where CO is depleted, so the N_2H^+ emission will be distributed in a ring whose inner radius marks the CO snowline location. Therefore, Qi et al. (2015) propose that observations of $C^{18}O$ and N_2H^+ are very powerful as they directly probe the temperature of the disc midplane. This is important for calculations of the vertical hydrostatic equilibrium in discs which crucially depend on the conditions in this disc region. Note however that recent findings by van't Hoff et al. (2017) show some uncertainty in the robustness of N_2H^+ as a tracer of the CO snowline location and imply that detailed chemical modelling is needed.

However, the exact freeze-out temperature of CO is not known unambiguously, depends on the conditions of the environment and is assumed to be between ~ 17 K (Qi et al., 2013b, in TW Hya) and ~ 30 K (Jørgensen et al., 2015, in an embedded protostar). Also, the composition of the ice will influence the freeze-out temperature (~ 20 K for pure CO ice, ~ 30 K for mixed CO-H_2O ice, Collings et al. 2004). In addition, the gas pressure

can also have an impact on the freeze-out temperature (Fray and Schmitt, 2009); however Stammler et al. (2017) find that changes in the gas pressure in the disc midplane are not sufficient to shift the CO snowline radius by amounts which would cause an observable effect in the observations. Nevertheless, measurements of the snowline location are important as they give constraints on the midplane temperature profiles of discs.

The same principle applies for the water snowline, however for temperatures of $T \approx 150\,\mathrm{K}$. This makes it harder to observe the H_2O snowline, as it is located at very small radii and therefore difficult to resolve (van Dishoeck, 2017). Therefore the chances for directly observing the water snowline are higher in systems where this location has moved outwards, for example because the system undergoes protostellar outbursts (see e.g. Cieza et al., 2016, for the example of V883 Ori) or in young and hot discs (see e.g. Harsono et al., 2015). The snowlines are depicted schematically in Figure 1.16.

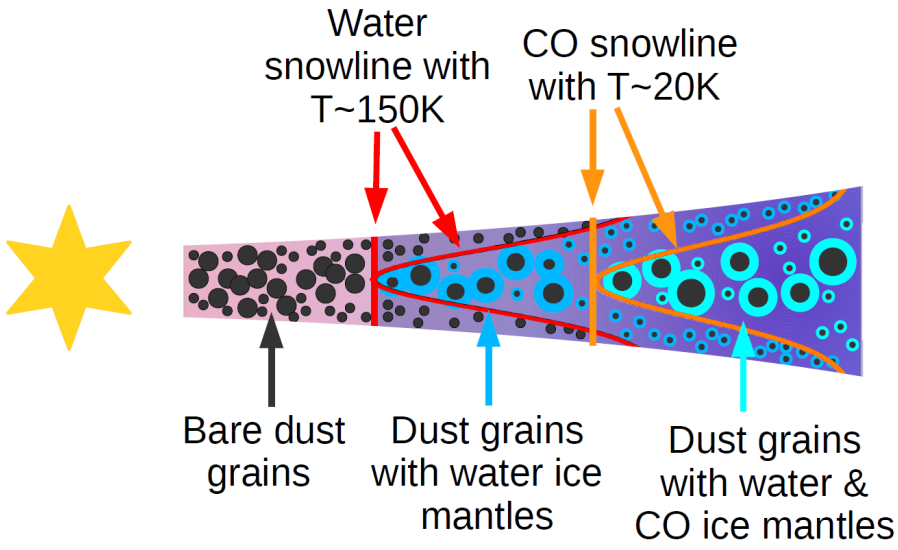

Figure 1.16 Schematic picture of the water snowline (red) and CO snowline (orange) in a protoplanetary disc

The red vertical line indicates the location of the H_2O snowline. Outside of this radius, water will be frozen out onto dust grains in regions where this temperature criterion is fulfilled, i.e. close to the disc midplane. In disc regions higher up, higher temperatures sublimate the water ice again. This leads to the presence of an entire region around the midplane where water will be frozen out (indicated by the red line in the figure, which denotes the water ice surface). The same holds true for the freeze-out of CO (and its isotopologues), but for a lower temperature. Therefore the CO snowline (vertical orange line) is located outside of the H_2O snowline.

This can be observed as a steep decline in the CO density (especially $C^{18}O$ as its emis-

sion is mostly optically thin) or by the presence of other molecular tracers such as N_2H^+ and DCO^+ (Qi et al. 2011, 2013b; Mathews et al. 2013) as detailed before. Note again that such observations are very powerful as they directly probe the temperature of the disc midplane, which is important for calculations of the vertical hydrostatic equilibrium in discs. In Chapter 3, I will make use of the knowledge of the location of the CO snowline as inferred from observations to learn about the disc structure of HD 163296. In Chapter 4, the location of the water snowline will play an important role.

Other processes altering the abundance of CO are photodissociation in the upper disc atmosphere, chemical depletion or C-sequestration in ices. All of these depletion mechanisms need to be taken into account when calculating the disc gas mass based on CO observations. Uncertainties on the abundance of CO will be addressed in more detail in Chapter 3 using the example of $C^{18}O$ $J = 2 - 1$ emission in HD 163296.

With ALMA yielding data of unprecedented spatial and spectral resolution, one can try and obtain a measure of thermal and turbulent line broadening from line observations. The influence of microturbulence on the line width is detailed in Section 2.6. There I also introduce other line broadening mechanisms as well as the theory behind line emission and absorption. Note that in general the difficulty is in knowing the underlying line profile. This requires detailed modelling for the temperature structure of the line emitting region in order to know which emission is from the line and which a result of the broadening (see e.g. Teague et al., 2016, who study the turbulence in TW Hya). By employing different CO isotopologues with different optical depths, $v_{\rm turb}$ can be mapped vertically in a disc. However, obtaining the level of turbulence from line observations is still difficult as the impact on the line width is generally very small. It has been done for the disc of HD 163296 (Flaherty et al., 2015), where very low levels of turbulence were inferred ($v_{\rm turb} < 0.1 c_{\rm s}$), and for TW Hya (Teague et al., 2016), where $v_{\rm turb} \approx (0.2 - 0.4) c_{\rm s}$ was derived.

Note also that the maximum turbulent velocity is connected to the turbulent mixing parameter $\alpha_{\rm turb}$ by (Ormel and Cuzzi, 2007)

$$v_{\rm turb} = c_s \sqrt{\frac{9\alpha_{\rm turb}}{2}}\,, \tag{1.42}$$

which will be used to estimate the turbulent line broadening in Chapter 3. The impact of $\alpha_{\rm turb}$ on the disc structure is explained in more detail in Section 2.7.1 for the case of the Monte Carlo radiative transfer code MCMax.

2

Methods: Radiative transfer

In order to understand protoplanetary discs, it is crucial to determine their physical properties from observations. That is, we have to understand the emission of radiation from the disc and propagation towards an observer. As we shall discuss in this chapter, this "radiative transfer" is sufficiently complex that it typically has to be solved numerically. I will briefly describe the formal radiative transfer equation and how it can be solved computationally using a Monte Carlo approach. I will give an overview of the radiative transfer for both dust continuum and molecular lines and will then describe the computational codes I have used in this thesis. In this section, I will follow the description and nomenclature of Dullemond (2013).

2.1 The formal radiative transfer equation

The efficiency of a medium to absorb photons can be quantified by the *mean free path* of a photon l_{free}, which is a function of frequency and position in space. The number of l_{free} which the photons travel is called the *optical depth*[1] τ. The *extinction coefficient* can be defined as

$$\alpha_\nu = \frac{1}{l_{\nu,\text{free}}} \,. \tag{2.1}$$

The extinction coefficient can also be expressed as

$$\alpha_\nu = \rho \kappa_\nu \tag{2.2}$$

with ρ being the mass density of the medium and κ_ν the *mass-weighted opacity* (see also Figure 1.7 for a plot of the opacity as a function of wavelength for different sized grains). The *optical depth* between two points s_0 and s_1 along a ray can be written as

$$\tau_\nu(s_0, s_1) = \int_{s_0}^{s_1} \alpha_\nu(s) ds \,. \tag{2.3}$$

[1] As already described in Chapter 1, a medium with $\tau \gg 1$ is optically thick and one with $\tau \ll 1$ optically thin. On average, the fraction of photons that manage to travel through a cloud of optical depth τ is $\exp(-\tau)$.

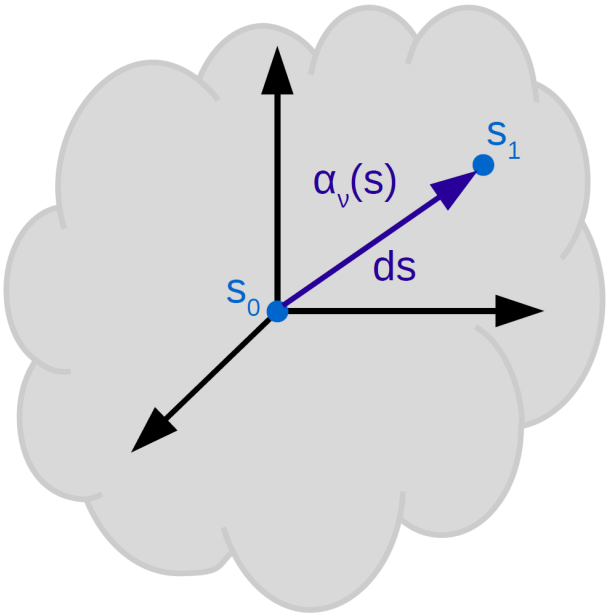

Figure 2.1 Schematic depiction of a segment ds of the ray between points s_0 and s_1.

This is depicted schematically in Figure 2.1, where s_0 and s_1 are marked and ds is the path between them with extinction coefficient $\alpha_\nu(s)$. For a medium consisting of dust particles of radius a that are very large compared to the wavelength λ, the cross section per particle is equal to the geometrical cross section $\sigma = \pi a^2$. For cases where $\lambda \gg a$, the cross section is smaller than the geometrical σ. For a particle of mass m, we find that the mass-weighted opacity can be written as

$$\kappa_\nu = \frac{\sigma_\nu}{m} \,. \tag{2.4}$$

Taking into account extinction, the variation in intensity along a ray in direction **n** can be expressed as

$$\frac{dI_\nu(\mathbf{n}, s)}{ds} = -\alpha_\nu(s) I_\nu(\mathbf{n}, s) \,, \tag{2.5}$$

which is the formal radiative transfer equation for a purely absorbing (i.e. non emitting) medium. In integrated form it reads

$$I_\nu(\mathbf{n}, s_1) = I_\nu(\mathbf{n}, s_0) e^{-\tau_\nu(s_0, s_1)} \tag{2.6}$$

with τ specified in Equation 2.3. For a case where the medium is also emitting, Equation 2.5 can be modified to give the complete **formal radiative transfer equation:**

$$\frac{dI_\nu(\mathbf{n}, s)}{ds} = j_\nu(s) - \alpha_\nu(s) I_\nu(\mathbf{n}, s) \,, \tag{2.7}$$

where the source term j_ν is the *emissivity*. In integral form it reads

$$I_\nu(\mathbf{n}, s_1) = I_\nu(\mathbf{n}, s_0)e^{-\tau_\nu(s_0,s_1)} + \int_{s_0}^{s_1} j_\nu(s)e^{-\tau_\nu(s,s_1)}ds\,. \tag{2.8}$$

Note that in general the first term is zero for the case of a protoplanetary disc as we are interested in emission from the disc itself but not in the light from a background source travelling through the disc. An exception to this is the case where the central star can be seen through a flared, edge-on disc, where these effects need to be taken into account. This is for example the case for some discs in the Orion Nebula Cluster, which were observed with the Hubble space telescope (Smith et al., 2005). The second term describes the emission generated at each point of the disc, which is then attenuated by the disc on its way to the observer. Integrating the second term then gives the $(1 - e^{-\tau})$ term that was used in the derivation of the minimum dust mass of an optically thin disc in Equation 1.37.

In a medium that is in *local thermodynamic equilibrium (LTE)*, irrespective of the optical depth of the medium, the intensity I_ν is equal to the Planck function $B_\nu(T)$ described in Equation 1.27. This is due to the fact that the Planck function represents the equilibrium distribution of photons that are in thermal equilibrium with a medium of temperature T.[2] Thus Equation 2.7 has to be $= 0$ and therefore

$$j_\nu(s) - \alpha_\nu(s)I_\nu(\mathbf{n}, s) = j_\nu(s) - \alpha_\nu(s)B_\nu(T) = 0\,, \tag{2.9}$$

giving *Kirchhoff's law*:

$$\frac{j_\nu}{\alpha_\nu} = B_\nu(T)\,. \tag{2.10}$$

Thus for a medium in thermal equilibrium any emissivity j_ν and extinction α_ν are allowed as long as their ratio is the Planck function. In LTE the formal radiative transfer equation can thus be written as

$$\frac{dI_\nu(\mathbf{n}, s)}{ds} = \alpha_\nu(s)\left[B_\nu(T(s)) - I_\nu(\mathbf{n}, s)\right]\,. \tag{2.11}$$

Therefore the intensity I_ν is trying to asymptotically approach the Planck function. For a temperature that is constant along the ray, I_ν exponentially approaches $B_\nu\,[T(s)]$, for T varying along the ray, I_ν will try to approach B_ν, but will lag behind by a few mean free paths.

[2] Usually a Planck function implies that the photons have at some stage had many interactions with a medium of a given temperature - i.e. that they originated in an optically thick region of that temperature.

2.2 The source function

Equation 2.11 is only valid for LTE, but it can be generalised by defining a *source function*

$$S_\nu = \frac{j_\nu}{\alpha_\nu}\,, \tag{2.12}$$

so the formal radiative transfer equation can be written as

$$\frac{dI_\nu(\mathbf{n},s)}{ds} = \alpha_\nu(s)\left[S_\nu(s) - I_\nu(\mathbf{n},s)\right]\,. \tag{2.13}$$

In LTE, the source function is equal to B_ν and the equation takes the form of Equation 2.11. The source function acts as an "attractor" for the intensity as at every point along the ray I_ν wants to approach the source function S_ν. Note that this is the time-independent form of the equation, which is valid to assume if the light propagation through the medium is much faster than the timescale on which the medium changes. This is generally a fair assumption to make for protoplanetary discs as they evolve on timescales of 10^6 yr (see e.g. Figure 1.6).

2.3 The 'Monte Carlo' method

The problem for solving the radiative transfer equation is that in general the emissivity j_ν and the extinction coefficient α_ν are not known in advance: the radiation field I_ν that we are interested in can affect the medium through which it travels and therefore influence j_ν and α_ν, which in turn then affect the radiation field. Also, the problem will have to be solved for all rays through the medium simultaneously: rays are not independent of each other and the intensity along one ray can affect j_ν and α_ν, therefore influencing the conditions for the next ray. In order to tackle this, numerical radiative transfer codes are used. There are various ways of solving the radiative transfer equation, I will focus on the *Monte Carlo* method here.

The Monte Carlo method (Lucy, 1999) is a probabilistic approach, where the radiation from the star is divided into photon packages. These are then propagated through the medium (where they can undergo scattering, absorption and re-emission) to determine the complete radiation field in the medium, which allows to calculate the temperature structure. The direction in which the photon is emitted is determined by drawing a random number. Then along its path, the photon package has a certain probability to be scattered or absorbed. Based on the drawing of another random number, the location of

the next scattering of the photon on its way along the path is determined. This process is repeated for a large number of photon package (thousands or even millions), until a good statistical sample of the photon paths has been reached. If one considers a grid of cells, the energy of each cell can be calculated after the interaction with a photon package. Note that the energy of the photon package is not only added to the cell if the photon is absorbed, as in that way very optically thin cell would never be sampled because the photons would just go through without being absorbed. Instead, the time a photon packet spends in each cell is counted. If the photon - travelling at the speed of light c - traverses a length l through a cell, the time spent is given by l/c. Thus, if the photon package had energy E, it adds energy El/c to the cell. Calculating the energy of each cell then allows to compute the final temperature of the cell, taking into account heating and cooling effects. I will explain this in more detail in Section 2.5 for the case of dust radiative transfer.

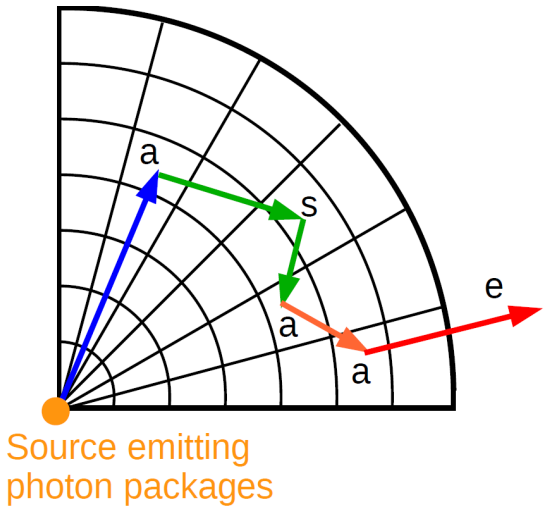

Figure 2.2 Schematic picture of the random walk of a photon packet across the grid (in this example a spherical grid). The "a" denotes an absorption event (frequency and propagation direction of the re-emitted photon package are changed), "s" a scattering event (where the frequency stays the same, but the direction is changed) and "e" is where the photon package leaves the grid. Figure based on Haworth (2010).

The random walk of a photon package is schematically illustrated in Figure 2.2. Due to the finite number of photon packages used, there is a stochastic error on the disc temperature, which can be reduced by increasing the number of photons (which in turn increases the computational cost). Note that in Monte Carlo radiative transfer the noise is *Poisson noise*. Therefore for a number of photon packets N the signal scales as $\sqrt{N}$. This makes it difficult to substantially increase the signal-to-noise by increasing the number of photons. One advantage of the Monte Carlo method is that it mimics the propagation of photons in a three-dimensional way.

2.4 Ray tracing

In order to obtain observables such as synthetic data cubes from radiative transfer calculations, the method of *ray tracing* can be used. This method is basically solving the radiative transfer equation along a single direction (interpolating the opacities and emissivities along the way), from some origin across the entire computational domain, for example from the centre of a cell right through to the observer. This is often used to produce synthetic images as it is straightforward and quite efficient (as rays are only sent in the required regions), however it is inefficient if one is for example solving for the temperature. This type of ray tracing is called *long characteristic*. There is an alternative method called *short characteristic* that works better for temperature calculations. For more details on ray tracing see e.g. Hogerheijde and van der Tak (2000); Rundle et al. (2010).

From the ray tracing one can calculate what the object would look like for an observer, by e.g. specifying the viewing angle of the observer. Note that the images obtained in this way are "perfect images" without observational noise. Therefore, in order to compare them with actual observations, they will have to be post-processed to take account of instrumental response and disturbances by the Earth's atmosphere such as water vapour and the thermal motion of molecules in the atmosphere blurring the image. One example of this is given in Chapter 3, where synthetic $C^{18}O$ data cubes are processed to mimic ALMA observations.

2.5 Dust continuum radiative transfer

Dust grains play a crucial role in setting the disc temperature as they dominate the continuum opacities. In the short wavelength regime, the stellar emission is scattered, absorbed and polarised by the dust grains, whereas at longer wavelengths, dust grains thermally re-emit the absorbed radiation. The temperature of a dust grain in a protoplanetary disc is set by the radiation field, which must be computed self-consistently taking into account heating and cooling (for a review on continuum radiative transfer see e.g. Dullemond, 2013; Pinte, 2015).

One of the most widely used methods to calculate dust radiative transfer in the method by Bjorkman and Wood (2001). In the case where a photon gets scattered, its frequency stays the same, but it might be scattered non-isotropically. If the photon gets absorbed in a cell, its energy is added to that of the cell. The photon then gets re-emitted in a random direction and its frequency will in general be changed. This leads to either heating or

cooling of the cell as follows: the photon packages travelling through the medium have a certain energy. Part of this energy will be injected into a cell in the case of an absorption and re-emission event. The amount of energy deposited in a cell depends on the opacity of the cell as well as the length of the ray through the cell and its volume. From the energy E_i of each cell, the temperature T_i can then be calculated, taking into account that we want to determine the temperature that is required for that cell to emit the respective amount of energy E_i over a 4π steradian:

$$E_i = 4\pi \int_0^\infty \alpha_\nu^{\text{abs}} B_\nu(T_i) d\nu \,. \tag{2.14}$$

For the case where the photon that is absorbed is the first one to do so, a new photon will be re-emitted, but with a spectrum that corresponds to the new temperature of the cell and the dust opacity of the cell. In the case where the cell has previously already absorbed and re-emitted photon packages before this new absorption event, the photon that is now emitted will have a spectrum that takes into account the difference in cell temperature before and after the absorption.

This can then be done for all photon packages in order to determine a final temperature of the cell. In order to conserve luminosity, photon packages cannot be destroyed (unless they are emitted back to the star or escape the medium into infinity.) It is important to note that a photon package that is emitted with a frequency ν still has the same energy as it had initially, which means that the number of photons in the package will have changed. This is due to the fact that in radiative equilibrium photon number is not conserved, but energy is.

The heating rate is given by adding the energy absorbed per second from the photons at all frequencies (Pinte, 2015):

$$Q_+ = 4\pi \int_0^\infty \kappa_\nu^{\text{abs}} J_\nu d\nu \,, \tag{2.15}$$

where J_ν is the mean intensity and thus the angular average of I_ν:

$$J_\nu = \frac{1}{4\pi} \int_\Omega I_\nu(\mathbf{n}) d\Omega \,. \tag{2.16}$$

For a dust grain of temperature T, the cooling rate is given by

$$Q_- = 4\pi \int_0^\infty \kappa_\nu^{\text{abs}} B_\nu(T) d\nu \,, \tag{2.17}$$

defined by the energy emitted per second by this grain.

In radiative equilibrium, $Q_+ = Q_-$ (thermal balance). Equating Equations 2.15 and 2.17 then sets the temperature of the dust grain. This means that for a given radiation field J_ν, the dust temperature is determined by the shape of the opacity. For the case of a protoplanetary disc (where the radiation field is dominated by the stellar emission), the ratio of opacities at the wavelength of the peak of the stellar photosphere to the peak of the dust emission sets the dust temperature. This can be understood as follows (see also Pinte 2015): large (mm) grains have a rather flat opacity law between optical and MIR wavelengths (see Figure 1.7 or Min 2015). They thus absorb less stellar emission and can re-emit efficiently in the IR. Therefore their temperature is much lower than that of the very small (sub-μm) grains, whose κ is very steep in this wavelength range, i.e. they do not emit efficiently in the MIR. Thus to re-emit, they have to attain higher temperatures.

Taking into account the scattering of photons on dust grains makes the calculations more complicated as on the one hand they can be scattered away from the beam, but also into the beam from other directions. Therefore the absorption, extinction and scattering cross sections must be taken into account in the radiative transfer equation, relating the radiation fields in all directions at all positions. As an additional complication, for an optically thick medium, optical depth effects need to be taken into account. The intensity $I_\nu(\mathbf{n}, s)$ depends on the source function, which in turn is dependent on the specific intensity emitted by the other points in the disc, for both the scattering and re-emission. This makes solving the radiative transfer equation a highly complicated problem.

If a photon packages finds itself in a region of high optical depth it could undergo millions (or even more) scatterings before it manages to escape. Regions of high optical depth are computationally expensive (the run time scales approximately as τ^2) as they need a large number of photon packages in order to get a statistically correct temperature. However, two simplifications can be made in order to speed up the computation and mitigate this problem (see e.g. Min et al., 2009; Mulders, 2013, Harries et al. (in prep.) for a more detailed description).

The first one is the *partial diffusion approximation*. There, energy transport is dominated by radiative diffusion (described by a diffusion equation, see e.g. Wehrse et al. 2000). In the limit of very optically thick dust, solving the diffusion equation is actually much more efficient than the Monte Carlo radiative transfer. In these optically thick disc midplane regions where photon packets cannot easily penetrate, the diffusion equation is solved locally using neighbouring cells (whose temperature can be determined from the Monte Carlo packet propagation) as a boundary condition. With this approximation, the number of photon packages needed to calculate the midplane temperature can be reduced by two orders of magnitude (see e.g. Min et al., 2009, for an implementation of this approximation in the code MCMax).

The second approximation is the *modified random walk*. Photon packages can get lost in regions of high optical depth, where it can then take a large number of scattering events until the package can leave the region. Although this usually only happens for a few photons, these will dominate the computation time. This can be overcome by setting up a sphere within the grid cell and using diffusion theory to move the packet to the boundary of the sphere in one computational step instead of multiple interactions (Fleck and Canfield, 1984). This process is described in detail in Min et al. (2009) for the application in MCMax and in Robitaille (2010).

2.6 Molecular line radiative transfer

Gas opacities in protoplanetary discs are in general dominated by molecular line emission from *bound-bound transitions*, where molecules change their state between two sharply defined states of energy. Collisions between molecules make them jump from one discrete energy state to the next (*collisional transitions*), whereas *radiative transitions* on the other hand are caused by sending out or absorbing a photon, causing the transition from one energy level to the next. In this section, we will follow the description and nomenclature in Dullemond (2013).

Level populations, statistical weights and the partition function

Let us consider the case of a molecule with N_{levels} discrete quantum-mechanical energy states E_i (where $i = 1...N_{\text{levels}}$). The number of molecules per occupational state in a volume of gas gives the *occupation number density* N_i of each state. To obtain the total number N of molecules per unit volume, one can sum up all the N_i and the *fractional occupation number* can be defined as

$$n_i = \frac{N_i}{N}\,, \tag{2.18}$$

which is normalised such that $\sum_i n_i = 1$. Calculations of these fractional occupation numbers can be done with line radiative transfer calculations.

As mentioned above, collisions between molecules can change the state of a molecule. In regions of high density, collisions occur so frequently that one can assume that the system is in LTE. Therefore, the occupation numbers n_i are thermally distributed (following

a Boltzmann distribution):

$$\frac{n_j}{n_i} = \frac{N_j}{N_i} = \frac{\exp\left(\frac{-E_j}{k_\mathrm{B}T_\mathrm{gas}}\right)}{\exp\left(\frac{-E_i}{k_\mathrm{B}T_\mathrm{gas}}\right)} . \tag{2.19}$$

In regions of low density however, radiative processes can dominate the transitions, leading to a non-LTE environment, where Equation 2.19 is no longer valid. I will come back to this later in the section.

Another effect that needs to be taken into account is the *degeneracy of states*, where molecules have different states with exactly the same energy, due to rotational symmetry. Treating all orientations of a state with the same energy as a single state i (instead of individual states), one can introduce the *statistical weight* g_i. Equation 2.19 can then be written as

$$\frac{n_j}{n_i} = \frac{N_j}{N_i} = \frac{g_j \exp\left(\frac{-E_j}{k_\mathrm{B}T_\mathrm{gas}}\right)}{g_i \exp\left(\frac{-E_i}{k_\mathrm{B}T_\mathrm{gas}}\right)} . \tag{2.20}$$

This gives the *ratio* of the fractional occupation numbers, so in order to calculate the n_i themselves, one has to take into account the *partition function* $Z(T)$ as follows

$$Z(T) = \sum_i g_i \exp\left(\frac{-E_i}{k_\mathrm{B}T_\mathrm{gas}}\right) , \tag{2.21}$$

where the sum is over all states. The **fractional occupation number in LTE** (giving the fraction of molecules in state i) is then given by

$$n_i = \frac{g_i}{Z(T)} \exp\left(\frac{-E_i}{k_\mathrm{B}T_\mathrm{gas}}\right) = \frac{g_i \exp\left(\frac{-E_i}{k_\mathrm{B}T_\mathrm{gas}}\right)}{\sum_i g_i \exp\left(\frac{-E_i}{k_\mathrm{B}T_\mathrm{gas}}\right)} . \tag{2.22}$$

Thus, the probability for a molecule to occupy a certain state is strongly dependent on the temperature. Note that in Chapter 3 we will use these considerations to calculate the level populations and thus the emission of $C^{18}O$ in the disc of HD 163296.

Collisions

As already mentioned above, collisions between molecules can change the state. This happens especially frequently in regions of high density. The *rate* at which the transition from

level i to j happens can be expressed as

$$C_{i\to j} = NK_{i\to j}(T)\,, \tag{2.23}$$

where N is the number density of particles and $K_{i\to j}(T)$ the *collision coefficient*, which is often complicated to calculate.

For the case where the molecule loses energy in the collision (i.e. $E_j < E_i$), the collision coefficient only has a weak temperature dependence and it can often be found in tabulated form. The collision coefficient for the upward transition $K_{j\to i}(T)$ is then dependent on $K_{i\to j}(T)$ in a way that preserves the LTE populations (see Equation 2.22):

$$n_j C_{j\to i} = n_i C_{i\to j}\,. \tag{2.24}$$

Using Equation 2.20, this then gives

$$C_{j\to i} = C_{i\to j}\frac{g_i \exp\left(\dfrac{-E_i}{k_{\rm B}T_{\rm gas}}\right)}{g_j \exp\left(\dfrac{-E_j}{k_{\rm B}T_{\rm gas}}\right)}\,. \tag{2.25}$$

It is important to keep in mind that molecules do not only undergo collisions with molecules of the same species, but also with different types of molecules. In each case a specific set of $C_{i\to j}$ needs to be used.

Line emission and absorption

Cases where the transition between states is facilitated by emitting or absorbing a photon are called *radiative transitions* or *spectral line transitions*. These are dominant in regions of lower density, where collisional transitions are not that prevailing and therefore the assumption of LTE cannot be made. This is for example considered in the radiative transfer code DALI (described below) which is used in Chapter 4 to calculate the CO emission also in disc regions of low density. In order to describe the radiative transitions, we have to solve the radiative transfer equation (Equation 2.13) that was introduced earlier in the chapter

$$\frac{dI_\nu}{ds} = j_\nu - \alpha_\nu I_\nu\,, \tag{2.26}$$

with the emissivity j_ν and the extinction coefficient α_ν. The energy difference between two levels ($E_i > E_j$) is given by

$$h\nu_{ij} = E_i - E_j\,. \tag{2.27}$$

In general, j_ν and α_ν are only non-negligible very close to this frequency ν_{ij}. There are various processes that can broaden the line (and will be discussed later in this section) and therefore the photon that is absorbed or emitted does not have to be exactly at ν_{ij}. We can define a *line profile* $\Phi(\nu)$, which describes how likely a transition is because of photons of frequency ν. It is normalised such that $\int_0^\infty \Phi(\nu)d\nu = 1$ and has a maximum at $\nu = \nu_{ij}$. Also, it quickly drops off for frequencies smaller or larger than ν_{ij}.

Let us consider the case of a protoplanetary disc, which rotates around the central star. Considering gas moving at velocity **v**, the lines will be Doppler-shifted with respect to an observer in the rest frame of the lab, depending on the direction of the observations. In general, the frequency will be shifted according to $\nu = \nu_{ij}(1 - v/c)$. This then yields the following line profile (see also Figure 1.13 for a schematic diagram):

$$\Phi_{ij}(\nu, \mathbf{v}) = \Phi_{ij}\left[\nu_{ij}\left(1 - \frac{\mathbf{n}\cdot\mathbf{v}}{c}\right)\right] , \tag{2.28}$$

where **n** is the direction of the radiation and the velocity **v** depends on the location. Therefore, the Doppler shift and the line profile can change along the ray for a given ray with given direction. Note that the line profile can be broadened by microscopic processes, which I will discuss later in this section.

Let us now focus on three types of radiative transitions:

- **Spontaneous radiative decay/emission:** For a given $\Phi(\nu)$, the emissivity due to spontaneous decay (emitting a photon) can be written as

$$j_{ij,\nu} = \frac{h\nu_{ij}}{4\pi} N_i A_{ij} \Phi_{ij}(\nu) , \tag{2.29}$$

  where A_{ij} is the *radiative decay rate* (also called *Einstein A-coefficient*) and N_i is given by Equation 2.18. This implies that A_{ij}^{-1} is the average time that a molecule can stay in i before radiatively decaying into j (in case there are no collisions taking place that could also alter the state).

- **Spontaneous extinction:** This process can excite a molecule from a lower to a higher state by absorbing a photon. The extinction coefficient α_ν can be written as

$$\alpha^0_{ij,\nu} = \frac{h\nu_{ij}}{4\pi} N_j B_{ji} \Phi_{ij}(\nu) , \tag{2.30}$$

  using the *Einstein-B coefficient for extinction* B_{ji}.

- **Stimulated emission:** This process can be expressed by adding a negative opacity to the extinction in Equation 2.30, leading to

$$\alpha_{ij,\nu} = \alpha^0_{ij,\nu} - \frac{h\nu_{ij}}{4\pi} N_i B_{ij} \Phi_{ij}(\nu) = \frac{h\nu_{ij}}{4\pi}(N_j B_{ji} - N_i B_{ij})\Phi_{ij}(\nu)\,, \tag{2.31}$$

  with B_{ji} the *Einstein B-coefficient for stimulated emission.*

The Einstein coefficients are connected by the *Einstein relations*:

$$A_{ij} = \frac{2h\nu^3_{ij}}{c^2} B_{ij}\,; \quad B_{ji} g_j = B_{ij} g_i\,, \tag{2.32}$$

which must be valid in order to conserve Equation 2.22 in a radiation field B_ν at the same temperature. The values of A_{ij} haven been tabulated from lab experiments; from them B_{ij} and B_{ji} can be calculated.

In general, molecular lines preferentially originate from regions close to where the critical density is reached and where the optical depth of the line approaches 1. The critical density can be defined as

$$n_{\rm cr} = \frac{A_{ul}}{C_{u\to l}}\,, \tag{2.33}$$

where A_{ul} is the Einstein coefficient of spontaneous radiative decay and $C_{u\to l}$ the collision rate between the levels u and l of the line transition. Generally, line fluxes are dependent on the level populations (i.e. on the column density of a molecule in the upper energy level). For the simplified case where β is the probability of a line photon that is emitted in a column of gas to escape the medium, the line flux F_{ul} can be written as (see e.g. Kamp, 2015):[3]

$$F_{ul} \approx N_u A_{ul} h\nu_{ul} \beta(\tau_{ul}) \frac{\Omega_{\rm source}}{4\pi}\,. \tag{2.34}$$

Here, τ_{ul} is the optical depth at the line centre with frequency ν_{ul}, N_u the column density of the upper level and $\Omega_{\rm source}$ the solid angle of the region that emits the line. Therefore, in order to calculate line fluxes, it is important to calculate the respective column densities, which in turn depend on the level populations. For regions with density larger than $n_{\rm cr}$ (which will be in LTE), collisional coupling will be very efficient and therefore the level populations will follow the Boltzmann distribution as discussed in Equation 2.22. As already mentioned, this is what is taken into account for the calculation of the $C^{18}O$ line emission in Chapter 3.

[3] The equation can be obtained by using Equation 2.26 in integrated form, employing the definitions of α, j and τ from Equations 2.31, 2.29 and 2.3, respectively and integrating over the resulting intensity to obtain the flux density.

In the cases where the assumption of LTE is non-prudent (e.g. in low density regions), all radiative and collisional processes determining the level populations have to be taken into account. A detailed description thereof can be found e.g. in Dullemond (2013); Kamp (2015). The calculation of the level populations in non-LTE requires a level list (with detailed information of E_i and g_i for each level i), a table for the collisional transition rates C_{ij} and a line list (where the respective indices i and j are listed, as well as the A_{ij}). As it is difficult to measure the collision rates C_{ij} in lab experiments, this makes the computation of non-LTE even more complicated (Dullemond, 2013).

Rotational lines

In Chapters 3 and 4, I will be using emission from the CO molecule, more specifically the rotational transitions $J = 3-2$ and $J = 2-1$. CO is a linear molecule, where the rotational quantum number J gives the total angular momentum of the molecule. The statistical weight is then given by

$$g = 2J + 1 \tag{2.35}$$

and the energy levels by

$$E = \frac{\hbar^2}{2I} J(J+1)\,, \tag{2.36}$$

where I is the *moment of inertia* of the molecule ($I = 1.46 \times 10^{-39}$ g cm^2 for the CO molecule). Radiative transitions can only take place between levels $J \rightarrow J-1$ as the photon with a spin of 1 requires the change of angular momentum to be ± 1 (due to the conservation of angular momentum). Thus the frequencies have to follow the *rotational ladder* (see Equation 2.27):

$$h\nu = E_{\mathrm{J}} - E_{\mathrm{J\text{-}1}} = \frac{\hbar^2}{2I}[J(J+1) - (J-1)J] = \frac{\hbar^2}{I} J\,. \tag{2.37}$$

Therefore the frequencies of the lines increase linearly with J. This is sketched schematically in Figure 2.3.

As an example, the $J = 2-1$ transition takes place at a frequency of $\nu \approx 231$ GHz and the $J = 3-2$ transition at $\nu \approx 346$ GHz. These are generally the strongest lines in protoplanetary disc in the (sub-)mm wavelength regime. The reason for this is also that the H_2 molecule - which is the most abundant - is a symmetric molecule that does not possess a permanent dipole moment and therefore upon rotation does not produce dipole radiation. Also, its lower mass implies that the quantum levels are at much higher energies and therefore shorter wavelengths (see Equation 2.36). Thus CO (the second most abundant molecule in discs) is the strongest emitter of lines in the (sub-)mm.

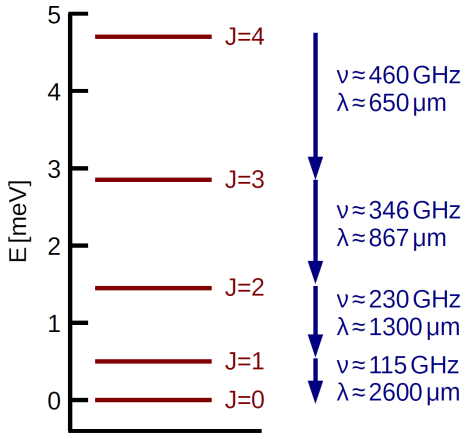

Figure 2.3 Schematic illustration of the first four energy levels of the CO molecule ("rotational ladder"), including frequency and wavelength of the respective transition.

Line broadening mechanisms

The line profile function $\Phi(\nu)$ was introduced earlier in this chapter (see Equation 2.28). I will now give an overview of the mechanisms broadening the molecular lines:

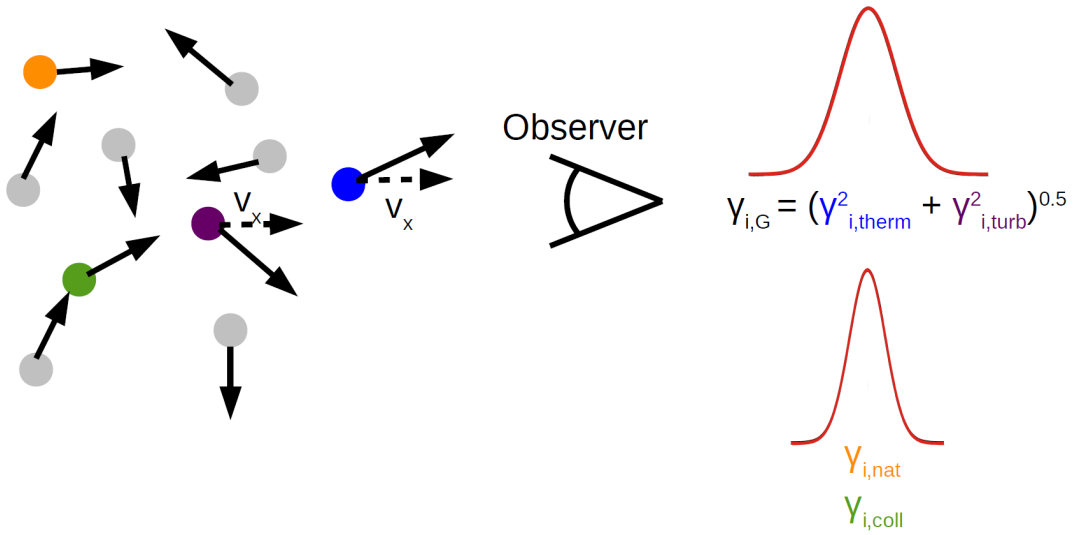

Figure 2.4 Schematic picture of line broadening due to thermal effects (dark blue), microturbulence (purple), natural line broadening (orange) and collisions (green). Figure based on and adapted from Kamp (2015).

- **Thermal broadening:** The thermal motion of the gas particles can broaden the line. A molecular line at frequency ν_i in the rest frame of the molecule will thus experience a Doppler-shift if the particle is moving with respect to the observer. Particles that are moving thermally have a random velocity distribution (projected along the line

of sight towards the observer) of

$$P(v_x) = \frac{1}{\sigma_x\sqrt{2\pi}} \exp\left(-\frac{v_x^2}{2\sigma_x^2}\right) \tag{2.38}$$

with the variance of the velocity distribution $\sigma_x^2 = \sqrt{\langle v_x^2\rangle} = \sqrt{k_\mathrm{B}T_\mathrm{gas}/m}$ for a molecule of mass m. Thus the line profile can be written as

$$\Phi(\nu) = \frac{1}{\gamma_{i,\mathrm{thermal}}\sqrt{\pi}} \exp\left[-\frac{(\nu-\nu_i)^2}{\gamma_{i,\mathrm{thermal}}^2}\right], \tag{2.39}$$

which is a Gaussian profile with width $\gamma_{i,\mathrm{thermal}} = \nu_i/c\,\sqrt{2k_\mathrm{B}T_\mathrm{gas}/m}$. Therefore the Doppler broadening depends on the mass of the molecule (i.e. the broadening is weaker for molecules of larger mass). This line broadening mechanism is shown schematically in blue in Figure 2.4.

- **Turbulent broadening:** Microturbulence is another effect Doppler-shifting the line. Turbulent motions can be treated as a velocity dispersion and the probability distribution of the velocities is then of Gaussian form (see Equation 2.38), where the variance σ_x^2 is now independent of m and T_gas. Usually the turbulent velocity dispersion can be employed in terms of an additional term $\gamma_{i,\mathrm{thermal}}$ to the thermal line width. Given that for the CO in protoplanetary discs mostly thermal and turbulent broadening play a role, we will focus on the joint effect of these here. The combination of both gives a Gaussian profile:

$$\Phi_{i,\mathrm{G}}(\nu) = \frac{1}{\gamma_{i,\mathrm{G}}\sqrt{\pi}} \exp\left[-\frac{(\nu-\nu_i)^2}{\gamma_{i,\mathrm{G}}^2}\right] \tag{2.40}$$

with the width $\gamma_{i,\mathrm{G}} = \sqrt{\gamma_{i,\mathrm{thermal}}^2 + \gamma_{i,\mathrm{turb}}^2}$. Here, $\gamma_{i,\mathrm{turb}}$ is given by

$$\gamma_{i,\mathrm{turb}} = \frac{\nu_i}{c} a_\mathrm{turb}\,, \tag{2.41}$$

where $a_\mathrm{turb} = \sqrt{2}\langle v_{x,\mathrm{turb}}^2\rangle = \sqrt{\frac{2}{3}}\langle v_\mathrm{turb}^2\rangle$. This is illustrated in purple in Figure 2.4. Note however that turbulent line broadening is a minor factor in discs and is limited by the maximum turbulent velocity, i.e. the sound speed in the midplane of the disc given by

$$c_s = \sqrt{\frac{k_\mathrm{B}T_\mathrm{mid}(r)}{\mu m_\mathrm{H}}}\,, \tag{2.42}$$

as introduced in Section 1.4.

- **Collisional broadening:** Collisions of gas particles decrease the lifetimes in the respective energy level. Let us consider the case of a molecule in the rotational ground state with frequency ν_i. The molecule is vibrating with an oscillation that can be described by a cosine function. If the molecule however undergoes collisions, the oscillation will no longer be a stable cosine. If this molecule then interacts with radiation, not only photons with an exact energy of $h\nu_i$ will interact with it, but also photons with a slightly shifted frequency. The corresponding line profile is of Lorentzian shape and given by

$$\phi(\nu) = \frac{1}{\pi} \frac{\gamma_{i,\mathrm{coll}}}{(\nu - \nu_i)^2 + \gamma_{i,\mathrm{coll}}^2} \tag{2.43}$$

  with the collisional broadening parameter $\gamma_{i,\mathrm{coll}}$. This parameter depends on the exact details of the collisions and the collision partners and is usually taken from laboratory tables. The process is schematically depicted in green in Figure 2.4.

  Overall, collisional broadening only plays a minor role in protoplanetary discs as the necessary high densities for this effect are only reached in the very inner disc midplane regions. However, most of the CO emission does not originate from these regions, therefore collisional broadening can in general be neglected for these lines.

- **Natural broadening:** This line broadening mechanism is caused by the uncertainty principle, i.e. $\Delta E \Delta t \approx \hbar = h/2\pi$. Thus, the shorter the lifetime of a state, the larger the uncertainty of its energy. Note that for this process the oscillation of the molecule is perturbed by a radiative process instead of a collision with another molecule. The line profile resulting from this is again a Lorentzian profile:

$$\phi(\nu) = \frac{1}{\pi} \frac{\gamma_{i,\mathrm{nat}}}{(\nu - \nu_i)^2 + \gamma_{i,\mathrm{nat}}^2}\,, \tag{2.44}$$

  where the width $\gamma_{i,\mathrm{nat}} = (2\pi\Delta t)^{-1}$ with lifetime of the state Δt, which can be calculated from the uncertainty principle. This is illustrated in orange in Figure 2.4.

  For cases where spontaneous decay (with coefficient A_i) prevails, the average lifetime of the state is given by $\Delta t = A_i^{-1}$. However, this broadening effect does not play a major role for molecular lines.

Note again that these microscopic mechanisms are all broadening the lines, whereas the overall shape (i.e. the double-peaks) is influenced by macroscopic effects such as the rotation of the disc (see also Figure 1.13).

2.7 Computational codes used in this thesis

For the projects presented in this thesis I have used three different radiative transfer codes. These are based on the theory explained at the beginning of this chapter, I will now describe key features and why the respective tools were used.

2.7.1 MCMax

MCMax is a radiative transfer code (Min et al., 2009). It uses the Monte Carlo method outlined by Bjorkman and Wood (2001) to calculate the temperature structure of the disc (see also Section 2.3 for a description of the Monte Carlo method). The radiative transfer equations are solved in 3D, however an axisymmetric geometry is assumed and the code employs a spherical grid. The partial diffusion approximation as well as the modified random walk discussed above are implemented and used in high density regions. For a detailed description see Section 2.5 and also Min et al. (2009); Mulders (2013). I use MCMax to calculate a self-consistent density and temperature structure of a disc as well as the resulting SED. MCMax is only capable of dust radiative transfer calculations, therefore its output is processed further with the tool TORUS in order to obtain synthetic line observations as detailed in Section 2.7.2.

In MCMax the vertical profile of the dust (including dust settling) is obtained by solving a diffusion equation for each dust particle size bin (see below) and normalising the vertically averaged value of the gas-to-dust ratio at each radius to the input value of g/d.

The solution is self-consistent in the sense that the dust and gas profiles are not independently prescribed: the dust affects the hydrostatic equilibrium of the gas by setting the temperature whereas the gas profile affects the degree of dust settling and hence, through variation of the amount of starlight intercepted, the temperature profile of the dust. For each iteration on the thermal structure of the dust, photon packages emitted from the star (which is the source of heating) are followed through the disc. They are (re-)absorbed, re-emitted and scattered off the dust grains multiple times. This is the primary source of heating for the dense regions of the disc which are of interest for the $C^{18}O$ emission. This treatment would probably not be suitable for the inner few au of the midplane, where viscous heating usually dominates.

Based on the stellar properties and the disc structure, a 2D temperature profile for the disc is thus obtained in thermal equilibrium. The initial vertical structure is based on Equation 1.7, where H is calculated using the sound speed of the optically thin temperature (Mulders, 2013). MCMax then iterates the gas density profile so as to obtain vertical

hydrostatic equilibrium given by (see also the more detailed derivation in Chapter 1 and Equations 1.4 and 1.5):

$$\frac{dP}{dz} = -\rho g_z \,, \tag{2.45}$$

where P is the pressure, ρ the gas density and g_z the vertical component of gravity. This iterative process is depicted schematically in Figure 2.5.

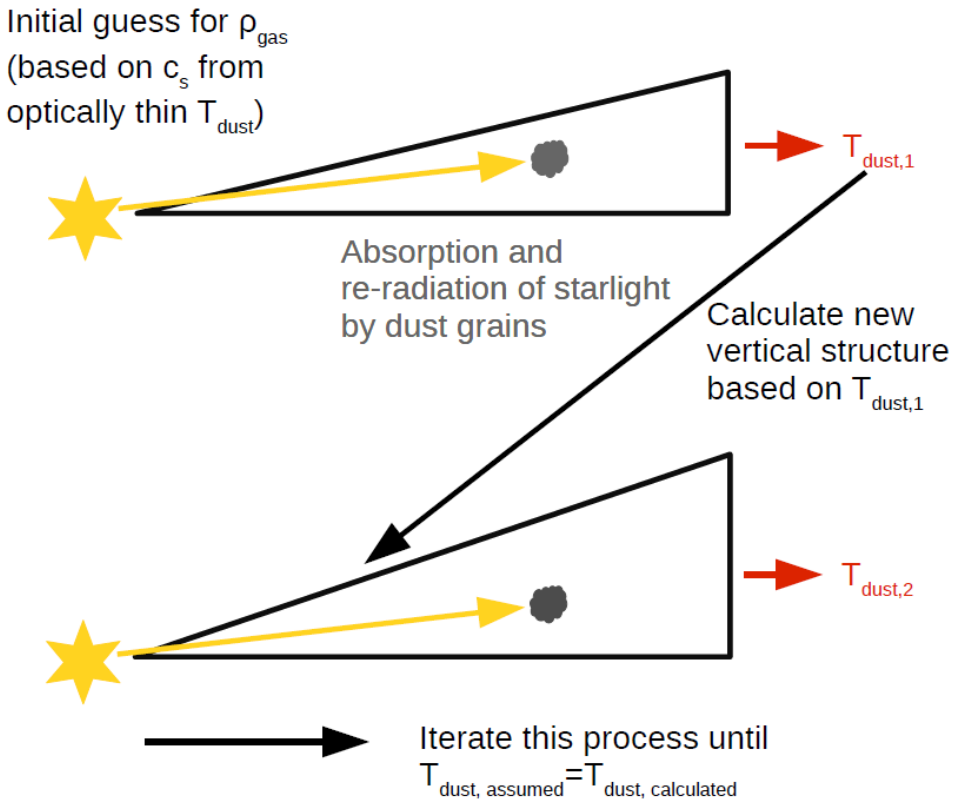

Figure 2.5 Schematic diagram of the iterative process used in MCMax to produce models in vertical hydrostatic equilibrium.

Dust settling is included in MCMax by solving a diffusion equation for each grain size as detailed in Mulders and Dominik (2012) and described schematically in Section 1.2.4. The position of the dust (and thus the disc temperature) is influenced by the gas: increasing the turbulent mixing parameter $\alpha_{\rm turb}$ leads to a stronger mixing of gas and dust, enabling more small dust grains to be stirred up to the disc atmosphere where they can intercept more stellar light. All MCMax models with the same dust properties (mass and grain sizes) and constant $M_{\rm gas} \times \alpha_{\rm turb}$ yield exactly the same SED and CO snowline location. This holds true as in MCMax the gas mass is set by fixing a dust mass and a g/d ratio. This can be understood following the discussion in Youdin and Lithwick (2007): for a regime where the dimensionless stopping time (see Section 1.2.4) $\tau_{\rm s}$ is smaller than the dimensionless eddy turnover time $\tau_{\rm e}$,

i.e. $\tau_s < \tau_e < 1$, the scale height of particles H_p divided by the scale-height of the gas H_{gas} is given by (see Equation 1.22)

$$\frac{H_p}{H_{gas}} \propto \sqrt{\frac{\alpha_{turb}}{\tau_s}}\,. \tag{2.46}$$

Given that $\tau_s \propto t_{stop}$, Equation 2.46 can be modified in the Epstein regime, where $t_{stop} \propto \rho_{grain}\, a\, (c_s\, \rho_{gas})^{-1}$ (with ρ_{grain} being the internal grain density, a the grain size, c_s the sound speed and ρ_{gas} the gas density, see Equation 1.20), hence

$$\frac{H_p}{H_{gas}} \propto \sqrt{\alpha_{turb} \times \rho_{gas}}\,. \tag{2.47}$$

This implies that $H_p \times H_{gas}^{-1}$ and thus the temperature and dust structure are kept invariant when $\rho_{gas} \times \alpha_{turb}$ (and thus $g/d \times \alpha_{turb}$) are kept constant.[4] Consequently, models that fulfil this criterion have exactly the same SED, temperature structure and dust density structure.

2.7.2 TORUS

TORUS is a radiative transfer and hydrodynamics code (Harries, 2000; Rundle et al., 2010; Haworth and Harries, 2012, Harries et al., in prep.). However for the purposes of the projects described in this thesis (see especially the modelling in Chapter 3) I just use the molecular line transfer module. It can perform molecular statistical equilibrium calculations and produce synthetic data cubes.

The gas density and dust temperature distribution that MCMax provides can be used as an input for TORUS in order to perform molecular line radiative transfer calculations. In order to do so, the density and temperature structure from the 2 dimensional spherical MCMax grid is mapped onto the 2D cylindrical TORUS grid using a bilinear interpolation in r and θ. The dust temperature from MCMax is directly mapped onto the gas temperature, which is a fair assumption for protoplanetary discs where densities are sufficiently high for gas and dust to be thermally coupled. TORUS can then be used to calculate LTE level populations as detailed above in Equation 2.22. The code is capable of also performing non-LTE molecular line radiative transfer, however for the disc midplane regions that are the focus of Chapter 3, the assumption of LTE is prudent due to the high densities there.

Freeze-out of molecules such as CO can be taken into account in TORUS as follows (the details of the implementation of $C^{18}O$ freeze-out focus are described in Section 3.3.2): The abundance of the respective molecule is dropped to a negligible value if the temperature is below the freeze-out temperature. To evaluate the effect of photodissociation

[4] Note again that this is only true because the dust mass is kept constant.

of CO by the stellar irradiation, a simple criterion is implemented, qualitatively similar to that of Williams and Best (2014). I assume that for a CO particle column density of $N_{\rm CO} \approx 10^{18}\,{\rm cm}^{-2}$ in the line of sight from the star all CO molecules will be photodissociated. This is only a crude estimate, however it allows to check how much of the total gas mass is affected and to gauge the impact on the model. The impact of photodissociation can then be probed by adopting a range of values for the critical threshold. In Chapter 3, column density thresholds as high as $\approx 10^{20}\,{\rm cm}^{-2}$ are explored for the models of the disc of HD 163296.

In addition, a value for the turbulent line broadening can be specified. The theory of this is explained earlier in this chapter (see Section 2.6). Synthetic data cubes can then be calculated using ray tracing (using the *long characteristic method* as described in Section 2.4 and detailed in Rundle et al., 2010), taking into account the desired observer viewing angle (i.e. inclination and position angle) and flexible spatial and spectral resolution. These synthetic data cubes can then for example be post-processed in order to mimic observations with telescopes such as ALMA and then directly be compared with observations.

2.7.3 DALI

For the project described in Chapter 4, I use the radiation thermo-chemical disc code DALI (Dust And LInes). It is described in detail in Bruderer et al. (2012); Bruderer (2013). The adaptations I made in order to obtain a model in vertical hydrostatic equilibrium are explained in Section 4.3.

In general, DALI solves the continuum radiative transfer equations to obtain the dust temperature, and the thermal balance and chemical abundances to compute the gas temperature structure. The ray tracing module is then used to calculate both an SED and CO fluxes that can be compared against the observations.

DALI reads in the stellar parameters such as the stellar spectrum and bolometric luminosity, which are key in determining the temperature structure. In DALI, gas and dust distributions that are not necessarily co-spatial can be taken into account, as in contrast to MCMax, dust temperatures are not needed to calculate the gas temperature and level populations. Therefore a case such as the truncated disc in Chapter 4, where the gas extends to much larger radii than the dust, can be modelled consistently.

For this project, I use two dust grain populations with small grains being coupled to the gas distribution (which is in vertical hydrostatic equilibrium) and large grains that are settled with respect to the gas (by adopting a parameter by which the scale height of the large grains is decreased in contrast to the gas). DALI uses a 2 dimensional grid in r and

z, where the radial bins can be set logarithmically or linearly depending on the desired resolution. Cylindrical symmetry is then assumed in order to ray trace observables from a 3 dimensional structure.

After setting up the density structure based on the parameters given, Monte Carlo continuum radiative transfer calculations are performed using the diffusion approximation in the dense disc regions as outlined in Section 2.5. Once the dust radiative transfer part is finished, the chemical network data is read in. It contains 10 elements, 109 species (such as H_2, CO, CH_4 etc.) and 1463 reactions. The code takes into account effects such as freeze-out, thermal and non-thermal desorption, photodissociation, gas-phase reactions, X-ray induced processes etc. (see e.g. Bruderer et al., 2012, for more details).

After the reading in of the chemical network data, the thermo-chemical calculation of all the cells is performed. The chemical structure of the disc is solved iteratively with thermal balance: initially a gas temperature is assumed, based on which the line excitation is computed. Heating and cooling processes are then calculated and a new gas temperature is determined. This process is iterated until convergence is reached. The computation of the gas temperature is one of the key modules of DALI.

This is then followed by the ray tracing of each line, such that synthetic datacubes as well as abundance and contribution function plots (i.e. primarily emitting disc regions for the respective transition of the molecule as a function of radius and height in the disc) of the molecular lines can be obtained. DALI is capable of time-independent (steady-state) as well as (pseudo) time-dependent chemistry calculations. In the latter case, in regions where the temperature of the gas and the temperature of the dust are different, initially the thermal balance is calculated using the steady-state chemistry solver. Then a time-dependent chemistry solver is run, followed by computation of the molecular excitation and a recalculation of the heating and cooling. Note however that the $T_{\rm gas}$ stays the same. Chemical timescales can become very long in the disc midplane regions, which does generally not affect optically thick lines or molecular line emission that originates from disc regions higher up. However for more optically thin isotopologues such as e.g. $C^{18}O$, the midplane abundances are important. In equilibrium, CO is converted into CH_4 in the disc midplane regions by pressure and temperature. This process takes place on long timescales, therefore the results of the CO abundance might differ in the disc midplane regions when comparing time-dependent and independent models. An example of this is presented in Chapter 4. Note however that the long timescales assumed in the time-independent case might even be longer than the lifetime of the disc of $\sim 10^6$ yr (see Figure 1.6), so time-dependent models might be more appropriate there if one is interested in the midplane regions of optically thin line emission.

2.8 Thesis work in context

So far, I have described the gas and dust structure as well as the temperature profile of a protoplanetary disc from a theoretical point of view (see Chapter 1). Then I gave an overview of observational signatures of discs - both of the gas and dust components - and how information about discs can be inferred from them. In Chapter 2, I have introduced the general principles of radiative transfer and more specifically the application thereof in three radiative transfer codes. All of this will be vital for the following two Chapters 3 and 4, where I present my modelling of two protoplanetary discs from different ends of the stellar mass spectrum. The models I obtain are then matched to observational SED fluxes, ALMA observations of the dust continuum (yielding an additional data point for the SED) and ALMA CO line observations (either the line profile or the integrated line emission). These models are then analysed in order to study what they imply for the disc gas and dust structure and how they can be put into context with respect to previous studies and observations of other discs.

3

The midplane conditions of protoplanetary discs: a case study of HD 163296

One quantity that is of great interest for assessing the planet formation potential of a protoplanetary disc is its mass of gas. Disc gas masses are, however, traditionally inferred from measured dust masses by applying an assumed standard gas-to-dust ratio of $g/d = 100$. Furthermore, measuring gas masses based on CO observations has been hindered by the effects of CO freeze-out, as detailed in Section 1.4. In this chapter, I present a novel approach to study the midplane gas by combining $C^{18}O$ line modelling, CO snowline observations and the spectral energy distribution (SED). I apply the modelling technique to the disc around the Herbig Ae star HD 163296 with particular focus on the regions within the CO snowline radius. The technique outlined here can be applied to a range of discs and opens up a possibility of measuring gas and dust masses in discs within the CO snowline location without making assumptions about the gas-to-dust ratio.

3.1 Introduction

New observational facilities such as ALMA provide data of protoplanetary discs of unprecedented resolution and sensitivity. We therefore have the opportunity to study the disc structure and through it the processes that lead to planet formation in more detail than ever before. However, interpretation of these observations is reliant upon comparison with the expected emission properties from numerical models of discs. As already described in Chapter 1, discs consist of gas and dust. In the interstellar medium (ISM), the mass ratio of these two components is canonically assumed to be $g/d = 100$ as has been inferred from ISM observations (see e.g. Frerking et al., 1982; Lacy et al., 1994). Due to the lack of observational constraints thereof, this value is often also adopted for discs. Panić et al. (2008) obtain a range between 25 and 100 for g/d from their modelling of the Her-

big Ae/Be star HD 169142, where they base their mass estimates on modelling of various CO isotopologues and assumptions about their abundances and dust opacities. Meeus et al. (2010) narrowed down this range to $\sim 22 - 50$ by first obtaining a model that reproduces the continuum observations and then fitting various line fluxes (such as [OI], [CII] and CO isotopologues) simultaneously. They mention however that systematic uncertainties in their modelling make the determination of the gas mass difficult. In 51 Oph, Thi et al. (2013) find a value of g/d consistent with 100, the same holds true for HD 141569 (Thi et al., 2014). This result is based on thermo-chemical modelling, matching observed continuum emission and line fluxes, which yields some small uncertainties in the g/d due to disagreement between results from the various gas tracers. The study of several T Tauri stars by Williams and Best (2014) yields g/d that are relatively low ($\lesssim 40$; the values they obtain for a few Herbig Ae/Be stars are also rather low, with the exception of HD 163296, where they obtain $g/d = 170$). Their results are based on modelling of ^{13}CO and C^{18}O. They state however that the gas masses they obtain from their modelling might be underestimating the actual gas masses (and therefore the g/d) if the CO abundances assumed are too high. Note that in all these cases, the modelling yields an overall g/d ratio for the *entire* disc.

However, the gas and dust in discs do not necessarily need to be co-spatial. Therefore the question arises whether dust can or should actually be used to draw conclusions about the gas. As described in Section 1.2.4, large grains should drift inwards radially with respect to the gas, leading to a difference in gas and dust outer radii (see e.g. Panić et al., 2009; Rosenfeld et al., 2012, for observational examples of this segregation). This also implies that the gas-to-dust ratio does not need to be spatially constant and even its global value does not necessarily have to match the ISM value of $g/d = 100$, as gas and dust can accrete onto the star at different rates. Therefore, in this chapter I will not rely on measurements of the dust mass and then obtaining a gas mass by applying a g/d, but will use observations of the optically thin C^{18}O emission. Note however that there is some controversy in the literature about whether CO is overall a better predictor of total gas mass than the dust due to uncertainties in the CO abundances that are needed for the modelling (see e.g. Manara et al., 2016, who find that the CO based gas massed are too low to explain disc accretion rates). I will come back to this point in Section 3.4.6.

The gas governs the disc dynamics and motion of the dust, whereas dust provides the opacity to capture the stellar flux, re-radiate it and heat the disc. In order to understand the structure of discs, it is therefore crucial to study the spatial distribution and properties of both components (see e.g. Beckwith and Sargent, 1987; Dutrey et al., 1994; Isella et al., 2007; Panić et al., 2008; Qi et al., 2011; Panić et al., 2014). Planets are believed to form in the disc midplane and thus understanding the disc conditions in these regions is particularly

important for constraining models of planet formation (see e.g. Boley and Durisen, 2010; Forgan and Rice, 2013).

Many discs have bright emission in the mm continuum (e.g. Beckwith et al., 1990; Dutrey et al., 1996; Mannings and Sargent, 1997; Andrews and Williams, 2007; Andrews et al., 2009, 2010; Qi et al., 2011), tracing the dust in the disc. Due to the uncertainties associated with g/d and the dust grain properties, inferring the disc mass from continuum measurements is however only a rough approximation. Therefore, molecular emission lines are used alternatively or additionally and allow the inference of spatial and temperature structure. The most abundant molecule in discs is cold H_2 gas, however this is difficult to observe due to the lack of a dipole moment and its low transition probability. Thus, as outlined previously, molecules such as ^{12}CO, ^{13}CO and C^{18}O and their respective transitions are employed instead.

Abundances of molecular tracers are influenced by the conditions in the disc: for example CO can be photodissociated in the disc atmosphere or frozen out in the disc below a temperature of $T \approx 19\,\mathrm{K}$ (Qi et al., 2011, and see also Section 1.4.2). Recently it has been claimed that the exact value of the freeze-out temperature can vary from disc to disc (e.g. Qi et al. (2015) model the snowline at a temperature of $17\,\mathrm{K}$ in TW Hya and $25\,\mathrm{K}$ in HD 163296) and depends on the chemical history of the ice (Garrod and Pauly, 2011). Moreover, the transitions of the CO emission lines become optically thick at different heights within the disc, depending on the abundance of the particular isotopologue (e.g. van Zadelhoff et al., 2001; Dartois et al., 2003; Miotello et al., 2014) and thus optical depth effects compromise the ability to obtain disc masses from the more abundant species. C^{18}O is an important diagnostic of the unfrozen part of the disc mass, being much less abundant than other CO species ([^{16}O]/[^{18}O]=557 ± 30, Wilson 1999). Its transitions in the mm wavelength regime are mostly optically thin throughout the whole disc and thus provide an excellent probe of the disc midplane. This is evidently of great importance since most of the gas mass resides near the disc midplane and it is here that planets are expected to form. However, only a handful of observations of C^{18}O exist so far, including AB Aurigae (Semenov et al., 2005), HD 169142 (Panić et al., 2008), MWC480 (Akiyama et al., 2013), HD 142527 (Perez et al., 2015) and HD 163296 (Qi et al., 2011; Rosenfeld et al., 2013). There are also C^{18}O data available on several T Tauri stars studied by Williams and Best (2014). Furthermore, there exist observations of C^{18}O in TW Hya, V4046 Sgr, DM Tau, GG Tau and IM Lup (see Williams and Best, 2014, and references therein).[1]

As detailed in Section 1.4, the *CO snowline radius* is the location in the disc midplane at which CO condenses from the gas phase and freezes out onto dust grains. It can be ob-

[1]Note that this was the state of the field when I studied and modelled HD 163296, since then there has been a wealth of further C^{18}O observations, e.g. Fedele et al. (2017); Long et al. (2017); Ansdell et al. (2018).

served as a steep decline in the $C^{18}O$ density or by the presence of other molecular tracers (e.g. N_2H^+ and DCO^+). Qi et al. (2015) propose that observations of $C^{18}O$ and N_2H^+ are very powerful as they directly probe the temperature of the disc midplane. This is crucial for calculations of the vertical hydrostatic equilibrium of the gas in discs which depend on the conditions in this disc region. However, the exact freeze-out temperature of CO is not known unambiguously and depending on the composition of the ice can be between $\sim 20 - 30$ K. This is described in more detail in Section 1.4. Nevertheless, measurements of the CO snowline location are important as they provide constraints on the midplane temperature profile of discs.

As already detailed in Chapter 1, another important tool for studying protoplanetary discs is the SED that combines independent measurements in a range of wavelength regimes, which trace different parts of the disc (see e.g. Boss and Yorke, 1996; Dullemond, 2002; Meijer et al., 2008; Woitke, 2015; Panić and Min, 2017, for studies of the influence of disc parameters on the resulting SED). As the dust content of the disc influences its opacity and thus determines how much stellar flux can be intercepted and re-radiated by the disc, the SED crucially depends on the properties and vertical distribution of dust. Thus a combination of $C^{18}O$ observations, additional data on the CO snowline radius and the SED provide a powerful combination of observables to model protoplanetary discs, combining independent measurements of both gas and dust.

In this chapter, I model the disc around the $2.3\,M_\odot$ (Qi et al., 2011) Herbig Ae star HD 163296, that is assumed to have an age of ~ 5Myr (Natta et al., 2004). It is situated at a distance of about $D = 122$ pc (van den Ancker et al., 1998) with a luminosity of $L = 37.7\,L_\odot$ and an effective temperature of $T_{\rm eff} = 9250$ K (Tilling et al., 2012). The observational properties of both the star and disc are listed in Table 3.1. Interestingly, the outer radius of the disc as inferred from CO emission studies (Qi et al., 2011; de Gregorio-Monsalvo et al., 2013) and scattered light (Grady et al., 2000) is about double the value of the disc outer radius observed in the continuum (de Gregorio-Monsalvo et al., 2013). It is worth noting that HD 163296 is a relatively bright Herbig Ae star (L_*=37.7 $L_\odot$, Tilling et al. 2012), thus, its disc is comparatively warm and its $C^{18}O$ line emission strong. Furthermore, the disc is observed to have a gap in polarised light at $R_{\rm gap} \sim 70$ au (Garufi et al., 2014). Its molecular lines (mostly CO) and continuum have been studied in detail in the mm and sub-mm (Mannings and Sargent, 1997; Natta et al., 2004; Isella et al., 2007; Qi et al., 2011) and recently also with ALMA (de Gregorio-Monsalvo et al., 2013; Rosenfeld et al., 2013; Mathews et al., 2013; Flaherty et al., 2015; Qi et al., 2015; Guidi et al., 2016).

Rosenfeld et al. (2013); de Gregorio-Monsalvo et al. (2013) and Qi et al. (2015) employed ALMA data for modelling of the disc of HD 163296 but this study is the first to use the $C^{18}O$ $J = 2 - 1$ data to model disc parameters. Rosenfeld et al. (2013) focused mainly on

Table 3.1 Observational stellar and disc properties of HD 163296 from: [1]Qi et al. (2011), [2]Tilling et al. (2012), [3]Natta et al. (2004), [4]Grady et al. (2000), [5]de Gregorio-Monsalvo et al. (2013), [6]Guidi et al. (2016) and [7]Qi et al. (2015). For the star, a Kurucz model is used.

Stellar properties	**Value**
Spectral type[1]	A1
Mass[1] M_*	$2.3\,\mathrm{M}_\odot$
Effective temperature[2] T_{eff}	$9250\,\mathrm{K}$
Luminosity[2] L_*	$37.7\,\mathrm{L}_\odot$
Distance[1] D	$122\,\mathrm{pc}$
Age[3] t	$\sim 5\,\mathrm{Myr}$
Disc parameters	**Value**
Outer radius (scattered light)[4] $R_{\mathrm{out,\,sc}}$	$\sim 450\,\mathrm{au}$
Outer radius (continuum, 850 μm)[5,6] $R_{\mathrm{out,\,cont}}$	$\sim 240 - 290\,\mathrm{au}$
Outer radius (CO observations)[5] $R_{\mathrm{out,\,CO}}$	$\sim 550\,\mathrm{au}$
CO snowline radius[7] R_{sl}	$90\,\mathrm{au}$

modelling CO and ^{13}CO, whereas de Gregorio-Monsalvo et al. (2013) analysed the Band 7 data (^{12}CO $J = 3 - 2$ and continuum) and Guidi et al. (2016) were most interested in the dust properties and hence the continuum observations. Qi et al. (2015) also studied the C^{18}O emission, but they focused on analysing the snowline location and comparing the C^{18}O and N_2H^+ emission. In addition, Flaherty et al. (2015) used the available C^{18}O data, but studied the turbulence in the disc. I describe the relevant ALMA observations in the next section and stress that the modelling is based on the available ALMA C^{18}O data as a crucial ingredient.

Qi et al. (2011) had inferred a snowline radius $R_{\mathrm{sl}} \sim 155\,\mathrm{au}$ from ^{13}CO observations which was consistently also derived by Mathews et al. (2013) from DCO^+ observations. However, more recent studies by Qi et al. (2015) find a snowline radius $R_{\mathrm{sl}} \sim 90\,\mathrm{au}$ from both N_2H^+ and C^{18}O ALMA observations.

I do not aim to provide one best-fitting model for the disc around HD 163296, but rather want to emphasise the degeneracies in the parameters of the modelling process and propose a way to overcome them. The main goal is to investigate the midplane gas temperature and density in this disc using a novel modelling approach. In Section 3.2, I summarise and discuss the observations. In Section 3.3, the modelling process and all the steps involved are described in detail. In Section 3.4, I specify the models I obtain, their implications and potential degeneracies and also discuss their properties. The findings and conclusions are summarised in Section 3.5.

Table 3.2 Summary of the available ALMA Science Verification observations (molecular lines in Bands 6 and 7)

Molecular lines	**Synthesised beam**[arcsec]	**rms** (σ) [**Jy beam**$^{-1}$]
$C^{18}O$ $J = 2-1$ (SV)	0.73×0.58	2×10^{-2}
^{12}CO $J = 2-1$ (SV)	0.68×0.55	5×10^{-2}
^{13}CO $J = 2-1$ (SV)	0.72×0.57	3×10^{-2}
^{12}CO $J = 3-2$ (SV)	0.65×0.42	5×10^{-2}

3.2 Observations

Science verification data of HD 163296 were taken by ALMA in Band 6 and 7 (Rosenfeld et al., 2013). The ALMA observations are provided as 3D fits cubes with two spatial and one spectral axis (velocity/frequency) on the ALMA Portal[2]. There are calibrated and cleaned data with a resolution of ~ 0.7 arcsec (~ 85 au at $D = 122$ pc) available for ^{12}CO $J = 2-1$, ^{13}CO $J = 2-1$ and $C^{18}O$ $J = 2-1$ (all Band 6), as well as for ^{12}CO $J = 3-2$ (Band 7). The corresponding RMS noise values and beam sizes are listed in Table 3.2. I use the *Common Astronomy Software Applications* CASA software package version 4.4.0 (McMullin et al., 2007) to analyse the respective transitions. Amongst the transitions listed above, the $C^{18}O$ $J = 2-1$ is relatively unexplored and the one on which this work focuses. I employ the already self-calibrated and cleaned Science Verification data provided on the ALMA Portal.

The $C^{18}O$ $J = 2-1$ observations (Band 6) of HD 163296 (RA= $17^h56^m21^s.281$, Dec.= $-21°57'22''.36$; J2000) were taken with 24 ALMA antennas (12 m) in 2012, on June 9 and 23 and July 7 with baselines spanning $20-400$ m and a total on-source time of 84 min (Rosenfeld et al., 2013). For a detailed summary of the spectral windows and calibrations, see Rosenfeld et al. (2013). The beam size of the reduced and cleaned $C^{18}O$ data is 0.73 arcsec $\times 0.58$ arcsec, the spectral resolution is 0.33 km s^{-1} (~ 0.24 MHz) with 150 channels, ranging from 219.571 GHz to 219.534 GHz, where the rest frequency of the transition is 219.56 GHz. The integrated emission and intensity weighted velocity maps of $C^{18}O$ $J = 2-1$ are plotted in Figure 3.1 and described in more detail in the next section. I find an integrated flux density of $C^{18}O$ $J = 2-1$ of 6.2 ± 0.4 Jy km s^{-1}, which is consistent with the values obtained by Qi et al. (2011, 2015) and Rosenfeld et al. (2013).

I plot the frequency-integrated intensity maps and intensity-weighted velocity maps for both transitions of ^{12}CO, as well as $C^{18}O$ and ^{13}CO in Figure 3.1[3]. I will focus on $C^{18}O$

[2] https://almascience.nrao.edu/alma-data/science- verification/overview

[3] As already pointed out in Rosenfeld et al. (2013), the SV data of ^{12}CO $J = 3-2$ have a velocity offset and are falsely centred around a velocity of 6.99 km s^{-1} instead of the systemic velocity of 5.8 km s^{-1}. This offset has been taken into account for the respective velocity map.

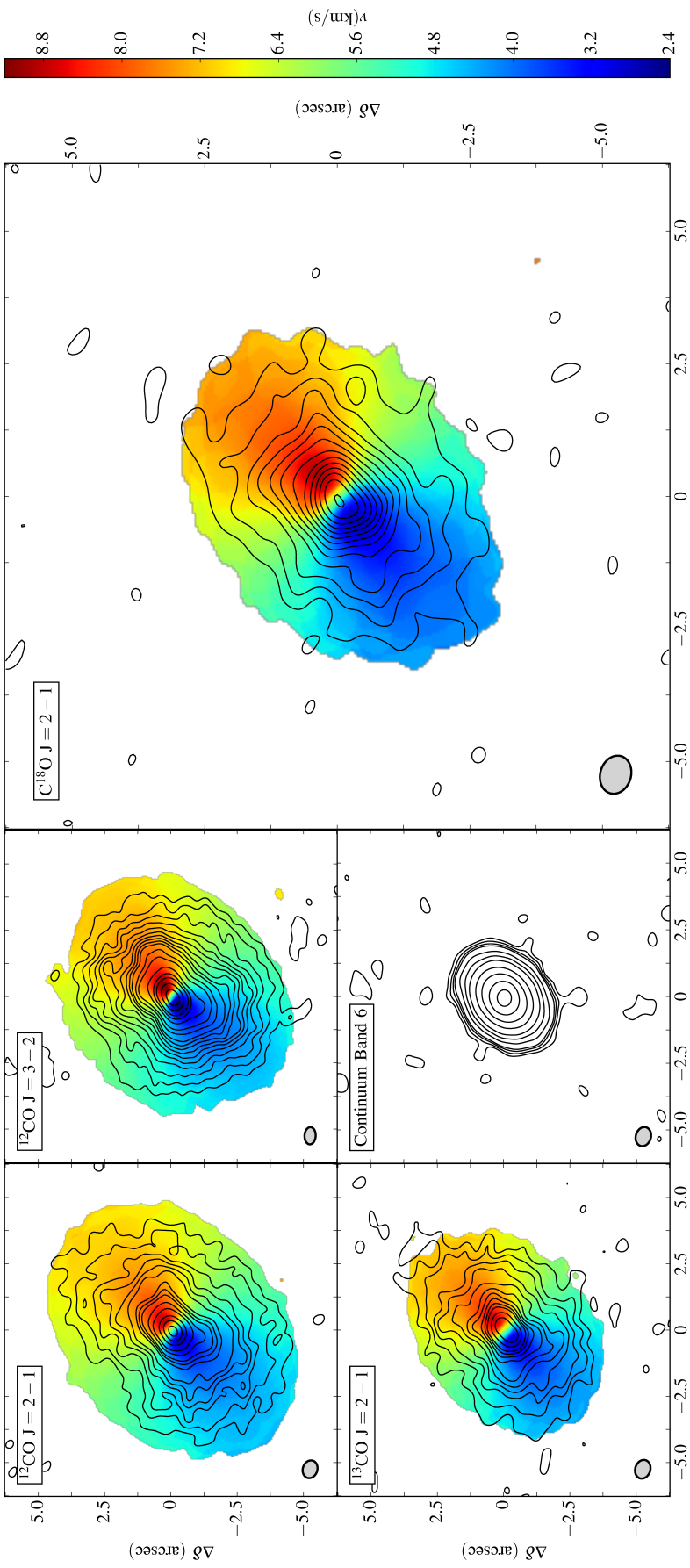

Figure 3.1 Integrated line emission (contours) and intensity-weighted velocity (colour) maps of ^{12}CO $J = 2 - 1$, ^{12}CO $J = 3 - 2$, ^{13}CO $J = 2 - 1$, C^{18}O $J = 2 - 1$ and continuum map of Band 6. The contours are levels of $(2, 4, 6, 8, ...) \times \sigma$ noise. The innermost contour has the following levels: $\sim 100 \times \sigma$ (^{12}CO $J = 2 - 1$), $\sim 100 \times \sigma$ (^{12}CO $J = 3 - 2$), $\sim 28 \times \sigma$ (^{13}CO $J = 2 - 1$), $\sim 52 \times \sigma$ (C^{18}O $J = 2 - 1$) and $\sim 796 \times \sigma$ (continuum). The velocity maps discard the data at a level $\lesssim 5 \times \sigma$ noise. The respective σ are given in Table 3.2. The synthesised beam is plotted in the bottom left corner of each panel.

Table 3.3 Molecular species and continuum emission in Bands 6 and 7 and the respective PAs and inclinations ($i = 0$ is face-on) including their errors obtained from their integrated intensity maps with CASA.

Molecular species and continuum	**PA[°]**	**Inclination i[°]**
^{12}CO $J = 2-1$	138.0 ± 2.0	48.4 ± 2.3
^{13}CO $J = 2-1$	133.7 ± 2.7	46.5 ± 1.5
C^{18}O $J = 2-1$	132.8 ± 3.4	47.9 ± 1.6
Continuum Band 6	131.4 ± 2.1	42.8 ± 0.1
^{12}CO $J = 3-2$	140.4 ± 1.9	44.7 ± 0.9
Continuum Band 7	130.3 ± 1.1	43.1 ± 0.1

in more detail in this study, but show all of these maps here as the disc geometry is also explored by using these other molecular species. Additionally, I present the continuum map of Band 6. From the extent of the disc in the panels of Figure 3.1, it is clear that the molecular species and the continuum trace different parts of the disc. The CO isotopologues with different abundances trace down to varying depths in the disc, due to their different opacities.

Using the CASA software package, one can determine the position angle (PA) of the disc from C^{18}O observations (image deconvolved from beam), which I find to be PA=(132.8 ± 3.4) °. This is in agreement with what other studies have found from CO and continuum observations (Qi et al., 2011; Rosenfeld et al., 2013). Fitting a 2D Gaussian to the spatial profile of the emission with CASA (using the 2D Gaussian fitting tool in the viewer) allows to determine the inclination of the disc for the different tracers shown in Figure 3.1 (using Equation 1.41; $i = 0$ corresponds to the disc being face-on). From the C^{18}O emission, I obtain an inclination of i =(47.9 ± 1.6) °, which is comparable to the inclination of i =44° used by Qi et al. (2011). For the other molecular species, the same analysis is performed and I get the values given in Table 3.3. The value for the PA from the ^{12}CO $J = 3-2$ is comparable with the one from de Gregorio-Monsalvo et al. (2013), however, I find a larger inclination in comparison to their value (38 °). The PA and inclination for the continuum emission in Band 6 and 7 are slightly lower than the values obtained from the gas lines. However, gas and dust can trace regions of the disc with different outer radii. It might thus be possible that the inner regions of the disc have a different inclination. Also, the calculations of the PA and inclination from the CO emission might be influenced by the fact that the line emission seems to have a slightly boxy shape in comparison to the ellipses in the continuum (see Figure 3.1). For my models, I will adapt a PA=132 ° and an inclination of $i = 48$ °, which is broadly in agreement with the values obtained from the fits.

3.3 Methods

3.3.1 Modelling the 2D disc structure and the SED with MCMax

The modelling process is two-fold: I first model the 2D temperature and density structure of the disc using the radiative transfer code MCMax (Min et al., 2009), ensuring that the models match the observed SED and CO snowline radius. These models are then taken as an input to the TORUS code (Harries, 2000) which performs molecular line radiative transfer; I use synthetic $C^{18}O$ line profiles to further narrow down the range of viable models. This process is schematically depicted in Figure 3.2.

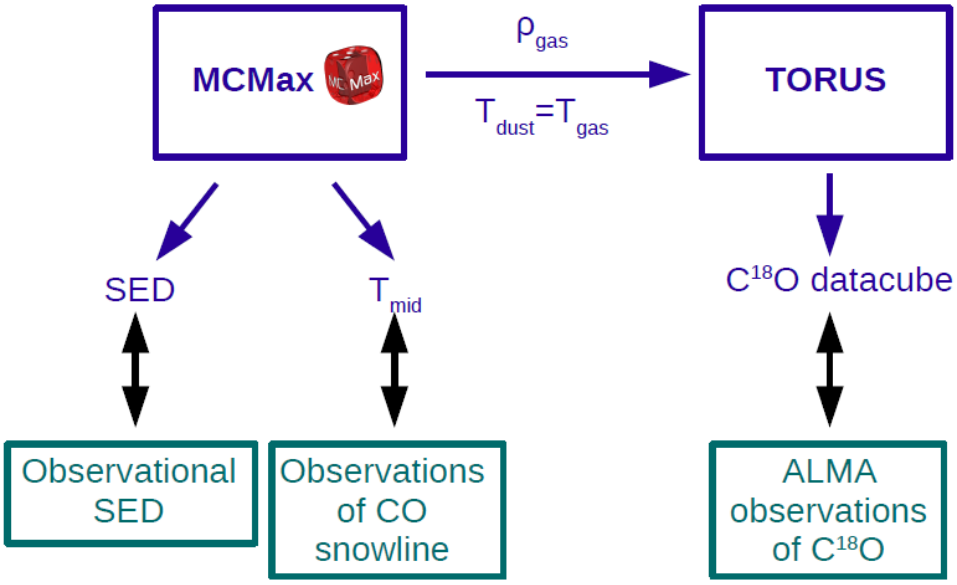

Figure 3.2 Schematic description of the modelling process: MCMax is used to obtain an SED and a midplane temperature profile, which can then be compared with the observational SED and observations of the CO snowline location. The density and temperature structure from MCMax is then used as an input to TORUS, with which synthetic $C^{18}O$ data cubes and line profiles are calculated. These can then be directly compared against the ALMA observations.

.

I primarily aim to determine the magnitude of various parameter degeneracies, rather than to calculate a single best-fit model. I use the 3D radiative transfer code MCMax, which self-consistently calculates a 2D temperature and density structure of the model with Monte Carlo radiative transfer (Min et al., 2009). This is described in more detail in Chapter 2 of this thesis, here I will just summarise the key features relevant to this chapter. The input parameters are the radial variation of the gas and dust surface density (fixed as being proportional to r^p where p is in the range -1 to -1.2), the total dust mass (and grain size distribution, $a_{\rm min}$ and $a_{\rm max}$), the gas-to-dust ratio g/d and the turbulent mixing

parameter $\alpha_{\rm turb}$. MCMax is then used to iteratively compute the temperature, and from it the resulting vertical profile of the gas density. This profile satisfies hydrostatic equilibrium normal to the disc plane in the gas and thermal equilibrium in the dust (assuming the gas and dust temperatures are equal). Details of this as well as concerning the vertical profile of the dust density are described in more detail in Section 2.7.1.

MCMax derives a 2D temperature structure of the disc and as detailed earlier, the gas density profile is iterated in order to obtain vertical hydrostatic equilibrium. The dust in MCMax is influenced by the turbulent mixing strength of the gas. I explore values of the turbulent mixing parameter in MCMax between $\alpha_{\rm turb} = 10^{-4}$ and 10^{-2}, which is a frequently adopted range of values for protoplanetary discs (Mulders and Dominik, 2012). The value of $\alpha_{\rm turb}$ is hard to derive from observations and is assumed to be in the range of $\sim 0.5 - 10^{-4}$ (Isella et al., 2009). For HD 163296, Flaherty et al. (2015) find a value of $\alpha_{\rm turb} \leq 9 \times 10^{-4}$ in the upper layers of the outer disc. In general, this parameter determines the strength of the mixing of the gas and dust components for a given gas-to-dust mass ratio g/d. Furthermore, $\alpha_{\rm turb}$ is in general lower at low altitudes in the disc (Simon et al., 2015).

As described in detail in Section 2.7.1, in MCMax models with the same $g/d \times \alpha_{\rm turb}$ have the same temperature and dust density structure (and thus also the same SED). For the modelling process I first run models with a turbulent mixing strength of $\alpha_{\rm turb} = 10^{-4}$ and fit these to the observed SED, but then run additional calculations for these models, exploring larger values of $\alpha_{\rm turb}$ (10^{-3} and 10^{-2}) while decreasing the gas masses in these models by factors of 10 and 100, accordingly, to keep the temperature structure and SED the same. The new models are named A-E/10 and A-E/100, respectively. All models that have the same dust parameters and constant $\alpha_{\rm turb} \times g/d$ will be called models of the same series.

The mass accretion rate of HD 163296 is derived to be within the range $(0.8-4.5) \times 10^{-7}$ M$_\odot$yr^{-1} (Garcia Lopez et al., 2015) from Br-γ observations, so depending on its value, viscous heating could potentially be important in the very inner disc regions ($\sim$few au). Given that I am interested in midplane regions further out, I do however not take this effect into account.

The above described iterations are performed using 5×10^7 photon packages and 350 grid cells in the azimuthal direction and 400 in radial direction. I have checked for convergence in the Monte Carlo radiative transfer calculation by increasing the number of photon packets. However, since the Poisson noise scales with the square root of the number of photon packets, this is inefficient. I therefore stack the average density and temperature structure over the last few well converged iterations of the MCMax calculation to reduce both the noise and computational expense.

In general, each of the models is unique in some aspect (see *distinctive feature* in last column of Table 3.5 where the individual model parameters are listed). An extreme assumption is made for one of the varied parameters at a time and then I search for the SED fit in order to obtain the wide range of properties without the necessity of doing a complete parameter space exploration. I generate a range of models by varying the following parameters: the mass of dust $M_{\rm dust}$, the minimum dust grain size $a_{\rm min}$, maximum grain size $a_{\rm max}$ and the gas-to-dust ratio g/d (alone, as well as in combination with the turbulent mixing strength $\alpha_{\rm turb}$). In every case it is assumed that the grains follow a power law size distribution of $n(a) \propto a^{-q}$ (see Equation 1.23), where a is the grain size. The value for ISM grains, that is often also adopted for discs, is $q = 3.5$ (see e.g. Mathis et al. 1977; Clayton et al. 2003), which results in most of the dust mass being in the largest grains, while the opacity is provided by the smallest dust.

These five disc parameters were chosen to be varied in the modelling as they have the biggest effect on the SED (see e.g. Meijer et al., 2008; Woitke, 2015; Panić and Min, 2017, and discussion in Section 1.3.2). I explore a range of $M_{\rm dust}$ going from the lowest possible value that can still reproduce the mm flux in the SED (as I will describe in Section 3.4.1) up to ~ 0.1 per cent of the stellar mass. Initially, g/d is varied between 10 and 200 to explore an extreme range around the ISM value (while fixing $\alpha_{\rm turb} = 10^{-4}$). Once a combination of $\alpha_{\rm turb}$ and g/d is found that provides a match, other combinations of these two parameters are explored, taking into account the above described degeneracy of $\alpha_{\rm turb} \times g/d$. The grains sizes I assume range from pristine dust (sub-micron-sized) to mm or even cm-sized grains in some cases.

The stellar properties used for all of the models are listed in Table 3.1 and are kept fixed. I use a Kurucz model for the star, which sets the stellar emission. Given the values for the outer radius as inferred from CO observations, I use a value of $R_{\rm out} = 540$ au for the models. I then investigate how the parameter choices affect the resulting SED and the predicted radius of the CO snowline. Rather than finding the single model that provides the best fit to these observables, I instead identify a range of models that provide an acceptable fit and then, as detailed in the following section, further isolate the models that additionally match the line fluxes in $C^{18}O$.

3.3.2 Molecular line modelling with TORUS

The models obtained from the analysis described above are then taken as an input density and temperature structure for the next modelling step. I use the radiation transport and hydrodynamics code TORUS to perform molecular line transfer calculations in this study (see e.g. Harries, 2000; Rundle et al., 2010; Haworth and Harries, 2012). TORUS is

capable of molecular statistical equilibrium calculations and the production of synthetic data cubes (e.g. for one specific molecular transition). I give an introduction to the code in Section 2.7.2 of this thesis. Full details of the main molecular line transfer algorithm are described in Rundle et al. (2010), however some key and new features are summarised below.

The gas density and temperature distributions from the 2D spherical MCMax calculations are mapped on to the 2D cylindrical TORUS grid using a bilinear interpolation in r and θ. I assume that the gas and dust are thermally coupled (allowing to map the dust temperature directly on to the gas). Although TORUS is capable of non-local thermodynamic equilibrium (LTE) molecular line transport, for application to these disc models the densities are sufficiently high and the assumption of LTE produces identical results as non-LTE calculations.[4] Therefore, the level populations can be characterised as a Boltzmann distribution, that is as a simple function of temperature as detailed in Equation 2.22. With the level populations computed, synthetic data cubes are calculated using ray tracing (Rundle et al., 2010). A model for freeze-out is implemented, whereby the $C^{18}O$ abundance drops to a negligible value if the temperature is below the freeze-out temperature $T_{\rm midplane}(90\,{\rm au})$ of the respective model. These temperatures are listed in Table 3.5. To evaluate the effect of photodissociation of CO by the stellar irradiation, a simple criterion is implemented, qualitatively similar to that of Williams and Best (2014). It is assumed that for a CO particle column density of $N_{\rm CO} \approx 10^{18}$ cm^{-2} in the line of sight from the star all CO molecules will be photodissociated. This is only a crude estimate, however it allows to check how much of the total gas mass is affected and to gauge the impact on my model. The value I adopt implies a larger role for photodissociation than that employed by Williams and Best (2014) (who use $N_{\rm H_2} \approx 1.3 \times 10^{21}$ cm^{-2}, corresponding to $\rm N_{CO} \approx 1.3 \times 10^{17}$ cm^{-2} for $f_{\rm CO} \approx 10^{-4}$). I also explore the effect of adopting even larger column density thresholds of $N_{\rm CO} \approx 10^{19}$ cm^{-2} and 10^{20} cm^{-2}, the latter of which certainly exaggerates the effect of photodissociation.

Turbulence affects the line emission to a much lesser extent than the temperature and density do, and these effects are only marginally discerned in observations of higher signal to noise lines, such as those of ^{12}CO and at a high spectral resolution. The assumption of turbulent velocity $v_{\rm turb}$ therefore does not significantly affect the fit to the $C^{18}O$ data. As explained in Chapter 1, the maximum turbulent line broadening possible is set by the

[4] The assumption of LTE is prudent in the midplane for mm lines (in which I am interested as they preferentially probe the disc midplane), but might not be sufficient for the infrared (IR) lines.

sound speed in the outer midplane (see Equation 1.42) with

$$c_{\rm s} = \sqrt{\frac{k_{\rm B} T_{\rm mid}(r_{\rm out})}{\mu m_{\rm H}}}\,, \tag{3.1}$$

where $k_{\rm B}$ is the Boltzmann constant, $T_{\rm mid}$ the midplane temperature, μ the mean molecular weight and $m_{\rm H}$ the atomic mass of hydrogen. Following Simon et al. (2015), I employ a value of $0.01-0.1c_{\rm s}$, suitable in the outer disc midplane, for the turbulent line broadening in TORUS. Given that the temperature in the outer midplane is approximately $T \approx 8\,$K, one finds

$$v_{\rm turb} = (0.01-0.1)c_{\rm s}(8\,{\rm K}) = (0.0017-0.017)\,{\rm km\,s^{-1}}\,, \tag{3.2}$$

where I use $\mu = 2.37$. The recent study by Flaherty et al. (2015) also suggests that turbulence is relatively weak in the HD 163296 disc ($v_{\rm turb} < 0.03c_{\rm s}$ in the upper layers of the outer disc), supporting the low value of $v_{\rm turb}$. Changing $v_{\rm turb}$ by a factor of 10 in my models does not alter the fit to the observations of $C^{18}O$, as the data quality does not allow to probe $v_{\rm turb}$ sufficiently well. Also, since $C^{18}O$ is mainly optically thin, turbulent broadening will cause slight smearing of the line profile, but will not affect the line flux. This would be different if I were studying a more optically thick transition like for example CO $J = 3-2$ (see e.g. Flaherty et al., 2015). The turbulent line broadening is related to the turbulent mixing parameter $\alpha_{\rm turb}$ by (Ormel and Cuzzi, 2007)

$$v_{\rm turb} \sim \sqrt{\alpha_{\rm turb}} c_{\rm s}\,, \tag{3.3}$$

as given by Equation 1.42. The above means that $\alpha_{\rm turb} = 10^{-4}-10^{-2}$ is implicit in this calculation. Flaherty et al. (2015) find $\alpha_{\rm turb} < 9.6\times10^{-4}$ from their modelling of HD 163296. I explore this range of values of $\alpha_{\rm turb}$ in Section 3.4.1, but I hereby stress that for a wide range of $\alpha_{\rm turb}$ and corresponding values of $v_{\rm turb}$ the fit to the line emission remains unaffected.

Another aspect to take into account is that the fractional abundance (by number density) of $C^{18}O$ is uncertain. This abundance is given by

$$f_{\rm C^{18}O} = \frac{[{\rm CO}]}{[{\rm H_2}]} \times \frac{[{\rm C^{18}O}]}{[{\rm CO}]}\,, \tag{3.4}$$

where I assume that $[C^{18}O]/[CO] = [^{18}O]/[^{16}O]$. Therefore uncertainty in the isotopic ratio of ^{16}O to ^{18}O as well as in the fractional abundance of CO have to be taken into account. The mass of $C^{18}O$ is related to the mass of H_2 by

$$M_{\rm C^{18}O} = \frac{m_{\rm C^{18}O}}{m_{\rm H_2}} \times f_{\rm C^{18}O} \times M_{\rm H_2}\,, \tag{3.5}$$

where $m_{C^{18}O}$ and m_{H_2} are the mass of a $C^{18}O$ and H_2 molecule, respectively. The abundance of CO is altered due to freeze-out (midplane) and photodissociation (surface) (see e.g. Panić et al. 2008; Miotello et al. 2014). The ISM abundance of [CO]/[H_2] $\sim 10^{-4}$ (Aikawa and Nomura, 2006) is usually also assumed for discs. However, it is important to note that there is a significant scatter around this value: Lacy et al. (1994) find a maximum value of the fractional abundance of ^{12}CO of 9.1×10^{-4}, whereas Frerking et al. (1982) obtain a value of $\sim 8.5 \times 10^{-5}$ in ρ Oph and Taurus. Given the isotopic ratio of [^{16}O]/[^{18}O] and its errors (557±30; Wilson (1999)), the resulting $C^{18}O$ fractional abundance I employ is in a range between

$$1.4 \times 10^{-7} < \frac{[C^{18}O]}{[H_2]} < 1.7 \times 10^{-6}\,. \tag{3.6}$$

The maximum effect of this uncertainty on the line emission is achieved in the optically thin case, where the line emission scales linearly with the abundance. This is fully taken into account when presenting the results of the calculations of the $C^{18}O$ line emission. I will discuss further mechanisms for CO depletion in Section 3.4.6 of this chapter. $C^{18}O$ $J = 2 - 1$ is excited by molecular collisions within the disc. The shape of its line is thus dependent on the temperature and density structure of the disc and on the $C^{18}O$ mass available. Using the CASA software package, I further process the data cubes to obtain synthetic ALMA observations that take into account filtering and instrumental and thermal noise effects. These can then be directly compared with or fitted to the observational $C^{18}O$ data (e.g. molecular line profiles). In order to postprocess the synthetic TORUS data cubes, the CASA routines *simobserve* and *clean* are used with the parameters listed in Table 3.4. These are based on the values in the Science Verification observations in order to make the synthetic images as realistic as possible.

3.4 Results and discussion

3.4.1 Initial mass estimate from the SED modelling

I have explored in total over 100 models varying $M_{\rm dust}$, $a_{\rm min}$, $a_{\rm max}$ and g/d (alone, and in combination with $\alpha_{\rm turb}$) and have found 15 models that fit the observed SED, the details of the models are given in Table 3.5.

In order to fit the model to the observed SED, I start from an initial estimate of the minimum dust mass, which determines the overall SED shape. If the resulting fluxes in the SED are too high compared to the observations, the dust mass is decreased. If the mm-wavelength fluxes are too high at shorter wavelengths, but not in the mm, the g/d

Table 3.4 CASA routines and a selection of the parameters used in order to postprocess the synthetic TORUS datacubes. The first column gives the CASA parameter, the second one the value used and the last column the meaning of the parameter.

	Parameter	**Value**	**Meaning**
simobserve	incenter	2.1956036e11Hz	frequency of the line transition
	inwidth	244126.1Hz	channel width
	compwidth	8GHz	total bandwidth
	totaltime	84min	total time of observation
	antennalist	alma.out06.cfg	interferometer antenna position file
	sdantlist	aca.tp.cfg	single dish antenna position file
	pwv	0.5	precipitable water vapour (in mm)
clean	mask	customised mask	mask image
	imsize	[432, 432]	x and y image size in pixels
	cell	0.05arcsec	x and y cell size
	weighting	briggs	weighting of uv
	robust	0.0	Briggs robustness parameter

ratio is reduced. I then make further improvements on the fit by varying the minimum and maximum grain sizes, taking into account the effects of the individual disc parameters on the SED. For model series B-E, the initial dust mass estimate is based on the following considerations: for optically thin emission, the dust mass is given by

$$M_{\text{dust}} = \frac{F_\nu D^2}{\kappa_\nu B_\nu(T)}\,, \tag{3.7}$$

where F_ν is the flux at a certain frequency, D the distance of the source and κ_ν the opacity at frequency ν as derived in Equation 1.37. B_ν is the Planck function depending on the temperature as given in Equation 1.27. For a distance of $D \approx 120$ pc (van den Ancker et al., 1998), temperature $T \approx 20$ K and at a frequency of $\nu \approx 350$ GHz, I find a flux density of $F_\nu \approx 2.1$ Jy (Guidi et al., 2016). Thus a minimum dust mass of $M_{\text{dust,min}} \sim 8 \times 10^{-4}\,\text{M}_\odot$ can be estimated. Here, the opacity assumed is given in Draine (2006), who shows that at $\lambda \approx 1$ mm (corresponding to $\nu \approx 350$ GHz), dust grains of size $a \approx 1$ mm are most efficient emitters with $\kappa_\lambda \approx 4\,\text{cm}^2\,\text{g}_{\text{dust}}^{-1}$ as they contain most of the mass (they are however not the most efficient emitters per unit mass). Table 3.5 shows that this grain size is comparable to the maximum grain size a_{max} of model series C-E. These models therefore represent the case when the bulk of the mass is in ~ 1 mm-sized grains and M_{dust} is low. For a maximum grain size of 0.4 mm as in model series B, κ_λ from Draine (2006) is a little lower, leading to a slightly higher minimum dust mass than in model series D to reproduce the same SED.

Table 3.5 Parameters of the 15 models that fit the observed SED: $M_{\rm dust}$, $M_{\rm gas}$, g/d, $a_{\rm min}$, $a_{\rm max}$ and $T_{\rm midplane}$ at the location of the CO snowline radius $R_{\rm sl} = 90$ au. I also give the power law exponent p of the surface density profile $\Sigma \propto r^p$. I list as well the turbulent mixing strength $\alpha_{\rm turb}$ and the mm opacity $\kappa_{\rm mm}$ of the dust grains that MCMax uses. The respective distinctive characteristics of the models are given in the last column. Models (A-E)/10 and (A-E)/100 have the same dust properties as models A-E, but their g/d (and thus their $M_{\rm gas}$) are divided by factors of 10 (100) and their $\alpha_{\rm turb}$ multiplied by 10 (100) in comparison with models A-E. The models given in boldface are the models that also match the observed $C^{18}O$ line profiles as I will discuss in the next section.

Model	$M_{\rm dust}[M_\odot]$	$M_{\rm gas}[M_\odot]$	g/d	$a_{\rm min}[\mu m]$	$a_{\rm max}$[mm]	$T(90\,{\rm au})$[K]	p	$\alpha_{\rm turb}$	$\kappa_{\rm mm}[\frac{\rm cm^2}{\rm g_{dust}}]$	Distinctive features
A	3.0×10^{-3}	3.0×10^{-1}	100	0.8	35	25.0	-1.0	10^{-4}	~ 0.9	high $M_{\rm dust}$ and $M_{\rm gas}$
B	8.0×10^{-4}	1.4×10^{-1}	180	0.8	0.4	22.5	-1.0	10^{-4}	~ 4.0	high g/d
C	8.0×10^{-4}	8.0×10^{-2}	100	0.5	1.1	22.0	-1.0	10^{-4}	~ 3.6	intermediate-sized dust
D	$\mathbf{9.5 \times 10^{-4}}$	$\mathbf{1.0 \times 10^{-2}}$	**10.5**	**0.02**	**1.4**	**23.5**	**-1.0**	$\mathbf{10^{-4}}$	$\mathbf{\sim 3.3}$	**low g/d, pristine dust**
E	$\mathbf{1.3 \times 10^{-3}}$	$\mathbf{1.2 \times 10^{-2}}$	**9.2**	**0.05**	**1.4**	**20.0**	**-1.2**	$\mathbf{10^{-4}}$	$\mathbf{\sim 3.3}$	**steeper Σ(r)-profile**
A/10	$\mathbf{3.0 \times 10^{-3}}$	$\mathbf{3.0 \times 10^{-2}}$	**10**	**0.8**	**35**	**25.0**	**-1.0**	$\mathbf{10^{-3}}$	$\mathbf{\sim 0.9}$	-
B/10	$\mathbf{8.0 \times 10^{-4}}$	$\mathbf{1.4 \times 10^{-2}}$	**18**	**0.8**	**0.4**	**22.5**	**-1.0**	$\mathbf{10^{-3}}$	$\mathbf{\sim 4.0}$	-
C/10	$\mathbf{8.0 \times 10^{-4}}$	$\mathbf{8.0 \times 10^{-3}}$	**10**	**0.5**	**1.1**	**22.0**	**-1.0**	$\mathbf{10^{-3}}$	$\mathbf{\sim 3.6}$	-
D/10	9.5×10^{-4}	1.0×10^{-3}	1.05	0.02	1.4	23.5	-1.0	10^{-3}	~ 3.3	-
E/10	1.3×10^{-3}	1.2×10^{-3}	0.92	0.05	1.4	20.0	-1.2	10^{-3}	~ 3.3	-
A/100	3.0×10^{-3}	3.0×10^{-3}	1	0.8	35	25.0	-1.0	10^{-2}	~ 0.9	-
B/100	8.0×10^{-4}	1.4×10^{-3}	1.8	0.8	0.4	22.5	-1.0	10^{-2}	~ 4.0	-
C/100	8.0×10^{-4}	8.0×10^{-4}	1	0.5	1.1	22.0	-1.0	10^{-2}	~ 3.6	-
D/100	9.5×10^{-4}	1.0×10^{-4}	0.11	0.02	1.4	23.5	-1.0	10^{-2}	~ 3.3	-
E/100	1.3×10^{-3}	1.2×10^{-4}	0.09	0.05	1.4	20.0	-1.2	10^{-2}	~ 3.3	-

Note, however, that the above calculation is only used to get an initial value for $M_{\rm dust}$, employing standardised values for the opacity. The mm opacities $\kappa_{\rm mm}$ used with MCMax are given in Table 3.5, they depend on the dust grain size, thus they vary from model to model and differ slightly from the values given in Draine (2006), which are for a material of specific chemical composition and properties assumed to be similar to ISM dust. However, the mm opacities only influence the exact location of the mm point in the SED.

3.4.2 Description of models obtained with MCMax

The SEDs of all my models are given in Figure 3.3. As discussed above, all models of a given model series have the same SED due to the degeneracy of $\alpha_{\rm turb}$ and g/d. A zoom-in of the far-infrared (FIR) and mm region of the SED is included as this is the wavelength regime that is most crucial for the analysis presented here. All my models match the observed SED in this wavelength range very well, therefore the different models are hardly distinguishable there. I do not try to fit the observed SED at wavelengths of a few mm because emission in this regime is dominated by free-free-emission (Isella et al., 2007; Wright et al., 2015; Guidi et al., 2016), which is not included in my calculations.[5] Note that the only models which can reproduce the $\lambda > 2$ mm observations by *thermal* emission - and no free-free emission at all - are the models of series A, D and E, where series A needs large grains (35 mm) and all three of them need a high dust mass.

Furthermore, the models do not match the near-infrared (NIR) excess at $\lambda < 10\,\mu$m very well, but this is sensitive to the exact dust grain composition and geometry of the very inner disc (inner few au; Meijer et al., 2008). Including a puffed-up inner disc rim, which could potentially cast a shadow on to the disc surface, might be expected to provide a better fit to the NIR SED. However Acke et al. (2009) find that this would only influence the NIR regime of the SED (not the FIR or mm). Therefore a puffed-up inner rim would not improve the fit over a substantial wavelength range. The NIR fit does not alter the results for the dust mass, which is calculated using the longer wavelength component of the SED. Furthermore, adjusting the scale height in the inner disc would violate the self-consistency of the models. For simplicity, a model for a puffed up inner rim is therefore not included at this stage.

Firstly, the general characteristics of each of these models will be discussed. I find that model A has a relatively high $M_{\rm dust}$ and $M_{\rm gas}$ (of the order of 10 per cent of the stellar mass

[5] Subtracting the free-free component, Isella et al. (2007) obtain a millimetre spectral index $\alpha_{\rm mm}$ ($F_\nu \propto \lambda^{-\alpha_{\rm mm}}$) of ≈ 3 between 1-7 mm, assuming that the free-free emission contributes 27 per cent of the observed flux at a wavelength of 7 mm.

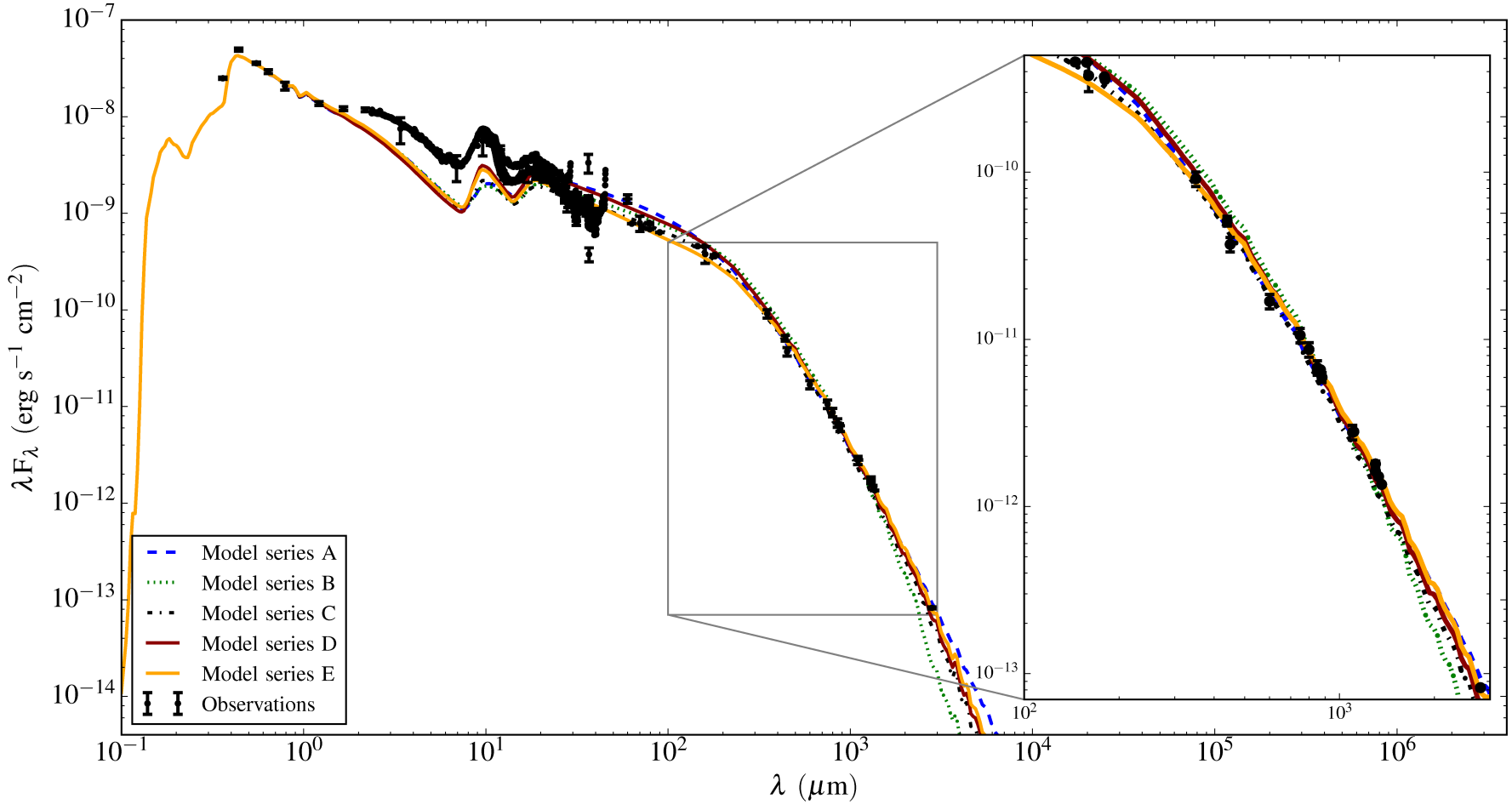

Figure 3.3 SEDs of my best-fitting models (parameters can be found in Table 3.5). Due to the degeneracy of $\alpha_{\rm turb}$ and g/d, the SEDs within each model series are exactly the same (see text). The observations are plotted as black circles including the respective error bars. The observational data are taken from Berrilli et al. (1992); Mannings and Sargent (1997); Bouwman et al. (2000); Isella et al. (2007); Qi et al. (2011); Tilling et al. (2012); Mendigutía et al. (2012); de Gregorio-Monsalvo et al. (2013) and the Spitzer c2d legacy survey.

$M_* = 2.3\,\mathrm{M}_\odot$). This will in general produce relatively high fluxes, so in order to compensate for the high masses, its grains have to be quite evolved. This will ensure that not too many small grains are situated in the disc atmosphere, where they could intercept stellar irradiation and thus boost the fluxes of the SED. Models B and C have the same M_{dust}, but due to their different g/d ratios, their M_{gas} values differ by about a factor of 2. In order for them to give the same SEDs, model B with the higher g/d has to have different grain sizes from model C: its minimum grain size is a little larger than for model C, while its maximum grain size is about a factor of 3 smaller. The distinctive feature of model B is its high g/d ratio which I compensate for by making its minimum grain size bigger than in model C. Therefore - as described for model A - the fluxes in the SED are reduced. Models D and E have a much lower gas mass than the other models I found, but they all have the same SED. This is caused by these two models being the only ones with very small grains. These are coupled to the gas, dragged to higher layers and thus intercept more stellar flux. In general, models A-C have relatively large grain sizes (which probably correspond to a more evolved state), otherwise the SEDs would produce too high values in the FIR. Model E is similar to model D, but employs a different radial dependence of the surface density: for models series A-D I assumed $\Sigma \propto r^{-1}$, for model series E a slightly steeper profile of $r^{-1.2}$ is taken, although still well within the range of observationally measured values for protoplanetary discs (Andrews et al., 2010). Model series E yields a lower midplane temperature at the location of the CO snowline radius than the other models, as I will discuss shortly.

One can calculate the optical depth of the continuum emission for the models (using the surface density and mm opacity), which yields that the mm continuum emission for all my models is optically thin, except for model series E, where it becomes optically thick within the inner ~ 10 au. This enables obtaining a reliable estimate of the dust mass in the disc. I would like to highlight that some of the models reach the maximum mm opacity (as obtained by Draine 2006) and are indicative of the minimum $M_{\mathrm{dust}} \sim 8 \times 10^{-4}\,\mathrm{M}_\odot$ as derived earlier in this section. Much lower κ_{mm} are of course possible if a big fraction of the mass is hidden in pebbles and larger bodies, which do not contribute to the mm flux. In such cases, M_{dust} in my models is just indicative of the mass of the mm dust and thus a much higher total mass of solids can be achieved. However, SEDs of such models would not differ.

Models A-E have a turbulent mixing strength of $\alpha_{\mathrm{turb}} = 10^{-4}$, but as described above additional calculations are run for these models, exploring larger values of α_{turb} (10^{-3} and 10^{-2}) while decreasing the gas masses in these models by factors of 10 and 100. All the remaining parameters of models A-E are left unchanged, as listed in Table 3.5. Indeed, I find that the observational constraints given by the SED and midplane temperature requirements can be matched by all the models A-E, by changing the M_{gas} and adjusting the

$\alpha_{\rm turb}$ accordingly, to keep $M_{\rm gas} \times \alpha_{\rm turb}$ (and therefore the dust diffusion solution, resulting temperature structures and the SEDs within each model series) constant. In general, all models A-E/10 and A-E/100 yield low to very low g/d ratios by construction. In order to compensate for the lower gas masses, higher levels of turbulent mixing are needed to transport the dust grains to higher altitudes in the disc where they can absorb the stellar light and give the same SED. Given that the dust grain properties within a certain series are exactly the same, the above description of the distinctive features of models A-E holds true for (A-E)/10 and (A-E)/100, respectively.

In general, a surprising result of this modelling approach is that it is able to match both the SED and CO snowline radius by making very different assumptions on the basic parameters, such as dust grain size and gas mass. Higher emission can for example be caused by a higher dust or gas mass, but also by smaller dust grains present in the disc. Some of these parameter degeneracies are also discussed in Woitke et al. (2016); Panić and Min (2017). It is therefore important to note that SED modelling alone does not provide unambiguous physical models of the disc structure, but is highly degenerate.

3.4.3 Disc regions contributing to the SED

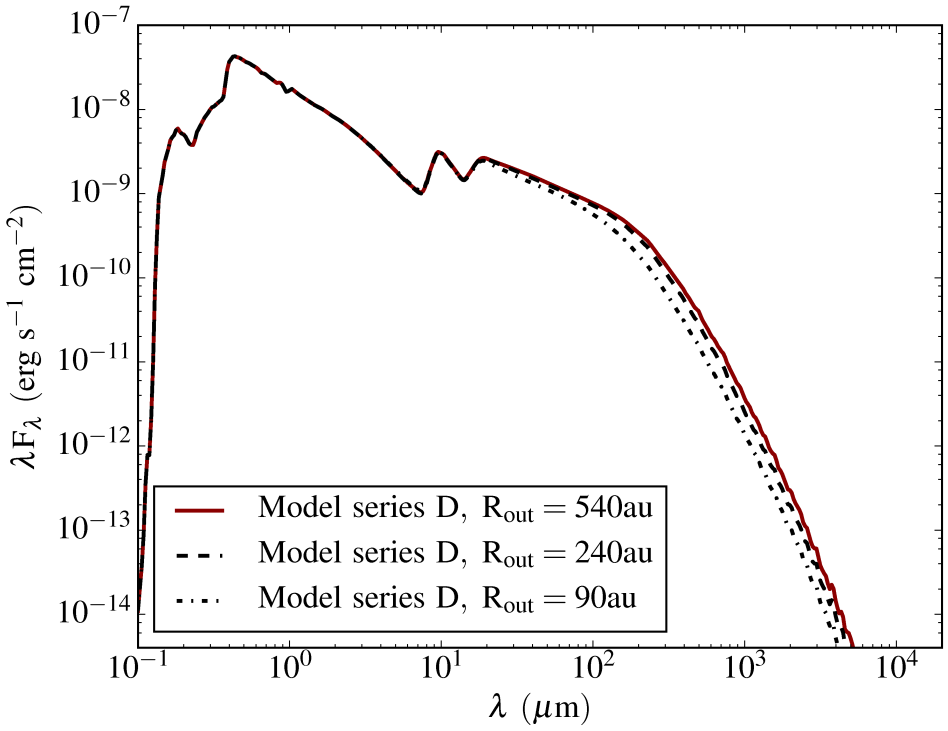

Figure 3.4 SED of the whole disc $R < 540$ au (*red solid line*), from within $R < R_{850\,\mu\rm m\ dust} = 240$ au (*black dashed line*) and from $R < R_{\rm sl} = 90$ au (*black dash-dotted line*).

Fitting observed SEDs in general is most suited for disc regions that are not too far out, since dust grains there do not intercept sufficient stellar light to contribute substantially to the SED. I have checked that the SEDs as obtained from the whole discs ($R = 540$ au) of my 15 models (as shown in Figure 3.3), are only marginally changed when taking the emission from within 240 au, which is the observed mm dust radius. This is plotted in Figure 3.4 for model series D, the same behaviour is found for the other models. Thus the fact that my model discs are described by a single power law surface density distribution out to 540 au (whereas the observed dust distribution extends only to $\sim$ 240 au) will not have a significant effect on my SED fits. I will later focus on the gas budget of the disc within the CO snowline ($R_{\rm sl} = 90$ au) and note that, in the models, this region contributes around $40-50$ per cent of the flux at sub-mm wavelengths. The SED for the emission from within the snowline radius is also overplotted in Figure 3.4.

3.4.4 Models matching the CO snowline location

As an additional constraint one has to make sure that the MCMax models are consistent with the observed CO snowline location. Therefore I analyse the midplane temperature profile $T_{\rm midplane}(r)$ for all my models that match the observed SED, which is plotted in Figure 3.5. As mentioned above, models of the same series have the same temperature structure.

I find that all of them have midplane temperatures between $\sim$ 20 and 25 K at the observed snowline radius of $R_{\rm sl} \approx 90$ au (Qi et al., 2015). These are well within the range of values generally assumed and observed for the freeze-out temperature of CO: The freeze-out temperature can vary between $\sim$ 20 and $\sim$30 K depending on whether CO is binding to pure CO ice or a mixture with water ice (Collings et al., 2004), which is, in turn, also dependent on the chemical history of the ice (Garrod and Pauly, 2011). In general, the CO freeze-out temperature is not known unambiguously and might vary from system to system (Hersant et al., 2009; Qi et al., 2015): Qi et al. (2013b) found a freeze-out temperature of CO of 17 K from their modelling of TW Hya, whereas Jørgensen et al. (2015) obtain temperatures of about 30 K in their study of embedded protostars. Qi et al. (2011) assume a freeze-out temperature for CO of $T \approx 19$ K (pure CO ice) for HD 163296. However, in Qi et al. (2015) they perform a new analysis with higher-resolution observational data and use a temperature in the midplane at $R_{\rm sl}$ of $T \approx 25$ K (mixed CO/H_2O ice).

Thus all my models have temperatures in the disc midplane at the location of the snowline radius that are well within the plausible range. The exploration of self-consistent models confirms that all the freeze-out temperatures assumed in these previous literature references fall within the plausible range of temperatures for HD 163296. If the freeze-out

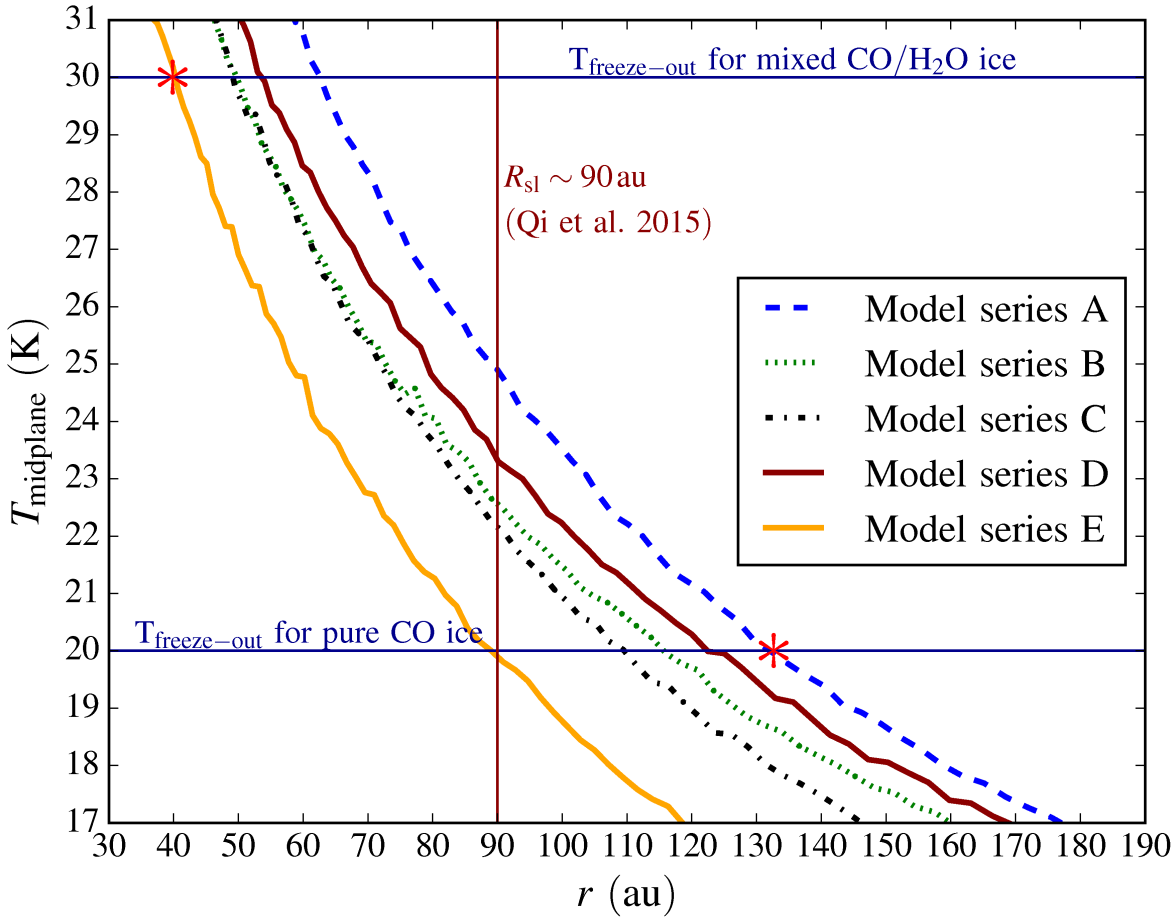

Figure 3.5 Midplane temperature as a function of radius for the 15 disc models that match the observed SED. Models from the same series have exactly the same midplane temperature structure (see Section 3.3.1). In dark red (*vertical line*) I plot the observed snowline radius ≈ 90 au (Qi et al., 2015). The upper and lower limits of the freeze-out temperature ($\sim 20 - 30$ K) as found by e.g. Collings et al. (2004) are plotted as horizontal lines. The red asterisks indicate where the snowline location could be (between ~ 40 and 135 au) due to a plausible range of freeze-out temperatures of $20 - 30$ K if the snowline location was not known unambiguously from observations.

temperature of CO was known unambiguously, this would, in combination with an observationally determined CO snowline location, be a powerful model discriminant and may allow the exclusion of models based on this constraint. Since, however, it is unclear what exactly the relevant freeze-out temperature is, I find that all the models can match the observed snowline location of 90 au. This weak model discrimination also means that it is impossible to *predict* the CO snowline radius from SED model fitting alone or even from fitting the molecular line emission together with the SED (Qi et al., 2011): given the uncertainty in the sublimation temperature of CO, the viable SED fits imply predicted radii in the range $\sim 40 - 135$ au as denoted by the red asterisks in Figure 3.5. In general, I find that the location of the CO snowline radius does not further discriminate between models in comparison to the criterion given by the SED; however it sets the radial location inwards

of which no freeze-out is taking place in the models, and which is therefore important for the interpretation of the $C^{18}O$ emission. It is important to note that an SED fit does not determine the CO snowline location and that, vice versa, a CO snowline observation does not discriminate amongst possible SED models.

One can conclude that all the 15 models match the SED and CO snowline location within the uncertainties in the freeze-out temperature. The SED modelling is especially powerful for the inner ~ 240 au and describes the disc structure inside the CO snowline location well.

3.4.5 Modelling the $C^{18}O$ J $= 2 - 1$ emission with TORUS

As discussed in Section 3.3.2, the density and temperature structures of the MCMax models are used to calculate the $C^{18}O$ line emission with TORUS. The aim of this work is to interpret the observed $C^{18}O$ $J = 2$–1 line profile, especially from the inner disc regions, in the context of a physically self-consistent model that matches other relevant observations such as R_{sl} and the SED. I show the $C^{18}O$ $J = 2 - 1$ line profile as observed by ALMA in Figure 3.6, both taking the emission from the whole disc and from within the 90 au snowline radius. These are very different, especially in the peaks of the spectrum, as these are dominated by the emission from the outer disc regions. The goal is to model the disc regions with $R < 90$ au, as these are independent of the details of freeze-out in the outer disc.

As mentioned previously, the fractional abundance of $C^{18}O$ has a large uncertainty and is observed (in star-forming clouds) to be in a range between 1.4×10^{-7} and 1.7×10^{-6} (see Section 3.3.2), thus spanning an order of magnitude. From matching the observed $C^{18}O$ $J = 2 - 1$ line profile with my models, one can unambiguously calculate the mass of $C^{18}O$ in the disc. However, when then converting this mass to a mass of H_2 one has to take this range of $C^{18}O$ abundance into account.

Matching the observed $C^{18}O$ line profile, I find that - considering the range of plausible abundances - only five of the models can fulfil this criterion, namely (A-C)/10, D and E. I will thus focus on these models in the further discussion.

Another aspect to take into account is that the abundance of $C^{18}O$ in comparison to H_2 can be altered due to freeze-out in the disc midplane, as already discussed in the previous section. This effect has been implemented in TORUS by setting the abundance of $C^{18}O$ to a negligible value when the disc temperature drops below the freeze-out temperature. For the individual models, the midplane temperature of the respective model at the observed snowline radius is used (as given in Figure 3.5).

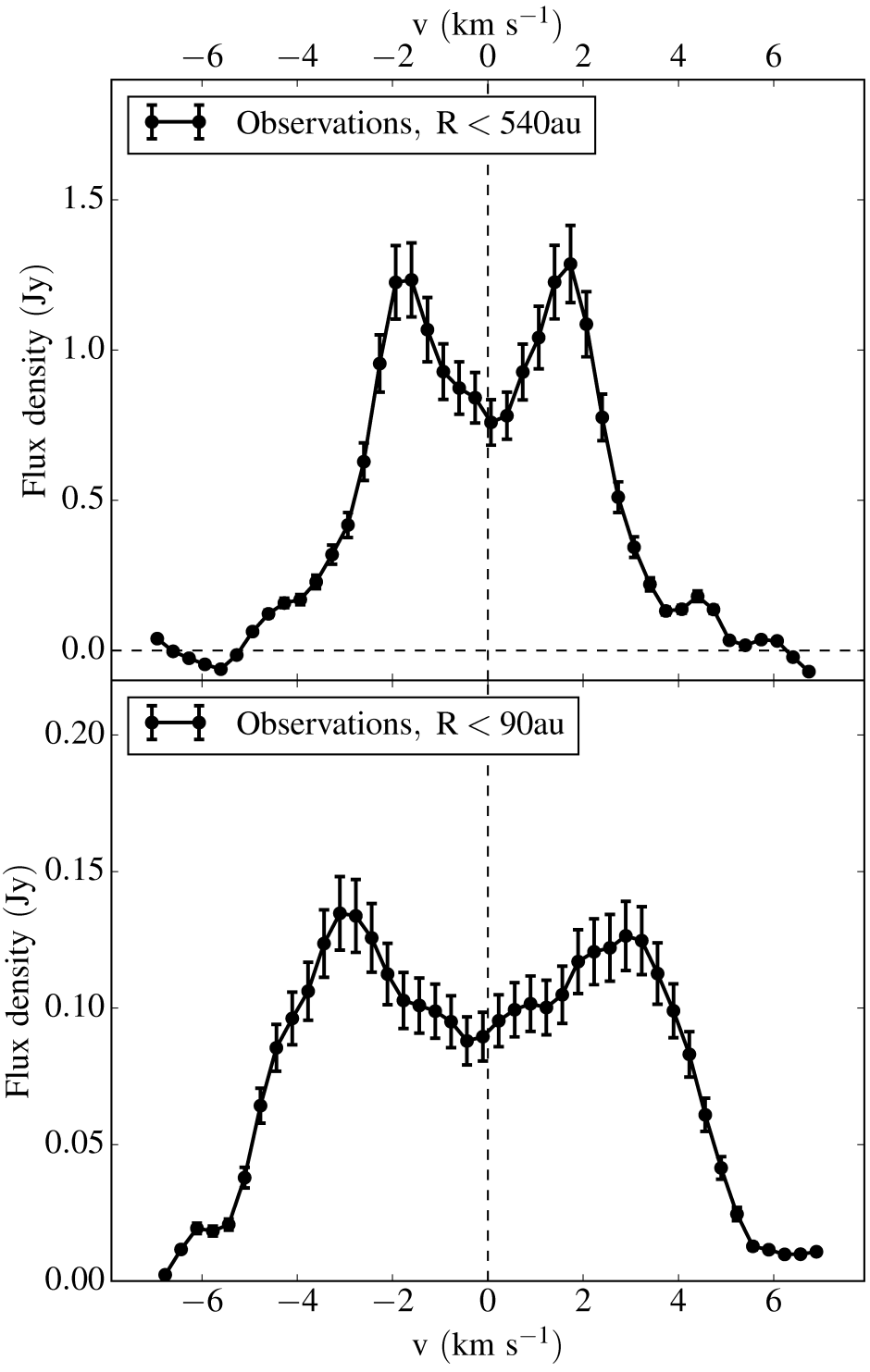

Figure 3.6 $C^{18}O$ $J = 2-1$ line profile (ALMA observations) using the emission from the whole disc (*upper panel*) and from within the 90 au snowline radius (*lower panel*). The error bars represent a 10 per cent flux calibration uncertainty (Guidi et al., 2016). The spectra are centred on 0 km s^{-1}. The systemic velocity is $v_{\rm sys}$=5.8 km s^{-1}.

Table 3.6 Freeze-out temperatures (midplane temperatures at 90 au) and fractions of the CO mass removed in the various model series due to freeze-out.

Model series	**A**	**B**	**C**	**D**	**E**
$T_{\text{freeze-out}}(90\,\text{au})$ [K]	25.0	22.5	22.0	23.5	20.0
	$\sim 48\%$	$\sim 45\%$	$\sim 40\%$	$\sim 27\%$	$\sim 23\%$

The fraction of the $C^{18}O$ mass removed by freeze-out in the respective models is given in Table 3.6. I find that this effect is stronger for models (A-C)/10 than for models D and E, because the former have slightly higher gas masses and bigger grains, thus a higher fraction of the mass will be concentrated in the cooler disc midplane regions and thus subject to freeze-out. However, the exact impact of freeze-out on the line profile depends on the details of the vertical temperature profile and thus on the location of the CO ice surface.

The second most relevant source of CO-removal from the gas-phase is photodissociation (Visser et al., 2009; Miotello et al., 2014). As described in Section 3.3.2, this has been taken into account in the modelling. This is done by setting the $C^{18}O$ abundance to a negligible value for a threshold column density of gas calculated from the star in different azimuthal directions covering the entire disc height. These threshold column densities vary from N_{CO}=10^{18} cm^{-2}, 10^{19} cm^{-2} and 10^{20} cm^{-2} (corresponding to 10^{22} H_2 cm^{-2}, 10^{23} H_2 cm^{-2} and 10^{24} H_2 cm^{-2}, respectively, assuming $f_{\text{CO}} \sim 10^{-4}$).

I find that overall only a small fraction of $C^{18}O$ is photodissociated within the 90 au snowline location in the models. For the first threshold, the fraction of the CO gas mass photodissociated is $\sim$ 0.1 per cent in all models, for $N_{\text{CO}} = 10^{19}$ cm^{-2} it is $\sim$ 1 per cent and even for the extreme case, only $\sim$ 3 per cent is photodissociated within the snowline radius. The $C^{18}O$ line emission for $R < 90$ au after removing CO from the photodissociated layer is calculated for the three explored cases (N_{CO}=10^{18} cm^{-2}, 10^{19} cm^{-2} and 10^{20} cm^{-2}). This is presented for the example of model D in Figure 3.7. Given that in the analysis I mostly focus on the regions within the 90 au snowline radius that are not subject to freeze-out and not strongly affected by photodissociation, the models are not dependent on the exact details of these processes.

For 5 out of my 15 initial models, one can match the observed $C^{18}O$ $J = 2-1$ line profile within the range of plausible $C^{18}O$ abundances between 1.4×10^{-7} and 1.7×10^{-6} (Equation 3.6). The $C^{18}O$ spectra arising from the regions inside the 90 au snowline radius in these models are showed in the left-hand panels panels of Figure 3.8. I will call these five models (A-C)/10, D and E "fiducial" models in the further discussion.

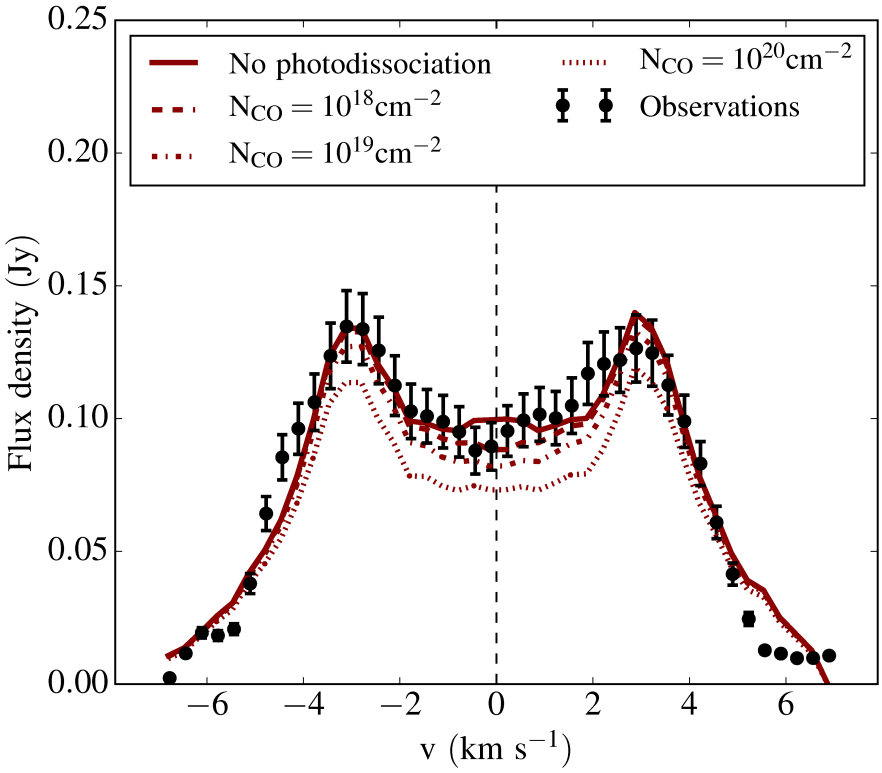

Figure 3.7 $C^{18}O$ flux density for model D (from regions with $R < R_{sl} = 90$ au) employing different column density thresholds for photodissociation: no photodissociation (solid), N_{CO}=10^{18} cm^{-2} (*dashed*), 10^{19} cm^{-2} (*dash-dotted*) and 10^{20} cm^{-2} (*dotted*). Even in the most extreme case, only ~ 3 per cent of the CO mass is affected. For reference, the observed line profile for this disc region is given by the black points with error bars (10 per cent flux calibration uncertainty). I find a very similar behaviour for the other models and thus do not show the respective plots here.

These spectra can be obtained from the synthetic and ALMA data cubes using the CASA software in the following way: I calculate the emission from an elliptical region, centred on the centre of the disc using a PA=132° and the ratio of minor to major axis introduced in Equation 1.41 ($b/a = \cos(i)$, where $i = 48°$). These values of PA and inclination are the ones obtained in the analysis of the observations (see Section 3.2). All of them match the observations well within the error bars (given by the $\sim$ 10 per cent flux calibration uncertainty of the ALMA observations, Guidi et al. 2016).

The fractional abundances of $C^{18}O$ of these models can be found in Table 3.7. Given these abundances and the gas masses in the respective models, one can calculate the mass of $C^{18}O$ within the snowline radius, as the $C^{18}O$ $J = 2 - 1$ transition is mainly optically thin throughout the whole disc. I have calculated the optical depth of the $C^{18}O$ $J = 2 - 1$ transition and found that it is indeed optically thin throughout the whole line profile and at all radii for all my models that match the observations. Although the models are optically thin, this would not have been a necessary precondition for the modelling process as the radiative transfer calculation self-consistently accounts for optical depth effects.

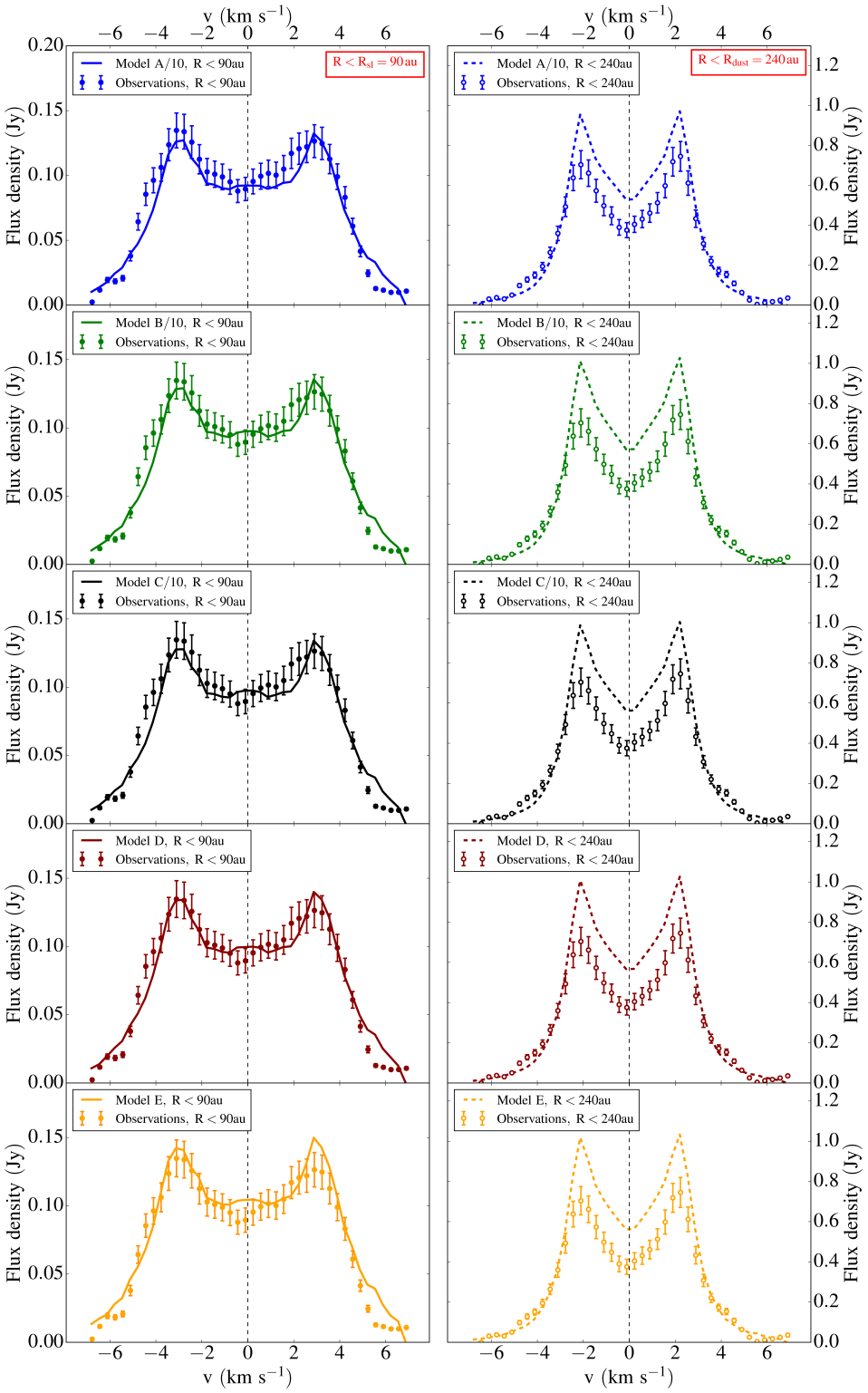

Figure 3.8 $C^{18}O$ $J = 2 - 1$ line profiles of the five models: emission from within $R_{sl} = 90$ au (*left*) as well as from within $R < 240$ au ($R_{mm\,cont.}$, *right*). The line profiles from the models are given by the lines (*solid* for $R = 90$ au, *dashed* for $R = 240$ au), the observations by the respective dots. The error bars reflect the 10 per cent flux calibration uncertainty of the observations. All models of the same series that have abundances in the range of $C^{18}O$ abundances I consider will have the same flux densities because the $C^{18}O$ masses and temperature structures are the same. The profiles were centred around 0 km s^{-1} (with $v_{sys} = 5.8$ km s^{-1}).

Table 3.7 Properties of the five best-fitting (fiducial) models: fractional abundance of $C^{18}O$ as obtained by matching the observed line profile within the 90 au snowline radius, the mass of $C^{18}O$ within this radius, the H_2 mass within the snowline radius, the average g/d within 90 au and α_{visc} for the respective cases.

	A/10	**B/10**	**C/10**	**D**	**E**
$f_{C^{18}O}$	2.7×10^{-7}	6.4×10^{-7}	1.0×10^{-6}	6.6×10^{-7}	6.8×10^{-7}
$M_{C^{18}O}(R < 90\,\text{au})$ [$M_\odot$]	1.9×10^{-8}	2.1×10^{-8}	1.9×10^{-8}	1.6×10^{-8}	2.7×10^{-8}
$M_{gas}(R < 90\,\text{au})$ [$M_\odot$]	5.0×10^{-3}	2.3×10^{-3}	1.3×10^{-3}	1.7×10^{-3}	2.9×10^{-3}
$M_{dust}(R < 90\,\text{au})$ [$M_\odot$]	5.0×10^{-4}	1.3×10^{-4}	1.3×10^{-4}	1.6×10^{-4}	3.1×10^{-4}
g/d	10	18	10	10.5	9.2
$\alpha_{visc}(R < 90\,\text{au})$	0.2	0.4	0.7	0.5	0.3

However, the low optical depth emphasises how essential $C^{18}O$ is as a tracer for the disc midplane. That implies that one can unambiguously calculate the $M_{C^{18}O}$ within 90 au which should be approximately the same for all the models. The values I obtain are listed in Table 3.7 and are in a range of (see also Equation 3.5):

$$M_{C^{18}O}(R < 90\,\text{au}) \approx 2 - 3 \times 10^{-8}\,M_\odot\,. \tag{3.8}$$

The value that Qi et al. (2011) obtain for this inner disc region is comparable to these. In the right-hand panels of Figure 3.8, I plot the emission from a bigger disc region, namely from within the outer dust radius $R_{dust} \approx 240$ au. The models still closely match the wings of the spectrum and thus the emission from the inner disc regions. However, one can see that the models slightly over-predict the emission from the outer disc regions (i.e. in the peaks of the spectrum) there. The height of the peaks depends crucially on the exact vertical temperature structure of the models as freeze-out will reduce the $C^{18}O$ emission, especially in the outer disc regions. However, I do not attempt to match these disc regions, but focus on the innermost 90 au.

So far, only the five models from the initial Table 3.5 that also match the $C^{18}O$ line profile have been explored. However, it is interesting to look into the extreme cases, i.e. models with minimum and maximum plausible $C^{18}O$ abundance (and thus maximum and minimum g/d and M_{gas}), while still matching the observed $C^{18}O$ and thus the $C^{18}O$ masses within 90 au I just calculated. The properties of the extreme models are given in Table 3.8. It is important to note that models D_{max} and E_{max} can be excluded as their α_{turb} is lower than the minimum of 10^{-4} I consider.

Table 3.8 "Extreme" cases of model series A-E: models with the highest possible g/d (and thus $M_{\rm gas}(R < 90\,{\rm au})$) are denoted by the "max", the corresponding lowest models by "min". I give the following parameters: fractional abundance of $C^{18}O$ as obtained by matching the observed line profile within the 90 au snowline radius, the mass of $C^{18}O$ within this radius, the H_2 mass within the snowline radius, the average g/d within 90 au, $\alpha_{\rm turb}$ and $\alpha_{\rm visc}$ for the respective cases. Models $D_{\rm max}$ and $E_{\rm max}$ can be excluded as their $\alpha_{\rm turb}$ is outside the range I consider.

	$f_{C^{18}O}$	$M_{C^{18}O}(R < 90\,{\rm au})$ [$M_\odot$]	$M_{\rm gas}(R < 90\,{\rm au})$ [$M_\odot$]	$M_{\rm dust}(R < 90\,{\rm au})$ [$M_\odot$]	g/d	$\alpha_{\rm turb}$	$\alpha_{\rm visc}(R < 90\,{\rm au})$
$A_{\rm min}$	1.7×10^{-6}	1.9×10^{-8}	7.9×10^{-4}	5.0×10^{-4}	2	6.3×10^{-3}	1.2
$A_{\rm max}$	1.4×10^{-7}	1.9×10^{-8}	9.6×10^{-3}	5.0×10^{-4}	19	5.3×10^{-4}	0.1
$B_{\rm min}$	1.7×10^{-6}	2.1×10^{-8}	8.7×10^{-4}	1.3×10^{-4}	7	2.7×10^{-3}	1.1
$B_{\rm max}$	1.4×10^{-7}	2.1×10^{-8}	1.1×10^{-2}	1.3×10^{-4}	82	2.2×10^{-4}	0.1
$C_{\rm min}$	1.7×10^{-6}	1.9×10^{-8}	7.6×10^{-4}	1.3×10^{-4}	6	1.7×10^{-3}	1.2
$C_{\rm max}$	1.4×10^{-7}	1.9×10^{-8}	9.3×10^{-3}	1.3×10^{-4}	71	1.4×10^{-4}	0.1
$D_{\rm min}$	1.7×10^{-6}	1.6×10^{-8}	6.6×10^{-4}	1.6×10^{-4}	4	2.6×10^{-4}	1.4
$D_{\rm max}$	1.4×10^{-7}	1.6×10^{-8}	8.0×10^{-3}	1.6×10^{-4}	50	2.1×10^{-5}	0.1
$E_{\rm min}$	1.7×10^{-6}	2.7×10^{-8}	1.2×10^{-3}	3.1×10^{-4}	4	2.5×10^{-4}	0.8
$E_{\rm max}$	1.4×10^{-7}	2.7×10^{-8}	1.4×10^{-2}	3.1×10^{-4}	45	2.0×10^{-5}	0.1

Models D and E both have this minimum value of $\alpha_{\rm turb} = 10^{-4}$. Therefore for model series D and E, the highest possible values of g/d and therefore $M_{\rm gas}$ within 90 au are the ones given in Table 3.7. The highest possible values of g/d for models that match the observed $C^{18}O$ line profiles are 82 and 71 (for models $B_{\rm max}$ and $C_{\rm max}$, respectively); the lowest value is 2 (model $A_{\rm min}$). I take these three cases into account for the further discussion as they are the extreme ends of the g/d range I obtain.

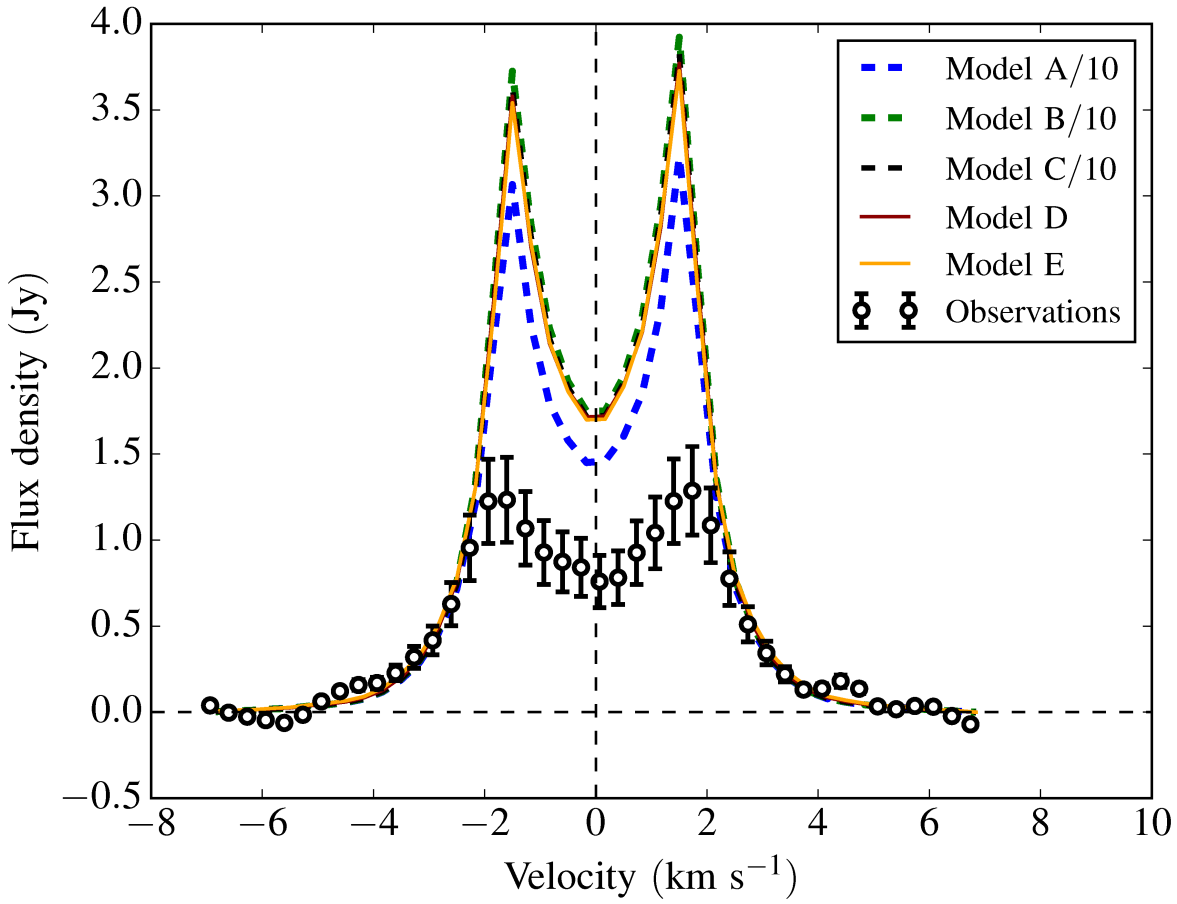

Figure 3.9 $C^{18}O$ $J = 2-1$ line profile for the whole disc for my five fiducial models (*colours*) and as observed (*dots*, error bars represent a 10 per cent flux calibrations uncertainty, Guidi et al. 2016). The profiles were centred around a velocity of 0 km s^{-1}. All models from the same series (that have $C^{18}O$ abundances in the allowed range) have the same line profile (as they have different $C^{18}O$ abundances and gas masses, but the same $C^{18}O$ mass). My models match the emission from the inner disc regions (wings of the line profile) very well, whereas they over-predict the emission in the outer disc regions (peaks of the spectrum). The modelling approach is however best suited for the inner disc regions.

Finally, for completeness, I compare the synthetic line profile for the whole disc with observations in Figure 3.9. The models over-predict the emission from the outer disc regions, i.e. the emission in the peaks of the spectrum. However, as mentioned earlier, the SED does not provide information about the structure of the outermost disc regions. Also,

it is known that there are radial differences in the structure of the outer disc and the inner 240 au and I therefore limit my attention to the disc inner regions in this study. It might however be interesting to combine this modelling approach for the inner disc regions with high-resolution imaging of multiple isotopologues in the outer disc regions (see e.g. Qi et al., 2011; de Gregorio-Monsalvo et al., 2013).

3.4.6 Physical properties of the models

Gas mass within the snowline radius

The match to the observed $C^{18}O$ spectrum within the CO snowline for the five models unambiguously constrains the mass of $C^{18}O$ in this disc region. In Equation 3.8, I gave this mass within the snowline radius. Thus the mass of H_2 in this disc region can be calculated from $M_{C^{18}O}(90\,\text{au})$ by taking into account the abundance of $C^{18}O$ given in Table 3.7 and the mass ratio of these molecules $m_{C^{18}O}/m_{H_2} \approx 14$ (see Equation 3.5). I find that the mass of H_2 within the snowline radius is in a range of $M_{\text{gas}}(R < 90\,\text{au}) \approx (1.3 - 5.0) \times 10^{-3}\,M_\odot$.

Adding this to the uncertainty in the $C^{18}O$ abundance, one obtains the full range of M_{gas} that can possibly be present in the disc within 90 au based on the calculation of the extreme cases (see Table 3.8):

$$6.6 \times 10^{-4}\,M_\odot \lesssim M_{\text{gas}}(R < 90\,\text{au}) \lesssim 1.1 \times 10^{-2}\,M_\odot\,. \tag{3.9}$$

The $C^{18}O$ surface number density for the five models and three extreme cases is plotted in Figure 3.10 as solid coloured lines (left y-axis).

The $C^{18}O$ surface density profile derived by Qi et al. (2015) falls within the range shown by the models (black dotted line in Fig. 3.10, extrapolated from 50 au inwards). In Figure 3.10, I also give the corresponding H_2 column densities in the same plot (dashed lines, right y-axis), where the corresponding $C^{18}O$ abundances are given in Table 3.7.

It is important to note that all eight models yield very similar $C^{18}O$ surface densities. However, due to their different $C^{18}O$ abundances (see Table 3.7), their corresponding gas masses within 90 au are different by approximately an order of magnitude. Not surprisingly, models B_{max} and C_{max} yield the highest H_2 column densities, given that they have the lowest possible $C^{18}O$ abundance and thus the highest gas mass. Model A_{min}, on the other hand, has the lowest H_2 column density of the models I plot here, as it has the lowest gas mass of all of them. If one were to plot the same for models for $(\text{B-D})_{\text{min}}$, this would be comparable to A_{min}.

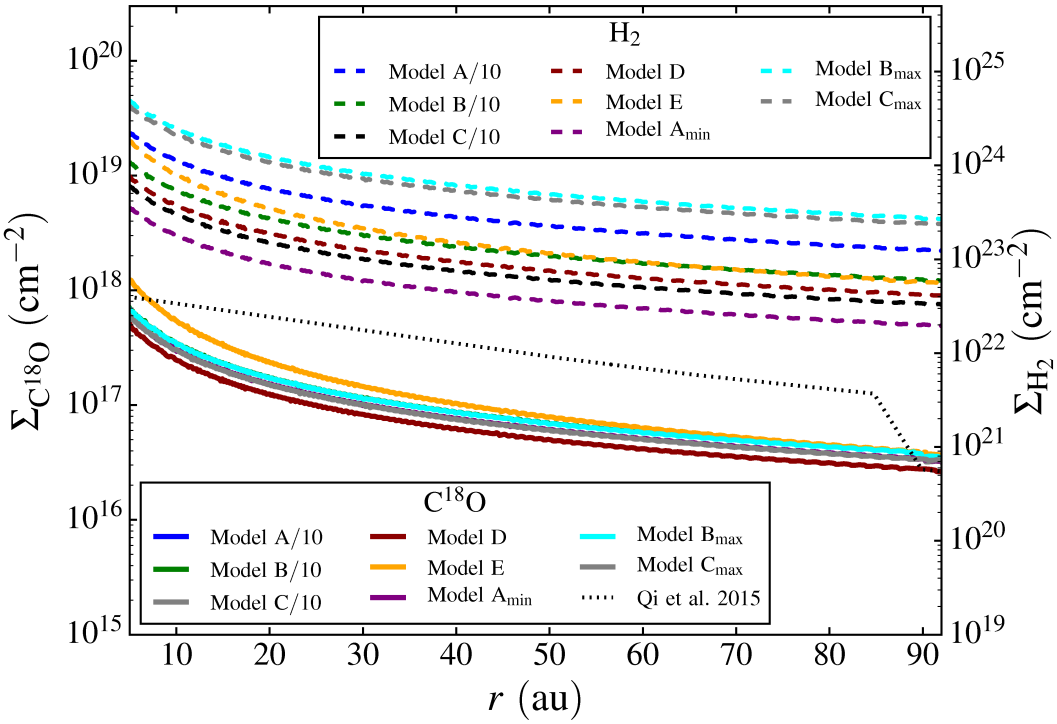

Figure 3.10 *Left y-axis*: column number density of $C^{18}O$ for models (A-C)/10, D, E, A_{min}, B_{max} and C_{max} for regions within the 90 au snowline radius, given by the solid colourful lines. I overplot the one obtained by Qi et al. (2015) (dotted black line, extrapolated from 50 au inwards). *Right y-axis*: corresponding column density of H_2, given by the dashed lines for the individual models. The masses of both $C^{18}O$ and H_2 that correspond to these column densities are given in Table 3.7.

Gas-to-dust mass ratios

Here I present an analysis of the average g/d in the inner disc regions. The g/d values for the individual models are given in Table 3.7 for the fiducial models (A-C)/10, D and E and for the extreme cases in Table 3.8. It is striking that all models (excluding the extreme cases) have very low g/d values ($9 \lesssim g/d \lesssim 20$). This is significantly lower than the standard value of 100 as observed in the ISM. However, models B_{max} and C_{max} do - by construction - have more ISM-like g/d values (~ 80 and ~ 70, respectively). These are the maximum g/d values (and thus the maximum $M_{gas}(< 90\,\text{au})$) the models can obtain while still matching the $C^{18}O$ line profiles, as both of these models have the lowest possible fractional abundance of $C^{18}O$ that is considered here (see Equation 3.6). I comment more on the possibility of lower $C^{18}O$ abundances below.

It is important to note that similarly one can also obtain models based on A-E - employing the highest possible abundance - that yield the lowest possible g/d while still matching the $C^{18}O$ line profile. These are the cases denoted by "min" in Table 3.8. For these the g/d values go to values as low as 2 (A_{min}).

Kama et al. (2015) infer a low value of $g/d \sim 55$ for the inner disc of HD 163296 via measuring abundances in both the disc and the stellar photosphere from absorption lines. This measurement agrees with the range of g/d that I obtain for the innermost 90 au. On the other hand, this range is significantly lower than the value reported by Williams and Best (2014) ($g/d = 170$). These quantities cannot be compared directly however because, as pointed out earlier, my results are derived specifically for the $R < 90$ au region, whereas the modelling by Williams and Best (2014) involves disc emission as a whole and therefore is affected by the assumptions made on the disc vertical structure at large scales inasmuch as this affects the amount of CO that is frozen out. One should also note that the very small contribution of such radii to the SED means that the temperature structure of the outer disc is poorly constrained observationally.

$C^{18}O$ abundance

To estimate the maximum gas mass, the lowest possible value of the abundance of $C^{18}O$ is adopted (as given in Equation 3.6). This corresponds to the lowest CO abundance measured in the ISM (Frerking et al., 1982), combined with the highest isotopic ratio of ^{16}O to ^{18}O of 587 (Wilson, 1999). This maximum H_2 mass sets an upper limit to the possible g/d in my models.

In Section 3.3.1, I discussed the direct degeneracy between $M_{\rm gas}$ and $\alpha_{\rm turb}$ in setting the vertical structure of the disc as constrained by the SED. One can see in Table 3.8 that for some of the models $\alpha_{\rm turb}$ could be decreased further, to be compensated with a proportional increase in $M_{\rm gas}$, (e.g. models $\text{(A-C)}_{\rm max}$) if one did not impose a limit on the $C^{18}O$ abundance as discussed above. If indeed the $C^{18}O$ abundance were a free parameter, models (A-C) would be compatible with an ISM-like g/d of 100. An assumption of the minimum value for the turbulent mixing strength $\alpha = 10^{-4}$ yields a $C^{18}O$ abundance as low as $\sim 2.6 \times 10^{-8}$ (in model series A, corresponding to $g/d \sim 100$). This is lower than the minimum value derived based on the observations of the ISM by a factor of ~ 5 . For models D and E, ISM-like g/d cannot be achieved as one is limited by the lower threshold of $\alpha_{\rm turb}$ as discussed above, and therefore the g/d in these models cannot reach higher values than ~ 10. One can conclude that $g/d = 100$ is possible if one is prepared to assume lower $C^{18}O$ abundances. However, this is only true for model series A-C which are the least plausible of my models because their $a_{\rm min}$ values of $0.5 - 0.8\,\mu$m are only marginally consistent with the result of Garufi et al. (2014), where the scattered light observations of HD 163296 imply that the disc surface is dominated by sub-micron-sized grains.

Thus far, direct comparison of the CO (and isotopologue) abundance to the H_2 density has only been possible for one, particularly old disc, TW Hya (Favre et al., 2013; Schwarz

et al., 2016). These works measure the abundance of CO and its isotopologues to be about 100 times lower than their ISM values. There are various mechanism discussed in the literature in order to explain this deviation from ISM-abundances.

One possibility to sequester carbon is the following: in the disc atmosphere the reaction $CO + He^+ \rightarrow C^+$ liberates carbon from CO; from reactions with H_2, electrons and C^0, hydrocarbons can then be produces, which might store some of the gas-phase C (Aikawa et al., 1999; Bergin et al., 2014; Furuya and Aikawa, 2014; Kama et al., 2016).

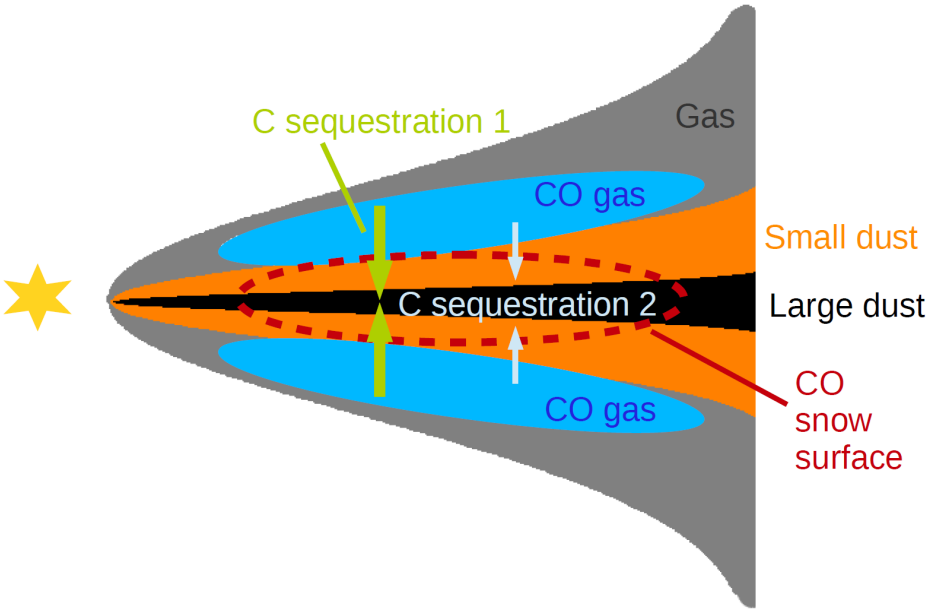

Figure 3.11 Diagram of carbon sequestration by freeze-out in a protoplanetary disc: the green arrows indicate the first possibility whereby CO mixes to within the snow surface and freezes out onto large grains in the disc midplane. The white arrows represent the second case whereby CO is frozen-out onto small grains for a short time. The grey area marks the gas structure, whereas in orange, the small dust (mostly coupled to the gas) is overplotted as well as the large (mostly settled) grains in black. The blue regions indicate where CO exists in the gas-phase, the red dotted line marks the CO snow surface.

Another process to lock a substantial amount of CO such that it is not in gas-phase CO is by freezing it out onto dust grains. One way this could take place is by gas mixing to disc regions within the snow surface where the CO will then freeze out as CO or H_2O ice onto the large midplane grains (see also Figure 1.16 for a diagram of the snow surface). This takes place over a long timescale as mixing processes might loft grains up again (Kama et al., 2016). This is indicated by the green arrows in Figure 3.11. On shorter timescales, a slightly different freeze-out process might take place, namely short-term freeze-out onto the small dust grains that are coupled to the gas. This is illustrated by the white arrows in Figure 3.11. In order to keep a substantial amount of C sequestered in this way, one has to ensure that these small grains grow and settle before they are mixed up to higher disc

regions above the snow surface where the CO would sublimate again (see e.g. Krijt et al., 2016; Du et al., 2015, 2017, where the latter focuses on water). Both of these processes might be very effective and models have produced two orders of magnitude of depletion of the CO abundance.

Especially the second mechanism described above locks CO in ices in the disc midplane regions. An additional method of UV processing these ices and creating further refractory ice species with higher sublimation temperatures is described in Reboussin et al. (2015). Through this mechanism, C atoms are generated through the photodissociation of CO by cosmic ray induced UV in the ices in the disc midplane. They are then effectively removed through the formation of species other than CO ices (e.g. CO_2 and CH_4). Note that photodissociation that is not caused by cosmic rays is normally localised in the disc surface. Thus the $C^{18}O$ abundance may be affected only if the CO dissociating photons were able to penetrate to the midplane, or if the surface continued to be depleted of CO over very long timescales.

The processes described here can thus lower the CO abundance and in turn would then allow again for higher (and thus more "normal" or ISM-like) g/d. Note however that the exact details of these processes are not yet fully understood.

Dust dynamics

The outer regions of the disc are known to be deficient in sub-mm grains (as deduced from the outer radius in the sub-mm continuum compared with that in CO; see also Guidi et al. 2016). Such concentration of sub-mm dust in the inner disc can be explained in terms of drag-mediated migration of solids. The midplane density and temperature profiles of the favoured models can be used to estimate the Stokes number (ratio of drag timescale to dynamical timescale) as a function of grain size (see also Equation 1.20). I obtain a Stokes number of close to unity (which corresponds to maximal radial migration) for mm-sized grains in the region of the CO snowline.

The majority of the models have g/d ratios that are considerably below the ISM ratio of 100. Indeed, it is only possible to approach this value if one assumes a very low fractional abundance of $C^{18}O$ *and* assumes a grain population that is highly depleted in submicron grains (this latter is required in order not to over-predict the infrared flux, given the relatively high temperatures obtained in the case of dust supported in gas-rich discs). However, Garufi et al. (2014) find from their studies of scattered light that there are submicron-sized particles present in the inner disc regions, thus the $a_{\rm min} = 0.8$ and $0.5\,\mu$m in models B_{max} and C_{max} are only marginally consistent with this requirement. One can conclude that the available data require significant deviation from primordial conditions,

either in terms of depletion of gas or else in terms of depletion of small grains.

Midplane gas-to-dust ratios

It is important to note that the g/d values I have presented so far are average values. Focusing on the ratio of the gas-to-dust density in the inner disc midplane now, I show a plot of their ratio in Figure 3.12.

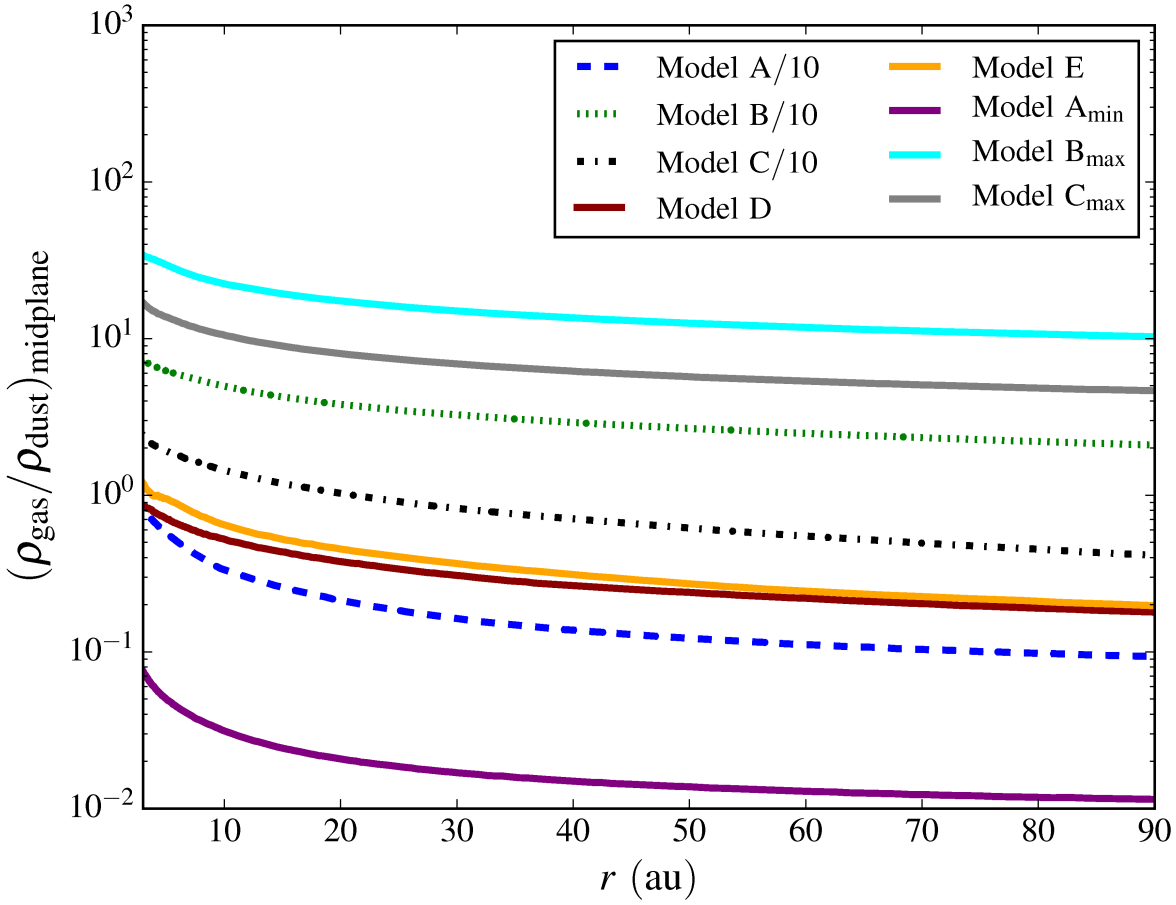

Figure 3.12 Gas-to-dust mass ratio in the disc midplane for models (A-C)/10, D, E, A_{min}, B_{max} and C_{max} in the inner disc regions ($R < 90$ au).

All the models show very low ratios of ρ_{gas}/ρ_{dust} in the midplane (between $\sim 0.01 - 20$) within a radius of 90 au. It is interesting to mention that model B/10, B_{max} and C_{max} have the highest ratio (around $\sim$ 10). Model A_{min} has a g/d of as low as $\sim$ 0.01, which is not surprising given that its average g/d ratio is $\sim$ 2 and thus the lowest possible in all the models. The fact that ρ_{gas}/ρ_{dust} in the midplane is lower than the average g/d as discussed above is a result of the dust settling in the models.

Viscosity

Using the mass of H_2 within a radius of 90 au (Table 3.7), one can calculate the viscosity parameter $\alpha_{\rm visc}$ of the inner disc regions. The mass accretion rate of HD 163296 is measured to be within the range $(0.8 - 4.5) \times 10^{-7}\,{\rm M}_\odot\,{\rm yr}^{-1}$ (Garcia Lopez et al., 2015). The dynamical timescale of my models at 90 au is

$$\tau_{\rm dyn}(90\,{\rm au}) = \frac{1}{\Omega_{\rm k}} \sim 100\,{\rm yr}\,. \tag{3.10}$$

From Equation 1.17 one can thus derive the viscosity parameter

$$\alpha_{\rm visc} = \left(\frac{H}{r}\right)^{-2} \frac{1}{\tau_{\rm visc}\Omega_{\rm k}} = \left(\frac{H}{r}\right)^{-2} \frac{\tau_{\rm dyn}}{\tau_{\rm visc}}\,. \tag{3.11}$$

The timescale of the flow can be obtained by (see Equation 1.18)

$$\tau_{\rm flow}(90\,{\rm au}) = \frac{M_{\rm gas}(90\,{\rm au})}{\dot{M}}\,, \tag{3.12}$$

which will thus vary depending on the masses of H_2 within 90 au as given in Table 3.7. The scale height of the models is $H/r \sim 0.1$. Equating $\tau_{\rm visc}$ and $\tau_{\rm flow}$, one obtains from Equation 3.11 a range of $\alpha_{\rm visc}$ of

$$0.2 \times \left(\frac{\dot{M}}{10^{-7}\,{\rm M}_\odot{\rm yr}^{-1}}\right) < \alpha_{\rm visc} < 0.7 \times \left(\frac{\dot{M}}{10^{-7}\,{\rm M}_\odot{\rm yr}^{-1}}\right)\,, \tag{3.13}$$

as given in detail for the respective models in Table 3.7. When considering the models with minimum and maximum $M_{\rm gas}$ (Table 3.8), the range of $\alpha_{\rm visc}$ is between 0.1 and 1.4. The values I obtain for $\alpha_{\rm visc}$ are much higher than those found in magneto-hydrodynamical simulations of the outer regions of discs in T Tauri stars (Simon et al., 2013b), suggesting that more efficient angular momentum transport (such as that linked to a large scale net magnetic field and associated wind; Simon et al. 2013a) may be required. Note also that the derived $\alpha_{\rm visc}$ values are around two orders of magnitude greater than the maximum values of $\alpha_{\rm turb}$ allowed by the modelling. This suggests that the efficient transport of angular momentum in this disc is not accompanied by the vigorous level of vertical motions that would be expected in the case of a turbulent viscosity model.

Gravitational instability

One can assess the gravitational stability of HD 163296 by evaluating the Toomre stability parameter

$$Q = \frac{c_s \Omega_k}{\pi \Sigma_{gas} G} < 1 \tag{3.14}$$

of the models, where c_s is the sound speed, Ω_k the Keplerian frequency and Σ_{gas} the disc surface density (Toomre, 1964). The rotational support (preventing large-scale collapse) is represented by the Ω_k, the pressure support (preventing collapse on small scales) by the sound speed. Both of these are counter acting the impact of gravity (represented by the denominator). Thus, self-gravity becomes important at a Q-value of close to unity, with the disc becoming gravitationally unstable for $Q < 1$. Therefore regions of massive or cold discs can more easily become susceptible to gravitational instability than hot and low-mass discs.

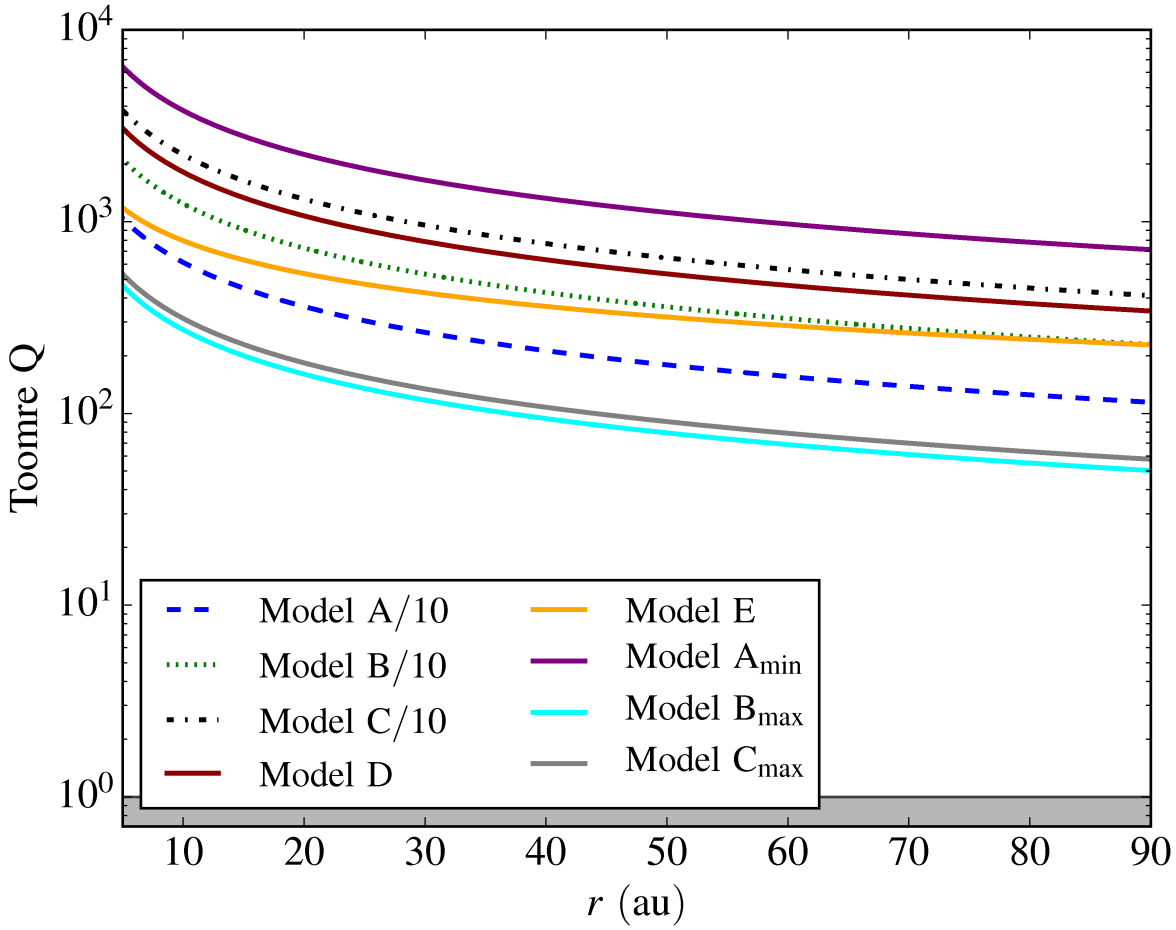

Figure 3.13 Range of Toomre Q parameter for models (A-C)/10, D, E, A_{min}, B_{max} and C_{max} which match the observed SED, the snowline radius and the $C^{18}O$ emission within 90 au. The region where $Q < 1$ (and where a disc is potentially gravitationally unstable) is shaded in grey. I find that none of my models reaches this critical regime and all are well above the threshold.

If regions of a disc become gravitationally unstable, this can lead to the formation of spiral arms or other disc features, influencing the transport of angular momentum in a disc. In general, assessing the stability of a disc is not a trivial task, however the modelling process presented here allows to determine the relevant parameters and thus to study the stability of the disc.

One can thus calculate the midplane Q parameter as a function of radius in all eight disc models (A-C)/10, D, E, A_{min}, B_{max} and C_{max}; the results are plotted in Figure 3.13. I find that all of my models are well above the threshold value of $Q = 1$. This implies that none of the models are close to being gravitationally unstable at radii < 90 au. However, I caution that this quantity cannot be assessed in the outer disc, given the sensitivity to the degree of freeze-out in these outer disc regions.

3.5 Conclusions

I combine SED fitting, the location of the CO snowline and spatially resolved $C^{18}O$ line emission to help resolve degeneracies in the determination of protoplanetary disc properties, using the example of HD 163296, of which I estimate the properties. The following main conclusions can be drawn from this work:

1. Any one of the aforementioned diagnostics is on its own insufficient to robustly determine the disc properties; however, I demonstrate that together they become much more powerful tools. SED and CO snowline fitting alone could result in a disc mass almost an order of magnitude higher than the mass obtained when constraints from $C^{18}O$ observations are included. Note however that the uncertainty remains as to what the abundance of $C^{18}O$ is exactly. This will have to be pinned down in future studies.

2. The observed $C^{18}O$ line flux, together with SED and CO snowline modelling, unambiguously indicates the mass of gas-phase $C^{18}O$ within the 90 au snowline radius, $M_{C^{18}O}(R < 90\,\text{au}) \approx (2-3) \times 10^{-8}\,M_\odot$. I obtain a total gas mass $M_{gas}(R < 90\,\text{au}) \approx (0.7-11) \times 10^{-3}\,M_\odot$ within the snowline radius, taking into account the uncertainties in the fractional abundance of $C^{18}O$.

3. This modelling approach is best suited for the inner disc regions within the snowline radius. The emission from the outer disc regions is crucially dependent on the vertical temperature structure and the location of the CO ice surface, so I do not aim to match these. From this, one can conclude that it is important to constrain the vertical temperature of the disc well through physically consistent SED models

for the inner disc (as I presented here) and combine these with, for example, high-resolution imaging of multiple CO isotopologues in the outer disc (see e.g. Qi et al., 2015).

4. For the range of $\alpha_{\rm turb}$ from $(0.1 - 6.3) \times 10^{-3}$, most of my models of HD 163296 imply gas-to-dust mass ratios in the range $g/d = 10 - 20$, significantly lower than the ISM value of 100. If one is prepared to also consider models with minimum dust grain sizes of ~ 0.5 μm that are not fully consistent with scattered light observations (Garufi et al., 2014) that also have very low (high) fractional abundance of $C^{18}O$, models with g/d as large as 80 (as small as 2) also match the observations. On top of this and only for these extreme models, $g/d = 100$ may be achieved if the CO abundance is anomalous due to e.g. C-sequestration.

5. I obtain a high $\alpha_{\rm visc} \sim 0.2 - 0.7$ for the models of the inner disc regions, or even up to values of $\alpha_{\rm visc} \sim 1.4$ (0.1), if one allows for $C^{18}O$ to be very over- (under-)abundant with respect to the ISM abundances. The notably high ratio of $\alpha_{\rm visc}$ to $\alpha_{\rm turb}$ provides evidence against a turbulent model for angular momentum transport in this disc.

6. From analysis of the temperature and density profiles obtained from the models, I find that the disc is not likely to be susceptible to gravitational instability.

The approach to interpretation outlined in this study will allow to maximise the value of existing and future high-quality observations with ALMA. This work stresses the importance of $C^{18}O$ observations especially for the warm Herbig Ae discs, which are the prime targets for the application of the methods outlined in this study.

4

The extremely truncated circumstellar disc of V410 X-ray 1: a precursor to TRAPPIST-1?

Protoplanetary discs around brown dwarfs and very low mass stars offer some of the best prospects for hosting Earth-sized planets in their habitable zones. The unprecedented sensitivity of ALMA now allows us to characterise these small and faint discs. To this end, I study the nature of the disc around the very low mass star V410 X-ray 1, whose SED is indicative of an optically thick and very truncated dust disc, with my modelling suggesting an outer radius of only 0.6 au. In this chapter, I investigate two scenarios that could lead to such a truncation, and find that the observed SED is compatible with both.

4.1 Introduction

As detailed in Chapter 1, there are two main categories explaining the formation of a BD or very low mass star (see e.g. Whitworth et al., 2007). In the first scenario, BDs form as a scaled-down version of solar mass star formation, whereas in the second one, these objects are mostly shaped by their formation surroundings.

Perhaps the most important observational discriminants are the radii of discs around BD and VLM stellar objects. Ejections resulting from dynamical encounters are expected to truncate circumstellar discs at a radius of around a third of the distance of closest approach (e.g. Hall et al., 1996; Breslau et al., 2014; Winter et al., 2018). Massive objects tend to remain within their natal gas reservoirs after encounters and can thus re-accrete disc material. Ejected objects (which are preferentially low mass) however bear the imprint of their last dynamical encounter in the form of a truncated disc. Given the stochastic nature of dynamical interactions, the range of closest approaches for BDs in dynamical simulations is very large (around three orders of magnitude); moreover, in the simulations of Bate (2009) around a half of all BDs have suffered encounters on a scale of a few au. It

is thus a prediction of dynamical star formation scenarios that BDs or VLM stars should have a much larger range of disc radii than higher mass stars, and that some population of extremely compact discs is to be expected. Companions can also leave an imprint on the disc size. It is expected that for a binary system the disc radius will be truncated at about $20-50$ per cent of the semi-major axis of the binary (Artymowicz and Lubow, 1994).

There is increasing interest in the planet formation potential of discs in the BD and VLM star regime. This is partly because of the growing realisation that lower mass host stars provide the best prospects for the detection of Earth-like planets in the habitable zone. Recent results have borne out this expectation, in particular the discovery of seven terrestrial planets within 0.06 au around the $0.08\,M_{\odot}$ star TRAPPIST-1 (Gillon et al., 2017). Such systems imply an extraordinary concentration of solid material at small orbital radii and raise a number of unanswered questions about the evolutionary scenario that produced them. In particular, it is of obvious interest to ask what would be the distribution of dust and gas in such a system at an age of a few million years?

To date, a number of studies have identified and characterised the population of young BDs and VLM objects which have large discs (>70 au; Ricci et al. 2013, 2014). The large discs have been imaged with ALMA and the Combined Array for Research in Millimeter-wave Astronomy (CARMA), and have broadband SEDs which are consistent with extended circumstellar discs (Alves de Oliveira et al., 2013). Additionally, their infrared colours in the $2-12\,\mu$m and $12-70\,\mu$m range lie in the domain of Classical T Tauri stars (Rodgers-Lee et al., 2014). van der Plas et al. (2016) surveyed 8 brown dwarf discs in Upper Scorpius and Ophiuchus with ALMA, which, being unresolved in these observations, limits the discs to being $R \lesssim 40$ au. Recently, Testi et al. (2016) discovered discs around BDs in the ρ Oph star-forming region with ALMA that have sharp outer edges at radii of 25 au.

However, there seems to be a population of even smaller discs: Bulger et al. (2014) present SEDs of a large sample of low mass members of Taurus, and mention the possibility of a 'truncated disc' population, based on a steeply declining SED from $\sim 20\,\mu$m, appearing to follow the Rayleigh-Jeans limit. Hints for small discs around VLM Objects and BDs have also been found by Hendler et al. (2017) using $63\,\mu$m continuum and [O I] observations from the PACS spectrometer in the Taurus and Chamaeleon I regions. Assuming disc geometry and dust properties based on T Tauri stars, they obtain from their SED modelling discs with radii between $\sim 1-80$ au. However they stress that further (spatially resolved) ALMA observations are needed to confirm this.

Recent studies have attempted to determine the amount and properties of dust in discs around BDs or VLM stars. These can give important hints as to the evolution of the discs, but also the propensity for the discs to form planets. Ward-Duong et al. (2018) modelled 24 BD/VLM objects in Taurus, finding a range of dust masses between $0.3-20\,M_{\oplus}$ and an

approximately linear relationship between the stellar mass and dust mass in these discs. BD discs are expected to have a smaller population of mm-size grains in comparison to discs around higher mass T Tauri stars because the radial drift velocities of these grains are higher. However, Pinilla et al. (2017) have examined the 3 mm continuum fluxes of three BD discs in the Taurus star forming region with the IRAM/Plateau de Bure Interferometer combined with previous studies of the 0.89 mm fluxes obtained with ALMA. They find that from millimetre spectral indices, large grains actually seem to be present in these discs.

Greenwood et al. (2017) have recently performed thermochemical modelling of BD discs, including predictions for future ALMA observations of molecular tracers such as CO, HCN and HCO^+. Their models suggest that BD discs are similar to T Tauri discs and that similar (thermochemical) diagnostics can be used. Interestingly, Bayo et al. (2017) find from recent ALMA Band 6 continuum observations of the disc around the even lower-mass object OTS44 ($M \sim 6 - 17\,M_{jup}$) that it also possesses a disc and even falls onto a power law relation between stellar mass and dust disc mass.

Two broad explanations for truncated discs exist. Firstly, a dramatic segregation of dust and gas may occur due to the radial migration of millimetre-sized dust within what could be termed a 'normal' sized gas disc. Indeed, simulations of dust particles in BD discs have shown that migration can be more significant than in T Tauri discs (Pinilla et al., 2013). Secondly, the small radial extent may be shared by both the dust and the gas in the disc. Such a scenario would imply a dynamical origin for the small radial extent. In order to determine which of these scenarios may be causing the observed population of truncated BD discs, it is crucial to examine both the dust and gas components of the discs.

In this chapter, I present observations and detailed modelling of a candidate VLM star possessing a very truncated disc – V410 X-ray 1. I describe the observational data that go into the modelling in Section 4.2 and present the thermochemical modelling with DALI in Section 4.3. The results of the modelling are then given in Section 4.4, where two possible explanations for the truncation of the dust disc of V410 X-ray 1are discussed. In Section 4.5, I summarise the findings and present the main conclusions of this work.

4.2 Observations

V410 X-ray 1 is a very low mass star located within the Taurus star forming region L1495 at a distance of $D \sim 140$ pc, lying at co-ordinates RA$= 04^h17^m49\overset{s}{.}655$, Dec.$= +28°29'36\overset{''}{.}27$ (J2000). It has a spectral type determined to be M4 (Andrews et al., 2013) or M2.6 (Herczeg and Hillenbrand, 2014). In order to compile an SED of V410 X-ray 1, I draw on photometric measurements from the literature from multiple instruments spanning a range of wave-

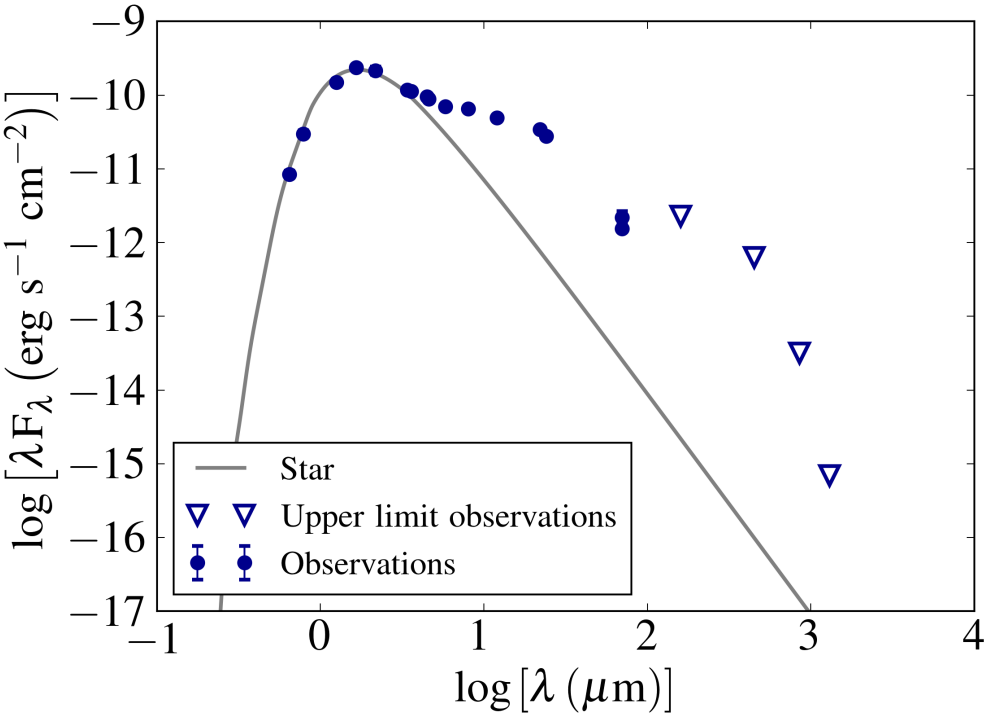

Figure 4.1 SED of V410 X-ray 1. The fluxes and corresponding references are listed in Table 4.1. Upper limits are given by triangles. The limit derived on the continuum flux from ALMA observations is given by the blue triangle at $\lambda = 1.3$ mm. The error bars are shown, but are of the order of the size of the data points.

lengths from the optical to the sub-millimetre. The wavelengths, fluxes and appropriate references for these data are given in Table 4.1.

In addition to the published fluxes, there are also archival ALMA observations of V410 X-ray 1 (Simon et al., 2017). The observations were taken on 2015-09-19 in Band 6 (230 GHz, 1.3 mm) and the on-time source was 6 minutes. The data were pipeline reduced, giving a synthesised beam of $0.26\,\mathrm{arcsec} \times 0.21\,\mathrm{arcsec}$ (or 36 au $\times$ 29 au at a distance of 140 pc). In addition to the continuum, the observations also covered the ^{12}CO $J = 2 - 1$ transition with a velocity resolution of 0.2 km s^{-1}. Both the continuum and line observations with ALMA resulted in a non-detection. Based on these non-detections, one can calculate a 3σ upper limit for the continuum flux at 1.3 mm to be 0.3 mJy. This can be done by using the CASA viewer, selecting an area of the continuum map and reading off the rms values given there. In general, these would be in units of Jy/beam, however given that the observations are not resolved, the 1/beam can be omitted. In order to give a 3σ upper limit, this value has to be multiplied by a factor of 3, which then gives the 0.3 mJy upper flux limit at 1.3 mm. In order to calculate the upper limit of the ^{12}CO $J = 2 - 1$ line flux, I choose six areas of varying size and compute the flux in every velocity bin of width $\Delta v = 0.2$ km s^{-1}.

Table 4.1 Wavelengths (λ) and associated flux densities (F) used for compilation of the SED of V410 X-ray 1.

λ (μm)	F (mJy)	Band	Reference
0.65	1.8	Rc	Bulger et al. (2014)
0.79	7.8	Ic	Bulger et al. (2014)
1.25	62	2MASS J	Cutri et al. (2003)
1.65	131	2MASS H	Cutri et al. (2003)
2.17	155	2MASS Ks	Cutri et al. (2003)
3.4	133	WISE W1	Wright et al. (2010)
3.6	136	IRAC 3.6	Luhman et al. (2010)
4.5	143	IRAC 4.5	Luhman et al. (2010)
4.6	136	WISE W2	Wright et al. (2010)
5.8	136	IRAC 5.8	Luhman et al. (2010)
8.0	175	IRAC 8.0	Luhman et al. (2010)
12	196	WISE W3	Wright et al. (2010)
22	253	WISE W4	Wright et al. (2010)
24	221	MIPS 24	Rebull et al. (2010)
70	36	PACS 70	Rebull et al. (2010)
70	51	MIPS 70	Rebull et al. (2010)
160	$<$122	PACS 160	Rebull et al. (2010)
450	$<$94	SCUBA-2	Mohanty et al. (2013)
850	$<$9	SCUBA-2	Mohanty et al. (2013)
1300	$<$0.3	ALMA B6	This work

To obtain the flux limit, one can calculate the following:

$$F_{\rm CO} = \Delta v \sqrt{N} \sigma_{\rm F} \,, \tag{4.1}$$

where N is the number of velocity channels and $\sigma_{\rm F}$ the standard deviation of the flux (the calculation is done for each of the six areas and then the result is averaged). I base the calculation on the assumption of a total line width of $10\,{\rm km\,s^{-1}}$, appropriate for the conditions expected in this disc. This velocity corresponds roughly to a radius of a few au around a $0.1\,{\rm M_\odot}$ star. The line width is set by the inner radius of the CO emission, which is usually much further out than the inner disc radius (0.04 au in this case). The modelling of the CO emission as presented later in this chapter does indeed confirm that the inner radius of the CO emission is further out, such that a line width of $10\,{\rm km\,s^{-1}}$ should be wide enough to comprise the entire emission. Note that even if this estimate is slightly wrong, it only enters the calculation of the flux with a square root dependence. This thus gives a number of $N = 10\,{\rm km\,s^{-1}}/0.2\,{\rm km\,s^{-1}} = 50$ velocity channels. One therefore obtains an upper limit for the ^{12}CO $J = 2-1$ line flux of $0.4\,{\rm Jy\,km\,s^{-1}}$. I include the 1.3 mm upper limit in Table 4.1 and Figure 4.1, and use the ^{12}CO $J = 2-1$ upper limit in the analysis inSection 4.4.

4.3 Methods

In this chapter, I explore various scenarios for the circumstellar environment of V410 X-ray 1 that are consistent with the SED shown in Figure 4.1 and with the upper limits on the ^{12}CO $J = 2-1$ flux.

To this end I use the radiation thermo-chemical disc code DALI (Dust And LInes, Bruderer et al. 2012; Bruderer 2013) with adaptations as detailed below to model the gas and dust emission in V410 X-ray 1. DALI solves the continuum radiative transfer equations to obtain the dust temperature, and the thermal balance and chemical abundances to compute the gas temperature structure (see Section 2.7.3 for more details). The ray tracing module is then used to compute both an SED and CO fluxes that can be compared against the observations.

As described in Section 2.7.3, in DALI gas and dust distributions that are not necessarily co-spatial can be taken into account. I use two dust grain populations with small grains being coupled to the gas distribution and large grains that are settled with respect to the gas. For the study described in Section 4.4.1, size ranges of $5\,\mathrm{nm}-10\,\mu\mathrm{m}$ and $10\,\mu\mathrm{m}-0.3\,\mathrm{mm}$ are used for small and large grains, respectively. Following the description in Section 1.2.4, the corresponding fraction of large grains can be calculated using Equation 1.24. Using the values for the maximum grain sizes of the large and small population given above and a size distribution parameter of $q = 3$ gives a fraction of large grains of $f = \frac{30}{30+1} = 0.968$ (see Equation 1.24). For a total surface density of dust $\Sigma_{\mathrm{tot}} = \Sigma_{\mathrm{large}} + \Sigma_{\mathrm{small}}$ one therefore obtains a mass ratio of large to small grains of

$$\frac{\Sigma_{\mathrm{large}}}{\Sigma_{\mathrm{small}}} = \frac{f\Sigma_{\mathrm{tot}}}{(1-f)\Sigma_{\mathrm{tot}}} = \frac{f}{1-f}\,, \tag{4.2}$$

which gives a value of 30.25 for the case discussed here.

The parameter choices for a model with spatially variable maximum grain size are discussed in Section 4.4.2. The large grains are settled with respect to the gas such that their scaleheight is reduced to $0.2h_{\mathrm{gas}}$. The dust opacities are taken from the opacity library used by Facchini et al. (2017a,b). More specifically, opacities are computed from Mie theory using the `miex` code (Wolf and Voshchinnikov, 2004). Optical constants are taken from Draine (2003) for graphite and Weingartner and Draine (2001) for silicates.

I have adapted the code such that the gas is in vertical hydrostatic equilibrium, which in turn therefore also influences the vertical distribution of the dust. In the radial direction,

the gas surface density profile is set up as follows:

$$\Sigma_{\rm gas} = \Sigma_{\rm c} \left(\frac{r}{R_{\rm c}}\right)^{-\gamma} \exp\left[-\left(\frac{r}{R_{\rm c}}\right)^{2-\gamma}\right], \tag{4.3}$$

where $\gamma = 0.8$ is used. When referring to the gas radius of the models I adopt $R_{\rm gas} \approx 3R_{\rm c}$, since this bounds the region from which typically more than 90 per cent of the emission arises.

In order to obtain vertical hydrostatic equilibrium in the gas, the following steps are performed:

1. For the model in step 1, the scale height as a function of r is guessed and prescribed with the DALI parameters for the flaring angle $h = h_{\rm c}(r/R_{\rm c})^{\psi}$, where ψ and $h_{\rm c}$ are chosen such that the model SED roughly matches the observed SED. I then calculate the corresponding density distribution $\rho_1(r,z)$ assuming the surface density distribution given in Equation 4.3 and a Gaussian density dependence on z with the prescribed scale height $h(r)$ (see Equation 1.7). DALI is then run to obtain the initial thermal equilibrium temperature distribution $T_1(r,z)$. The density and temperature structure of this step are plotted for one example disc in Figure 4.2.

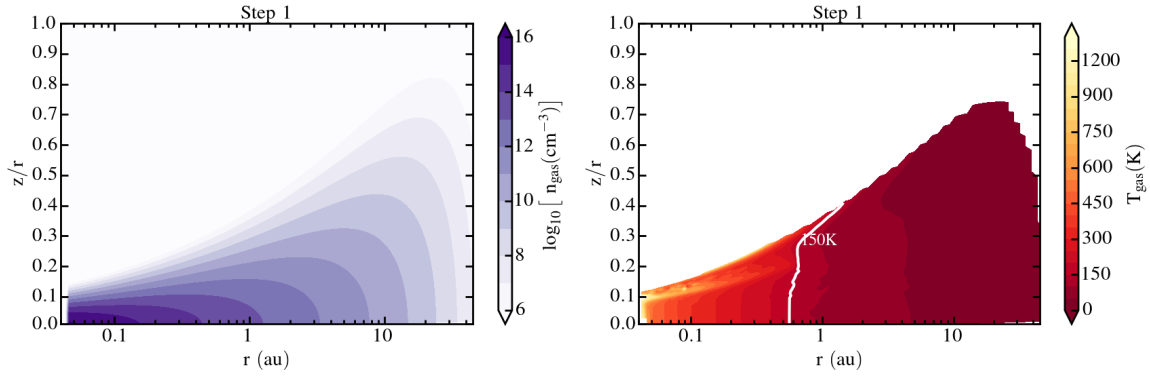

Figure 4.2 Gas density (left) and temperature (right) structure of the model after step 1.

2. The density distribution is then recalculated $(\rho_2(r,z))$ as a local Gaussian with its scale height now given by that predicted in hydrostatic equilibrium ($H = c_{\rm s}/\Omega_{\rm k}$, see Section 1.2) if the disc was vertically isothermal with $T(r) = T_1(r, z = 0)$. DALI is then run to obtain the thermal equilibrium temperature distribution, $T_2(r,z)$, with the new density profile $\rho_2(r,z)$. Both of these are plotted in Figure 4.3 for the same example as in Figure 4.2.

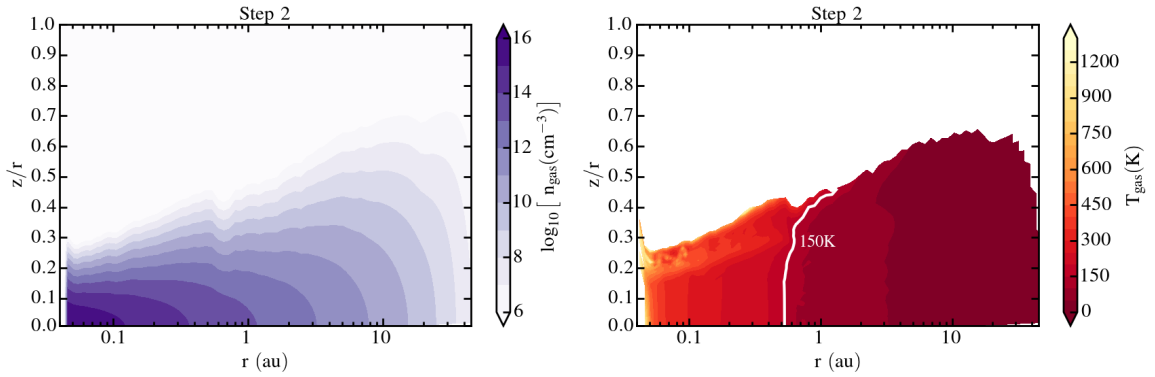

Figure 4.3 Gas density (left) and temperature (right) structure of the model after step 2.

3. In the final step, the density distribution is recalculated ($\rho_3(r,z)$) as the density profile that is in vertical hydrostatic equilibrium given $T_2(r,z)$, basically solving Equation 1.6. Note that this density distribution is no longer necessarily Gaussian because the disc is no longer assumed to be vertically isothermal. DALI is then run a third time to obtain the thermal equilibrium temperature distribution $T_3(r,z)$ corresponding to $\rho_3(r,z)$. The plot of the temperature and density map is given in Figure 4.4.

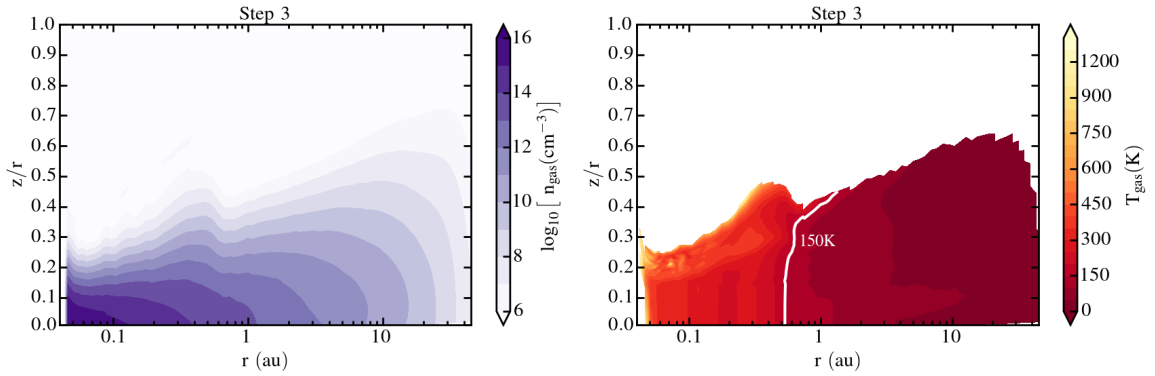

Figure 4.4 Gas density (left) and temperature (right) structure of the model after step 3. This model is in vertical hydrostatic equilibrium.

As a consistency check, $\rho_3(r,z)$ is compared with $\rho_4(r,z)$, which is the density profile that is in hydrostatic equilibrium given $T_3(r,z)$. It is found that the differences between $\rho_3(r,z)$ and $\rho_4(r,z)$ are negligible (except at extremely low densities), and thus the final density and temperature profiles are in both thermal and hydrostatic equilibrium. This is shown for one example radius $r = 23$ au in Figure 4.5. The black line is $\rho_3(r = 23\,\text{au}, z)$, which is the vertical density after step 3 and the red curve is the density profile $\rho_4(r = 23\,\text{au}, z)$ calculated for a model in hydrostatic equilibrium given $T_3(r = 23\,\text{au}, z)$.

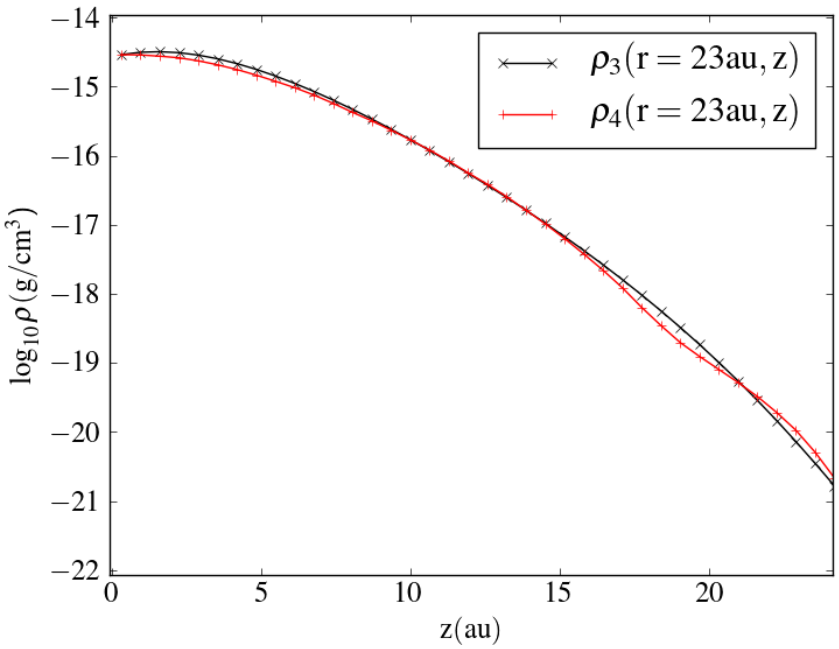

Figure 4.5 Comparison of $\rho_3(z)$ (density structure used by DALI in step 3, *black*) and $\rho_4(z)$ (density structure for a disc in hydrostatic equilibrium given $T_3(z)$, *red*). The above density structure is for a radius of 23 au, but similar trends are seen for all disc radii.

I only present the vertical density at one example radius here, but the same holds true for all other radial bins. This shows that the model is indeed converged. Observational diagnostics are derived from the models with $T_3(r,z)$ and $\rho_3(r,z)$, which are consistently reddened for comparison with the real observations assuming $A_v = 3.8$ and $R_v = 3.1$. The process of obtaining a model in vertical hydrostatic equilibrium is summarised in the schematic illustration in Figure 4.6.

The stellar parameters are kept fixed and are given in Table 4.2. I have slightly adapted the stellar parameters given by Bulger et al. (2014) in order to provide a better match to the stellar part of the SED. They are compatible with the values quoted in Andrews et al. (2013). As the inclination of the disc is unknown, I use an inclination of $i = 45°$ for my fiducial model. However, note that the choice of inclination does not affect the results except for highly inclined discs. This can be seen in Figure 4.7, where the SED of the same model, but with a range of inclinations is plotted. In the edge-on case ($i = 90°$), the IR to mm fluxes are lowest as the emitting area as seen by the observer is smallest. In contrast the fluxes in this wavelengths regime are highest for the face-on case $i = 0°$. However in the NIR the fluxes of the models with $i = 30-60°$ are higher than those of the face-on case, which can be explained by the fact that in these cases more of the inner disc rim (which is directly illuminated by the star, therefore very hot and dominating this wavelength regime) is visible due to the inclination.

Table 4.2 Parameters adopted for both the central star and those that are kept constant during the disc modelling procedure.

Stellar properties		**Disc parameters**	
M_* ($M_\odot$)	$0.1^\dagger$	$R_{\rm dust,1}$ (au)	0.6
L_* ($L_\odot$)	0.4	Inclination i (°)	45
$T_{\rm eff}$ (K)	3000	Inner disc radius $R_{\rm in}$ (au)	0.04
R_* ($R_\odot$)	2.3		
A_V (mag)	3.8		

†: based on D'Antona and Mazzitelli (1997); Andrews et al. (2013)

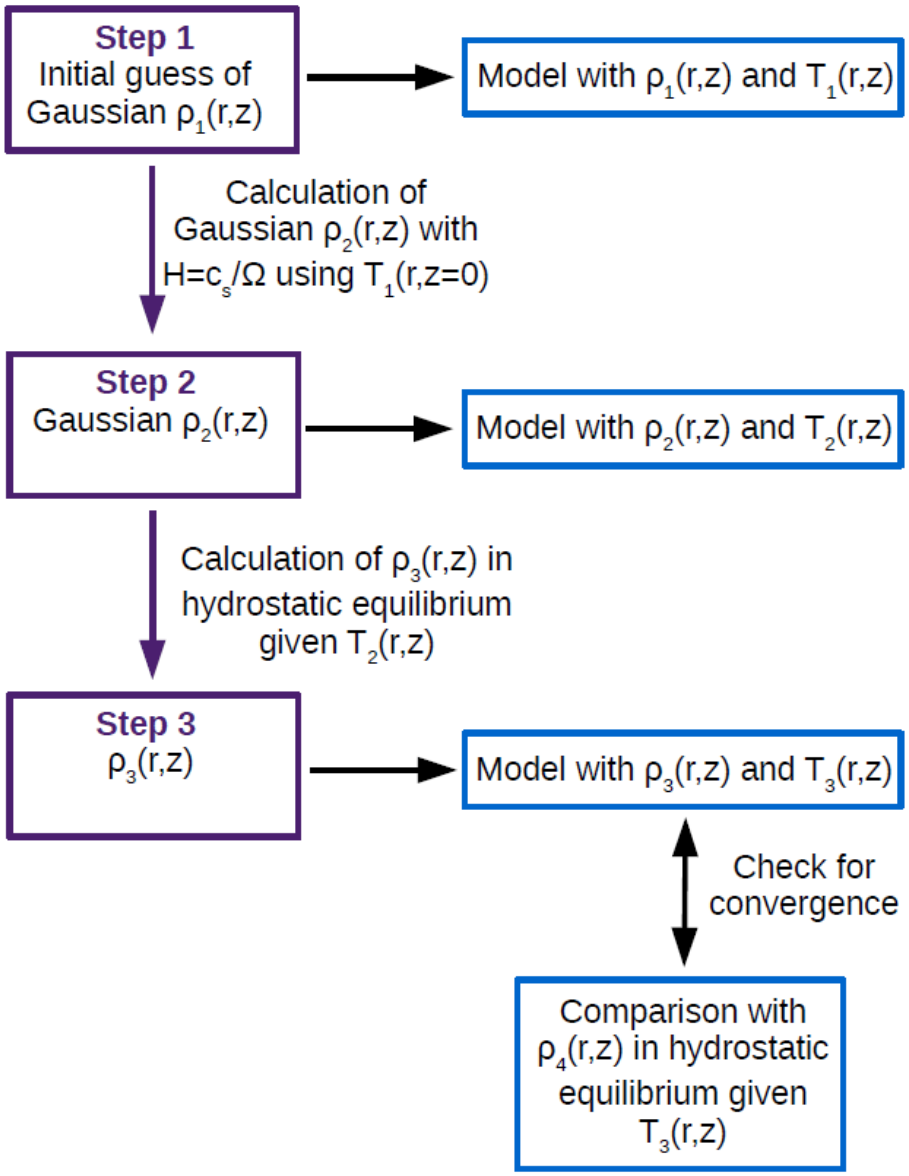

Figure 4.6 Schematic depiction of the steps and assumptions used in order to obtain a model in vertical hydrostatic equilibrium.

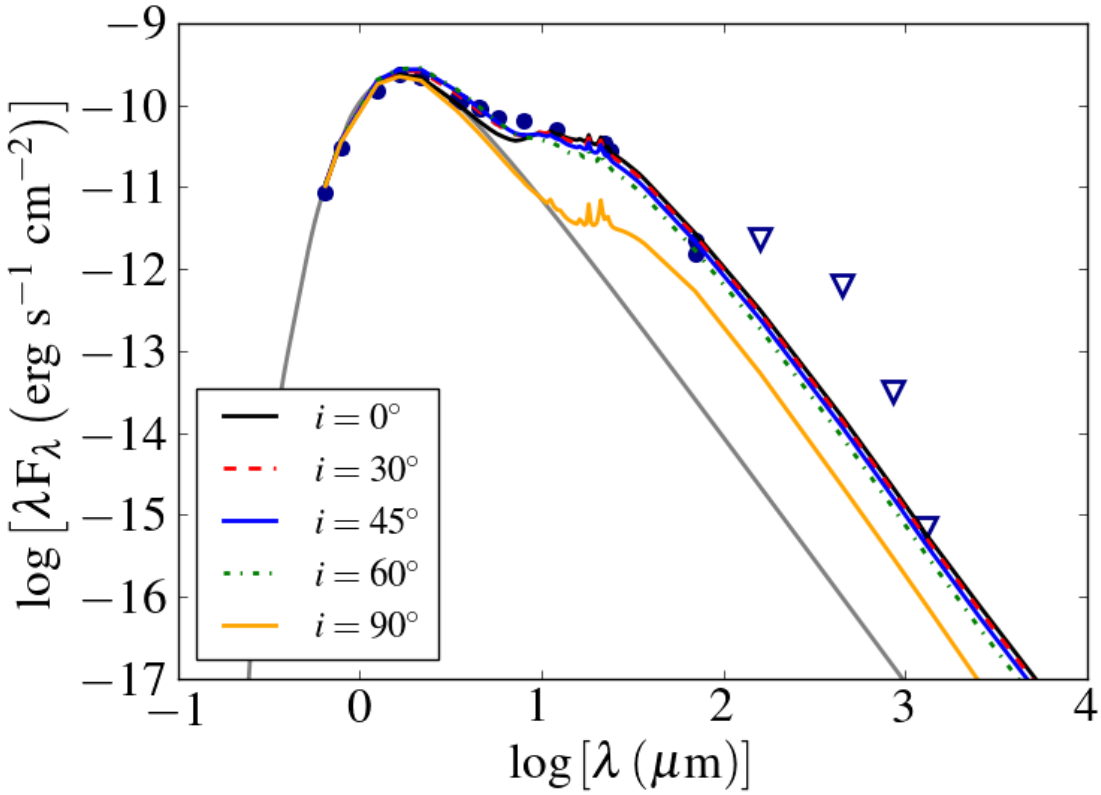

Figure 4.7 SED of the same disc model, but with a range of inclinations from $i = 0°$ (face-on) to $i = 90°$ (edge-on).

The accretion luminosity of V410 X-ray 1 is unknown, and as such it is not possible to assign a mass accretion rate in the models. However, I have verified that accretion rates as high as $\dot{M} \approx 10^{-8}\,\mathrm{M}_\odot\ \mathrm{yr}^{-1}$ have no discernible effect on the appearance of the SED[1], and values above this would lie far outside the measured accretion rates for such low mass objects (see, e.g., Herczeg et al., 2009). Manara et al. (2015) even find that typical accretion rates of BDs in young star forming regions are of the order $< 10^{-9.5}\mathrm{M}_\odot\ \mathrm{yr}^{-1}$. I use an X-ray luminosity of $L_\mathrm{x} = 10^{28}\,\mathrm{erg\ s}^{-1}$ based on Strom and Strom (1994). The inner radius of the disc (in gas and dust) is set to $R_\mathrm{in} = 0.04\,\mathrm{au}$, based on a calculation of the dust sublimation radius around a star with the parameters given in Table 4.2 and assuming a dust sublimation temperature $T_\mathrm{subl} \sim 1500\,\mathrm{K}$ (Wood et al., 2002; Monnier and Millan-Gabet, 2002).

[1] In this extreme case the CO fluxes can become slightly higher (by a factor of ~ 2) for large discs. However, for more realistic lower accretion rates the difference will then be much lower.

4.4 Results and discussion

4.4.1 Constraining the radial extent of the dust via SED fitting

The dust disc radius is well constrained by the SED morphology in the Herschel bands. The slope of -3 in the $\lambda F_\lambda, \lambda$ plane between 24 and $70\,\mu$m suggests that the SED is here dominated by the Rayleigh-Jeans tail of the coolest disc material, while the location of the spectral steepening (between 10 and 24μm) implies that this corresponds to dust at around 150 K (see Equation 1.31). This is suggestive of the spectrum expected from a truncated optically thick disc, consistent with the designation of V410 X-ray 1 as a member of the 'truncated disc' class identified by Bulger et al. (2014). Further constraints on the properties of the dust and gas require dedicated modelling, which I perform here.

I have explored the range of dust properties that are compatible with Figure 4.1 and find that, in line with the simple argument above, the SED is best reproduced by models that are optically thick out to a radius where the effective temperature is ~ 140 K (consistent with the onset of the Rayleigh-Jeans tail at $24\,\mu$m) and devoid of dust at larger radii. Naturally, one cannot rule out small quantities of optically thin dust beyond this truncation radius (just how much dust can be accommodated at larger radius in the context of a specific physical model is quantified in Section 4.4.2). Nevertheless, trace dust at large radii is not *required* to reproduce the SED.

The stringent requirement is instead that the spectrum follows the Rayleigh-Jeans slope at wavelengths beyond 24μm. In practice, given the luminosity of the star, the radiative transfer modelling implies that the outer radius is at $R_{\rm dust,\,1} \sim 0.6$ au – Figure 4.8 demonstrates the effect of three different truncation radii for discs that are optically thick everywhere at $70\,\mu$m. Despite the non-detection of the flux at 1.3 mm the radius determined from the SED is remarkably well constrained due to the relatively high sensitivity of the ALMA observations. The two measurements of the 70 μm flux from PACS and MIPS along with the uncertainty on the disc inclination lead to a relatively modest uncertainty in the radius of approximately 10 per cent. Clearly, larger (or smaller) truncation radii cause the $70\,\mu$m flux to be over- (or under-) predicted. I will henceforth describe this model as the 'truncation' scenario.

Constraints on the required dust *mass* are instead weak and imply only a total dust mass of $M_{\rm dust} \gtrsim 0.01\,{\rm M}_\oplus$ in order for the disc to be optically thick at $70\,\mu$m. However, for models with dust masses significantly below $\sim 0.7\,{\rm M}_\oplus$, the fluxes in the NIR become too low in comparison with the observations. For a disc truncated at 0.6 au, the disc is optically thick out to 1.3 mm for a disc dust mass in excess of $\sim 1\,{\rm M}_\oplus$, and thus models with dust

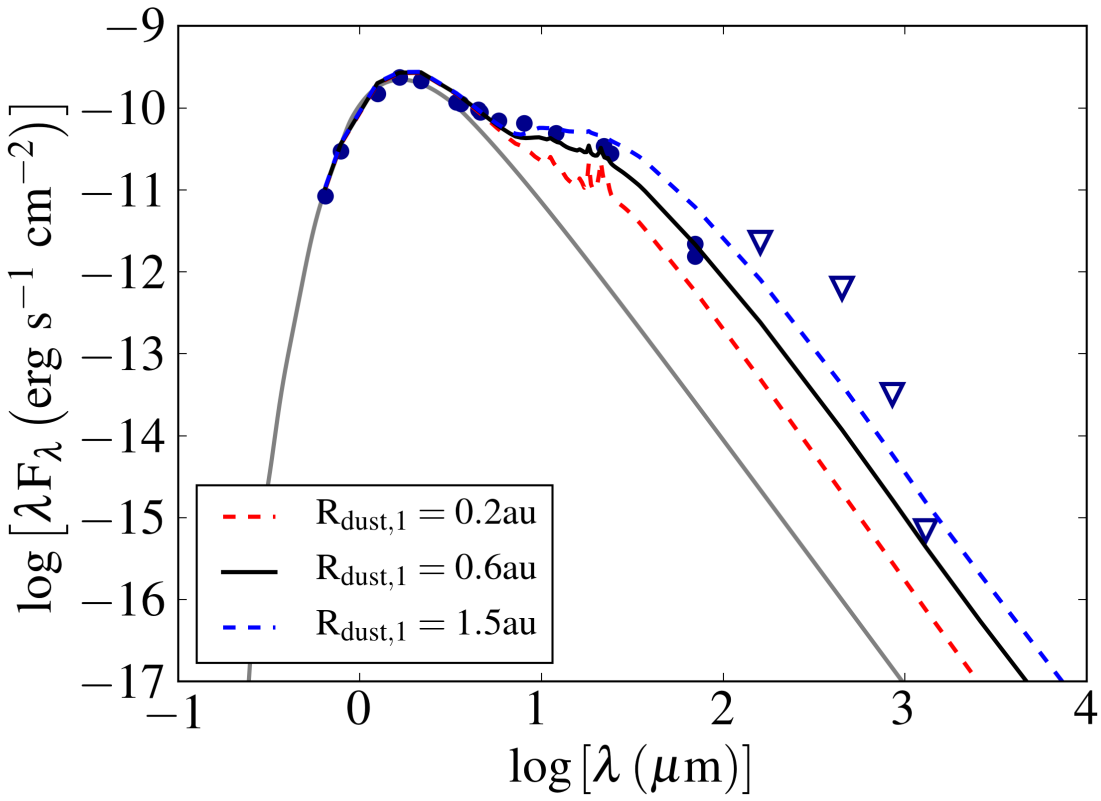

Figure 4.8 SEDs of models with various $R_{\mathrm{dust,1}}$. The model with $\mathrm{R_{dust,1}} = 0.6$ au corresponds to the 'truncation' scenario. The observational data are identical to those presented in Figure 4.1.

mass higher than this limit will share the SED shown in black in Figure 4.8 (whose flux at 1.3 mm is slightly below the 3σ upper limit provided by ALMA). This implies that dust masses higher than $\sim 1\,\mathrm{M_\oplus}$ can be present within the innermost 0.6 au.

Such a large budget of raw planet-forming material contained within such a relatively small radius suggests that V410 X-ray 1 may be a precursor of one of the many systems of tightly packed inner planets (STIPs) that have recently been discovered (see, e.g., Lissauer et al., 2011; Fabrycky et al., 2014). Perhaps the most well known example of a compact system of planets is TRAPPIST-1, which contains at least seven Earth-sized planets within 0.06 au of the central star (Gillon et al., 2017). The combined mass of the planets discovered so far in TRAPPIST-1 (what might be termed a 'minimum mass TRAPPIST-1 nebula') is $5.28\,\mathrm{M_\oplus}$. My analysis of the SED cannot rule out the presence of a comparable amount of dust within the inner disc of V410 X-ray 1, suggesting that it may in fact be a precursor to a similarly compact system of terrestrial planets.

4.4.2 The origin of the truncated disc: truncation or dust migration?

Having shown that the observed SED is consistent with an optically thick dust disc with radius 0.6 au, I enquire into possible origins for such a configuration. One possibility is that the disc has been truncated by a dynamical encounter or due to the presence of a companion (see bottom panel of Figure 4.9). A truncation radius of 0.6 au would imply an encounter within a few au which would be extremely unlikely only considering encounters within the star forming environment, even in the densest star forming regions, let alone the rather sparse environment in which V410 X-ray 1 is situated. A dynamical origin for this compact disc would instead need to invoke interactions occurring between bound companions in a multiple system. Stamatellos and Whitworth (2009) found that this mechanism could account for a wide range of disc radii: very small discs, as in V410 X-ray 1 would not however have been resolved in their simulations and would have been recorded as disc-less outcomes.

In the following subsection, I explore whether the steep decline in the SED can also be described in terms of dust radial drift (see top panel of Figure 4.9). In particular, note that the temperature at the outer edge of the inner dust disc is suggestively close to that at the water snowline ($T \sim 150$ K) and I therefore explore whether the observed spectrum is consistent with a discontinuous change in grain properties associated with this snowline.

Outside of the snowline, water is frozen out into ice mantles on the grains. Therefore, grains do not fragment there as easily and can grow to large sizes (Gundlach and Blum, 2015). This in turn means that their dynamics progressively decouple from the influence of the gas and the grains thus drift inwards radially. Once they reach the water snowline, the ice mantles are sublimated; this leaves the grains prone to fragmentation, which decreases their sizes. This decrease in grain sizes causes the grains' dynamics to be more closely coupled to the gas which slows their radial drift. Consequently the surface density of dust should *rise* interior to the water snowline. This process is depicted schematically in the top panel of Figure 4.10 (see also Banzatti et al., 2015). Ormel et al. (2017) discuss this mechanism as a way of concentrating dust and making the TRAPPIST-1 system. I will henceforth refer to this model as the 'migration' scenario.

In the following, I will study the process described quantitatively above more qualitatively. Note also that the basics of dust physics were introduced in Section 1.2.4. The key property that changes across the snowline is $v_{\rm frag}$, the maximum collision velocity of grains for which coagulation, rather than fragmentation, is to be expected. Following Blum and Wurm (2000); Gundlach and Blum (2015), $v_{\rm frag}$ is reduced by an order of magnitude interior to the snowline. If grain growth is limited by fragmentation, the local value of $v_{\rm frag}$ is linked to the maximum expected grain size through equating the relative collision veloc-

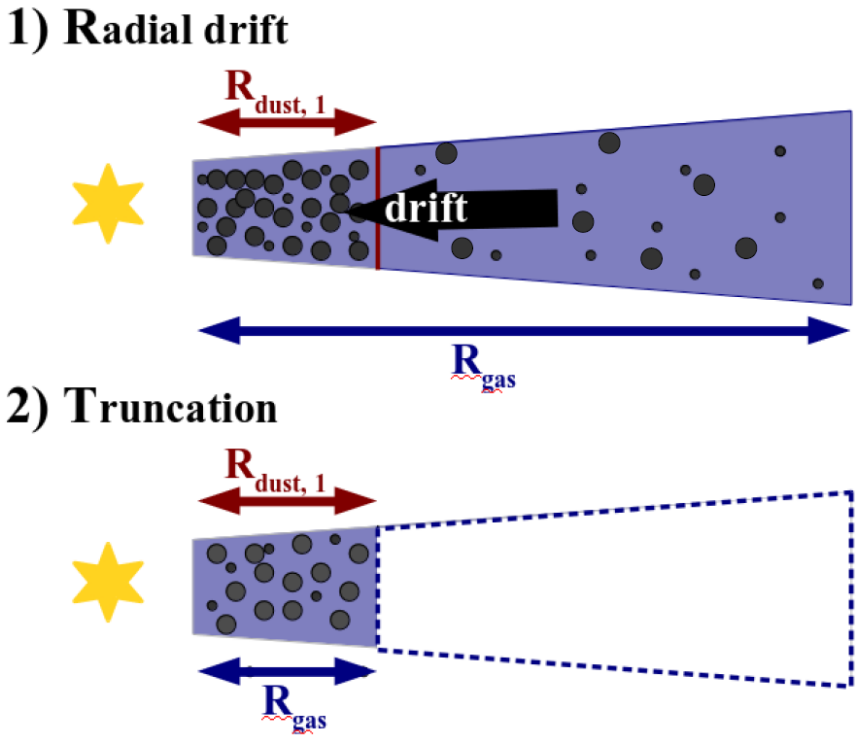

Figure 4.9 Schematic illustration of the two scenarios considered here. *Top:* Radial drift and dust migration, leading to a small optically thick inner dust disc and a more extended optically thin disc with large grains in the outer regions, as well as an extended gas disc. *Bottom:* Truncated dust and gas disc.

ity Δv for the largest grains at any location with $v_{\rm frag}$. Δv for grains that are coupled to a turbulent flow via drag forces is given by (Voelk et al., 1980; Ormel and Cuzzi, 2007):

$$\Delta v \approx \sqrt{\alpha\,{\rm St}}\,c_{\rm s}\,, \tag{4.4}$$

where α is the Shakura-Sunyaev viscosity parameter (Shakura and Sunyaev, 1973), $c_{\rm s}$ the sound speed and St is the local Stokes number (ratio of drag time to dynamical time) for the largest grains. In the Epstein drag regime, the midplane St for grains of size $a_{\rm max}$ is given by (see Equation 1.20)

$$a_{\rm max} = \frac{2\,\Sigma_{\rm gas}\,{\rm St}}{\pi\rho_{\rm grain}}\,, \tag{4.5}$$

where I have assumed a Gaussian vertical structure (see Equation 1.7). When growth is limited by fragmentation, the size of the largest grains (radius $a_{\rm max}$) is set by $\Delta v \approx v_{\rm frag}$. Combining Equations 4.4 and 4.5 then yields

$$a_{\rm max} \propto v_{\rm frag}^2\,. \tag{4.6}$$

This change in maximum grain size also affects the radial drift of the largest grains (which

for typical expected grain size distributions dominate the local dust mass budget; see Equations 1.23 and 1.25). Since the rate of radial drift for particles with St<1 scales as St, one also expects

$$v_{\rm drift} \propto v_{\rm frag}^2 \,. \tag{4.7}$$

Continuity then implies that the local dust surface densities at an interface where $v_{\rm frag}$ changes steeply scales as

$$\Sigma_{\rm dust} \propto v_{\rm frag}^{-2} \tag{4.8}$$

on each side of the interface. In summary, then, such a model predicts (if $v_{\rm frag}$ varies by a factor 10 at the snowline) that the maximum grain size should be *reduced* by two orders of magnitude within the snowline, while the total surface density of solids should *increase* by the same factor.

In order to derive the radial dependence of $a_{\rm max}$ outside of the water snowline in the fragmentation dominated regime, one can rearrange Equation 4.4 and invoke the thin disc hydrostatic equilibrium relation $c_s = (H/r)v_\Phi$ so as to obtain the Stokes number of the largest grains:

$$\mathrm{St}_{\rm frag} = \frac{0.37}{3\alpha}\left(\frac{v_{\rm frag}}{v_\Phi}\right)^2\left(\frac{r}{H}\right)^2 , \tag{4.9}$$

where $v_\Phi = v_{\rm k} = \sqrt{GM_{\rm star}/r}$ for a Keplerian disc, and the numerical factors are determined from fits to simulations (Birnstiel et al., 2012). Using $c_{\rm s}^2 \propto r^{-0.5}$ and $\Sigma_{\rm gas}$ from Equation 4.3 one then obtains from Equation 4.5 an expression for the radial dependence of the maximum grain size of the form:

$$a_{\rm max}(r) \propto r^{-0.3}\exp\left[-\left(\frac{r}{R_{\rm c}}\right)^{1.2}\right] . \tag{4.10}$$

This is plotted in the right panel of Figure 4.10. In order to calculate the radial profile of the dust surface density I invoke a state of steady flow (i.e. the radial mass flow is independent of radius, see Equation 1.18) so that

$$\Sigma_{\rm dust}\, v_{\rm drift}\, r = \mathrm{const} \,. \tag{4.11}$$

In the limit $\mathrm{St} < 1$ the radial drift velocity is given by

$$v_{\rm drift} \sim \mathrm{St}_{\rm frag}\left(\frac{H}{r}\right)^2 v_\Phi \tag{4.12}$$

(Takeuchi and Lin, 2002) and substituting for $\mathrm{St}_{\rm frag}$ from Equation 4.9 then yields the radial

dependence of $\Sigma_{\rm dust}$ outside of 0.6 au as

$$\Sigma_{\rm dust} \propto r^{-1.5}\,, \tag{4.13}$$

where the exponential cut-off of the gas distribution cancels out. This is plotted in the left panel of Figure 4.10.

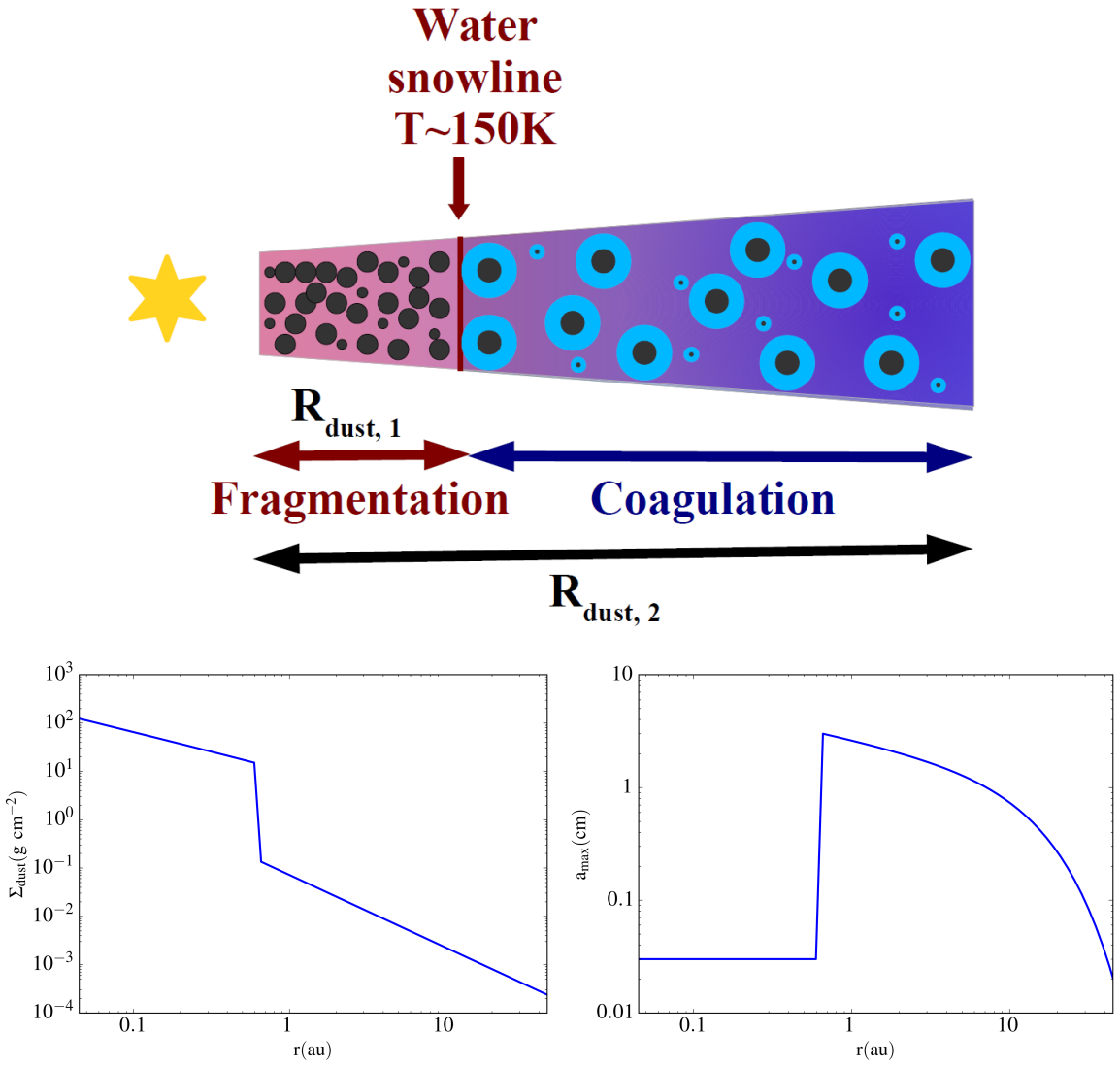

Figure 4.10 *Top:* Schematic depiction of the behaviour of dust at the water snowline. Dust grains beyond the water snowline possess large icy mantles which increase the fragmentation velocity, leading to enhanced grain growth and inward drift. Dust grains interior to the snowline possess no ice mantles, are prone to fragmentation, and are thus unable to grow as quickly to larger sizes. *Left:* Surface density of solids as a function of radius assumed in the 'migration' scenario, with a steep drop-off due to the H_2O snowline at 0.6 au. *Right:* Maximum grain size as a function of radius assumed in the 'migration' scenario, with a steep jump due to the H_2O snowline at 0.6 au.

The water snowline in this disc coincides well with the location at which I have so far assumed the radial truncation of the dust disc. In order to model whether the observed SED can also be explained with radial drift and fragmentation at the water snowline, I implement the effects on $a_{\rm max}$ and $\Sigma_{\rm dust}$ into DALI. In detail, within 0.6 au a single distribution of grain sizes with size distribution index $q = 3$ in the range 5nm to the local $a_{\rm max} = 0.3$ mm is employed but the population is split at $10\,\mu$m so that small grains follow the gas while larger grains are vertically settled. Outside of 0.6 au a grain population (also with $q = 3$, appropriate for an evolved grain population, see e.g. Birnstiel et al. 2012) is used that extends in size from $10\,\mu$m to the local $a_{\rm max}$ value. This entire population is treated as being settled (on the grounds that the large $a_{\rm max}$ values and low surface densities in any case imply negligible emission from small grains in this region). DALI in its fiducial form cannot handle grains sizes that change with radius, but can only take into account constant $a_{\rm max}(r)$. I therefore perform the steps described above to obtain a model in vertical hydrostatic equilibrium with a population of grains with a constant $a_{\rm max} = 3$ cm outside of 0.6 au and calculate the corresponding fluxes $F_{\text{const. } a_{\rm max}}$ for various wavelengths. However, the resulting fluxes are then scaled to take into account the effect of a non-constant $a_{\rm max}(r)$ (see Figure 4.10) according to the following considerations:

$$F_{a_{\rm max}(r)} = \frac{\left[\int_{0.6\text{ au}}^{R_{\rm out}} 2\pi r B_\nu\left[T(r)\right]\left[1-e^{-\kappa_\nu(r)\Sigma_d(r)}\right]dr\right]_{a_{\rm max}(r)}}{\left[\int_{0.6\text{ au}}^{R_{\rm out}} 2\pi r B_\nu\left[T(r)\right]\left[1-e^{-\kappa_\nu\Sigma_d(r)}\right]dr\right]_{\text{const. } a_{\rm max}}} \times F_{\text{const. } a_{\rm max}}\,. \tag{4.14}$$

Here I have made use of the considerations described in Section 1.3.3. Equation 4.14 takes into account opacities κ_ν that vary with radial location according to the local $a_{\rm max}(r)$ in the numerator and are radially constant in the denominator. This is only an estimate, but given that the temperatures in the disc midplane, which are crucial for this analysis, do not change significantly when varying $a_{\rm max}$ (or indeed between the truncation and migration scenario as we will see later), this is a fair assumption to make. The (sub-)mm fluxes obtained with this method are lower for the case of constant $a_{\rm max} = 3$ cm than for the case of $a_{\rm max}(r)$, as the opacities (and therefore also the fluxes) are higher for smaller $a_{\rm max}$ (see e.g. Figure 1.7).

Although I have argued for the form of the $a_{\rm max}$ and $\Sigma_{\rm dust}$ distributions given in Equations 4.10 and 4.13, there are three further parameters that are required to specify the model, i.e. the over-all normalisations of the dust surface density distribution and $a_{\rm max}$ distributions together with the outermost radius of the dust disc. Evidently, if one makes the outer radius sufficiently small then one can match the SED with a range of parameters since it is relatively easy to hide the spectral signatures of large dust particles if they

are only present over a limited radial zone. It is of more interest — in order to contrast with the scenario presented in Section 4.4.1 where there is *no* dust beyond 0.6 au — to see if there are any viable models which fit the SED and where the dust is radially extended. Figure 4.10 exemplifies such a solution.

The values of $a_{\rm max}$ and dust surface density just outside the water snowline (3 cm and 0.1 g cm^{-2}) provide an acceptable fit to the SED even if the dust extends to 45 au (see Figure 4.11). Smaller values of $a_{\rm max}$ or larger dust surface density normalisation over-predict the flux at large wavelengths (especially the mm) since both these trends lead to increased optical depth at mm wavelengths. Models in this category would require a lower outer dust radius in order to be compatible with the SED. On the other hand, larger values of $a_{\rm max}$ and lower values of dust surface density normalisation instead lower the optical depth in the near infrared to the point that they under-predict the SED in this region and can therefore be ruled out.

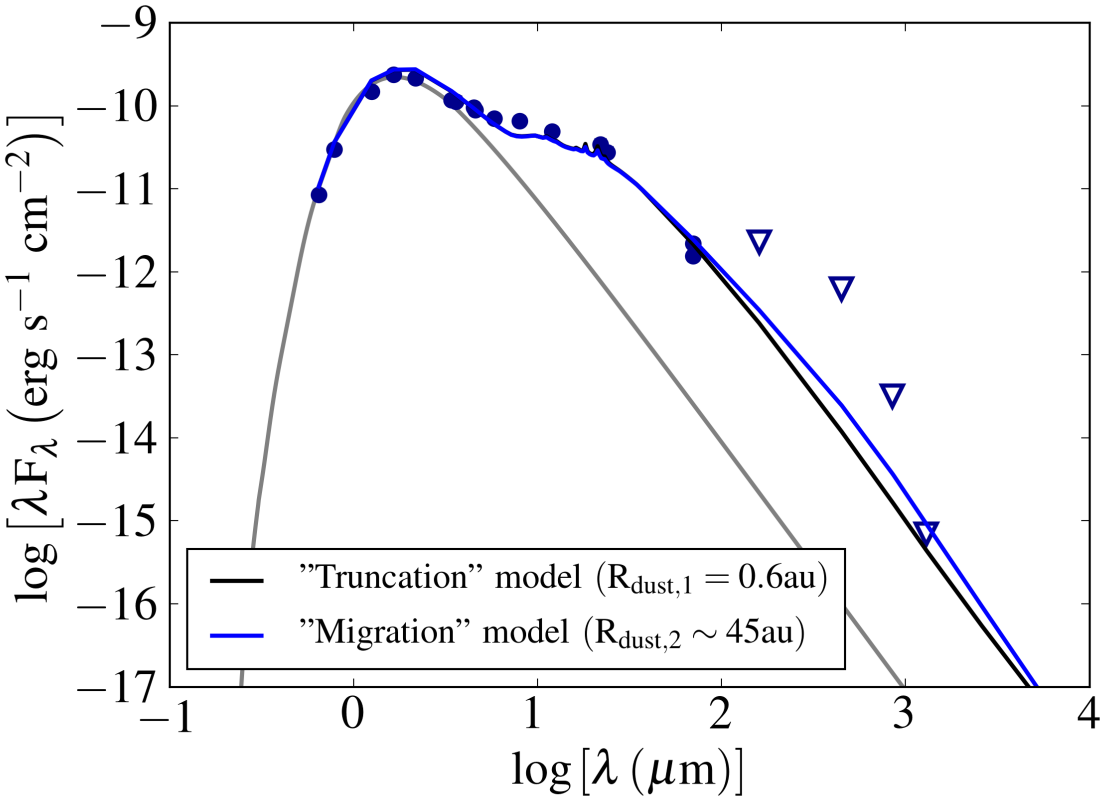

Figure 4.11 SED of the truncated model and the one with dust outside of 0.6 au: The black thick line is the truncated model with $R_{\rm dust,\,1} = 0.6$ au and no dust outside of this radius. The blue model has $R_{\rm dust,\,1} = 0.6$ au, but $R_{\rm dust,\,2} \sim 45$ au. Both of them comply with the observed upper limit on the flux density at 1.3 mm.

It is worth emphasising that the 'successful' model with an extended belt of large grains (Figure 4.11) is not necessarily a self-consistent outcome of dust growth models, since it is not guaranteed that the necessary value of $a_{\rm max}$ and dust surface density will be simultaneously achieved and that dust growth will be fragmentation limited at this point (as was assumed in the derivations presented above). Examining the properties of the 'successful' model, the dust surface density profile shown in Figure 4.10 (left) corresponds to total dust masses of $M_{\rm dust}(r < 0.6{\rm au}) \sim 1\,{\rm M}_{\oplus}$ and $M_{\rm dust}(r > 0.6{\rm au}) \sim 0.2\,{\rm M}_{\oplus}$.[2]

It is only possible to constrain the required *gas* masses corresponding to the $a_{\rm max}$ distribution shown in Figure 4.10 (right) if one specifies the value of α (Shakura and Sunyaev, 1973) that controls the strength of turbulence and the value of the fragmentation velocity, $v_{\rm frag}$. From Equation 4.4 and 4.5 the value of $\Sigma_{\rm gas}$ corresponding to a particular grain size distribution scales as $\alpha/v_{\rm frag}^2$; for $v_{\rm frag} = 5\,{\rm m\,s^{-1}}$ outside of 0.6 au (and therefore $v_{\rm frag} = 0.5\,{\rm m\,s^{-1}}$ inside of 0.6 au) and $\alpha = 10^{-3}$ the gas mass interior and exterior to 0.6 au is around $40\,{\rm M}_{\oplus}$ and $1200\,{\rm M}_{\oplus}$ respectively. However, given uncertainties in both α and $v_{\rm frag}$ the constraints on the *gas* mass from this modelling are very weak.

4.4.3 Gas radius as discriminant between scenarios

So far I have considered two situations for the disc around V410 X-ray 1 which would reproduce the observed SED (see Figure 4.11). The first involves a 'truncation' scenario in which the dust is entirely confined within 0.6 au (for example due to interaction with a companion). The second involves a 'migration' scenario in which a combination of radial drift outside and fragmentation inside the H_2O snowline produces an optically thick inner dust disc and a low density region of large dust extending over many tens of au. Whatever the cause, it is clear that SED modelling alone cannot distinguish between these scenarios.

A clear discriminating difference between these two scenarios would be the radial extent of the *gas* in the disc – in the former the gas would have a similarly small radius as the dust, while in the latter the gas disc would share a similarly extended configuration to the large dust grains.[3] As such, observations of gas tracers towards V410 X-ray 1 may have the ability to determine which configuration is at work. Figures 4.14 and 4.15 show the corresponding gas density and temperature structure for the two scenarios considered here, the respective dust density and temperature maps are given in Figures 4.12 and 4.13.

[2] Whereas the maximum dust mass inside of 0.6 au is unbounded in the truncation scenario, the interior dust mass in the migration scenario needs to be fine tuned to about $1\,{\rm M}_{\oplus}$ in order for the large grains outside the H_2O snowline not to over-predict the mm flux. This dependence arises as the dust mass inside and outside of 0.6 au are linked by the relationships plotted in Figure 4.10.

[3] Note however that the gas radius may even exceed the radius of the large grains (see Birnstiel and Andrews, 2014).

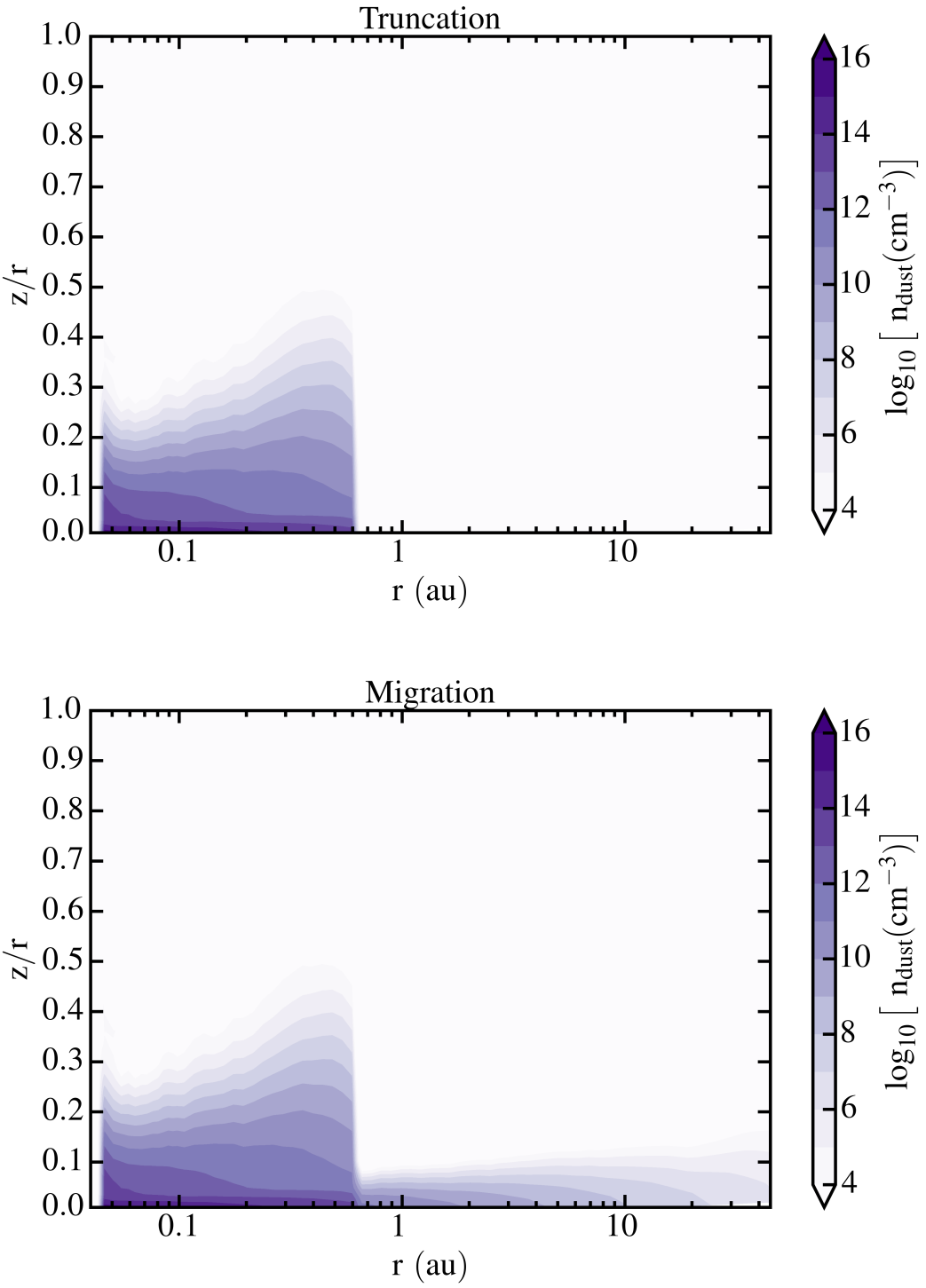

Figure 4.12 Dust density structure of the truncation (*top*) and migration (*bottom*) models.

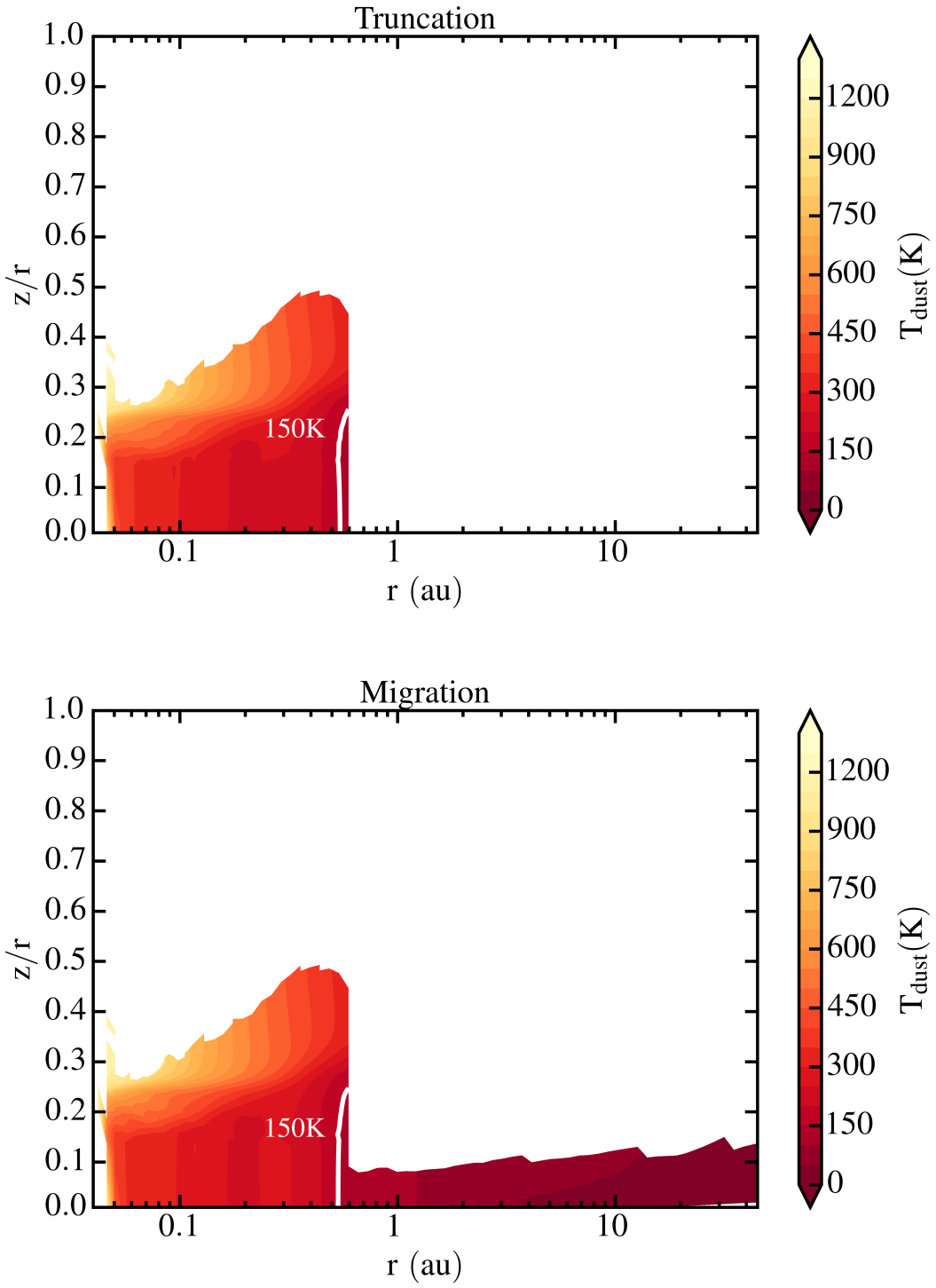

Figure 4.13 Dust temperature structure of the truncation (*top*) and migration (*bottom*) models. Contours of 150 K are marked.

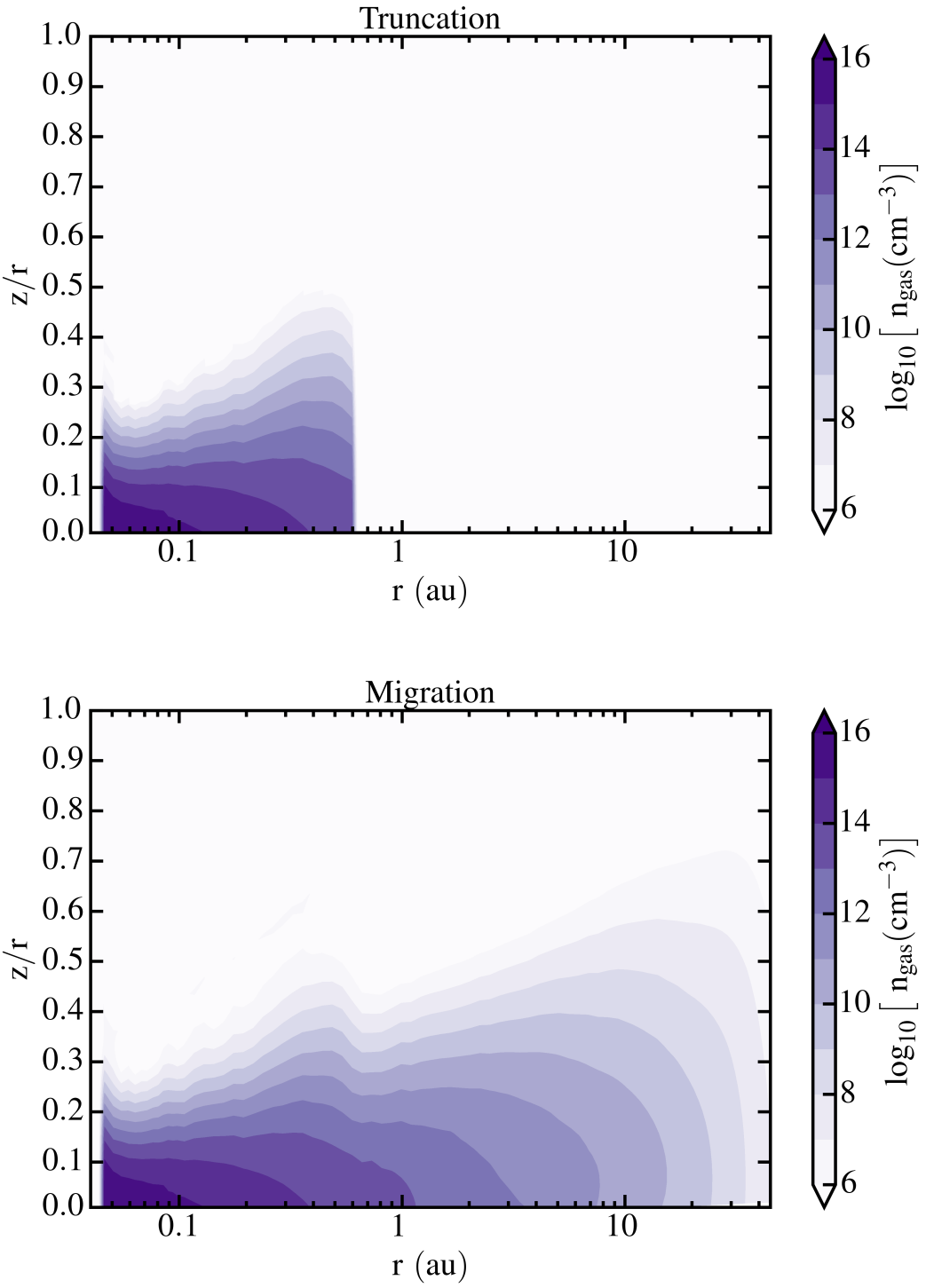

Figure 4.14 Gas density structure of the truncation (*top*) and migration (*bottom*) models. The bump in the gas density plot of the 'migration' scenario outside of 0.6 au is an effect of plotting z/r rather than z on the y-axis.

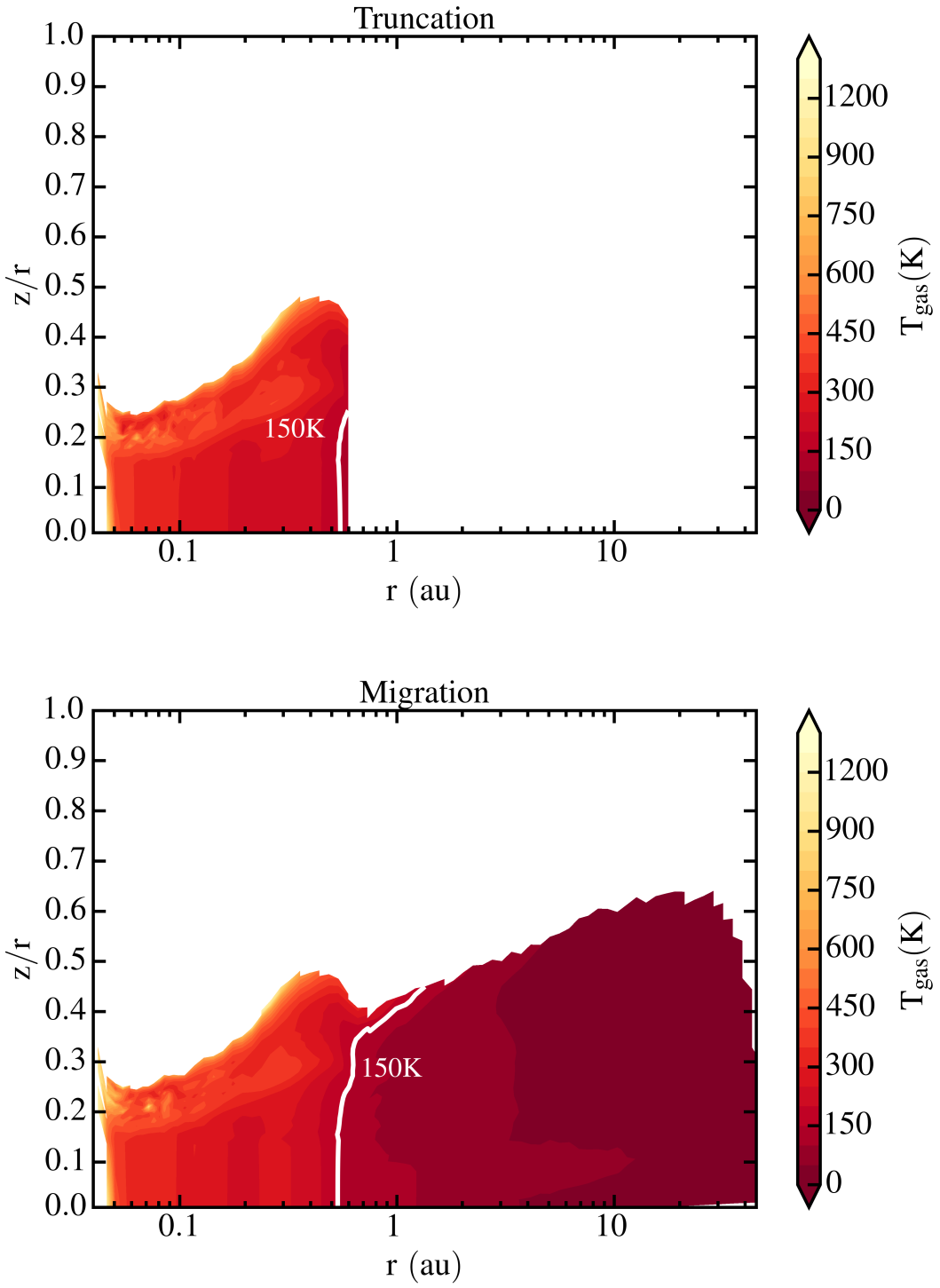

Figure 4.15 Gas temperature structure of the truncation (*top*) and migration (*bottom*) models. Contours of 150 K are marked.

In both scenarios, the dust interior to 0.6 au intercepts the stellar irradiation and causes flared structure to appear in the gas, typical of vertical hydrostatic equilibrium models (see, e.g., Woitke et al., 2009). The large dust in the 'migration' scenario is extremely settled, as such has little effect on the gas temperature in these regions. In these midplane regions, gas and dust temperatures are tightly coupled and in thermal equilibrium due to the high densities (e.g. Facchini et al., 2017a), as can be seen by the relatively invariant temperature contours.

The combined thermochemical nature of the DALI code allows to easily examine the line emission from these scenarios. In order to determine the extent of the gas in the disc, lines emitted at large radii must be considered. Given the faintness of the source and lack of any surrounding cloud material, I have chosen to examine the observability of the ^{12}CO isotopologue (hereafter referred to as CO). The upper panel of Figure 4.16 shows the abundance of CO throughout the disc for the 'migration' scenario using a *time-dependent* chemistry solver, where the gas disc extends to ~ 30 au. The highest abundances are seen in a warm molecular layer in the inner disc at relative heights of $z/r \sim 0.2 - 0.4$, and throughout the entirety of the disc exterior to 0.6 au. Disc layers above this are subject to significant amounts of UV irradiation which act to photodissociate the CO molecule. In the inner disc midplane regions with high temperatures, C is preferentially in CH_4, whereas in the colder midplane regions further out, CO will be depleted due to freeze-out (where dust grains are present). Despite the relative ubiquity of CO throughout this disc, the majority (75 per cent) of the emission of the $J = 2 - 1$ transition is confined to radii between $10 - 30$ au at a relative height of between $0.15 - 0.7$ (yellow hatched region). From inspection of the optical depth surfaces shown in the upper panel of Figure 4.16, it is clear that the CO emission originates far above the $\tau = 1$ surface for the dust at 1.3 mm (dotted line), but is beneath the $\tau = 1$ surface for the line (solid line), and is thus optically thick. Therefore, the CO $J = 2 - 1$ emission is a useful proxy of the outer gas disc radius. Nevertheless, Figure 4.16 only shows the results of a single model.

In the upper panel of Figure 4.17, I show the abundance of CO using the *time-independent* chemistry solver. There is a difference between the CO abundance in the two cases, especially in the disc midplane regions. This can mostly be explained by the fact that the time-independent solver produces more CH_4 in these disc regions (see lower panel of Figure 4.17), which tends to happen over long timescales and is therefore the predominant effect removing CO in these disc regions. This is explained in more detail in Section 2.7.3. In the time-dependent case however, much less CH_4 is produced (see lower panel of Figure 4.16) and therefore the CO abundance in this case looks much smoother in these disc midplane regions. Note however that models obtained with the time-dependent and independent solver yield the same CO $J = 2 - 1$ line fluxes ($F_{\text{time-dependent}} = 0.299$ Jy km s^{-1}

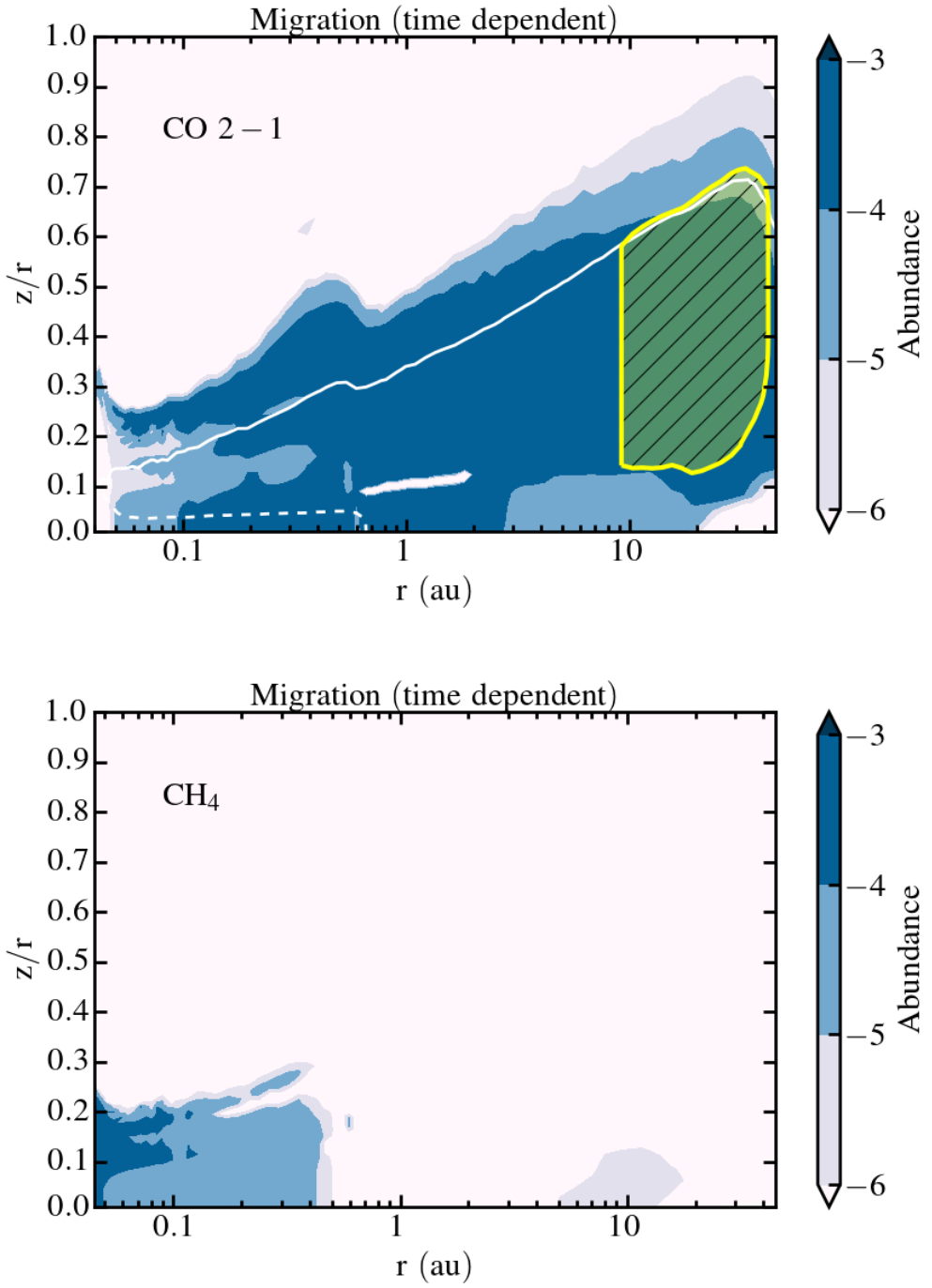

Figure 4.16 Fractional abundance of CO (*top panel*) and CH_4 (*bottom panel*) throughout a disc model in the 'migration' case with $R_{\rm gas} \sim 30$ au (colour scale) using the time-dependent chemistry solver in DALI. In the top panel, the region which is responsible for 75 per cent of the emission for the $J = 2 - 1$ transition is overlaid (yellow hatch). The integrated line flux is $F_{\rm time\text{-}dependent} = 0.299$ Jy km s^{-1}. The white solid line denotes the $\tau = 1$ surface for the $J = 2 - 1$ transition, while the white dashed line indicates the $\tau = 1$ surface for the dust at the wavelengths of this transition (i.e. 1.3 mm). The plot shows that in contrast to the time-independent case (Figure 4.17) much less CO is turned into CH_4.

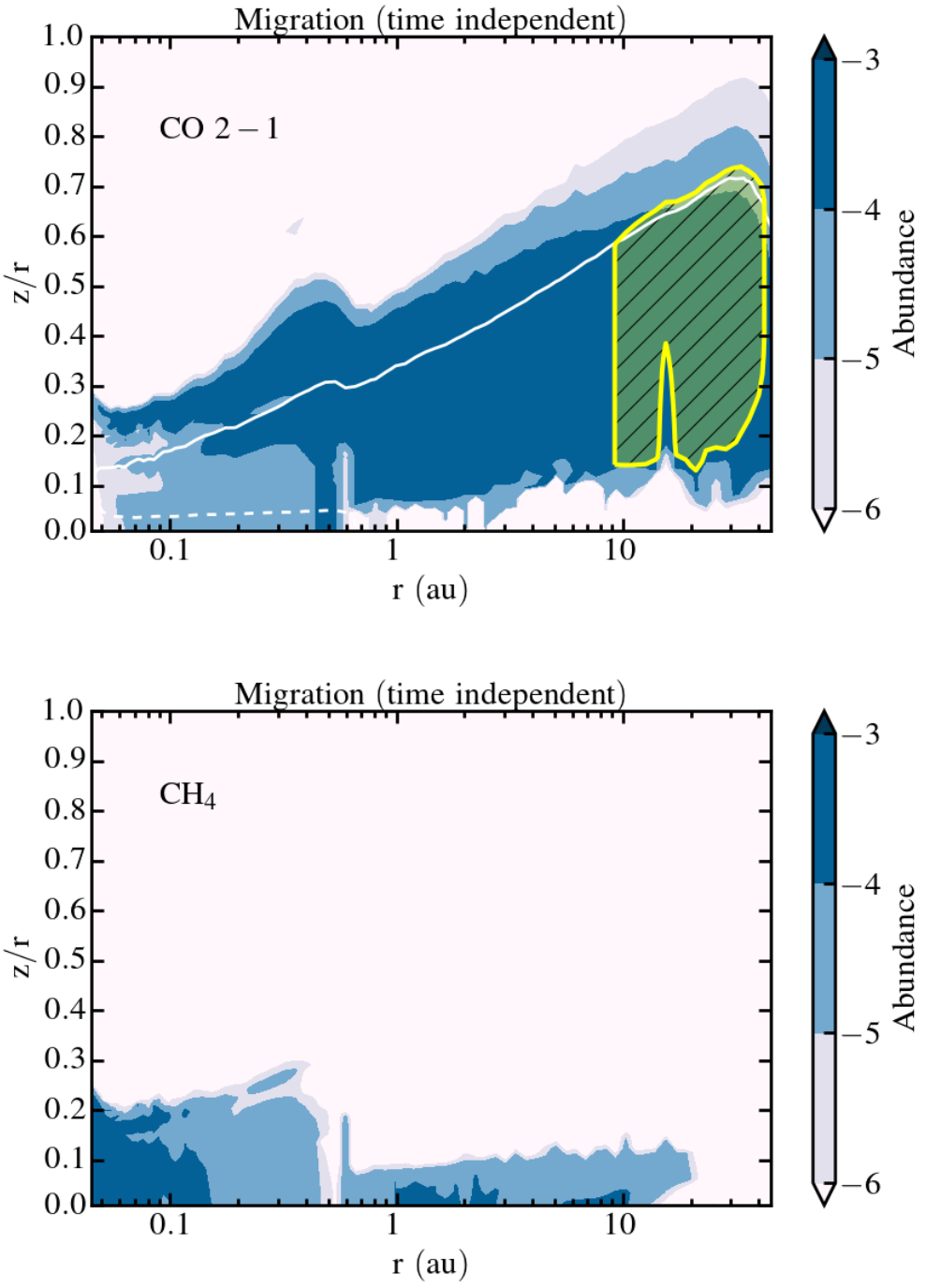

Figure 4.17 Fractional abundance of CO (*top panel*) and CH_4 (*bottom panel*) throughout a disc model in the 'migration' case with $R_{\rm gas} \sim 30$ au (colour scale) using the time-independent chemistry solver in DALI. In the top panel, the region which is responsible for 75 per cent of the emission for the $J = 2 - 1$ transition is overlaid (yellow hatch). The integrated line flux is $F_{\text{time-independent}} = 0.297$ Jy km s^{-1}. The white solid line denotes the $\tau = 1$ surface for the $J = 2 - 1$ transition, while the white dashed line indicates the $\tau = 1$ surface for the dust at the wavelengths of this transition (i.e. 1.3 mm). The plot shows that in the midplane regions devoid of CO this molecule has mostly turned into CH_4.

and $F_{\text{time-independent}} = 0.297$ Jy km s^{-1}, respectively), as the emission from this transition originates from a region that is not influenced by the production of CH_4. As discussed in Section 2.7.3, the fact that much more CH_4 is produced in the time-independent case is because of the long timescales of this process. In the time-dependent case however, abundances are integrated for a shorter timescale, which is more in line with the fact that discs only live for a few Myr.

The presence of large dust grains or the lack thereof outside of 0.6 au has essentially no effect on the CO abundance or temperature in the region where 75 per cent of the emission comes from. The integrated line flux for a case with no dust at $r > 0.6$ au and $R_{\text{gas}} \sim 30$ au is $F = 0.277$ Jy km s^{-1}. Therefore, the integrated CO $J = 2-1$ line fluxes of both scenarios are essentially identical. The reason is that the additional dust outside of 0.6 au is very settled and optically thin and therefore has a negligible effect on the temperature structure of the disc.

To investigate a larger parameter space, I have run a suite of 26 models. Each model produces a fit to the observed SED, but the gas radius R_{c} and the total gas mass M_{gas} are varied. All other stellar and disc parameters are kept fixed to the values listed in Table 4.2. The chosen ranges of gas mass are set by the requirement that the disc must obey gravitational stability (and thus $M_{\text{gas}} < 0.1\,\text{M}_*$), but must contain sufficient dust mass to reproduce the observed 70μm flux in the SED. The chosen ranges of gas radius span approximately 3 to 200 au. Figure 4.18 shows the resulting CO $J = 2-1$ line fluxes obtained from the models within the grid. Again, the presence of the very large grains outside of 0.6 au (or their lack) has no effect on the total CO fluxes in the models.

As can be seen, there is a weak dependence between the resulting $J = 2-1$ line flux and the value of M_{gas} assumed for gas masses greater than approximately $10^{-5}\,\text{M}_\odot$, due to the fact that the emission is largely optically thick in this regime. For gas masses lower than approximately $10^{-5}\,\text{M}_\odot$, a somewhat stronger dependence starts to emerge. However, by far the strongest dependence is between the $J = 2-1$ line flux and the value of R_{gas}. Such a result is not surprising, because due to the optically thick nature of the line emission, the line flux will simply scale geometrically with the emitting area. Though there is no firm detection of the $J = 2-1$ line flux toward V410 X-ray 1, a combination of the calculated non-detection of < 0.4 Jy km s^{-1} and my model grid already allows to exclude several configurations. These broadly consist of discs with an outer gas radius greater than 50 au and a gas mass greater than $10^{-4}\,\text{M}_\odot$.

Other studies of classical T Tauri Stars have used the ^{12}CO total flux (or upper limit) to constrain the radial extent of gaseous disks (e.g. Woitke et al., 2011) where spatially resolved observations were not available. Given the weak dependence on M_{gas}, but stronger dependence on R_{gas}, a firm detection (or more stringent non-detection) would likely lead

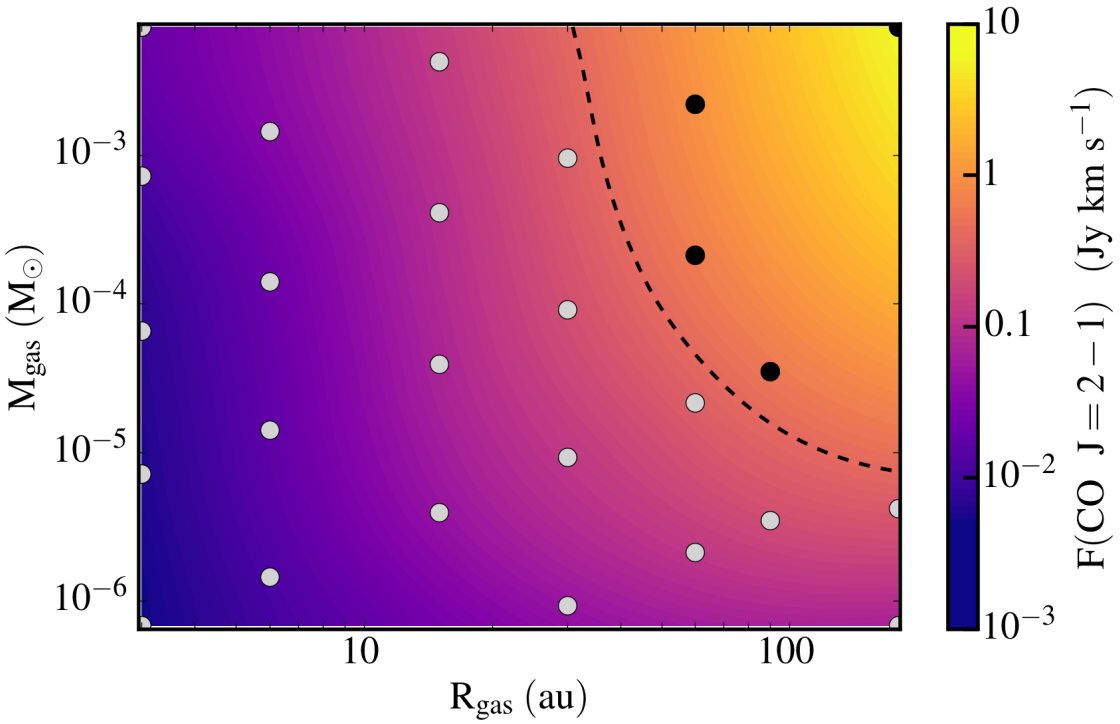

Figure 4.18 Resulting ^{12}CO $J = 2 - 1$ fluxes of the grid of models (*points*) in which I vary the gas radius and the gas mass. Values between these points are calculated using cubic interpolation on the triangular grid connecting each point. The dashed line indicates a flux of 0.4 Jy km s^{-1}, the upper limit for the ^{12}CO $J = 2 - 1$ derived in Section 4.2. Black points indicate models which violate this upper limit.

the gas radius to be determined rather unambiguously, possibly allowing the 'truncation' or 'migration' scenarios to be distinguished.

4.5 Conclusions

I have modelled the disc around the very low mass star V410 X-ray 1. Including an upper limit on the 1.3 mm continuum flux from recent ALMA observations gives an additional constraint on the disc structure. I find that its SED can be explained by a very truncated, optically thick dust component with $R_{\mathrm{dust,\,1}} = 0.6$ au. Two scenarios were explored that can potentially explain this finding. On the one hand, dynamical 'truncation' of the disc could have shrunk the dust disc to its tiny radius. On the other hand, the SED is also compatible with some amount of large dust outside of 0.6 au. For this scenario, radial 'migration' coupled with fragmentation interior to the H_2O snowline (located at 0.6 au) result in a cliff in Σ_{dust} of two orders of magnitude and in a sudden increase of grain sizes. My

modelling shows that this scenario matches the observed SED for outer dust disc radii of $R_{\text{dust, 2}} \lesssim 45$ au.

In both scenarios, a dust mass inside of 0.6 au bigger than $\sim 1\,\mathrm{M}_{\oplus}$ is required to match the observed SED, however due to the optically thick nature of the dust, one does not obtain an upper limit on the dust mass. In the 'migration' scenario, the dust mass needs to be fine-tuned to $\sim 1\,\mathrm{M}_{\oplus}$ inside the H_2O water snowline in order to match the SED as the dust masses inside and outside of 0.6 au are dependent on each other.

In order to distinguish further between these scenarios, the gas radius of the disc can offer important information. If it is truncated at very small radii as well, a dynamical truncation of the disc seems likely. If it is more extended, radial drift in combination with dust physics at the water snowline offers a plausible explanation. I present predictions for CO $J = 2 - 1$ fluxes, invoking various $M_{\text{gas}} - R_{\text{gas}}$ combinations, that will enable future observations to potentially distinguish between these two scenarios.

Finally, I note that regardless of the underlying mechanism for the small scale dust disc, its optically thick nature suggests that several $\mathrm{M}_{\oplus}$ of dust can be located within a small radial extent from the central star. Such a configuration suggests that V410 X-ray 1 may be a potential precursor to a system of tightly packed terrestrial planets, such as the recently discovered TRAPPIST-1 system.

5

Conclusions and outlook

In this thesis, I have performed detailed radiative transfer modelling of two discs from different ends of the stellar mass spectrum in order to determine their nature and physical properties. The first disc, surrounding the Herbig Ae star HD 163296, has a very extended gas and dust radius of several hundreds of au, the second one around the VLM star V410 X-ray 1 is truncated on the scale of ~ 1 au. For both of these studies, the combination of self-consistent gas and dust modelling is essential.

Refining modelling techniques in order to include effects such as for example magnetic fields, photoevaporation, dust evolution and the impact they could have on discs are just some of the great challenges for disc modellers (see e.g. Haworth et al., 2016, for a review paper on challenges in disc modelling). An important observational step towards discovering exoplanets and mapping their potential habitability will be the capabilities of the *James Webb Space Telescope* (JWST), which is scheduled to be launched into orbit in 2020. It will provide invaluable input for questions concerning exoplanet atmospheres and also for studying the planets in our own solar system in more detail.

Also on the observational side, ALMA will continue providing more and more observations of protoplanetary discs with unprecedented resolution and sensitivity. Mapping disc features such as spiral arms, rings and gaps will be key in developing an understanding of planet formation. In addition, observations of chemical tracers such as water might play an important role in learning for example about the water snowline and the effects it might have on the dust grain distribution and evolution in discs.

5.1 The midplane conditions of protoplanetary discs

5.1.1 The disc of HD 163296

In Chapter 3, I investigated the structure of the disc around HD 163296 with a special focus on the midplane disc regions inside the 90 au snowline location. In order to assess the

planet formation potential of protoplanetary discs, it is important to measure their gas mass. However, traditionally these are inferred from observed dust masses by applying a standard gas-to-dust ratio of $g/d = 100$. The inherent problem is that measurements of the g/d are usually taken from observations of the ISM and it is therefore uncertain whether this value can readily be applied to discs. In addition, g/d ratios do not need to be constant throughout a protoplanetary disc, but can vary radially as dust grains evolve and migrate towards the star. An additional problem to be taken into account is that measuring gas masses based on CO observations can be hindered by the effects of CO freeze-out and other sequestration mechanisms.

Therefore I have presented a novel approach to study the midplane gas by combining observations and modelling of the SED and the $C^{18}O$ line emission with observations of the CO snowline location and its implications for the disc temperature structure. This modelling technique was then applied to to the disc around the Herbig Ae star HD 163296 with particular focus on the regions within the CO snowline radius. The two radiative transfer codes MCMax and TORUS were combined in order to provide self-consistent models of the gas and dust components of the disc: I used MCMax in order to obtain disc models that are in vertical hydrostatic equilibrium and provided a dust temperature and density map as well as an SED that could be directly compared against observations. This was then used as an input for TORUS to model the $C^{18}O$ $J = 2 - 1$ line emission in order to fit ALMA Science Verification data.

The models yielded the mass of $C^{18}O$ in this inner disc region of $M_{C^{18}O}(< 90\,\mathrm{au}) \sim 2 \times 10^{-8}\,M_\odot$. I found that most of the models give a notably low $g/d < 20$, especially in the disc midplane ($g/d < 1$). The only models with a higher g/d required $C^{18}O$ to be underabundant with respect to the ISM abundances and a significant depletion of sub-μm grains, which is not supported by scattered light observations. This technique could be applied to a range of discs and opens up a possibility of measuring gas and dust masses in discs within the CO snowline location without making assumptions about the g/d ratio.

5.1.2 Future studies

In the case of HD 163296, the modelling I presented in Chapter 3 shows that comparatively simple modelling of the dust content and $C^{18}O$ line emission might provide a good handle on the gas and dust components of Herbig discs - at least inside their CO snowline locations. However, for this type of modelling a good knowledge of the $C^{18}O$ (and therefore CO) abundance is required. Further studies will have to show whether the CO fractional abundance of 10^{-4}, which is generally assumed in discs, does indeed hold true or whether processes such as C-sequestration do significantly alter the carbon abundance. Getting an

independent handle on the disc gas mass for example from HD observations will therefore be important in order to pin down CO abundances and make the type of modelling presented in Chapter 3 even more significant. This offers the opportunity of being able to avoid expensive modelling of the emission of many lines in order to study the midplane conditions of discs.

More recent high-resolution ALMA observations of HD 163296 have presented a wealth of sub-structure (rings and gaps) in the dust emission of this disc as well (Isella et al., 2016). It would be very interesting to see how implications derived from this data (that are of much better spatial resolution than the Science Verification data used in my modelling) compare to the work presented in Chapter 3, especially on the gas-to-dust ratios derived there. In general, examining in detail what causes the sub-structure in the HD 163296 disc, but also in discs such as HL Tau (ALMA Partnership et al., 2015), TW Hya (Andrews et al., 2016) etc. and studying if they could potentially be explained by the presence of planets, is one of the big challenges for future modelling.

5.2 Truncated discs around low mass stars

5.2.1 The disc of V410 X-ray 1

In Chapter 4, I studied a protoplanetary disc from a very different end of the stellar mass range - around the very low mass star V410 X-ray 1. Discs around brown dwarfs and very low mass stars offer some of the best prospects for hosting Earth-sized planets in their habitable zones. With the unprecedented sensitivity of ALMA it is now possible to characterise these small and faint discs, and perhaps even resolve them.

In order to get a handle on the dust and gas structure, I studied the nature of the disc around V410 X-ray 1, whose SED is indicative of an optically thick and very truncated dust disc. Including an upper limit on the continuum emission at a wavelength of 1.3 mm from recent ALMA observations provided an additional tight constraint on the disc extent. My modelling suggested an outer radius of the optically thick dust component of only 0.6 au. I investigated two scenarios that could explain such a truncation: The first involved the fact that a radial location of 0.6 au is close to the expected location of the H_2O snowline in the disc. As such, a combination of efficient dust growth, radial migration, and subsequent fragmentation within the snowline leads to an optically thick inner dust disc and larger, optically thin outer dust disc beyond the snowline. The second scenario involved the truncation of both the dust and gas in the disc, perhaps due to a previous dynamical interaction or the presence of an undetected companion.

To this end I used the radiation thermo-chemical disc code DALI, which I modified in order to provide disc models in vertical hydrostatic equilibrium. I find that the SEDs obtained from models of both scenarios are in line with the observed SED. In the first case, disc outer radii up to ~ 45 au are consistent with the observations. In order to distinguish between the two cases, the outer radius of the gas component can be indicative: in the migration scenario, the gas would extend to much larger radii than the optically thick dust, whereas in the truncation scenario both would share a similar extent. The ALMA observations only provide an upper limit on the CO $J = 2 - 1$ line flux and are not spatially resolved. Nevertheless, using a grid of models, I found that a firm measurement of the CO $J = 2 - 1$ line flux (or a more stringent non-detection) would allow me to distinguish between these two scenarios by enabling a measurement of the radial extent of gas in the disc. Such observations would only be feasible with ALMA with a modest integration time. Finally, I demonstrated that the models are all compatible with containing at least several Earth-masses of dust interior to 0.6 au. This is sufficient raw planet forming material to provide the mass for the formation of all the planets discovered so far in TRAPPIST-1 system ($5.28\,M_\odot$). This suggest that V410 X-ray 1 could be a precursor to a system with tightly-packed inner planets, such as TRAPPIST-1.

5.2.2 Future studies

In the case of the truncated disc of V410 X-ray 1, the archival ALMA data was based on a survey of a number of star-disc systems, however due to the very short integration time of only approximately six minutes, neither the CO emission nor the 1.3 mm continuum were detected. Future ALMA observations with an even moderate increase in integration time could however even spatially and spectrally resolve the disc and give invaluable input for studying its structure. A firm measurement of the continuum emission would show whether the disc is optically thick or optically thin at mm wavelengths and therefore constrain the dust mass within 0.6 au. On the other hand, observations of the CO $J = 2 - 1$ emission would allow to pin down the outer gas radius. This would then make it possible to learn about the formation and evolution of such an extremely truncated disc. This is especially interesting in order to examine the planet formation potential of such a disc - also in light of the recent detection of the Earth-like planets in the TRAPPIST-1 system. The high resolution and sensitivity of ALMA is key for observations of this sort, especially because the dust disc is expected to be so small that even ALMA might not be able to spatially resolve it, but definitely to put an upper limit on its radial extent and integrated line fluxes. Potential observations in ALMA Band 5 might also allow to observe the H_2O $3_{1,3}-2_{2,0}$ transition (with frequency $\nu \approx 183$ GHz and energy of the upper level of $E_{\rm up} = 204.7$ K),

which will allow to put even more stringent limits on the water snowline in this disc. I show a plot of the water abundance for the migration case in V410 X-ray 1 in Figure 5.1.

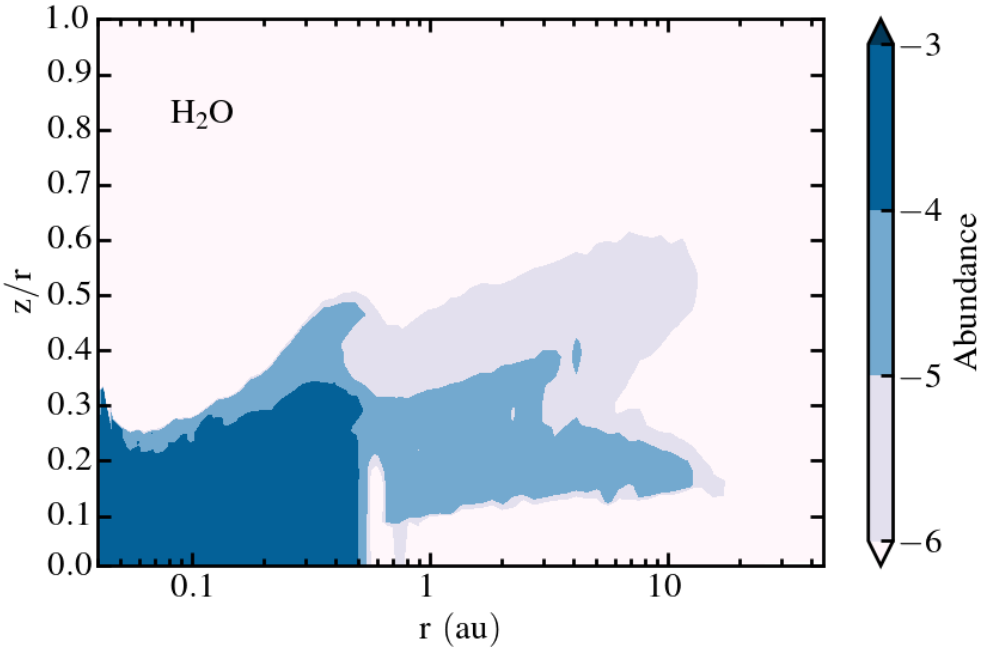

Figure 5.1 Water abundance of V410 X-ray 1 in the migration scenario. One can clearly see the impact of water freezing out onto dust grains in the midplane regions just outside the H_2O snowline at 0.6 au.

The effect of freeze-out on the water abundance at the snowline is clearly visible. More in depth modelling of the emitting regions for various water transitions would be very interesting, especially in light of potential observability with ALMA.

Note however, that the spatial resolution of ALMA in Band 5 ($\nu \sim 100$ GHz) is 0.042 arcsec, which for a distance of V410 X-ray 1 in Taurus of $D \sim 140$ pc corresponds to ~ 6 au. It will therefore not be possible to spatially resolve the water snowline in such a small disc.[1] However looking to the future, the *Next Generation Very Large Array* (ngVLA) will provide an even better spatial resolution at mm wavelengths (see white paper by Ricci et al., 2018). The total collecting area of the ngVLA is envisioned to be 10 times that of ALMA and its baselines 10 times longer than those of ALMA (i.e. up to 300 km). Therefore based on current plans, the resolution at 100 GHz will be on the order of 5×10^{-3} arcsec, which corresponds to ~ 0.7 au at the distance of Taurus. This would offer the amazing opportunity to spatially resolve even the inner dust disc in V410 X-ray 1. A comparison of ngVLA and ALMA in terms of frequency coverage and effective collecting is shown in Figure 5.2.

[1] Note that observations of water from the ground are complicated due to the high abundance of H_2O in the Earth's atmosphere. Observations of HDO may offer an alternative.

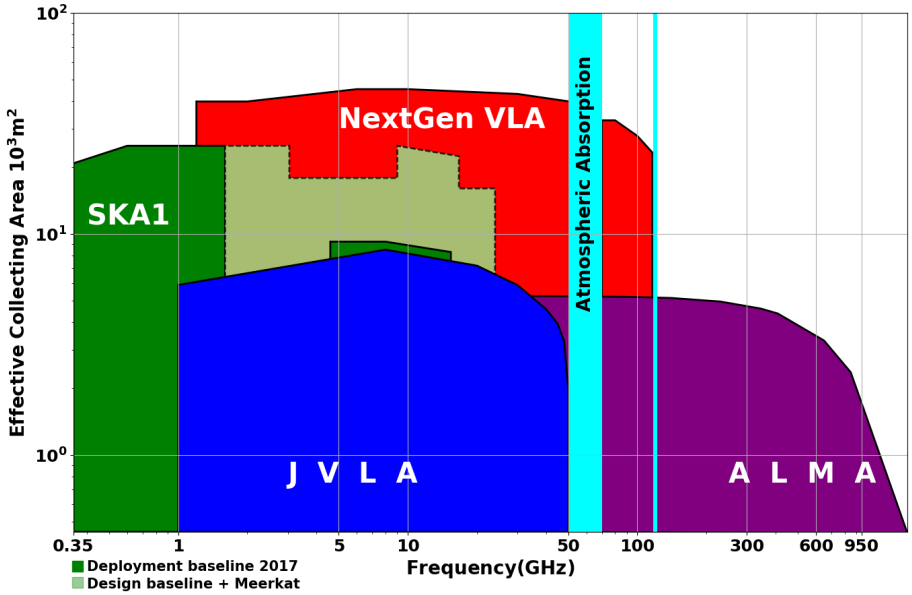

Figure 5.2 Comparison of frequency coverage and collecting area of the ngVLA and ALMA and other radio to sub-mm disc arrays that are expected to be operating in the 2030's. Figure from https://science.nrao.edu/futures/ngvla.

The amazing resolution and sensitivity of ALMA and future generation telescopes will also be invaluable for studying other truncated discs. In Bulger et al. (2014), they show the SEDs of eight potentially truncated discs around VLM stars or BDs. This is inferred from the steep slope of their SEDs in the wavelength regime between 24 μm and 70 μm ($\alpha_{24-70\,\mu\mathrm{m}} < -1.4$). The SEDs are plotted in Figure 5.3.

In Chapter 4, I presented the radiative transfer modelling of one of these - V410 X-ray 1 (top left corner). This object was chosen because of the archival ALMA data providing an additional constraint on the SED and also because it was listed in Bulger et al. (2014) as not having a known companion. This is especially interesting in light of examining the formation of VLM stars and BDs and their discs. Given that the disc modelling revealed that V410 X-ray 1 could either be truncated in both its gas and dust components or that effects at the water snowline might alter the grain size and distribution, it would be very interesting to also model the other seven candidates. This would allow to study whether the spectral steepening and potential truncation in these candidates is also related to the impact of the H_2O snowline or if it will have to be explained by other means.

In addition, it would be interesting to examine whether this kind of SED is also present in higher mass discs - and if so, at which wavelengths the steepening is happening. If it was to occur in the same wavelength regime as for the case of V410 X-ray 1, this would again be indicative of the disc being truncated at a disc location, where the temperature

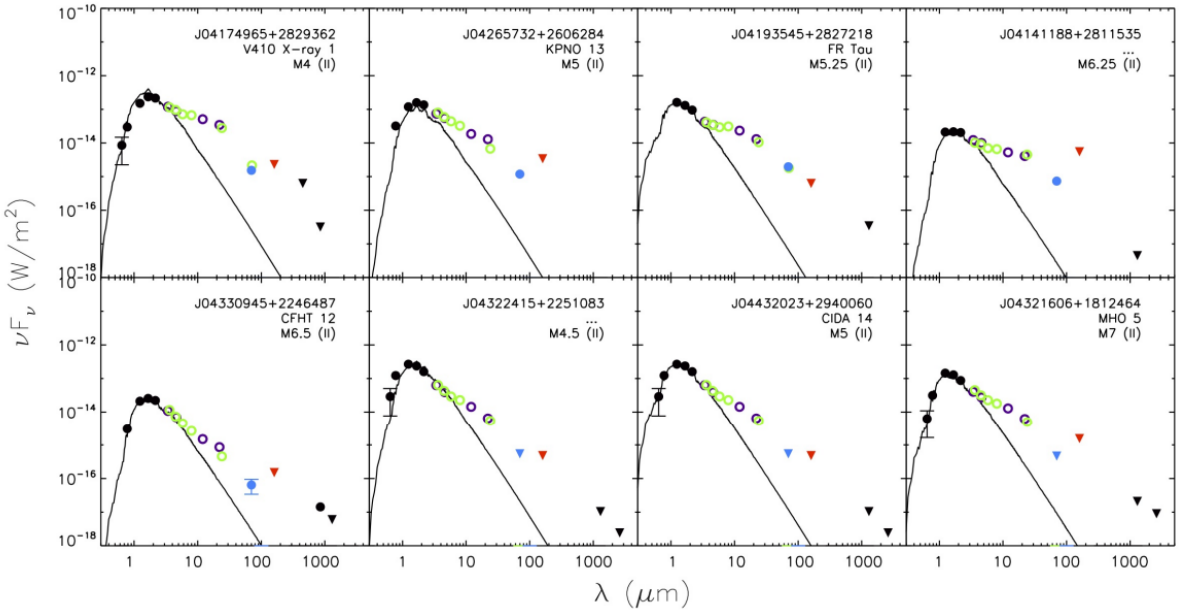

Figure 5.3 SEDs of the 8 candidate truncated discs as inferred from their spectral index between $24 - 70\,\mu$m< -1.4. The object names as well as their spectral types are given in each panel. The SED of V410 X-ray 1, the disc I studied in detail in Chapter 4, is given in the upper left panel. Figure from Bulger et al. (2014).

is approximately 150 K (see also description in Section 1.3 and Equation 1.31). Given that higher mass stars are more luminous, this disc location would be at larger radii than in the case of the VLM star V410 X-ray 1, making it easier to spatially resolve it. This would allow to study whether the effect of the water snowline on dust grain sizes, fragmentation velocities and drift is also significant in discs around higher mass stars. Thus these effects need to be taken into account in future disc modelling.

5.3 Final remarks

The capabilities of ALMA and upcoming telescopes make this a uniquely exciting time to study protoplanetary discs and their transition towards debris discs and finally planetary systems. These observations in combination with state-of-the-art gas and dust modelling will be of great importance in developing an overarching understanding of these processes. This thesis has shown that self-consistent modelling of the gas and dust components of protoplanetary discs is key in order to interpret observational data and to gain insight into the structure of discs. Observations of a wealth of chemical tracers will offer the unique chance to study the chemical structure of discs and how this is ultimately related to the composition of planets and their atmospheres. In order to do so, modelling of the dynamics of gas and dust in discs will be crucial to understand their spatial dis-

tribution and the impact this will have on forming planets. Taking all the processes into account that take place in discs (from microscopic to macroscopic effects), combining them to offer a self-consistent model, and matching them to observations is one of the biggest future challenges for studies of protoplanetary discs.

Bibliography

Acke, B., Min, M., van den Ancker, M. E., Bouwman, J., Ochsendorf, B., Juhasz, A., and Waters, L. B. F. M. (2009). On the interplay between flaring and shadowing in disks around Herbig Ae/Be stars. *A&A*, 502:L17–L20.

Adams, F. C., Hollenbach, D., Laughlin, G., and Gorti, U. (2004). Photoevaporation of Circumstellar Disks Due to External Far-Ultraviolet Radiation in Stellar Aggregates. *ApJ*, 611:360–379.

Adams, F. C., Lada, C. J., and Shu, F. H. (1987). Spectral evolution of young stellar objects. *ApJ*, 312:788–806.

Aikawa, Y. and Nomura, H. (2006). Physical and Chemical Structure of Protoplanetary Disks with Grain Growth. *ApJ*, 642:1152–1162.

Aikawa, Y., Umebayashi, T., Nakano, T., and Miyama, S. M. (1999). Evolution of Molecular Abundances in Protoplanetary Disks with Accretion Flow. *ApJ*, 519:705–725.

Akiyama, E., Momose, M., Kitamura, Y., Tsukagoshi, T., Shimada, S., Koyamatsu, S., and Hayashi, M. (2013). An Observational Study of the Temperature and Surface Density Structures of a Typical Full Disk around MWC 480. *PASJ*, 65:123.

Alexander, R. D., Clarke, C. J., and Pringle, J. E. (2006). Photoevaporation of protoplanetary discs - I. Hydrodynamic models. *MNRAS*, 369:216–228.

ALMA Partnership, Brogan, C. L., Pérez, L. M., Hunter, T. R., Dent, W. R. F., Hales, A. S., Hills, R. E., Corder, S., Fomalont, E. B., Vlahakis, C., Asaki, Y., Barkats, D., Hirota, A., Hodge, J. A., Impellizzeri, C. M. V., Kneissl, R., Liuzzo, E., Lucas, R., Marcelino, N., Matsushita, S., Nakanishi, K., Phillips, N., Richards, A. M. S., Toledo, I., Aladro, R., Broguiere, D., Cortes, J. R., Cortes, P. C., Espada, D., Galarza, F., Garcia-Appadoo, D., Guzman-Ramirez, L., Humphreys, E. M., Jung, T., Kameno, S., Laing, R. A., Leon, S., Marconi, G., Mignano, A., Nikolic, B., Nyman, L.-A., Radiszcz, M., Remijan, A., Rodón, J. A., Sawada, T., Takahashi, S., Tilanus, R. P. J., Vila Vilaro, B., Watson, L. C., Wiklind, T., Akiyama, E., Chapillon, E., de Gregorio-Monsalvo, I., Di Francesco, J., Gueth, F., Kawamura, A., Lee, C.-F., Nguyen Luong, Q., Mangum, J., Pietu, V., Sanhueza, P., Saigo, K., Takakuwa, S., Ubach, C., van Kempen, T., Wootten, A., Castro-Carrizo, A., Francke, H., Gallardo, J., Garcia, J., Gonzalez, S., Hill, T., Kaminski, T., Kurono, Y., Liu, H.-Y., Lopez, C., Morales, F., Plarre, K., Schieven, G., Testi, L., Videla, L., Villard, E., Andreani, P., Hibbard, J. E., and Tatematsu, K. (2015). The 2014 ALMA Long Baseline Campaign: First Results from High Angular

Resolution Observations toward the HL Tau Region. *ApJL*, 808:L3.

Alves de Oliveira, C., Ábrahám, P., Marton, G., Pinte, C., Kiss, C., Kun, M., Kóspál, Á., André, P., and Könyves, V. (2013). Herschel survey of brown dwarf disks in ρ Ophiuchi. *A&A*, 559:A126.

Andrews, S. M., Rosenfeld, K. A., Kraus, A. L., and Wilner, D. J. (2013). The Mass Dependence between Protoplanetary Disks and their Stellar Hosts. *ApJ*, 771:129.

Andrews, S. M. and Williams, J. P. (2007). High-Resolution Submillimeter Constraints on Circumstellar Disk Structure. *ApJ*, 659:705–728.

Andrews, S. M., Wilner, D. J., Hughes, A. M., Qi, C., and Dullemond, C. P. (2009). Protoplanetary Disk Structures in Ophiuchus. *ApJ*, 700:1502–1523.

Andrews, S. M., Wilner, D. J., Hughes, A. M., Qi, C., and Dullemond, C. P. (2010). Protoplanetary Disk Structures in Ophiuchus. II. Extension to Fainter Sources. *ApJ*, 723:1241–1254.

Andrews, S. M., Wilner, D. J., Zhu, Z., Birnstiel, T., Carpenter, J. M., Pérez, L. M., Bai, X.-N., Öberg, K. I., Hughes, A. M., Isella, A., and Ricci, L. (2016). Ringed Substructure and a Gap at 1 au in the Nearest Protoplanetary Disk. *ApJL*, 820:L40.

Ansdell, M., Williams, J. P., Trapman, L., van Terwisga, S. E., Facchini, S., Manara, C. F., van der Marel, N., Miotello, A., Tazzari, M., Hogerheijde, M., Guidi, G., Testi, L., and van Dishoeck, E. F. (2018). ALMA Survey of Lupus Protoplanetary Disks II: Gas Disk Radii. *ArXiv e-prints*.

Armitage, P. J. (2007). Lecture notes on the formation and early evolution of planetary systems. *ArXiv Astrophysics e-prints*.

Armitage, P. J. (2015). Physical processes in protoplanetary disks. *ArXiv e-prints*.

Artymowicz, P. and Lubow, S. H. (1994). Dynamics of binary-disk interaction. 1: Resonances and disk gap sizes. *ApJ*, 421:651–667.

Banzatti, A., Pinilla, P., Ricci, L., Pontoppidan, K. M., Birnstiel, T., and Ciesla, F. (2015). Direct Imaging of the Water Snow Line at the Time of Planet Formation using Two ALMA Continuum Bands. *ApJL*, 815:L15.

Bate, M. R. (2009). Stellar, brown dwarf and multiple star properties from hydrodynamical simulations of star cluster formation. *MNRAS*, 392:590–616.

Bayo, A., Joergens, V., Liu, Y., Brauer, R., Olofsson, J., Arancibia, J., Pinilla, P., Wolf, S., Ruge, J. P., Henning, T., Natta, A., Johnston, K. G., Bonnefoy, M., Beuther, H., and Chauvin, G. (2017). First Millimeter Detection of the Disk around a Young, Isolated, Planetary-mass Object. *ApJL*, 841:L11.

Beckwith, S. and Sargent, A. (1987). Interferometric images of ^{13}CO emission toward HL Tau. In Appenzeller, I. and Jordan, C., editors, *Circumstellar Matter*, volume 122 of *IAU Symposium*, pages 81–83.

Beckwith, S. V. W. and Sargent, A. I. (1991). Particle emissivity in circumstellar disks. *ApJ*, 381:250–258.

Beckwith, S. V. W., Sargent, A. I., Chini, R. S., and Guesten, R. (1990). A survey for circumstellar disks around young stellar objects. *AJ*, 99:924–945.

Benisty, M., Juhasz, A., Boccaletti, A., Avenhaus, H., Milli, J., Thalmann, C., Dominik, C., Pinilla, P., Buenzli, E., Pohl, A., Beuzit, J.-L., Birnstiel, T., de Boer, J., Bonnefoy, M., Chauvin, G., Christiaens, V., Garufi, A., Grady, C., Henning, T., Huelamo, N., Isella, A., Langlois, M., Ménard, F., Mouillet, D., Olofsson, J., Pantin, E., Pinte, C., and Pueyo, L. (2015). Asymmetric features in the protoplanetary disk MWC 758. *A&A*, 578:L6.

Bergin, E. A., Cleeves, L. I., Crockett, N., and Blake, G. A. (2014). Exploring the Origins of Carbon in Terrestrial Worlds. *Faraday Discussions*, 168.

Berrilli, F., Corciulo, G., Ingrosso, G., Lorenzetti, D., Nisini, B., and Strafella, F. (1992). Infrared emission from dust structures surrounding Herbig Ae/Be stars. *ApJ*, 398:254–272.

Birnstiel, T. and Andrews, S. M. (2014). On the Outer Edges of Protoplanetary Dust Disks. *ApJ*, 780:153.

Birnstiel, T., Klahr, H., and Ercolano, B. (2012). A simple model for the evolution of the dust population in protoplanetary disks. *A&A*, 539:A148.

Bjorkman, J. E. and Wood, K. (2001). Radiative Equilibrium and Temperature Correction in Monte Carlo Radiation Transfer. *ApJ*, 554:615–623.

Blum, J. and Wurm, G. (2000). Experiments on Sticking, Restructuring, and Fragmentation of Preplanetary Dust Aggregates. *Icarus*, 143:138–146.

Bohlin, R. C., Savage, B. D., and Drake, J. F. (1978). A survey of interstellar H I from L-alpha absorption measurements. II. *ApJ*, 224:132–142.

Boley, A. C. and Durisen, R. H. (2010). On the Possibility of Enrichment and Differentiation in Gas Giants During Birth by Disk Instability. *ApJ*, 724:618–639.

Boneberg, D. M., Facchini, S., Clarke, C. J., Ilee, J. D., Booth, R. A., and Bruderer, S. (2018). The extremely truncated circumstellar disc of V410 X-ray 1: a precursor to TRAPPIST-1? *MNRAS*, 477:325–334.

Boneberg, D. M., Panić, O., Haworth, T. J., Clarke, C. J., and Min, M. (2016). Determining the mid-plane conditions of circumstellar discs using gas and dust modelling: a study of HD 163296. *MNRAS*, 461:385–401.

Booth, R. A. and Clarke, C. J. (2016). Collision velocity of dust grains in self-gravitating protoplanetary discs. *MNRAS*, 458:2676–2693.

Boss, A. P. and Yorke, H. W. (1996). Protoplanetary Disks, Mid-Infrared Dips, and Disk Gaps. *ApJ*, 469:366.

Bouwman, J., de Koter, A., van den Ancker, M. E., and Waters, L. B. F. M. (2000). The composition of the circumstellar dust around the Herbig Ae stars AB Aur and HD 163296.

A&A, 360:213–226.

Breslau, A., Steinhausen, M., Vincke, K., and Pfalzner, S. (2014). Sizes of protoplanetary discs after star-disc encounters. *A&A*, 565:A130.

Bruderer, S. (2013). Survival of molecular gas in cavities of transition disks. I. CO. *A&A*, 559:A46.

Bruderer, S., van Dishoeck, E. F., Doty, S. D., and Herczeg, G. J. (2012). The warm gas atmosphere of the HD 100546 disk seen by Herschel. Evidence of a gas-rich, carbon-poor atmosphere? *A&A*, 541:A91.

Bulger, J., Patience, J., Ward-Duong, K., Pinte, C., Bouy, H., Ménard, F., and Monin, J.-L. (2014). The Taurus Boundary of Stellar/Substellar (TBOSS) Survey. I. Far-IR disk emission measured with Herschel. *A&A*, 570:A29.

Chiang, E. I. and Goldreich, P. (1997). Spectral Energy Distributions of T Tauri Stars with Passive Circumstellar Disks. *ApJ*, 490:368–376.

Cieza, L. A., Casassus, S., Tobin, J., Bos, S. P., Williams, J. P., Perez, S., Zhu, Z., Caceres, C., Canovas, H., Dunham, M. M., Hales, A., Prieto, J. L., Principe, D. A., Schreiber, M. R., Ruiz-Rodriguez, D., and Zurlo, A. (2016). Imaging the water snow-line during a protostellar outburst. *Nature*, 535:258–261.

Clarke, C. J. (2007). The photoevaporation of discs around young stars in massive clusters. *MNRAS*, 376:1350–1356.

Clayton, G. C., Wolff, M. J., Sofia, U. J., Gordon, K. D., and Misselt, K. A. (2003). Dust Grain Size Distributions from MRN to MEM. *ApJ*, 588:871–880.

Cohen, M. and Witteborn, F. C. (1985). Spectrophotometry at 10 microns of T Tauri stars. *ApJ*, 294:345–356.

Collings, M. P., Anderson, M. A., Chen, R., Dever, J. W., Viti, S., Williams, D. A., and McCoustra, M. R. S. (2004). A laboratory survey of the thermal desorption of astrophysically relevant molecules. *MNRAS*, 354:1133–1140.

Cutri, R. M., Skrutskie, M. F., van Dyk, S., Beichman, C. A., Carpenter, J. M., Chester, T., Cambresy, L., Evans, T., Fowler, J., Gizis, J., Howard, E., Huchra, J., Jarrett, T., Kopan, E. L., Kirkpatrick, J. D., Light, R. M., Marsh, K. A., McCallon, H., Schneider, S., Stiening, R., Sykes, M., Weinberg, M., Wheaton, W. A., Wheelock, S., and Zacarias, N. (2003). *2MASS All Sky Catalog of point sources.*

Cuzzi, J. N., Dobrovolskis, A. R., and Champney, J. M. (1993). Particle-gas dynamics in the midplane of a protoplanetary nebula. *Icarus*, 106:102.

D'Alessio, P., Calvet, N., and Hartmann, L. (2001). Accretion Disks around Young Objects. III. Grain Growth. *ApJ*, 553:321–334.

D'Antona, F. and Mazzitelli, I. (1997). Evolution of low mass stars. *Mem. Soc. Astron. Italiana*, 68:807.

Dartois, E., Dutrey, A., and Guilloteau, S. (2003). Structure of the DM Tau Outer Disk: Probing the vertical kinetic temperature gradient. *A&A*, 399:773–787.

de Gregorio-Monsalvo, I., Ménard, F., Dent, W., Pinte, C., López, C., Klaassen, P., Hales, A., Cortés, P., Rawlings, M. G., Tachihara, K., Testi, L., Takahashi, S., Chapillon, E., Mathews, G., Juhasz, A., Akiyama, E., Higuchi, A. E., Saito, M., Nyman, L.-Å., Phillips, N., Rodón, J., Corder, S., and Van Kempen, T. (2013). Unveiling the gas-and-dust disk structure in HD 163296 using ALMA observations. *A&A*, 557:A133.

Dent, W. R. F., Greaves, J. S., and Coulson, I. M. (2005). CO emission from discs around isolated HAeBe and Vega-excess stars. *MNRAS*, 359:663–676.

Dionatos, O. (2015). Gas line observations of disks. In *European Physical Journal Web of Conferences*, volume 102 of *European Physical Journal Web of Conferences*, page 00008.

Dominik, C. (2015). Disk formation and structure. In *European Physical Journal Web of Conferences*, volume 102 of *European Physical Journal Web of Conferences*, page 00002.

Draine, B. T. (2003). Scattering by Interstellar Dust Grains. I. Optical and Ultraviolet. *ApJ*, 598:1017–1025.

Draine, B. T. (2006). On the Submillimeter Opacity of Protoplanetary Disks. *ApJ*, 636:1114–1120.

Du, F., Bergin, E. A., Hogerheijde, M., van Dishoeck, E. F., Blake, G., Bruderer, S., Cleeves, I., Dominik, C., Fedele, D., Lis, D. C., Melnick, G., Neufeld, D., Pearson, J., and Yıldız, U. (2017). Survey of Cold Water Lines in Protoplanetary Disks: Indications of Systematic Volatile Depletion. *ApJ*, 842:98.

Du, F., Bergin, E. A., and Hogerheijde, M. R. (2015). Volatile depletion in the TW Hydrae disk atmosphere. *ApJL*, 807:L32.

Dubrulle, B., Morfill, G., and Sterzik, M. (1995). The dust subdisk in the protoplanetary nebula. *Icarus*, 114:237–246.

Dullemond, C. (2013). Lecture notes "Radiative transfer in astrophysics", Summer 2013. http://www.ita.uni-heidelberg.de/~dullemond/lectures/radtrans_2013/index.shtml, accessed: 2018-02-26.

Dullemond, C. P. (2002). The 2-D structure of dusty disks around Herbig Ae/Be stars. I. Models with grey opacities. *A&A*, 395:853–862.

Dullemond, C. P. and Dominik, C. (2004). The effect of dust settling on the appearance of protoplanetary disks. *A&A*, 421:1075–1086.

Dullemond, C. P. and Dominik, C. (2005). Dust coagulation in protoplanetary disks: A rapid depletion of small grains. *A&A*, 434:971–986.

Dullemond, C. P., Hollenbach, D., Kamp, I., and D'Alessio, P. (2007). Models of the Structure and Evolution of Protoplanetary Disks. *Protostars and Planets V*, pages 555–572.

Dutrey, A., Guilloteau, S., Duvert, G., Prato, L., Simon, M., Schuster, K., and Menard, F.

(1996). Dust and gas distribution around T Tauri stars in Taurus-Auriga. I. Interferometric 2.7mm continuum and ˆ13ˆCO J=1-0 observations. *A&A*, 309:493–504.

Dutrey, A., Guilloteau, S., and Simon, M. (1994). Images of the GG Tauri rotating ring. *A&A*, 286:149–159.

Elitzur, M., Asensio Ramos, A., and Ceccarelli, C. (2012). Rotating discs and non-kinematic double peaks. *MNRAS*, 422:1394–1402.

Evans, M. G., Ilee, J. D., Hartquist, T. W., Caselli, P., Szűcs, L., Purser, S. J. D., Boley, A. C., Durisen, R. H., and Rawlings, J. M. C. (2017). Gravitational instabilities in a protosolar-like disc - II. Continuum emission and mass estimates. *MNRAS*, 470:1828–1847.

Fabrycky, D. C., Lissauer, J. J., Ragozzine, D., Rowe, J. F., Steffen, J. H., Agol, E., Barclay, T., Batalha, N., Borucki, W., Ciardi, D. R., Ford, E. B., Gautier, T. N., Geary, J. C., Holman, M. J., Jenkins, J. M., Li, J., Morehead, R. C., Morris, R. L., Shporer, A., Smith, J. C., Still, M., and Van Cleve, J. (2014). Architecture of Kepler's Multi-transiting Systems. II. New Investigations with Twice as Many Candidates. *ApJ*, 790:146.

Facchini, S., Birnstiel, T., Bruderer, S., and van Dishoeck, E. F. (2017a). Different dust and gas radial extents in protoplanetary disks: consistent models of grain growth and CO emission. *A&A*, 605:A16.

Facchini, S., Pinilla, P., van Dishoeck, E. F., and de Juan Ovelar, M. (2017b). Inferring giant planets from ALMA mm continuum and line observations in (transition) disks. *ArXiv e-prints*.

Favre, C., Cleeves, L. I., Bergin, E. A., Qi, C., and Blake, G. A. (2013). A Significantly Low CO Abundance toward the TW Hya Protoplanetary Disk: A Path to Active Carbon Chemistry? *ApJL*, 776:L38.

Fedele, D., Carney, M., Hogerheijde, M. R., Walsh, C., Miotello, A., Klaassen, P., Bruderer, S., Henning, T., and van Dishoeck, E. F. (2017). ALMA unveils rings and gaps in the protoplanetary system <ASTROBJ>HD 169142</ASTROBJ>: signatures of two giant protoplanets. *A&A*, 600:A72.

Fedele, D., Tazzari, M., Booth, R., Testi, L., Clarke, C. J., Pascucci, I., Kospal, A., Semenov, D., Bruderer, S., Henning, T., and Teague, R. (2018). ALMA continuum observations of the protoplanetary disk AS 209. Evidence of multiple gaps opened by a single planet. *A&A*, 610:A24.

Fedele, D., van den Ancker, M. E., Henning, T., Jayawardhana, R., and Oliveira, J. M. (2010). Timescale of mass accretion in pre-main-sequence stars. *A&A*, 510:A72.

Flaherty, K. M., Hughes, A. M., Rosenfeld, K. A., Andrews, S. M., Chiang, E., Simon, J. B., Kerzner, S., and Wilner, D. J. (2015). Weak Turbulence in the HD 163296 Protoplanetary Disk Revealed by ALMA CO Observations. *ApJ*, 813:99.

Fleck, Jr., J. A. and Canfield, E. H. (1984). A random walk procedure for improving the

computational efficiency of the implicit Monte Carlo method for nonlinear radiation transport. *Journal of Computational Physics*, 54:508–523.

Font, A. S., McCarthy, I. G., Johnstone, D., and Ballantyne, D. R. (2004). Photoevaporation of Circumstellar Disks around Young Stars. *ApJ*, 607:890–903.

Forgan, D. and Rice, K. (2013). Towards a population synthesis model of objects formed by self-gravitating disc fragmentation and tidal downsizing. *MNRAS*, 432:3168–3185.

Fray, N. and Schmitt, B. (2009). Sublimation of ices of astrophysical interest: A bibliographic review. *Planet. Space Sci.*, 57:2053–2080.

Frerking, M. A., Langer, W. D., and Wilson, R. W. (1982). The relationship between carbon monoxide abundance and visual extinction in interstellar clouds. *ApJ*, 262:590–605.

Furuya, K. and Aikawa, Y. (2014). Reprocessing of Ices in Turbulent Protoplanetary Disks: Carbon and Nitrogen Chemistry. *ApJ*, 790:97.

Garcia Lopez, R., Tambovtseva, L. V., Schertl, D., Grinin, V. P., Hofmann, K.-H., Weigelt, G., and Caratti o Garatti, A. (2015). Probing the accretion-ejection connection with VLTI/AMBER. High spectral resolution observations of the Herbig Ae star HD 163296. *A&A*, 576:A84.

Garrod, R. T. and Pauly, T. (2011). On the Formation of CO_2 and Other Interstellar Ices. *ApJ*, 735:15.

Garufi, A., Quanz, S. P., Schmid, H. M., Avenhaus, H., Buenzli, E., and Wolf, S. (2014). Shadows and cavities in protoplanetary disks: HD 163296, HD 141569A, and HD 150193A in polarized light. *A&A*, 568:A40.

Gillon, M., Triaud, A. H. M. J., Demory, B.-O., Jehin, E., Agol, E., Deck, K. M., Lederer, S. M., de Wit, J., Burdanov, A., Ingalls, J. G., Bolmont, E., Leconte, J., Raymond, S. N., Selsis, F., Turbet, M., Barkaoui, K., Burgasser, A., Burleigh, M. R., Carey, S. J., Chaushev, A., Copperwheat, C. M., Delrez, L., Fernandes, C. S., Holdsworth, D. L., Kotze, E. J., Van Grootel, V., Almleaky, Y., Benkhaldoun, Z., Magain, P., and Queloz, D. (2017). Seven temperate terrestrial planets around the nearby ultracool dwarf star TRAPPIST-1. *Nature*, 542:456–460.

Grady, C. A., Devine, D., Woodgate, B., Kimble, R., Bruhweiler, F. C., Boggess, A., Linsky, J. L., Plait, P., Clampin, M., and Kalas, P. (2000). STIS Coronagraphic Imaging of the Herbig AE Star: HD 163296. *ApJ*, 544:895–902.

Greaves, J. S. (2004). Dense gas discs around T Tauri stars. *MNRAS*, 351:L99–L104.

Greenwood, A. J., Kamp, I., Waters, L. B. F. M., Woitke, P., Thi, W.-F., Rab, C., Aresu, G., and Spaans, M. (2017). Thermochemical modelling of brown dwarf discs. *A&A*, 601:A44.

Guidi, G., Tazzari, M., Testi, L., de Gregorio-Monsalvo, I., Chandler, C. J., Pérez, L., Isella, A., Natta, A., Ortolani, S., Henning, T., Corder, S., Linz, H., Andrews, S., Wilner, D., Ricci, L., Carpenter, J., Sargent, A., Mundy, L., Storm, S., Calvet, N., Dullemond, C., Greaves,

J., Lazio, J., Deller, A., and Kwon, W. (2016). Dust properties across the CO snowline in the HD 163296 disk from ALMA and VLA observations. *A&A*, 588:A112.

Gullbring, E., Hartmann, L., Briceño, C., and Calvet, N. (1998). Disk Accretion Rates for T Tauri Stars. *ApJ*, 492:323–341.

Gundlach, B. and Blum, J. (2015). The Stickiness of Micrometer-sized Water-ice Particles. *ApJ*, 798:34.

Hall, S. M., Clarke, C. J., and Pringle, J. E. (1996). Energetics of star-disc encounters in the non-linear regime. *MNRAS*, 278:303–320.

Harries, T. J. (2000). Synthetic line profiles of rotationally distorted hot-star winds. *MNRAS*, 315:722–734.

Harsono, D., Bruderer, S., and van Dishoeck, E. F. (2015). Volatile snowlines in embedded disks around low-mass protostars. *A&A*, 582:A41.

Hartmann, L., Calvet, N., Gullbring, E., and D'Alessio, P. (1998). Accretion and the Evolution of T Tauri Disks. *ApJ*, 495:385–400.

Haworth, T. (2010). Dissertation "Modelling Radiative Transfer In The Vicinity Of Massive Young Stars To Investigate Bipolar Cavity Structure", 2010. http://www.astro.ex.ac.uk/people/haworth/Dissertation.pdf, accessed: 2018-0306.

Haworth, T. J. and Harries, T. J. (2012). Radiation hydrodynamics of triggered star formation: the effect of the diffuse radiation field. *MNRAS*, 420:562–578.

Haworth, T. J., Ilee, J. D., Forgan, D. H., Facchini, S., Price, D. J., Boneberg, D. M., Booth, R. A., Clarke, C. J., Gonzalez, J.-F., Hutchison, M. A., Kamp, I., Laibe, G., Lyra, W., Meru, F., Mohanty, S., Panić, O., Rice, K., Suzuki, T., Teague, R., Walsh, C., Woitke, P., and Community authors (2016). Grand Challenges in Protoplanetary Disc Modelling. *Publ. Astron. Soc. Australia*, 33:e053.

Hendler, N. P., Mulders, G. D., Pascucci, I., Greenwood, A., Kamp, I., Henning, T., Ménard, F., Dent, W. R. F., and Evans, II, N. J. (2017). Hints for Small Disks around Very Low Mass Stars and Brown Dwarfs. *ApJ*, 841:116.

Henning, T. and Semenov, D. (2013). Chemistry in Protoplanetary Disks. *Chemical Reviews*, 113:9016–9042.

Herbig, G. H. (1960). The Spectra of Be- and Ae-Type Stars Associated with Nebulosity. *ApJS*, 4:337.

Herczeg, G. J., Cruz, K. L., and Hillenbrand, L. A. (2009). Measuring Tiny Mass Accretion Rates Onto Young Brown Dwarfs. *ApJ*, 696:1589–1599.

Herczeg, G. J. and Hillenbrand, L. A. (2014). An Optical Spectroscopic Study of T Tauri Stars. I. Photospheric Properties. *ApJ*, 786:97.

Hernández, J., Hartmann, L., Megeath, T., Gutermuth, R., Muzerolle, J., Calvet, N., Vivas, A. K., Briceño, C., Allen, L., Stauffer, J., Young, E., and Fazio, G. (2007). A Spitzer Space

Telescope Study of Disks in the Young σ Orionis Cluster. *ApJ*, 662:1067–1081.

Hersant, F., Wakelam, V., Dutrey, A., Guilloteau, S., and Herbst, E. (2009). Cold CO in circumstellar disks. On the effects of photodesorption and vertical mixing. *A&A*, 493:L49–L52.

Hogerheijde, M. R. and van der Tak, F. F. S. (2000). An accelerated Monte Carlo method to solve two-dimensional radiative transfer and molecular excitation. With applications to axisymmetric models of star formation. *A&A*, 362:697–710.

Hollenbach, D., Johnstone, D., Lizano, S., and Shu, F. (1994). Photoevaporation of disks around massive stars and application to ultracompact H II regions. *ApJ*, 428:654–669.

Huang, J., Öberg, K. I., Qi, C., Aikawa, Y., Andrews, S. M., Furuya, K., Guzmán, V. V., Loomis, R. A., van Dishoeck, E. F., and Wilner, D. J. (2017). An ALMA Survey of DCN/$H^{13}CN$ and $DCO^+/H^{13}CO^+$ in Protoplanetary Disks. *ApJ*, 835:231.

Isella, A., Carpenter, J. M., and Sargent, A. I. (2009). Structure and Evolution of Pre-main-sequence Circumstellar Disks. *ApJ*, 701:260–282.

Isella, A., Guidi, G., Testi, L., Liu, S., Li, H., Li, S., Weaver, E., Boehler, Y., Carperter, J. M., De Gregorio-Monsalvo, I., Manara, C. F., Natta, A., Pérez, L. M., Ricci, L., Sargent, A., Tazzari, M., and Turner, N. (2016). Ringed Structures of the HD 163296 Protoplanetary Disk Revealed by ALMA. *Physical Review Letters*, 117(25):251101.

Isella, A., Testi, L., Natta, A., Neri, R., Wilner, D., and Qi, C. (2007). Millimeter imaging of HD 163296: probing the disk structure and kinematics. *A&A*, 469:213–222.

Jørgensen, J. K., Visser, R., Williams, J. P., and Bergin, E. A. (2015). Molecule sublimation as a tracer of protostellar accretion. Evidence for accretion bursts from high angular resolution $C^{18}O$ images. *A&A*, 579:A23.

Kama, M., Bruderer, S., van Dishoeck, E. F., Hogerheijde, M., Folsom, C. P., Miotello, A., Fedele, D., Belloche, A., Güsten, R., and Wyrowski, F. (2016). Volatile-carbon locking and release in protoplanetary disks. A study of TW Hya and HD 100546. *A&A*, 592:A83.

Kama, M., Folsom, C. P., and Pinilla, P. (2015). Fingerprints of giant planets in the photospheres of Herbig stars. *A&A*, 582:L10.

Kamp, I. (2015). Line radiative transfer and statistical equilibrium. In *European Physical Journal Web of Conferences*, volume 102 of *European Physical Journal Web of Conferences*, page 00010.

Kenyon, S. J. and Hartmann, L. (1987). Spectral energy distributions of T Tauri stars - Disk flaring and limits on accretion. *ApJ*, 323:714–733.

Krijt, S., Ciesla, F. J., and Bergin, E. A. (2016). Tracing Water Vapor and Ice During Dust Growth. *ApJ*, 833:285.

Lacy, J. H., Knacke, R., Geballe, T. R., and Tokunaga, A. T. (1994). Detection of absorption by H2 in molecular clouds: A direct measurement of the H2:CO ratio. *ApJL*, 428:L69–

L72.

Lada, C. J. and Wilking, B. A. (1984). The nature of the embedded population in the Rho Ophiuchi dark cloud - Mid-infrared observations. *ApJ*, 287:610–621.

Larson, R. B. and Starrfield, S. (1971). On the formation of massive stars and the upper limit of stellar masses. *A&A*, 13:190–197.

Lissauer, J. J., Ragozzine, D., Fabrycky, D. C., Steffen, J. H., Ford, E. B., Jenkins, J. M., Shporer, A., Holman, M. J., Rowe, J. F., Quintana, E. V., Batalha, N. M., Borucki, W. J., Bryson, S. T., Caldwell, D. A., Carter, J. A., Ciardi, D., Dunham, E. W., Fortney, J. J., Gautier, III, T. N., Howell, S. B., Koch, D. G., Latham, D. W., Marcy, G. W., Morehead, R. C., and Sasselov, D. (2011). Architecture and Dynamics of Kepler's Candidate Multiple Transiting Planet Systems. *ApJS*, 197:8.

Long, F., Herczeg, G. J., Pascucci, I., Drabek-Maunder, E., Mohanty, S., Testi, L., Apai, D., Hendler, N., Henning, T., Manara, C. F., and Mulders, G. D. (2017). An ALMA Survey of CO Isotopologue Emission from Protoplanetary Disks in Chamaeleon I. *ApJ*, 844:99.

Lucy, L. B. (1999). Computing radiative equilibria with Monte Carlo techniques. *A&A*, 344:282–288.

Luhman, K. L., Allen, P. R., Espaillat, C., Hartmann, L., and Calvet, N. (2010). The Disk Population of the Taurus Star-Forming Region. *ApJS*, 186:111–174.

Lynden-Bell, D. and Pringle, J. E. (1974). The evolution of viscous discs and the origin of the nebular variables. *MNRAS*, 168:603–637.

Manara, C. F., Rosotti, G., Testi, L., Natta, A., Alcalá, J. M., Williams, J. P., Ansdell, M., Miotello, A., van der Marel, N., Tazzari, M., Carpenter, J., Guidi, G., Mathews, G. S., Oliveira, I., Prusti, T., and van Dishoeck, E. F. (2016). Evidence for a correlation between mass accretion rates onto young stars and the mass of their protoplanetary disks. *A&A*, 591:L3.

Manara, C. F., Testi, L., Natta, A., and Alcalá, J. M. (2015). X-Shooter study of accretion in ρ-Ophiucus: very low-mass stars and brown dwarfs. *A&A*, 579:A66.

Mannings, V. and Sargent, A. I. (1997). A High-Resolution Study of Gas and Dust around Young Intermediate-Mass Stars: Evidence for Circumstellar Disks in Herbig Ae Systems. *ApJ*, 490:792–802.

Mathews, G. S., Klaassen, P. D., Juhász, A., Harsono, D., Chapillon, E., van Dishoeck, E. F., Espada, D., de Gregorio-Monsalvo, I., Hales, A., Hogerheijde, M. R., Mottram, J. C., Rawlings, M. G., Takahashi, S., and Testi, L. (2013). ALMA imaging of the CO snowline of the HD 163296 disk with DCO^+. *A&A*, 557:A132.

Mathis, J. S., Rumpl, W., and Nordsieck, K. H. (1977). The size distribution of interstellar grains. *ApJ*, 217:425–433.

McMullin, J. P., Waters, B., Schiebel, D., Young, W., and Golap, K. (2007). CASA Architec-

ture and Applications. In Shaw, R. A., Hill, F., and Bell, D. J., editors, *Astronomical Data Analysis Software and Systems XVI*, volume 376 of *Astronomical Society of the Pacific Conference Series*, page 127.

Meeus, G., Pinte, C., Woitke, P., Montesinos, B., Mendigutía, I., Riviere-Marichalar, P., Eiroa, C., Mathews, G. S., Vandenbussche, B., Howard, C. D., Roberge, A., Sandell, G., Duchêne, G., Ménard, F., Grady, C. A., Dent, W. R. F., Kamp, I., Augereau, J. C., Thi, W. F., and Tilling, I. (2010). Gas in the protoplanetary disc of HD 169142: Herschel's view. *A&A*, 518:L124.

Meijer, J. (2007). *Theoretical studies of the infrared emission properties of proto-planetary disks*. PhD thesis, University of Amsterdam.

Meijer, J., Dominik, C., de Koter, A., Dullemond, C. P., van Boekel, R., and Waters, L. B. F. M. (2008). A parameter study of self-consistent disk models around Herbig AeBe stars. *A&A*, 492:451–461.

Mendigutía, I., Mora, A., Montesinos, B., Eiroa, C., Meeus, G., Merín, B., and Oudmaijer, R. D. (2012). Accretion-related properties of Herbig Ae/Be stars. Comparison with T Tauris. *A&A*, 543:A59.

Mie, G. (1908). Beiträge zur Optik trüber Medien, speziell kolloidaler Metallösungen. *Annalen der Physik*, 330:377–445.

Min, M. (2015). Dust Opacities. In *European Physical Journal Web of Conferences*, volume 102 of *European Physical Journal Web of Conferences*, page 00005.

Min, M., Dullemond, C. P., Dominik, C., de Koter, A., and Hovenier, J. W. (2009). Radiative transfer in very optically thick circumstellar disks. *A&A*, 497:155–166.

Miotello, A., Bruderer, S., and van Dishoeck, E. F. (2014). Protoplanetary disk masses from CO isotopologue line emission. *A&A*, 572:A96.

Miyake, K. and Nakagawa, Y. (1993). Effects of particle size distribution on opacity curves of protoplanetary disks around T Tauri stars. *Icarus*, 106:20.

Mohanty, S., Greaves, J., Mortlock, D., Pascucci, I., Scholz, A., Thompson, M., Apai, D., Lodato, G., and Looper, D. (2013). Protoplanetary Disk Masses from Stars to Brown Dwarfs. *ApJ*, 773:168.

Monnier, J. D. and Millan-Gabet, R. (2002). On the Interferometric Sizes of Young Stellar Objects. *ApJ*, 579:694–698.

Mulders, G. D. (2013). *Radiative transfer models of protoplanetary disks: Theory vs. observations*. PhD thesis, University of Amsterdam, gdmulders@gmail.com.

Mulders, G. D. and Dominik, C. (2012). Probing the turbulent mixing strength in protoplanetary disks across the stellar mass range: no significant variations. *A&A*, 539:A9.

Muzerolle, J., Calvet, N., Briceño, C., Hartmann, L., and Hillenbrand, L. (2000). Disk Accretion in the 10 MYR Old T Tauri Stars TW Hydrae and Hen 3-600A. *ApJL*, 535:L47–L50.

Natta, A. and Testi, L. (2004). Grain Growth in Circumstellar Disks. In Johnstone, D., Adams, F. C., Lin, D. N. C., Neufeeld, D. A., and Ostriker, E. C., editors, *Star Formation in the Interstellar Medium: In Honor of David Hollenbach*, volume 323 of *Astronomical Society of the Pacific Conference Series*, page 279.

Natta, A., Testi, L., Calvet, N., Henning, T., Waters, R., and Wilner, D. (2007). Dust in Protoplanetary Disks: Properties and Evolution. *Protostars and Planets V*, pages 767–781.

Natta, A., Testi, L., Neri, R., Shepherd, D. S., and Wilner, D. J. (2004). A search for evolved dust in Herbig Ae stars. *A&A*, 416:179–186.

Öberg, K. I., Guzmán, V. V., Merchantz, C. J., Qi, C., Andrews, S. M., Cleeves, L. I., Huang, J., Loomis, R. A., Wilner, D. J., Brinch, C., and Hogerheijde, M. (2017). H_2CO Distribution and Formation in the TW HYA Disk. *ApJ*, 839:43.

Oppenheimer, B. R., Kulkarni, S. R., and Stauffer, J. R. (2000). Brown Dwarfs. *Protostars and Planets IV*, page 1313.

Ormel, C. W. and Cuzzi, J. N. (2007). Closed-form expressions for particle relative velocities induced by turbulence. *A&A*, 466:413–420.

Ormel, C. W., Liu, B., and Schoonenberg, D. (2017). Formation of TRAPPIST-1 and other compact systems. *A&A*, 604:A1.

Panić, O., Hogerheijde, M. R., Wilner, D., and Qi, C. (2008). Gas and dust mass in the disc around the Herbig Ae star HD 169142. *A&A*, 491:219–227.

Panić, O., Hogerheijde, M. R., Wilner, D., and Qi, C. (2009). A break in the gas and dust surface density of the disc around the T Tauri star IM Lupi. *A&A*, 501:269–278.

Panić, O. and Min, M. (2017). Effects of disc mid-plane evolution on CO snowline location. *MNRAS*, 467:1175–1185.

Panić, O., Ratzka, T., Mulders, G. D., Dominik, C., van Boekel, R., Henning, T., Jaffe, W., and Min, M. (2014). Resolving HD 100546 disc in the mid-infrared: Small inner disc and asymmetry near the gap. *A&A*, 562:A101.

Pérez, L. M., Carpenter, J. M., Andrews, S. M., Ricci, L., Isella, A., Linz, H., Sargent, A. I., Wilner, D. J., Henning, T., Deller, A. T., Chandler, C. J., Dullemond, C. P., Lazio, J., Menten, K. M., Corder, S. A., Storm, S., Testi, L., Tazzari, M., Kwon, W., Calvet, N., Greaves, J. S., Harris, R. J., and Mundy, L. G. (2016). Spiral density waves in a young protoplanetary disk. *Science*, 353:1519–1521.

Perez, S., Casassus, S., Ménard, F., Roman, P., van der Plas, G., Cieza, L., Pinte, C., Christiaens, V., and Hales, A. S. (2015). CO Gas Inside the Protoplanetary Disk Cavity in HD 142527: Disk Structure from ALMA. *ApJ*, 798:85.

Pinilla, P., Birnstiel, T., Benisty, M., Ricci, L., Natta, A., Dullemond, C. P., Dominik, C., and Testi, L. (2013). Explaining millimeter-sized particles in brown dwarf disks. *A&A*, 554:A95.

Pinilla, P., Quiroga-Nuñez, L. H., Benisty, M., Natta, A., Ricci, L., Henning, T., van der Plas, G., Birnstiel, T., Testi, L., and Ward-Duong, K. (2017). Millimeter Spectral Indices and Dust Trapping By Planets in Brown Dwarf Disks. *ApJ*, 846:70.

Pinte, C. (2015). Continuum radiative transfer. In *European Physical Journal Web of Conferences*, volume 102 of *European Physical Journal Web of Conferences*, page 00006.

Pringle, J. E. (1981). Accretion discs in astrophysics. *ARA&A*, 19:137–162.

Qi, C., D'Alessio, P., Öberg, K. I., Wilner, D. J., Hughes, A. M., Andrews, S. M., and Ayala, S. (2011). Resolving the CO Snow Line in the Disk around HD 163296. *ApJ*, 740:84.

Qi, C., Öberg, K. I., Andrews, S. M., Wilner, D. J., Bergin, E. A., Hughes, A. M., Hogherheijde, M., and D'Alessio, P. (2015). Chemical Imaging of the CO Snow Line in the HD 163296 Disk. *ApJ*, 813:128.

Qi, C., Öberg, K. I., and Wilner, D. J. (2013a). H_2CO and N_2H^+ in Protoplanetary Disks: Evidence for a CO-ice Regulated Chemistry. *ApJ*, 765:34.

Qi, C., Öberg, K. I., Wilner, D. J., D'Alessio, P., Bergin, E., Andrews, S. M., Blake, G. A., Hogerheijde, M. R., and van Dishoeck, E. F. (2013b). Imaging of the CO Snow Line in a Solar Nebula Analog. *Science*, 341:630–632.

Reboussin, L., Wakelam, V., Guilloteau, S., Hersant, F., and Dutrey, A. (2015). Chemistry in protoplanetary disks: the gas-phase CO/H_2 ratio and the carbon reservoir. *A&A*, 579:A82.

Rebull, L. M., Padgett, D. L., McCabe, C.-E., Hillenbrand, L. A., Stapelfeldt, K. R., Noriega-Crespo, A., Carey, S. J., Brooke, T., Huard, T., Terebey, S., Audard, M., Monin, J.-L., Fukagawa, M., Güdel, M., Knapp, G. R., Menard, F., Allen, L. E., Angione, J. R., Baldovin-Saavedra, C., Bouvier, J., Briggs, K., Dougados, C., Evans, N. J., Flagey, N., Guieu, S., Grosso, N., Glauser, A. M., Harvey, P., Hines, D., Latter, W. B., Skinner, S. L., Strom, S., Tromp, J., and Wolf, S. (2010). The Taurus Spitzer Survey: New Candidate Taurus Members Selected Using Sensitive Mid-Infrared Photometry. *ApJS*, 186:259–307.

Reipurth, B. and Clarke, C. (2001). The Formation of Brown Dwarfs as Ejected Stellar Embryos. *AJ*, 122:432–439.

Ricci, L., Isella, A., Andrews, S. M., Birnstiel, T., Cuzzi, J. N., D'Angelo, G., Dong, R., Dutrey, A., Ercolano, B., Estrada, P. R., Flock, M., Li, H., Liu, S.-F., Lyra, W., Oberg, K., Okuzumi, S., Perez, L., Turner, N., van der Marel, N., Wilner, D., Youdin, A. N., and Zhu, Z. (2018). Witnessing Planetary Systems in the Making with the Next Generation Very Large Array. *ArXiv e-prints*.

Ricci, L., Isella, A., Carpenter, J. M., and Testi, L. (2013). CARMA Interferometric Observations of 2MASS J044427+2512: The First Spatially Resolved Observations of Thermal Emission of a Brown Dwarf Disk. *ApJL*, 764:L27.

Ricci, L., Testi, L., Natta, A., and Brooks, K. J. (2010a). Dust grain growth in ρ-Ophiuchi

protoplanetary disks. *A&A*, 521:A66.

Ricci, L., Testi, L., Natta, A., Neri, R., Cabrit, S., and Herczeg, G. J. (2010b). Dust properties of protoplanetary disks in the Taurus-Auriga star forming region from millimeter wavelengths. *A&A*, 512:A15.

Ricci, L., Testi, L., Natta, A., Scholz, A., de Gregorio-Monsalvo, I., and Isella, A. (2014). Brown Dwarf Disks with ALMA. *ApJ*, 791:20.

Robitaille, T. P. (2010). On the modified random walk algorithm for Monte-Carlo radiation transfer. *A&A*, 520:A70.

Rodgers-Lee, D., Scholz, A., Natta, A., and Ray, T. (2014). The Herschel view of circumstellar discs: a multiwavelength study of Chamaeleon-I. *MNRAS*, 443:1587–1600.

Rodmann, J., Henning, T., Chandler, C. J., Mundy, L. G., and Wilner, D. J. (2006). Large dust particles in disks around T Tauri stars. *A&A*, 446:211–221.

Rosenfeld, K. A., Andrews, S. M., Hughes, A. M., Wilner, D. J., and Qi, C. (2013). A Spatially Resolved Vertical Temperature Gradient in the HD 163296 Disk. *ApJ*, 774:16.

Rosenfeld, K. A., Qi, C., Andrews, S. M., Wilner, D. J., Corder, S. A., Dullemond, C. P., Lin, S.-Y., Hughes, A. M., D'Alessio, P., and Ho, P. T. P. (2012). Kinematics of the CO Gas in the Inner Regions of the TW Hya Disk. *ApJ*, 757:129.

Rundle, D., Harries, T. J., Acreman, D. M., and Bate, M. R. (2010). Three-dimensional molecular line transfer: a simulated star-forming region. *MNRAS*, 407:986–1002.

Rybicki, G. B. and Lightman, A. P. (1979). *Radiative processes in astrophysics*.

Scally, A. and Clarke, C. (2001). Destruction of protoplanetary discs in the Orion Nebula Cluster. *MNRAS*, 325:449–456.

Schwarz, K. R., Bergin, E. A., Cleeves, L. I., Blake, G. A., Zhang, K., Öberg, K. I., van Dishoeck, E. F., and Qi, C. (2016). The Radial Distribution of H_2 and CO in TW Hya as Revealed by Resolved ALMA Observations of CO Isotopologues. *ApJ*, 823:91.

Semenov, D., Pavlyuchenkov, Y., Schreyer, K., Henning, T., Dullemond, C., and Bacmann, A. (2005). Millimeter Observations and Modeling of the AB Aurigae System. *ApJ*, 621:853–874.

Shakura, N. I. and Sunyaev, R. A. (1973). Black holes in binary systems. Observational appearance. *A&A*, 24:337–355.

Shu, F. H., Adams, F. C., and Lizano, S. (1987). Star formation in molecular clouds - Observation and theory. *ARA&A*, 25:23–81.

Simon, J. B., Bai, X.-N., Armitage, P. J., Stone, J. M., and Beckwith, K. (2013a). Turbulence in the Outer Regions of Protoplanetary Disks. II. Strong Accretion Driven by a Vertical Magnetic Field. *ApJ*, 775:73.

Simon, J. B., Bai, X.-N., Stone, J. M., Armitage, P. J., and Beckwith, K. (2013b). Turbulence in the Outer Regions of Protoplanetary Disks. I. Weak Accretion with No Vertical Magnetic

Flux. *ApJ*, 764:66.

Simon, J. B., Hughes, A. M., Flaherty, K. M., Bai, X.-N., and Armitage, P. J. (2015). Signatures of MRI-driven Turbulence in Protoplanetary Disks: Predictions for ALMA Observations. *ApJ*, 808:180.

Simon, M., Guilloteau, S., Di Folco, E., Dutrey, A., Grosso, N., Piétu, V., Chapillon, E., Prato, L., Schaefer, G. H., Rice, E., and Boehler, Y. (2017). Dynamical Masses of Low-mass Stars in the Taurus and Ophiuchus Star-forming Regions. *ApJ*, 844:158.

Smith, N., Bally, J., Licht, D., and Walawender, J. (2005). New Silhouette Disks with Reflection Nebulae and Outflows in the Orion Nebula and M43. *AJ*, 129:382–392.

Stamatellos, D. and Whitworth, A. P. (2009). The properties of brown dwarfs and low-mass hydrogen-burning stars formed by disc fragmentation. *MNRAS*, 392:413–427.

Stammler, S. M., Birnstiel, T., Panić, O., Dullemond, C. P., and Dominik, C. (2017). Redistribution of CO at the location of the CO ice line in evolving gas and dust disks. *A&A*, 600:A140.

Strom, K. M. and Strom, S. E. (1994). A multiwavelength study of star formation in the L1495E cloud in Taurus. *ApJ*, 424:237–256.

Takeuchi, T. and Lin, D. N. C. (2002). Radial Flow of Dust Particles in Accretion Disks. *ApJ*, 581:1344–1355.

Tazzari, M., Testi, L., Ercolano, B., Natta, A., Isella, A., Chandler, C. J., Pérez, L. M., Andrews, S., Wilner, D. J., Ricci, L., Henning, T., Linz, H., Kwon, W., Corder, S. A., Dullemond, C. P., Carpenter, J. M., Sargent, A. I., Mundy, L., Storm, S., Calvet, N., Greaves, J. A., Lazio, J., and Deller, A. T. (2016). Multiwavelength analysis for interferometric (sub-)mm observations of protoplanetary disks. Radial constraints on the dust properties and the disk structure. *A&A*, 588:A53.

Teague, R., Guilloteau, S., Semenov, D., Henning, T., Dutrey, A., Piétu, V., Birnstiel, T., Chapillon, E., Hollenbach, D., and Gorti, U. (2016). Measuring turbulence in TW Hydrae with ALMA: methods and limitations. *A&A*, 592:A49.

Testi, L., Natta, A., Scholz, A., Tazzari, M., Ricci, L., and de Gregorio Monsalvo, I. (2016). Brown dwarf disks with ALMA: Evidence for truncated dust disks in Ophiuchus. *A&A*, 593:A111.

Thi, W. F., Ménard, F., Meeus, G., Carmona, A., Riviere-Marichalar, P., Augereau, J.-C., Kamp, I., Woitke, P., Pinte, C., Mendigutía, I., Eiroa, C., Montesinos, B., Britain, S., and Dent, W. (2013). Nature of the gas and dust around 51 Ophiuchi. Modelling continuum and Herschel line observations. *A&A*, 557:A111.

Thi, W.-F., Pinte, C., Pantin, E., Augereau, J. C., Meeus, G., Ménard, F., Martin-Zaïdi, C., Woitke, P., Riviere-Marichalar, P., Kamp, I., Carmona, A., Sandell, G., Eiroa, C., Dent, W., Montesinos, B., Aresu, G., Meijerink, R., Spaans, M., White, G., Ardila, D., Lebreton, J.,

Mendigutía, I., and Brittain, S. (2014). Gas lines from the 5-Myr old optically thin disk around HD 141569A . Herschel observations and modeling. *A&A*, 561:A50.

Thi, W.-F., van Zadelhoff, G.-J., and van Dishoeck, E. F. (2004). Organic molecules in protoplanetary disks around T Tauri and Herbig Ae stars. *A&A*, 425:955–972.

Tilling, I., Woitke, P., Meeus, G., Mora, A., Montesinos, B., Riviere-Marichalar, P., Eiroa, C., Thi, W.-F., Isella, A., Roberge, A., Martin-Zaidi, C., Kamp, I., Pinte, C., Sandell, G., Vacca, W. D., Ménard, F., Mendigutía, I., Duchêne, G., Dent, W. R. F., Aresu, G., Meijerink, R., and Spaans, M. (2012). Gas modelling in the disc of HD 163296. *A&A*, 538:A20.

Toomre, A. (1964). On the gravitational stability of a disk of stars. *ApJ*, 139:1217–1238.

Tsukamoto, Y. (2018). Homepage of Yusuke Tsukamoto. http://milkyway.sci.kagoshima-u.ac.jp/tsukamoto/study_en.htm, accessed: 2018-01-25.

van Boekel, R., Waters, L. B. F. M., Dominik, C., Bouwman, J., de Koter, A., Dullemond, C. P., and Paresce, F. (2003). Grain growth in the inner regions of Herbig Ae/Be star disks. *A&A*, 400:L21–L24.

van den Ancker, M. E., de Winter, D., and Tjin A Djie, H. R. E. (1998). HIPPARCOS photometry of Herbig Ae/Be stars. *A&A*, 330:145–154.

van der Plas, G., Ménard, F., Ward-Duong, K., Bulger, J., Harvey, P. M., Pinte, C., Patience, J., Hales, A., and Casassus, S. (2016). Dust Masses of Disks around 8 Brown Dwarfs and Very Low-mass Stars in Upper Sco OB1 and Ophiuchus. *ApJ*, 819:102.

van Dishoeck, E. F. (2017). Astrochemistry: overview and challenges. *ArXiv e-prints*.

van Zadelhoff, G.-J., van Dishoeck, E. F., Thi, W.-F., and Blake, G. A. (2001). Submillimeter lines from circumstellar disks around pre-main sequence stars. *A&A*, 377:566–580.

van't Hoff, M. L. R., Walsh, C., Kama, M., Facchini, S., and van Dishoeck, E. F. (2017). Robustness of N_2H^+ as tracer of the CO snowline. *A&A*, 599:A101.

Visser, R., van Dishoeck, E. F., and Black, J. H. (2009). The photodissociation and chemistry of CO isotopologues: applications to interstellar clouds and circumstellar disks. *A&A*, 503:323–343.

Voelk, H. J., Jones, F. C., Morfill, G. E., and Roeser, S. (1980). Collisions between grains in a turbulent gas. *A&A*, 85:316–325.

Walsh, C., Juhász, A., Pinilla, P., Harsono, D., Mathews, G. S., Dent, W. R. F., Hogerheijde, M. R., Birnstiel, T., Meeus, G., Nomura, H., Aikawa, Y., Millar, T. J., and Sandell, G. (2014). ALMA Hints at the Presence of two Companions in the Disk around HD 100546. *ApJL*, 791:L6.

Ward-Duong, K., Patience, J., Bulger, J., van der Plas, G., Ménard, F., Pinte, C., Jackson, A. P., Bryden, G., Turner, N. J., Harvey, P., Hales, A., and De Rosa, R. J. (2018). The Taurus Boundary of Stellar/Substellar (TBOSS) Survey. II. Disk Masses from ALMA Continuum Observations. *AJ*, 155:54.

Wehrse, R., Baschek, B., and von Waldenfels, W. (2000). The diffusion of radiation in moving media. I. Basic assumptions and formulae. *A&A*, 359:780–787.

Weidenschilling, S. J. (1980). Dust to planetesimals - Settling and coagulation in the solar nebula. *Icarus*, 44:172–189.

Weidenschilling, S. J. (1997). The Origin of Comets in the Solar Nebula: A Unified Model. *Icarus*, 127:290–306.

Weingartner, J. C. and Draine, B. T. (2001). Dust Grain-Size Distributions and Extinction in the Milky Way, Large Magellanic Cloud, and Small Magellanic Cloud. *ApJ*, 548:296–309.

Weintraub, D. A., Sandell, G., and Duncan, W. D. (1989). Submillimeter measurements of T Tauri and FU Orionis stars. *ApJL*, 340:L69–L72.

Whitworth, A., Bate, M. R., Nordlund, Å., Reipurth, B., and Zinnecker, H. (2007). The Formation of Brown Dwarfs: Theory. *Protostars and Planets V*, pages 459–476.

Williams, J. P. and Best, W. M. J. (2014). A Parametric Modeling Approach to Measuring the Gas Masses of Circumstellar Disks. *ApJ*, 788:59.

Williams, J. P. and Cieza, L. A. (2011). Protoplanetary Disks and Their Evolution. *ARA&A*, 49:67–117.

Wilson, T. L. (1999). Isotopes in the interstellar medium and circumstellar envelopes. *Reports on Progress in Physics*, 62:143–185.

Winter, A. J., Clarke, C. J., Rosotti, G., and Booth, R. A. (2018). Protoplanetary disc response to distant tidal encounters in stellar clusters. *MNRAS*, 475:2314–2325.

Woitke, P. (2015). Modelling and interpretation of SEDs. In *European Physical Journal Web of Conferences*, volume 102 of *European Physical Journal Web of Conferences*, page 00007.

Woitke, P., Kamp, I., and Thi, W.-F. (2009). Radiation thermo-chemical models of protoplanetary disks. I. Hydrostatic disk structure and inner rim. *A&A*, 501:383–406.

Woitke, P., Min, M., Pinte, C., Thi, W.-F., Kamp, I., Rab, C., Anthonioz, F., Antonellini, S., Baldovin-Saavedra, C., Carmona, A., Dominik, C., Dionatos, O., Greaves, J., Güdel, M., Ilee, J. D., Liebhart, A., Ménard, F., Rigon, L., Waters, L. B. F. M., Aresu, G., Meijerink, R., and Spaans, M. (2016). Consistent dust and gas models for protoplanetary disks. I. Disk shape, dust settling, opacities, and PAHs. *A&A*, 586:A103.

Woitke, P., Riaz, B., Duchêne, G., Pascucci, I., Lyo, A.-R., Dent, W. R. F., Phillips, N., Thi, W.-F., Ménard, F., Herczeg, G. J., Bergin, E., Brown, A., Mora, A., Kamp, I., Aresu, G., Brittain, S., de Gregorio-Monsalvo, I., and Sandell, G. (2011). The unusual protoplanetary disk around the T Tauri star ET Chamaeleontis. *A&A*, 534:A44.

Wolf, S. and Voshchinnikov, N. V. (2004). Mie scattering by ensembles of particles with very large size parameters. *Computer Physics Communications*, 162:113–123.

Wood, K., Lada, C. J., Bjorkman, J. E., Kenyon, S. J., Whitney, B., and Wolff, M. J. (2002).

Infrared Signatures of Protoplanetary Disk Evolution. *ApJ*, 567:1183–1191.

Wright, C. M., Maddison, S. T., Wilner, D. J., Burton, M. G., Lommen, D., van Dishoeck, E. F., Pinilla, P., Bourke, T. L., Menard, F., and Walsh, C. (2015). Resolving structure of the disc around HD100546 at 7 mm with ATCA. *MNRAS*, 453:414–438.

Wright, E. L., Eisenhardt, P. R. M., Mainzer, A. K., Ressler, M. E., Cutri, R. M., Jarrett, T., Kirkpatrick, J. D., Padgett, D., McMillan, R. S., Skrutskie, M., Stanford, S. A., Cohen, M., Walker, R. G., Mather, J. C., Leisawitz, D., Gautier, III, T. N., McLean, I., Benford, D., Lonsdale, C. J., Blain, A., Mendez, B., Irace, W. R., Duval, V., Liu, F., Royer, D., Heinrichsen, I., Howard, J., Shannon, M., Kendall, M., Walsh, A. L., Larsen, M., Cardon, J. G., Schick, S., Schwalm, M., Abid, M., Fabinsky, B., Naes, L., and Tsai, C.-W. (2010). The Wide-field Infrared Survey Explorer (WISE): Mission Description and Initial On-orbit Performance. *AJ*, 140:1868–1881.

Wyatt, M. C. (2008). Evolution of Debris Disks. *ARA&A*, 46:339–383.

Youdin, A. N. and Lithwick, Y. (2007). Particle stirring in turbulent gas disks: Including orbital oscillations. *Icarus*, 192:588–604.

Zinnecker, H. and Yorke, H. W. (2007). Toward Understanding Massive Star Formation. *ARA&A*, 45:481–563.